Benchmarking a single-stem PIV endoscope in a spray

by

Neetin Lad

Thesis submitted for the degree of

Doctor of Philosophy

at the University of Leicester

September 2011

To my darling Preena

ABSTRACT

Neetin Lad.
Benchmarking a single-stem PIV endoscope in a spray.

Flows with a limited optical access for PIV measurement can be probed using endoscopic PIV techniques. Conventional endoscopic PIV utilises two separate probes, one to relay a light sheet and the other to provide imaging optics to capture a two-dimensional image of the flow.

This research aims to validate the velocity measurements taken from the novel single-stem endoscopic PIV system. The specific objectives are to determine the accuracy of the single-stem endoscopic PIV result, identify any shortcomings in the technique, and identify improvements for future single-stem endoscopic PIV systems.

The single-stem endoscopic PIV system is applied to an atomised spray flow and velocity measurements are compared with conventional PIV and Pitot-static data. The endoscopic PIV system provides localised velocity maps that are comparable with the measurements from the conventional PIV system. This comparison is based on the spray ensemble mean flow field and its fluctuating velocity component statistics. A detailed analysis on the hardware setup, image capture, calibration and pre/post processing techniques is carried out to identify possible sources of systematic error in the measurement and how the measurement uncertainty accumulates.

The mean velocity vector map, recorded from the single-stem endoscopic PIV system was used to estimate the spray mass flow rate and its entrainment characteristics, the centreline velocity decay, and the spreading rate similar to the corresponding estimates from conventional PIV. Furthermore estimates of the localised Strouhal number and of the spray fluctuation are also compared.

By considering the measurement uncertainty as an accumulation of a series of component uncertainties, this study has identified and quantified the uncertainty contribution from each component. The largest sources of uncertainty are primarily due to two components. The first is the optical aberration, which leads to image defocusing and reduction in particle identification. The second component is the larger uncertainty source which is the uneven illumination of the measurement plane.

ACKNOWLEDGEMENTS

My special gratitude goes to my supervisor, Professor Abdelwahab Aroussi, who introduced me to the project and helped me obtain an excellent skill base which goes beyond those presented in this research. Not to forget the numerous opportunities provided to present research internationally to both the academic and industrial sectors.

I deeply appreciate the guidance from Dr. Aldo Rona, who put aside much of his time to work closely on this research. His expertise in jet flows and analysis techniques has been an invaluable input to this study.

I also must acknowledge all the members of the University of Leicester's engineering technical staff. In particular, Mr. Dipak Raval, Mr. Alan Wale, Mr. Paul Willams, Mr Julian Jones, Mr. Ian Bromley, Mr. Simon Millward and of course not to mention Mr. Pete Barwell. Without men like these no amount of experimental research could have been achieved. Their humour is not too bad either.

I would like to thank all the members of the PROVAEN consortium for sponsoring the project their inputs throughout the study.

I need to express my thanks to the 'Aroussi team', David, Lanre, Nora and Farid. All the academic discussions, the debates and also your general company have made a huge contribution to my research over the years. I wish you all the luck in the future.

Also I cannot forget my mother, father, my two wonderful sisters, my brother-in-law, my beautiful niece and intelligent nephew, for without their encouragement patience, comfort and financial support this experience may not have even started let alone finish. Without them I would not be where I am today.

A special thanks to my dearest, Preena Mistry, always there for me when I needed her most. Her patience is overwhelming. Her love, always encouraging and never faltering, the most perfect muse one could hope for.

And finally, thanks to all friends and family who are not mentioned here, you were always with me.

TABLE OF CONTENTS

NOMENCLATURE

A	Area (m^2)
$\mathbf{a}$	Acceleration
b	Jet half width
Ca	Capillary number
c_i	Sensitivity coefficient, $ci = \partial f/\partial x_i$
$\mathbf{D}$	Particle displacement within flow field
$\mathscr{F}$	Fourier transform operator
f	Frequency
F	Lens focal length
$f\#$	Lens F-number
F_o	Out-of-plane loss of correlation
$\mathbf{g}$	Gravitational Component (m/s^2)
H	Distance between the target surface and nozzle orifice
I, I'	Image intensity field of first and second exposure
k	Wavenumber
L_r	Distance of reference image (pixels)
l_r	Distance of reference point (mm)
l_t	Distance from target to lens (mm)
$\dot{m}$	Mass flow rate
n	Number of samples
Oh	Ohnesorge Number
P	Pressure
P_1, P_2	Correlation Peaks
q	Mei scattered normalised diameter
r, r_{vis}	Radius and visible radius of the jet
R_m	Jet momentum ratio
R_C	Mean background correlation
R_D	Displacement of correlation peak

Re	Reynolds number
R_F	Noise term due to random particle correlations
$R_{II'}$	Spatial cross-correlation
R_τ	Correlation of a particle image
$\mathbf{s}$	Separation vector in the correlation plane
$S_{II'}$	Spectrum of particle images
St	Strouhal number
T	Temperature (K)
t	Time (s)
t'	Time of second exposure (s)
U′	Fourier transform of u'
u'	Instantaneous velocity
u, v, w	Velocity components in x, y, z (m/s)
u_s	Particle velocity lag
We	Weber number
$\mathbf{X}$	Point in flow field
$\mathbf{x}$	Point in the image plane
x, y, z	Cartesian co-ordinates

Greek Symbols

Δ	Incremental value
μ	Dynamic viscosity (Ns/m^2)
α	Magnification factor (mm/pixel)
$\mathbf{\Gamma}$	State of the ensemble
δ	Standard uncertainty
ε	Combined uncertainty
θ	Perspective viewing angle for the captured image.
λ	Wavelength
ν	Kinematic viscosity (m^2/s)
ρ	Density (kg/m^3)
ϕ	Mass flux ratio
γ	Surface tension

σ_m	Measurement uncertainty
$\boldsymbol{\tau}$	Point spread function of the imaging lens
τ_F	Characteristic flow time
τ_s	Relaxation time
τ_V	Time response of particle

Subscripts

∞	Free stream value
0	Initial value
c	Centreline value
t	Time
u	Velocity
x	Displacement
p	Particle value
j	Spray exit conditions

Acronyms

ACC	Adaptive cross correlation
CI	Confidence interval
C-PIV	Conventional particle image velocimetry
DIA	Direct image analysis
DIC	Digital image correlation
IA	Interrogation area
PIV	Particle image velocimetry
SSE-PIV	Single-stem endoscopic particle image velocimetry

LIST OF FIGURES

LIST OF TABLES

CHAPTER 1: INTRODUCTION

1.1 Introduction to particle image velocimetry (PIV)

Particle image velocimetry (PIV) is a successful flow mapping technique that can optically quantify large portions of a flow regime. This enables the method to be completely non-intrusive in a well-designed experiment. The ability to perform non-intrusive anemometrical field measurements has allowed PIV to be used in a large range of industrial sectors for many applications. PIV equipment is very delicate and very expensive. It is most commonly used within controlled laboratory environments to avoid any contamination of the equipment and to ensure the proper laser alignment and the safety of the operator.

The PIV systems on the market today consist of a class 4, high power pulsed laser unit with outputs of 10-500 mJ. The laser unit is always secured to a firm base and the laser beam is manipulated via optics to illuminate the flow field. The second component is an imaging camera that can be triggered to capture an image via an external timing box. The camera should ideally be arranged perpendicular to the laser plane of illumination with a clear line of sight to the laser sheet. With the advancement in PIV equipment and capabilities, one can now map more than just the velocity field. Laser induced fluorescence can map velocity and temperature of each phase within a multiphase flow. Micro PIV can be used to quantify boundary layer flows. Time resolved PIV is used to accurately measure flow regimes that develop over time.

All these systems have a common limitation. A fundamental disadvantage of these conventional PIV techniques is that none can be used with flows which have no or limited optical access. This includes flows which occur in bearing chambers, in turbomachinery or enclosed pipes. To quantify these flows using PIV, transparent scale models are manufactured to replicate the flow to be investigated. The downside to this is that models can only provide a certain amount of accuracy, and can fall short from fully replicating the flow conditions experienced in industry.

1.2 Endoscopic PIV

Endoscopic PIV has been developed and used to overcome this barrier. Endoscopic PIV is carried out by relaying illumination and imaging optics through endoscopes or borescopes that can then access enclosed spaces via small bore holes. Due to this ability endoscopes have been used for visualisation in the medical sector for the past 50 years and also in combustion applications. Endoscopic PIV is conventionally approached using a two-probe method, that is, one for the light sheet optics and another for the imaging optics. In most cases these probes have very different setups, running parallel and offset or perpendicular to one another. In choosing the setup one must decide the point at which measurements are to be taken, given access areas and the optics available. It is most likely that some of these choices need some compromise to obtain optimum PIV analysis, for instance, adjusting to a less desirable measuring area that allows a two-probe access.

1.3 Single-stem endoscopic PIV

This study is part of an ongoing development of a newly developed single-stem endoscopic PIV system (SSE-PIV). The SSE-PIV integrates the imaging and light sheet optics through a single Ø10 mm cylindrical probe. The SSE-PIV system has a fixed laser sheet and camera viewing window which has a fixed focus position on the light sheet. This allows the laser sheet thickness to match the camera focal depth. The camera focus position is set to focus on the light sheet. Once the system is calibrated, it can be used in flow applications without further calibration steps. The primary advantage of the system is that it is contained in a single probe and hence only requires a single access port for measurements in a confined space. The SSE-PIV system can be used in industrial applications beyond the laboratory environment as shown in **Error! Reference source not found.**.

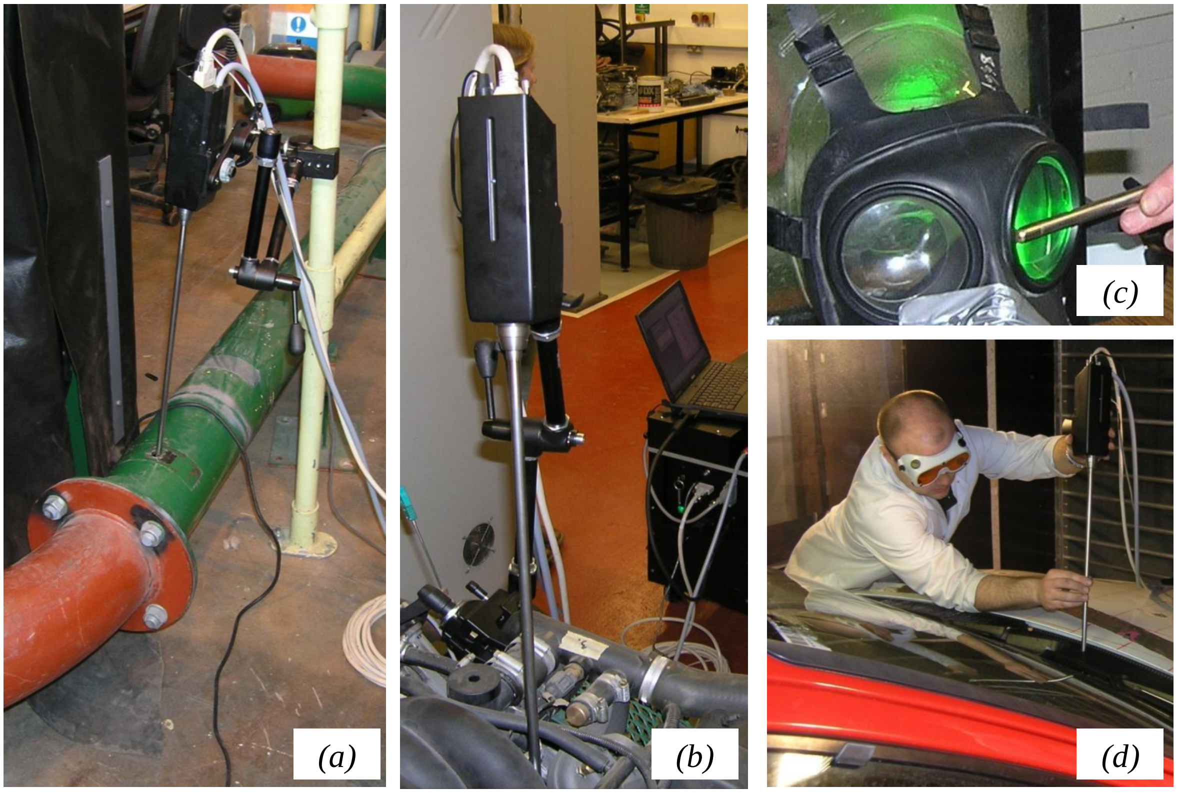

Figure 1.1: SSE-PIV used within industrial applications: *(a)* Particle conveying in pipe flows, *(b)* air transport within the automotive engine bay, *(c)* air convection within gas masks, *(d)* flow through the engine cowl. Images courtesy of Prof. A. Aroussi.

The primary aim of this research is to validate the measurements recorded by the SSE-PIV system to aid its development and use in industrial applications. To achieve this, the velocity measurements recorded using SSE-PIV are directly compared to reference results obtained by a conventional PIV (C-PIV) method. The test case selected for this validation is a free fully turbulent atomised spray flow. This flow has been chosen as it is very common in industry. Its complex flow field provides a challenge to the SSE-PIV system. The spray flow is also mapped using C-PIV and by Pitot anemometry.

1.4 SSE-PIV development programme

The current work was part of a research consortium (PROVAEN), where all partners contribute to the development of a patent produced by Aroussi and Menacer (2004) in to a marketable product. The patent provides the design parameters for a novel single-stem endoscopic PIV (SSE-PIV) probe and is now owned by Olympus Keymed Ltd. The idea involves integrating the laser illumination and image optics into a single probe for the effective purpose of visualisation and quantification of enclosed flow regimes. The consortium consists of many development areas such as the imaging optics (Olympus Keymed Ltd.), PIV software (Dantec Dynamics), Transportation of laser energy via optical cables, (Laser Zentrum Hannover e.V.), production and deliverance of the laser beam (Litron Lasers) and testing, feedback and surface improvement (University of Leicester).

The improvement to past endoscopic PIV applications is that the SSE-PIV tool only requires one access point within a casing to measure the flow within an enclosed flow system. Olympus Keymed Ltd. developed a prototype SSE-PIV system which has a fully integrated illumination and imaging optics within a 10mm diameter probe. This tool has never been validated in-terms of its capability and accuracy of measurement within industrial style flows.

From the outline of the consortium the SSE-PIV measurement tool is to be rigorously tested within industrial style flows, that is, fluid dynamic scenarios which represent flows which appear in real industrial applications. Four flow regimes were identified. These are 1) Jet flows which have been used for many applications from paint spraying and cleaning to internal combustion. 2) Single phase annular flows which represent flows which appear in bearing chambers and in turbomachinery. 3) Pipe flows which involve gas or gas-solid transport which represent coal conveyance in power generation systems. 4) Complex multiphase re-circulating and swirling flows which is most commonly found in particulate separation applications such as flotation cells or particle classification systems. While testing within these flow systems a detailed review of the obtained PIV data and the intrusive effects of the endoscope on the PIV data is reviewed to provide information to assist in the development of the first generation SSE-PIV.

The research provided in this study provides an in depth analysis of the data obtained by SSE-PIV within jet flows (test case 1) only. The data is compared to more established conventional PIV measurements against a reference result from Pitot anemometry. For the purpose of testing the SSE-PIV probe in a jet flow, consideration of the type of jet was needed. The choice of the jet used in this work is based on a common use within industrial applications. A common jet (or spray) system used industry is the spraying of diesel fuel. The reason for this is that these types of sprays usually occur within confined equipment where the flow regime is not accessible for non intrusive optical measuring techniques.

1.5 Relationship of present project to other work

In parallel to the work carried out to produce this thesis, a series of studies were produced by colleagues at the University of Leicester, who are also part of the consortium, to assist in the development of future test cases. This includes the characterisation of the above mentioned test cases 2-4 and impact of the SSE-PIV probe in said flow regimes.

For test case 2 Adebayo *et al*. (2009) and Adebayo *et al*. (2010) characterised the flow within an annular cavity both numerically and experimentally. To assist in test case 3 Aroussi *et al*. (2009) and Aroussi *et al*. (2010) determined the transport phenomena of particulate within air flow within pipes and cyclones. The characterisation of a laboratory scale flotation cell, test case 4, has been carried out by Lad *et al.* (2008a), Aroussi et al. (2009b) and Lad *et al.* (2010b) These base line laboratory experiments were characterised to provide a base line flow regime which can be compared using SSE-PIV and C-PIV.

A brief study of uniform single phase flow from a wind tunnel around a normally positioned cylindrical probe which represents the endoscope has been carried out by Aroussi *et al*. (2008) and Lad *et al*. (2008b). Adebayo *et al*. (2008a) furthered the development of the SSE-PIV probe by identifying and applying various passive control techniques which were then applied to a 10mm diameter shaft. The effect of the passive flow control techniques on the reduction of flow disturbances which propagate from the dummy SSE-PIV probe is then quantified. This work was carried out to reduce the impact the SSE-PIV probe has on the surrounding fluid.

Lad *et al*. (2010), Lad *et al*. (2010c), Lad *et al*. (2010d) Muhamad *et al*. (2009), Lad *et al*. (2011b) and Lad *et al*. (2011c) provide a series of publications which characterise an atomised spray flow and implement the passive control techniques observed by Adebayo *et al*. (2008a). The work carried out determines the effect of a 10mm diameter circular cylinder, which represents the endoscopic PIV, being placed within an atomised spray flow along the spray centreline within the fully developed region.

Adebayo *et al*. (2008a) and Adebayo *et al*. (2008b) applied these same passive control techniques within an annular flow regime. The effect of which is to reduce the disturbances caused by the cylinder within an annulus i.e. remove the effect of the probe downstream of the flow within a certain circumferential distance.

Lad *et al*. (2009), Aroussi *et al*. (2010b), Lad *et al*. (2010e) and Lad *et al*. (2011a) have focused on the visualisation and quantification of a spray flow regime using the SSE-PIV system. The studies produced in (2009) uses the first generation prototype from which a series of shortcomings in the optical quality and configuration, the data acquisition and illumination, which are indentified for further development. The same iterative process was repeated in Lad *et al*. (2010b) and Lad *et al*. (2010e). Due to the limitation to the time and resource limitation of the consortium agreement a final decision for the prototype optical configuration and baseline tests were carried out and can be found in Lad *et al*. (2011a).

The use of test case 2-4 and the implementation of a passive control technique to reduce the disturbance of the endoscopic PIV probe within the flow field will take place after the development of the components identified in this study has taken place.

1.6 Objectives & Contribution

The objectives of this thesis are to aid in the development of the SSE-PIV system by providing a rigorous calibration of the measurement and the image capture technique of SSE-PIV within a spray flow regime (test case 1, as mentioned in the development programme in section 1.4) against more established velocimetry standard measurement techniques. The spray flow system is to simulate sprays which occur within the range of diesel spray applications.

For the purpose of providing a benchmark for SSE-PIV tool by calibrating and validating the results against more well-established methods the spray system will not be confined. This is to allow optical access for conventional PIV measurements to take place.

This research provides comparative ensemble mean flow fields from both PIV techniques as well as a comparison of the measured unsteady spray characteristics. A detailed analysis on the hardware setup, image capture, calibration and pre/post processing techniques is carried out to identify sources driving the difference among measurements and how the measurement uncertainty is estimated in the SSE-PIV system.

This thesis gives the first systematic analysis of the sources of error in the SSE-PIV system and a framework for estimating the measurement uncertainty of the SSE-PIV system. It also identifies where future development efforts should be focused in upgrading the SSE-PIV system to obtain the greatest accuracy improvements.

The work is carried out in this study is part of an iterative process to assist in developing the SSE-PIV. The testing of the SSE-PIV system within other test cases (1-3) will commence after the successful integration of the elements outlined for development within this study.

1.7 Thesis layout

Chapter 2 provides a brief introduction to PIV and presents a review of endoscopic PIV for industrial applications. This review focuses on the experimental arrangement and the image output and analysis used in previous works. The review then identifies the motivations for developing a new single-stem endoscopic PIV system and thus the requirement for validating this new system to support its industrial use. Chapter 2 then covers the background of turbulent free jets, including empirical correlations used in previous work for describing the jet centreline velocity decay and the jet spreading rate.

Building upon the outline of PIV and of endoscopic PIV in Chapter 2, Chapter 3 discusses in detail the hardware and software used in C-PIV and in SSE-PIV experiments. Chapter 3 covers, in detail, the laser and the optical paths down the Ø10 mm SSE-PIV shaft and also provides a model representation of the image captured that explains the optical aberrations observed in the images acquired by the SSE-PIV system. Chapter 3 also provides a description to the pre and post-processing options available in the Dantec Dynamic Studio

PIV software suite, which was used for this work. The selected options used to carry out post processing of captured PIV images are identified in Chapter 4.

Chapter 4 focuses on the experimental setup. An experimental rig was set up to produce a fully turbulent free spray. This rig is instrumented using Pitot anemometry, C-PIV, and SSE-PIV. Chapter 4 reviews in detail the hardware supporting the instrumentation. Chapter 4 is concluded by a review of the PIV calibration and alignment methods along with preliminary results.

The results obtained from Pitot anemometry, C-PIV, and SSE-PIV are discussed in Chapter 5. The results identify the mean and temporal flow fields obtained by each measurement method. Pitot anemometry is used to validate the C-PIV measurements and thus making this result the ‘golden standard’. The SSE-PIV measurements are then compared to the ones from C-PIV.

Chapter 6 examines the uncertainty of the measurements obtained in Chapter 5. It quantifies the amount of uncertainty in the SSE-PIV measurements and compares it against the benchmark result from C-PIV. A detailed modelling of uncertainty inherent within the SSE-PIV system was conducted. This includes the system and acquisition uncertainty due to the optical, illumination and image calibration arrangement. The measurement uncertainty due to the number of samples and due to the selected image processing procedure is also modelled. Finally, the assessment of the amount of intrusion caused by the PIV probe of Ø10 mm and by the finite length on the SSE-PIV viewing window is presented.

Chapter 7 presents the conclusion on the outcomes of this study and identifies areas where the present research can be extended.

CHAPTER 2: LITERATURE REVIEW

2.1 Preface

As mentioned in chapter 1, the SSE-PIV tool is to be tested within industrial style flow regimes. As outlined in chapter 1 four test cases were identified. This research aims to calibrate and validate the SSE-PIV tool against more well established methods of flow quantification within a spray flow regime. The spray style in question resembles the characteristics of a diesel spray or fine coating applications. These test conditions are ideal as they appear commonly in industry and are usually assigned to enclosed conditions.

This chapter reviews the endoscopic particle image techniques used in past work in which the light sheet and the viewing optics are located in separate probes or passed through separate bore holes. The literature search also identifies the limitation and intrusion caused by using the two probe endoscopic PIV method. The main difference between these techniques and the single-stem PIV endoscope is detailed in chapter 3.

Secondly, before one may apply measurement techniques to a particular flow, one must study the general fluid characteristics and identify which properties to measure. In this chapter, the general characteristics and dynamics of sprays are described. The objective of this section is to give an overview of the main non-dimensional parameters that characterise a spray and introduce spray velocity profiles determined in previous works. As the spray flow is two-phase, this section introduces definitions of dispersed phase flows that apply specifically to droplet flows. A large amount of information on spray systems and atomisation is given by Lefebvre (1989). This provides the framework for understanding the physical processes of atomisation and gives useful guidelines for the atomiser structure and experimental design work presented in chapter 4.

This chapter then goes on to describe the some reviews on jets and sprays which are impinged by an obstacle. The reason for this is to firstly identify the correct positional placement of the endoscopic PIV probe within the spray with minimal intrusion, and the effects which may occur due to the flow disturbances caused by endoscopic PIV probe on the endoscopic view window.

2.2 Review of endoscopic PIV in applications

Although endoscopic PIV is relatively new compared to conventional PIV techniques it has been used in many research areas in the past. This section identifies the previous work which has been carried out in the past using the two-probe method endoscopic PIV.

Endoscopic PIV is carried out by aligning illumination and imaging optics through endoscopes or borescopes which can then access enclosed spaces via small bore holes. Due to this ability, endoscopes have been used for visualisation in the medical sector for the past 50. Applications of endoscopic PIV have been carried out in pore spaces by Klar *et al.* (2004). Klar *et al.* (2004) used fiberscopes in order to track the 3D motion of tracer particles within the pores of a gravel-bed. They successfully obtained a time series of the interstitial velocity components by spatial averaging of all instantaneous velocity vectors within the pore volume. However, fiberscopes, as compared with borescopes, have a low light transmittance and hence poor image resolution and contrast. Klar *et al.* (2004) thus concluded that the lack of illumination within the pore space was the biggest experimental limitation.

A similar limitation in endoscopic flow visualisation is also observed by Coutier-Delgosha and Devillers (2003). They used endoscopic visualisation to improve the understanding and to evaluate the local void ratio inside a sheet of cavitation which develops over a hydrofoil. Endoscopic visualisation was used due to the cloudiness of the image with classical methods of visualisation. The endoscopic field of view was 50°, and the focal length was 10 mm. This provided approximately a 9 mm diameter image. From this flow visualisation Coutier-Delgosha and Devillers (2003) discovered that, in the images obtained in the cavity wake, bubbles of vapour are clearly visible inside the mainly liquid medium. On the contrary, the images obtained inside the sheet of cavitation are filled with noise, as vapour bubbles too close to the endoscope mask and distort the image.

Miikkulainen *et al.* (2000) has studied the effect of a furnace environment on black liquor spray properties. Endoscopes were used to visualise and qualify the amount of spray break up within the furnace and compare it to visualized images preformed using a commercial camera and back lighting in a test chamber. Similar images were obtained between these two tests, although the endoscopic images have a poorer contrast and a large amount of vignetting and barrel distortion. The use of endoscopy within furnaces has also been carried out by Miikkulainen *et al.* (2004).

The use of water and nitrogen cooling jackets to protect the optical lenses has allowed the use of endoscopy to perform in flame monitoring in gas turbines and large-scale furnaces. Endoscopic PIV measurements of a high-temperature furnace were conducted by Rottier *et al.* (2010). The optical setup had a focal length of 14.3 mm and used a 2048 x 2048 pixel CCD imaging device. The entrance aperture was designed for thermal protection and also limited the vignetting (darkening of the image edge), however, it induced a low transmitted light flux. The raw image obtained showed a distinct barrel distortion. Corrected particle images were constructed in successive regions of 70 x 70 pixels, corresponding to 10 x 10 mm in the real object plane, by considering the equivalent trapezium in the raw image. PIV calculation was performed with a direct-image correction, which notably permits the use of rectangular interrogation windows in order to combine good spatial resolution and a large velocity dynamic range in the measurements. It was also noticed that, due to setup limitations, the full field of view of the optics could not be used, as increased light reflections occurred at the top and bottom of the image.

Kosasih *et al.* (2001) studied the flow of lubricant in bearing supply pockets using endoscopic PIV. An endoscope was attached to the CCD camera. The distorted image due to the endoscope optics causes inaccurate magnitude, direction, and positions of the velocity vectors. The endoscope was inserted normal to the bearing within the pocket cavity. The light sheet was generated by a pulsed Nd:YAG laser. Kosasih *et al.* (2001) also corrected the barrel distortion produced by the optics using vector-image correction.

A further example of the use of a borescope for PIV has been given by Culik (2010). A compressor was used to suck in air via an inlet duct to create a flow regime within a diffuser located downstream. The illumination device is a commercial laser system that angles the sheet via optics and slots through the compressor system. The imaging is carried out using the borescope connected to a timing box and a CCD camera. The research carried out only validated the use of the borescope. However, it was difficult to achieve repeatable results with this setup. The vector maps had numerous spurious vectors and surface reflection created a high amount of uncertainty. The positioning of the laser sheet was limited by the access port geometry and thus so was the borescope position, which ultimately produced poor PIV images.

Various setup configurations for endoscopic PIV are described for pipelines with bends or flow conditioners by Xiong and Merzkirch (1999), Xiong *et al.* (2003), and Ceccon *et al.* (2006). Studies of endoscopic PIV in internal combustion engines have been performed by Gindele and Spicher (1998), Nauwerck *et al.* (2000), Vattulainen *et al.* (2000), Dierksheide *et al.* (2001), Dierksheide *et al.* (2002), and Geis *et al.* (2002). Experiments in a low pressure turbine rig and turbomachinery have been performed by Wernet (2000)and Kegalj and Schiffer (2009).

In previous works intrusion within the flow was not necessarily an issue as the two probes used are stopped flush to the flow enclosure casing Dierksheide *et al.* (2001) enter the flow system and therefore have no real intrusion effects on the flow field. This was also the case in Blois *et al*. (2008) where the flow within a pore space was captured. The illumination source was applied downstream of the measurement area. in many of the mentioned cases the intrusion caused by the endoscope or boroscope using two probe endoscopic PIV is unmentioned. Kegali (2009) applied two-probe endoscopy to a low pressure turbine rig and placed both probes within the flow system. The illumination probe was upstream of the desired view window. The effects of which caused a similar problems as studies which report on flow around circular cylinders. Kegali (2009) used numerical simulation to discover the effects of blockage effect on the velocity observed within the view window. Kegali (2009) found that with an upstream velocity of 22 m/s, at 45 mm and 70 mm downstream of a 12 mm diameter probe a 1-2% and 1.5% deviation in velocity was observed respectively.

In all of the mentioned cases, endoscopic PIV was approached using a two-probe method, that is, one for the light sheet optics and another for the imaging optics. In all cases these probes have very different setups i.e. that is, they run parallel and offset or perpendicular to one another. In choosing the setup one must decide the point at which measurements are to be taken, given access areas and optics available. It is most likely that some of these choices need to be compromised to obtain the optimum PIV setup, for instance, by adjusting to a less desirable measuring area to allow probe access.

2.3 Spray flows

A spray is a dispersion of droplets with sufficient momentum to penetrate a surrounding medium. The dispersion device is usually a nozzle or an atomiser. Typically, the medium surrounding a spray is gaseous and the droplets are of liquid form. The spray has enough momentum to promote liquid droplet transport and promote mixing with the gaseous phase. The overall characteristics that define the spray functionality are usually the shape, patternation, and measurements of the droplet sizes. Sprays vary extensively depending on their use. The use of sprays is usually determined by the droplet size and by the spray momentum. Fine sprays are typically associated with combustion, fire suppression, and spray forming. In fine sprays, the droplet size range is $5\mu m < d_{0.5} < 80\mu m$ to achieve a rapid vaporisation. Increasing the droplet size range to $30\mu m < d_{0.5} < 370\mu m$ allows different spray processes to be undertaken, which include surface coating, usually in the form of paint, spray drying, and metal powder formation. Processes involving cleaning, de-scaling, or cooling of materials require high momentum impact and require much coarser sprays, in which the droplet size range is $350\ \mu m < d_{0.5} < 2000+\mu m$. The spray flow used for the testing of a single stem endoscope within this system has droplet sizes within the range 30 to 40

μm which situates the application of the spray within fine paint coatings and diesel spraying systems.

A "spray" is commonly described as any cloud of liquid droplets whilst a "jet" is a continuous column of fluid, which can be liquid or gas, which is in motion in a particular direction relative to the surrounding fluid. Within this study the spray is dispersed by injecting a continuous stream of liquid within a jet of carrier air. This would suggest that the droplets have no significant momentum of their own and it is the jet of carrier air which gives the spray its flow structure and thus its velocity distribution as axial distance increases. The liquid droplets are assumed to have no significant impact on the overall air jet structure and complete entrainment occurs. This type of spray system where atomised droplets are injected into the air jet is not uncommon. These types of sprays are seen in applications where the droplet mixing and surface coating is important. It is there for useful to control these processes by adjusting the air flow phase.

The liquid stream starts with lower velocity than the air stream at the point of injection, it is this initial velocity difference between the two phases that characterises the atomisation process and is quantified in non-dimensional form within the dimensionless parameters, which are defined further on in this section, and breaks up into small droplets which are then decelerated by aerodynamic drag until they are travelling at the same velocity as the air. The main assumption that is being made with the experimental setup is that this process is taking place well upstream of the part of the jet in which measurements are made. Due to the above assumptions the spray within this study can be treated as an air jet. Since the secondary phase has no significant impact on local momentum exchange between the air and liquid phase the spray structure is also to be jet like.

Therefore the literature in this study focuses on the droplet dynamic characteristics from sprays as to solidify the assumption of droplet behaviour to be similar to that of seeding particles, that is, droplets follow and have no impact on the overall air jet structure. Since it is determined that this spray behaves similar to that of an air jet it is important to determine the jet structures at various inlet conditions observed in past literature to be able to compare the jet like velocity distribution patterns observed from the spray within this study.

Sprays are typically defined by four non-dimensional parameters that are used to describe the overall conditions and governing forces acting on the spray. These are the spray momentum ratio, the gas phase Reynolds number, the aerodynamic Weber number, and the Ohnesorge number. The spray viscosity of the continuous gas phase to the viscosity of the dispersed spray phase is defined as the viscosity ratio and is shown in equation 2.1. The spray viscosity ratio affects many of the flow characteristics of the spray and is often used in correlations as a scalable, non-dimensional parameter to compare results across experiments.

$$R_{\mu} = \frac{\rho_{\mathrm{water}} \cdot u_{water}^{2}}{\rho_{\mathrm{air}} \cdot u_{air}^{2}} \tag{2.1}$$

The aerodynamic Weber number is a dimensionless number that defines the nature of the interaction in a flow where there is an interface between two phases. It is a measure of the fluid inertia compared to its surface tension. This quantity is useful in analyzing the formation of droplets and bubbles and is an indicator of the droplet breakup characteristics. The computation of the Weber number is shown by equation 2.2.

$$We = \frac{\rho_{\mathrm{air.}} u_{air}^{2} d_{e.}}{\gamma_{\mathrm{water}}} \tag{2.2}$$

where d_e is the nozzle equivalent diameter, u is the velocity of the continuous phase relative to that of the dispersed phase, and γ is the surface tension of the dispersed phase. At very low Weber numbers, near the critical value of about 6, the droplet surface becomes unsteady and may break up into two new droplets of equal size. For Weber numbers between 25 and 50, the new droplets become a bag shape and, as the Weber number increases, the bag will allow the stripping and forming of secondary smaller droplets. As the Weber number exceeds 50, there is a catastrophic droplet break up. More information on droplet break up is given by Lefebvre (1989) and Stiesch (2003). The air phase Reynolds number, *Re*, is defined in equation 2.3, where the terms for density, ρ, velocity, u, and dynamic viscosity μ refer to the air phase. d_e is the nozzle equivalent diameter. The Reynolds number in a spray characterises the turbulence and the kinetic energy of the flow in a scalable, non-dimensional fashion.

$$Re = \frac{\rho u d_e}{\mu} \tag{2.3}$$

The Ohnesorge number describes the dispersed phase characteristics by providing a non-dimensional ratio of the viscous forces to the square root of the internal and surface tension forces, as shown by equation 2.4.

$$Oh = \frac{\mu_{\text{water}}}{\sqrt{\rho_{\text{water}}.\, d_e.\, \gamma_{\text{water}}}} \tag{2.4}$$

The Ohnesorge number defines the rate of momentum exchange and the ability of the spray to become unstable. This dimensionless group may also be usefully viewed as a Reynolds number based on a characteristic capillary velocity, defined by $u_{cap}=\gamma/\mu$. Coating operations and spraying operations with Newtonian fluids are fully parameterized by the values of the Capillary number, $Ca=\mu u/\gamma$, and *Oh*, as discussed in Quéré (1999) and Basaran (2002). However, other combinations of these dimensionless parameters may also be used. Studies of high-speed jet breakup are commonly reported in terms of the *We* and *Oh* numbers.

The purpose of identifying the dimensionless parameters is to find resemblance between the spray used within this research against sprays used within industrial applications. The use of dimensionless parameters allows the dynamic scaling and the comparison of results with publications already available in the wider field. For the purpose of testing, the spray system used in test case 1 will equivalent to that of a diesel spray injection used within combustion applications or of a fine paint sprayer for accurate coatings.

However, spray structures are more complex than what can be parameterised by these four parameters, as the dispersed phase has its own local mass, momentum, and energy balance. Since it has been assumed that the droplet impact on the spray structure is minimal and no local exchange between phases occur the spray structure is not complex and behaves more jet like. Therefore, a more detailed analysis of the spray structure and of the dispersed phase characteristics will be covered in sections 2.3.1 and 2.3.2.

2.3.1 Structure of a turbulent free spray

As mentioned previously the spray within this study consists of droplets which are entrained by the carrier air. The spray structure is determined to be similar to that of an air jet. This section reviews the jet structures which have been reported in past work. McNaughton and Sinclair (1966) report four characteristic flow regimes for free jets. The dissipated laminar jet regime occurs at $Re_j<300$. At this flow regime, the viscous forces are large compared to the inertial forces and the jet diffuses rapidly into the surrounding fluid. Fully laminar jets occurs over the range $300<Re_j<1000$. Over this range there is no noticeable diffusion of the jet into the surrounding fluid. This is followed by the transitional or semi-turbulent jet regime at $1000<Re_j<3000$ and, finally, by the fully turbulent jet regime, at $Re_j>3000$. These regimes are further detailed by Polat *et al.* (1989) and Gauntner *et al.* (1970).

The structure of a turbulent free spray, also commonly referred to as a turbulent free jet, has been extensively reviewed by Pai (1952), Birkhoff and Zarantonello (1957), Abramovich (1963), Becker *et al.* (1967), Donaldson and Snedeker (1971), Rajaratnam (1976), Everitt and Robins (1978), Boguslawski and Popiel (1979), Fleckhaus *et al.* (1987). When considering the effect of the flow compressibility through a nozzle or slot, three flow regimes are possible, which are supersonic, sonic, and subsonic.

A subsonic jet is characterised by a nozzle pressure ratio in the range of $1.0 < P_0/P_\infty < 1.89$. In a subsonic jet, the pressure everywhere in the jet, including the throat pressure, P, is equal to the free stream pressure, P_∞. The jet is characterised by a potential core, surrounded by a mixing region. The radius of this potential core decreases to zero with increasing downstream distance, x, from the nozzle exit plane. Beyond this point, the jet goes through a transitional phase as it continues to expand, as its centreline velocity decays, in order to conserve axial momentum, and will eventually reach a fully developed, self-similar state.

It is very difficult to find a common agreement among the subsonic jet structures from past experiments due to the number of variables involved in determining the inlet conditions.

The nozzle or atomiser shape, the liquid viscosity and density, the mass flux, volume fraction, and the temperature all affect the jet structure. These difficulties are shown by the results of Kotsovinos (1976), who reported a non-linear jet spreading rate. Specifically, the jet spreading rate was reported to vary from db/dx=0.0913 at x<60b to db/dx=0.14 at $x>600b_0$, where b is the jet half width (where $u= 0.5u_c$) and u_c is the centreline velocity, as shown diagrammatically in figure 2.1. Schlichting (1968) states that b is proportional to the streamwise direction, x, multiplied by a constant. Bradbury (1965) suggested that the increase in the jet spreading rate was due to the fall in the mean velocity and turbulence intensity of the jet reaching the same order of magnitude as the velocity fluctuations of the draught in the laboratory background environment. Bradbury (1965) also reported that the increase in spreading rate corresponds to a background turbulent intensity of 0.5% of the inlet velocity. A typical axi-symmetric subsonic jet structure is sketched in Figure 2.1 where r is the radial component.

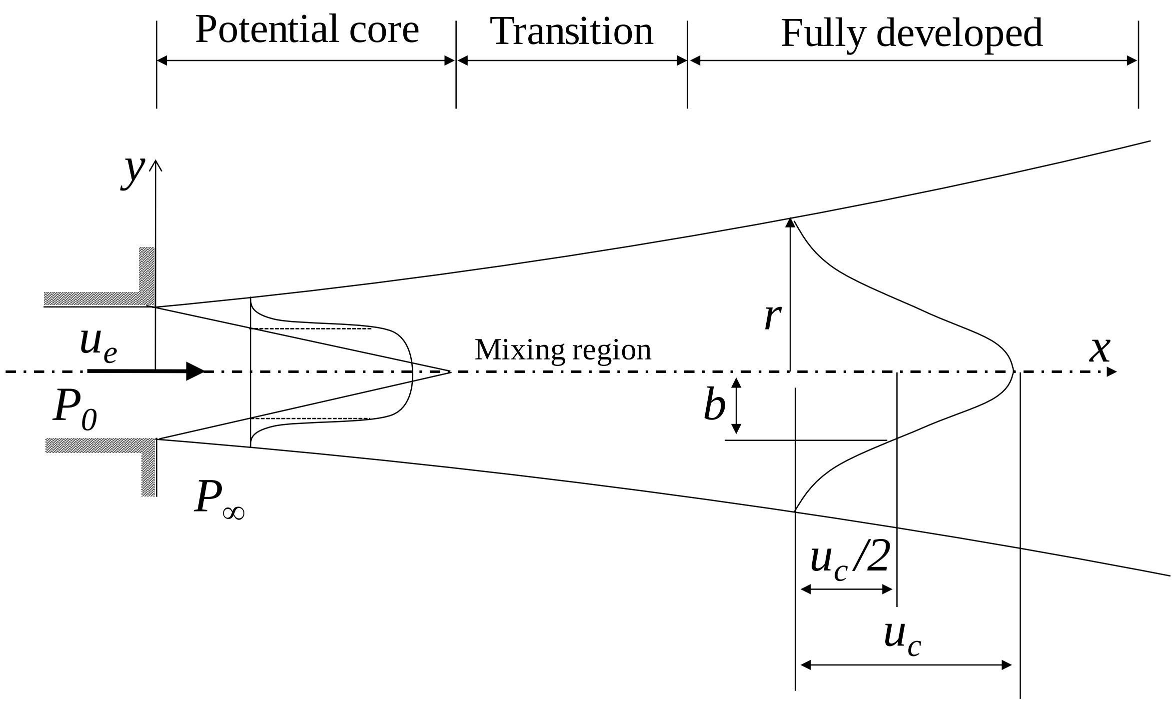

Figure 2.1: Schematic of an axi-symmetric jet from a subsonic nozzle, reproduced from Donaldson *et al.* (1971).

The boundaries of the expanding jet are diverging, due to the mixing with the ambient air. The tangential shear in the mixing region defined in figure 2.1 reduces the velocity of the jet and increases the velocity of the surrounding ambient air. By neglecting viscous forces in the mixing region, it can be assumed that the jet mean velocity profile becomes self-similar as the jet disperses downstream of the potential core. The self-similar mean velocity profile downstream of the nozzle has been modelled by many experimentalists in the past. Each model differs slightly, due to the variation in the jet characteristics. A summary of the self-similar velocity profiles used in past literature is given in table 2.1 and models for the centreline velocity decay with axial distance are given in table 2.2.

Table 2.1: Gaussian velocity profile models in subsonic jets.

Description	**Model**	**Source**	
Half Gaussian velocity profile in established flow region.	$\frac{u}{u_c} = e^{\left(-\frac{r^2}{2\sigma^2}\right)}$	Tabrizi (1996)	2.5
Half Gaussian velocity profile in established flow region.	$\frac{u}{u_e} = e^{-\left(\frac{r^2}{b^2}\right)}$	Lee (2003)	2.6

Table 2.2: Centreline velocity decay profile models in subsonic jets.

Description	**Model**	**Source**	
Using a simple average of α = 0.10. α varied from 0.09-0.12 (from Forthman (1936)).	$\frac{u_c}{u_e} = \frac{3.78}{\sqrt{x/b}}$	Abramovich (1963)	2.7
Using a 0.5 x 10 cm slot.	$\frac{u_c}{u_e} = \frac{3.52}{\sqrt{(x+b)/b}}$	Van der Hegge Zijnen (1958)	2.8
Using a 1 x 25cm slot.	$\frac{u_c}{u_e} = \frac{3.12}{\sqrt{(x+2.40b)/b}}$	Van der Hegge Zijnen (1958)	2.9
Using results from Reichardt (1951), σ = 7.67.	$\frac{u_c}{u_e} = \frac{3.39}{\sqrt{x/b}}$	Reichardt (1951)	2.10
Using own experiments.	$\frac{u_c}{u_e} = \frac{3.24}{\sqrt{x/b}}$	Albertson *et al.* (1950)	2.11
Assuming self similar velocity profiles in all sections of the principal area of the jet.	$\frac{u_c}{u_e} = \frac{1.21}{\sqrt{\alpha}} \cdot \frac{1}{\sqrt{x/b}}$	Tollmien (1945)	2.12

From the jet centreline decay rate, assuming a self similar profile, the jet spreading rate, db/dx is obtained analytically. The jet spreading rate is defined as db/dx. With increasing distance from the nozzle exit, the velocity of the centreline decreases and the curve of the velocity profile asymptotes to u=0. By the conservation of axial momentum in the jet as the centreline velocity decays, the jet spreads radially with increasing axial distance. Assuming a streamwise self-similar axial velocity profile, an axi-symmetric jet spreads laterally at a linear rate while its centreline velocity, u_c, varies inversely with axial distance. Chhabra *et al.* (2005) proposed a time-averaged self-similar streamwise velocity profile for axi-symmetric free jets in the form of the Gaussian profile of equation 2.13, where b is the local jet width at the 1/e point of the Gaussian profile.

$$u = u_c e^{-\left(\frac{r^2}{b^2}\right)} \qquad 2.13$$

This expression is close to the self-similar velocity profile used by Seiner and Ponton (1985) who studied the aerodynamics of high Reynolds numbers of supersonic jets. They defined a self-similar streamwise velocity profile as the half Gaussian curve of equation 2.14.

$$\frac{u}{u_c} = e^{\left(-\ln(2)\eta^2\right)} \quad , \quad \eta = \frac{r-h}{b} \qquad 2.14$$

In equation 2.14, h is the radius of the potential core, which is zero in the fully developed jet region. This gives $\eta=r/b$, making equation 2.14 similar to equation 2.13. In this study, the Seiner and Ponton (1985) spread rate model will be used.

2.3.2 Dynamics of the dispersed phase

This section outlines some of the critical factors that govern the behaviour of droplet motion within spray regimes. A large amount of information on multiphase flows with droplets and particles can be found in Crowe *et al.* (1998) and Kleinstreuer (2003).

Sprays can be characterised into two categories, dilute and dense. A dilute dispersed phase flow is one in which the particle motion is controlled by the fluid forces of drag and lift.

Dilute sprays can be best characterised as a multiphase flow in which the transport phenomena of the dispersed-phase elements, i.e. the liquid drops, are approximately the same as those for isolated drops immersed in an identical local flow. This implies a wide spacing between droplets within the continuous gaseous phase that gives a low volume fraction. The wide spacing implies that the collisions between droplets are infrequent and the mass, momentum, and energy balances of individual droplets are independent. In sprays, regions of liquid volume fractions greater than 10 % are typically located immediately downstream of the injector. Further detail on the effect of a dilute/dense spray, structure and behaviour of droplet break up properties, and jet mixing properties in atomised sprays are given in Faeth (1987), Faeth (1991), Faeth (1996), Faeth *et al.* (1995), Ruff *et al.* (1988), Ruff *et al.* (1991), and Ruff *et al.* (1992). Further downstream, the spray becomes more dilute. In a dense spray, the spacing between droplets are reduced, therefore the transport of the dispersed phase is dependent on droplet collision. Dense sprays are more susceptible to droplet coalescence and break up, which affect the dispersed phase transport. A spray system is termed dilute or dense depending on the volume fraction of the dispersed phase against the continuous gaseous phase. By considering a water droplet and air spray mixture within a control volume δV, the volume fraction of the dispersed phase (water) is defined by equation 2.15 and equivalently the volume fraction of the air continuous phase is defined by equation 2.16. The sum of the volume fractions of both phases within the spray system is unity, $\Delta_{\text{air}} + \Delta_{\text{water}} = 1$.

$$\Delta_{\text{water}} = \lim_{\delta V \to \delta V^0} \frac{\delta V_{\text{water}}}{\delta V} \qquad 2.15$$

$$\Delta_{\text{air}} = \lim_{\delta V \to \delta V^0} \frac{\delta V_{\text{air}}}{\delta V} \qquad 2.16$$

where δV^o is the limiting volume that ensures a stationary average. Another important parameter required to define dispersed flows is the mass concentration factor (C). The mass concentration value is the ratio of the dispersed phase density, ρ_{water}, to the continuous phase density, ρ_{air}.

The droplet loading, also known as the mass flux ratio (ϕ), is the ratio of the mass flow rate of the dispersed phase, $\dot{m}_{\text{water}}$, to the mass flow rate of the continuous phase $\dot{m}_{\text{air}}$. The mechanics of a dispersed flow depends significantly on the mean distance between each droplet. The distance between the droplets determines whether each droplet can be treated in isolation. If the diameter of the droplet is d_{p} and the distance between the neighbouring droplets is L, the distance between neighbouring droplets L in a dispersed flow can be estimated using the relationship in equation 2.17, where $k=C\rho_{\text{air}}/\rho_{\text{water}}$. This value is only a first estimate, since it assumes the arrangement of droplets within the dispersed phase form a perfect face centre cubic lattice arrangement.

$$\frac{L}{d_p} = \left(\frac{\pi}{6}\frac{1+k}{k}\right)^{\frac{1}{3}} \tag{2.17}$$

The droplet dynamics of the disperse phase is governed by the ability for the droplet to respond to changes in the continuous phase velocity. The Stokes number, related to the particle velocity, determines how close the particle velocity follows that of the continuous phase. It is defined as the ratio of the particle momentum response time over the flow system time, $St=\tau_V/\tau_F$ where τ_F is some characteristic flow time and τ_V is the momentum response time defined in equation 2.18.

$$\tau_V = \frac{\rho_{\text{water}} d_{\text{water}}^2}{18\mu_{\text{air}}} \tag{2.18}$$

where μ_{air} is the continuous phase viscosity.

2.3.3 Spray flow impingement on a surface

Spray flow impingement of a surface has been critically reviewed within this section to identify whether the single-stem endoscopic PIV probe will have any effect on the measurement uncertainty due to the endoscope probe intruding on the flow field.

As mentioned in chapter 1, a series of background studies have been carried out by colleagues at the University of Leicester in partnership with the PROVAEN consortium to determine the disturbances to the flow by inserting the endoscopic PIV probe normally within a spray flow and within flows developed for other test cases. The development idea was then further improved by suggestion a change to the surface geometry of the SSE-PIV probe to include a universal passive flow control configuration that provides an optimum reduction of flow disturbances within all four test cases test cases. The appliance of a universal passive control technique to the SSE-PIV surface geometry will not be used within this study and will be applied to future works.

Due to the lack of published information on the impingement of fully developed turbulent spray on slender cylindrical surfaces, a brief review on spray impingement on flat plates and other obstacles is presented in this section. This review is carried out in order to understand any effects which may occur due to an endoscopic probe intruding directly into the atomised spray.

The flow pattern of jets from a single round nozzle or slot impinging onto a surface has been previously described by Polat *et al.* (1989), Gauntner *et al.* (1970), Martin *et al.* (1977), Beltaos and Rajaratnam (1973), Beltaos and Rajaratnam (1974), and Kang and Greif (1992). Each of these authors agree, in the case of jet impingement on a surface, that the flow can be divided into four regimes. These are the potential core region, turbulent free jet region, stagnation region, and the wall jet region. The potential core and free jet regions have been described in sections 2.3.1 and 2.3.2. Within this section, the focus is primarily on the stagnation region (the impingement) and the wall jet region.

The stagnation region describes an area at which the jet impacts onto the leading surface of an obstacle. This region includes the point at which the flow comes to rest, the stagnation point. At this point, the flow velocity becomes zero relative to the surface velocity and the local pressure along the surface of the obstacle is at maximum. The most documented case for jet impingement is that on a flat plate. Gutmark *et al.* (1978) describes that the effect of the jet impingement on the flat plate is not noticeable upstream of one quarter distance between the nozzle and the surface. It was described by Schauer and Eustis (1963) that this distance is limited to 1.2 times the nozzle diameter. In this research, this information is re-interpreted using the jet exit diameter d_j, defined in section 5.4. The stagnation point has mainly been investigated in the context of heat transfer, where the heat transfer due to an impinging jet has been correlated to the "arrival flow condition". This is the flow condition at an equivalent location in a free jet Gordon and Akfirat (1965). The arrival flow condition is typically described by H/d, where H is the distance between the target surface and nozzle orifice and d is the nozzle diameter.

In the case of jet impinging perpendicularly on a flat plate, downstream of the plate stagnation point, the flow begins to accelerate parallel to the plate surface. This flow develops into a wall jet in which the maximum tangential velocity, $v_{max}=B/r^n$, where B and n are constants that vary with different jet characteristics and jet to target spacing ratio. Previous work by Glauert (1956), Poreh *et al.* (1967), and Bakke (1957) on a radial wall jet found the value of n to be greater than 1, which was deemed close to experimental values. In a free circular jet, the wall jet equation previously described is the equation for the centreline velocity decay, where n=1. In a radial wall jet, where n>1, $v_{\max}$ decays at a faster rate with increasing radial distance than that of a free jet. The system is stabilised by the wall jet acceleration, which causes the boundary layer to remain attached. Where a high deceleration occurs, transition to a turbulent boundary layer takes place. This increases the thickness of the boundary layer build up along the impinged surface. An extensive review of experiments and numerical simulations of various jet types impinging onto a flat plate is given by Tabrizi (1996).

A jet impinging on a circular cylinder differs from a free jet primarily in its dispersion and entrainment. Jet entrainment is mainly inviscid flow directed towards the jet axis. Entrainment is the inclusion of fluid from outside the jet boundaries into the main turbulent stream. The consequence of entrainment is that the axial mass flux increases with increasing distance from the nozzle exit plane. If there is a surface in close proximity to the jet, the space between the jet and surface will become partially evacuated because of the constant entrainment of the surrounding fluid into the jet. This partial evacuation forms a slight vacuum that draws the jet to adhere to the surface. This effect is known as the Coanda effect. Brahma *et al.* (1991), states that the Coanda effect appears typically when

H/*d* is large and when the jet has a high turbulent intensity. In a jet expanding beside a circular cylinder the Coanda effect is present. On the surface of the cylinder, the pressure becomes very low, with pressure recovery occurring at the rear of the cylinder. In this region, the flow adheres to the cylinder surface, removing the typical effects of flow separation.

Tabrizi (1996) performed a series of numerical and experimental investigations involving sprays onto circular cylinders that were both in-line and off-axis. Tabrizi (1996) adjusted the *H/d* parameter and studied its effects. The Reynolds number of the spray was approximately $1x10^5$. The investigation was focused around the application of jet cleaning, comparing a rectangular slot and round nozzles. It was concluded that, by increasing the spacing between the cylinder and the rectangular slot, the maximum shear stress increases slightly until H/d=2.51. When this value is increased further, the maximum shear stress rapidly decreases.

Most of the impinging jet flow investigations in the literature involve targets that are far greater in size than the jet exit diameter, for instance in Rockwell and Naudascher (1979). A study of vortex dynamics and energy transport caused by the jet impingement on a small cylinder was carried out by Chou *et al.* (2002), Hsiao *et al.* (1999), Hsiao *et al.* (2004) and Chou *et al.* (1996). These studies focused on the flow structures and dynamics obtained by a self-sustained oscillating flow induced by a plane jet and its impingement onto a small cylinder. In the latter two investigations, the small cylinder was fully submerged within the potential core region of the jet along the jet central axis. The cylinder was tested over the jet exit velocity range 2 m/s$<u_e<$26 m/s, which corresponds to the Reynolds number range $2.1x10^3<Re<2.7x10^4$. The Strouhal number of the resulting flow oscillation was found to be constant, at approximately 0.2. By submerging the cylinder within the potential core, the effect of the coherent structures in the jet shear layer was to act on the cylinder flow directly. Self-sustained oscillations were identified in the cylinder wake, driven by the jet impingement upon the small cylinder. It was noticed that, after impingement, the natural frequency of the structures in the jet shear layer varies from that of the free jet. This change is consistent with the shedding frequency in the cylinder wake. The vortex shedding from behind the cylinder is observed to act as an exciting source for a feedback mechanism to the cylinder jet exit plane. In 2002, Chou *et al*. extended the investigation by Chou *et al.* (1996) to observe the shear flow entrainment after the jet-cylinder interaction at a exit height and cylinder diameter ratio d/H =0.2 and a jet exit velocity u_e=10 m/s. The investigation compared the results against the ones from a free jet. The flow was measured using a hot-wire anemometer and the results were phase-averaged with respect to the cylinder vortex shedding Strouhal number of 0.2. The results obtained describe two separate flow regions the jet flow and the wake region. The two regions are separated by a narrow accelerated flow field across their common boundary. The criterion for finding the boundary between the wake and jet flow is where the velocity gradient is equal to zero. It was noticed that, in the wake flow region, the transverse and streamwise components of the fundamental vortex shedding frequency, f_r, is more significant. This makes the vortex shedding and merging of the jet flow and wake flow region the dominant flow dynamics within this flow system. Chou *et al.* (2002) describe the vortex merging that occurs further downstream in the wake region. Its location is determined using the saturation point of the sub-harmonic instability, f_r /2.

From the review of jet and spray impingement on an obstacle, alongside the developmental studies outlined in chapter 1 the endoscopic laser sheet and illumination optics was re-evaluated and set perpendicular to one another at an angle 45° from the SSE-PIV probe axis. With the judicious placement of the endoscopic probe the disturbances caused by probe intrusion within the measurement area can be reduced. This chosen configuration also allows the illumination plane to be parallel to the optical plane allowing the selection of focal point to be easier. Further detail on the SSE-PIV optical and illumination configuration is outlined in chapter 3 and the systematic approach to instrumentation setup using SSE-PIV is shown in chapter 4.

2.4 Summary

In this chapter a review of turbulent free jet structures were presented. The literature review identified the fundamental techniques of analysing the spray and providing analytical formulae from which the required data set can be derived. From a review of the analytical methods, one can determine the measurement planes and ensure a coherent experimental setup. The literature review also reports on past work of spray/jet impingement on a surface. The literature review shows a lack of information on the spray/jet impingement onto a slender circular cylinder outside the range of the potential core. This means the information on the intrusive effects caused by an endoscopic probe in a spray on its viewing window must be determined by this study. The literature review describes published work of endoscopic PIV applications. The setup of the endoscope in these past studies was that of a conventional two probe layout, as described in section 2.3. The literature review also showed that no documentation is available on a systematic validation of a single-stem endoscope PIV tool for free sprays. Therefore, a metrological study to aid in the validation of such a tool is required before its commercial use.

CHAPTER 3: PARTICLE IMAGE VELOCIMETRY FOR SPRAYS

3.1 Introduction

Particle Image Velocimetry (PIV) is a non-intrusive technique that obtains whole flow field information by using image correlation. The use of PIV is becoming more common and the mathematical algorithms used to translate spatial and temporal information into velocity information are becoming more advanced. The working fundamentals are quite simple, as PIV works on the basic calculation of *Speed* = *Displacement / Time*.

PIV uses a doubled pulsed laser that is directed into a series of optics in order to convert the laser beam into a sheet. The sheet provides an intensely illuminated 2D plane through a flow field of interest. An imaging source, most commonly a CCD camera, is focused upon the light sheet and captures images each time the laser pulses. Two images are captured, one for each pulse of light sheet. The correlation of the two images with the known time between the two frames provides the user with velocity component estimate across the field of view.

This study uses two PIV systems, the first being a conventional PIV system, and the second being a novel single-stem endoscopic PIV system. Both systems are used to describe the flow field of a water-in-air diluted spray. The aim of this study is to compare the results obtained by the two PIV techniques. Conventional PIV has the ability to capture, record, and process images over larger viewing areas and can therefore plot larger velocity maps which contain more information. However, the spray is very dense and fast at the nozzle outlet. The spray decelerates as the spray momentum is dispersed in the radial direction further downstream of the nozzle, to create a sparse and slow flow field. This causes a problem in the PIV correlation, since a large flow velocity difference means it is very difficult to find an optimum Δt between image frames when attempting to capture the entire flow system. In the endoscopic PIV system, the viewing window is smaller and provides only local velocity information. The velocity difference within this smaller field of view is comparatively smaller than in the conventional PIV image. This makes finding an optimum Δt between image frames simpler. This chapter describes the two PIV techniques, specifically, the hardware, and the image post-processing algorithms used in this work.

3.2 Conventional PIV

Conventional PIV relies primarily on an illumination source, an imaging source, and on seeding particles. A simple PIV schematic sourced from Dantec Dynamics is given in figure 3.1.

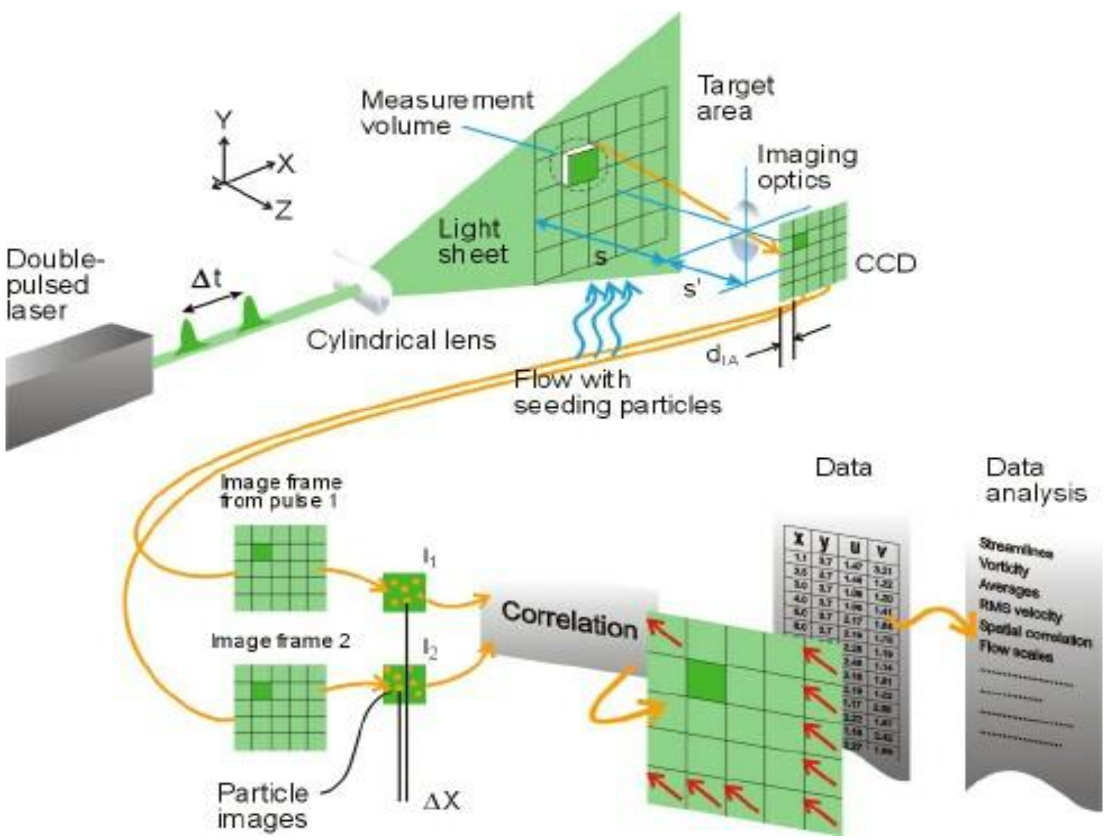

Figure 3.1: Schematic of a PIV system setup (sourced from http://www.dantecdynamics.com).

3.2.1 Seeding the flow

In this study the flow is seeded using 40 μm -50 μm hollow glass spheres in the water supply of spray. The seeding particles are used to enhance the Mei scatter from the flow. The particles are small enough to be neutrally buoyant and follow the desired flow regime but large enough to be able to scatter enough energy from the light sheet, so that the imaging camera can clearly detect each individual seeding particle.

The PIV measurement is indirect, that is, the PIV system determines the seeding or tracer particle velocity rather than the fluid velocity. Therefore, it is important to consider the dynamic properties of the particles to avoid any significant discrepancy between the particle and the fluid motion. The primary source of error is the influence of the gravitational forces if the particle density, ρ_p, and the fluid density, ρ, are different. The gravity induced velocity, u_g, can be determined from Stokes' drag law in order to assess the particles behaviour under the acceleration of gravity. By assuming the tracer particles are spherical and of uniform size within a viscous fluid at a low Reynolds number, u_g can be estimated as

$$u_\mathrm{g} = d_\mathrm{p}^2 \frac{(\rho_\mathrm{p} - \rho)}{18\mu} \mathbf{g} \qquad 3.1$$

where $\mathbf{g}$ is the acceleration due to gravity, μ is the dynamic viscosity of the fluid and d_p is the tracer particle diameter. Using u_g, the estimated velocity lag, u_s, for a continuously accelerating fluid can be determined by:

$$u_\mathrm{s} = u_\mathrm{p} - u = d_\mathrm{p}^2 \frac{(\rho_\mathrm{p} - \rho)}{18\mu} \mathbf{a} \qquad 3.2$$

where u_p is the particle velocity, $\mathbf{a}$ is the acceleration and u is the fluid velocity. The step response of u_p typically follows the exponential law if the density of the particle is much greater than the fluid density, that is:

$$u_{\mathrm{p}}(t) = u\left[1 - \mathrm{e}^{\left(-\frac{t}{\tau_{\mathrm{s}}}\right)}\right] \qquad 3.3$$

Where the relaxation time τ_s is given by:

$$\tau_{\mathrm{s}} = d_{\mathrm{p}}^2 \frac{\rho_{\mathrm{p}}}{18\mu} \qquad 3.4$$

Stokes drag law does not apply when the acceleration in the fluid is not constant. This occurs at higher velocities. A detailed review on the effect the of tracer size on the measurement flow speed is given in Raffel *et al.* (2007). When decreasing the field of view and thus increasing the optical resolution of the measurement image, d_p must also be decreased. The density of the seeding particles must not be too much as to increase the background noise.

The accuracy of a PIV measurement is directly proportional to the image definition, and the contrast of the image is directly proportional to the amount of light scattered by the tracer particles. The light scattered by the seeding particles is determined by the ratio of the refractive index of the particles to that of the surrounding medium, the particle size, shape, and orientation. The light scattering also depends on the polarization and on the observation angle. If a given d_p is larger than incident light wavelength, λ, the particle is seen through its Mei light scatter. This is $q=\pi d_p/\lambda$ where q is the scattered normalised diameter. This is discussed extensively in Ven de Hulst (1957).

3.2.2 Illumination source

The plane of illumination is typically a laser sheet. Commonly, a Nd:YAG (Neodymium Yttrium Aluminium Garnet) laser is used as the light source as it has a high energy intensity. Pulsed lasers need a certain amount of time to build up energy before delivering it in the form of a light pulse. To reduce the time between pulses, two cavities are used within the laser to deliver two pulses in rapid succession to take a pair of PIV images. The laser pulses have a duration of 5-10 ns and the energy in a single pulse is up to 400 mJ. A Nd:YAG laser emits a laser at the wavelength of 1064 nm. This is in the infrared range.

For PIV, this wavelength is undesirable, as typical CCD cameras have their maximum sensitivity over the range 430- 550 nm, which is the blue / green part of the visible spectrum. A built-in harmonic generator halves the original wavelength to 532 nm. The harmonic generator is less than 100% efficient so some of the remaining infrared light is removed by a separator and delivered to an infrared dump. The beam of laser that is emitted from the laser cavity is axi-symmetric in shape and is converted into a sheet by a cylindrical lens.

3.2.3 Image capture

A key feature for all PIV cameras is the ability to take double frame images over a short period of time. This is to ensure the same particles appear in both frames with a relatively small particle displacement between the two frames. These short exposure times can be achieved with high-speed cameras. The camera and laser are connected to a trigger control which synchronises the laser pulses and the camera exposure. A typical configuration for laser camera timing is shown in figure 3.2.

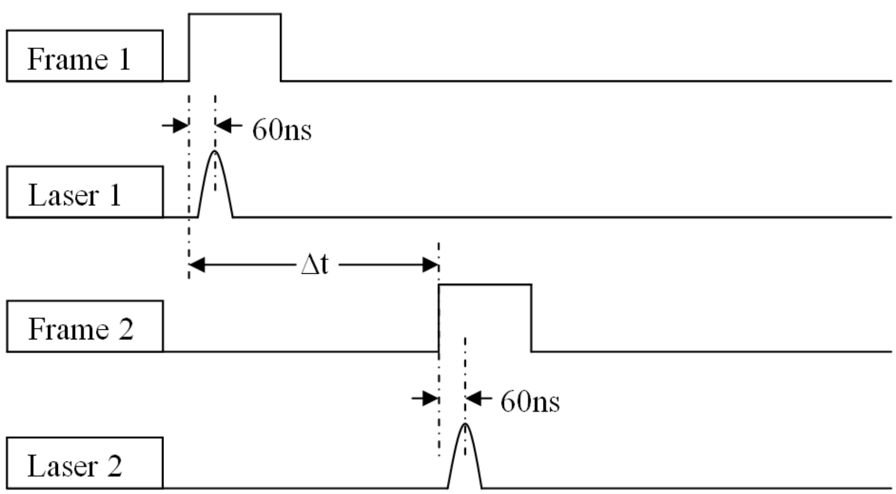

Figure 3.2: Laser and camera timing diagram.

Typically, PIV uses cameras with a frame rate of the order of 15 - 30 frames per second (fps). For high-speed flows, it is important to have a very short time between images. If the exposure times of the camera are too large, particles would appear more like streaks. In order to "freeze" the particle images at a specific time, a very short laser pulse is fired before each frame capture. As the spray being tested within this work is limited to an axial velocity of 50 m/s, no special arrangement was required to avoid streak-like images.

A threshold algorithm is then used to locate energy intensity peaks in both images over small areas. These energy peaks are related to the scattered energy from the seeding particles. The location of the intensity peaks is cross-correlated between the two images. The peak in the correlation should identify to the same particle in both images. The distance each particle moves in terms of pixels in the time separating the two images can then be calculated. This is converted to a physical displacement via a calibration factor α. The ratio of the physical displacement over the inter-frame time gives the seeding particle velocity vector in the measurement plane. This process is described in more detail in section 3.5.

3.3 Current PIV limitations

Although PIV is a very successful measurement technique, there are disadvantages associated with it. Firstly, the seeding particles can be one source of measurement error in PIV. Seeding particles are used according to the flow regime and the flow temperature. This is to keep the density of the particles similar to that of the flow under test. Temperature gradients affect the flow density and may disrupt the seeding particle ability to remain suspended the flow. Tracking seeding particles over large flow fields is fine when trying to observe general trends. However, for well-resolved measurements, a smaller interrogation area is needed. This is a direct consequence to the time between frames cross-correlation. It is very difficult for PIV images to accurately correlate flows that involve very high velocity gradients.

PIV is relatively limited in terms of industrial application. Due to the use of high energy lasers, all PIV applications must be done within safety monitored rooms by a trained user. This being the case, all PIV work must be done within laboratories. Hence, the success of a PIV application to a full scale flow problem is constrained by the complexity of the flow model that needs to be constructed. Furthermore, models are expensive to construct and are never able to fully produce the full working environment of industrial applications. Occasionally expensive and complex industrial flow systems, such as a turbine engines, are used for the purpose of PIV testing. This is carried out by fitting quartz windows in the engine casing and other areas of the engine to allow a direct route for a light sheet and a camera to focus on this light sheet. Modifying the engine casing in this way is an expensive process, however, it is the only method to date to fully measure the enclosed complex flows. Furthermore, the conventional PIV system is large, delicate, and rather expensive equipment and has limited portability. To introduce these systems within harsh or industrial environments maintaining the accuracy of PIV, from laser alignment to visual clarity, an improved setup is required.

This study provides a systematic metrological assessment of a single-stem endoscopic PIV system applied to an atomised turbulent free spray. The SSE-PIV differs from the applications in the literature in that it integrates the imaging and light sheet optics through a single Ø10mm cylindrical probe. The SSE-PIV system has a fixed laser sheet and camera viewing window which has a fixed focus position on the light sheet. This allows the laser depth of field to be of optimum thickness at the point of imaging. The camera focus position is set to focus on the light sheet. Once the system is calibrated, it can be used in flow applications without further calibration steps.

The primary advantage of the SSE-PIV system is that it is contained in a single probe and hence would only require a single access port for measurements in a confined space. The SSE-PIV system can be used online within industrial applications beyond the laboratory environment. The SSE-PIV measurements are benchmarked against conventional PIV and Pitot anemometry. The comparison among the measurements is supported by a systematic measurement uncertainty analysis.

3.4 The novel single-stem endoscope

Since 2004, Aroussi and co-workers have been developing a single-stem endoscope, which integrates a light source and an imaging device into a single 10 mm diameter probe. This simplifies the system setup with respect to the conventional two-probe endoscopy setup. Utilising a fixed laser and focus point from the imaging device permits an alignment, and calibration free setup. The endoscope can produce measurements of velocity as well as of particle size. This type of instrumentation was patented by Aroussi and Menacer (2004). The types of designs put forward are shown in figure 3.3. This patent is now owned by Olympus who put together a consortium of companies to develop the single-stem endoscopic PIV system. The University of Leicester is part of this consortium. Its role is to aid in the shaft development and also provide data validation against commercial PIV systems.

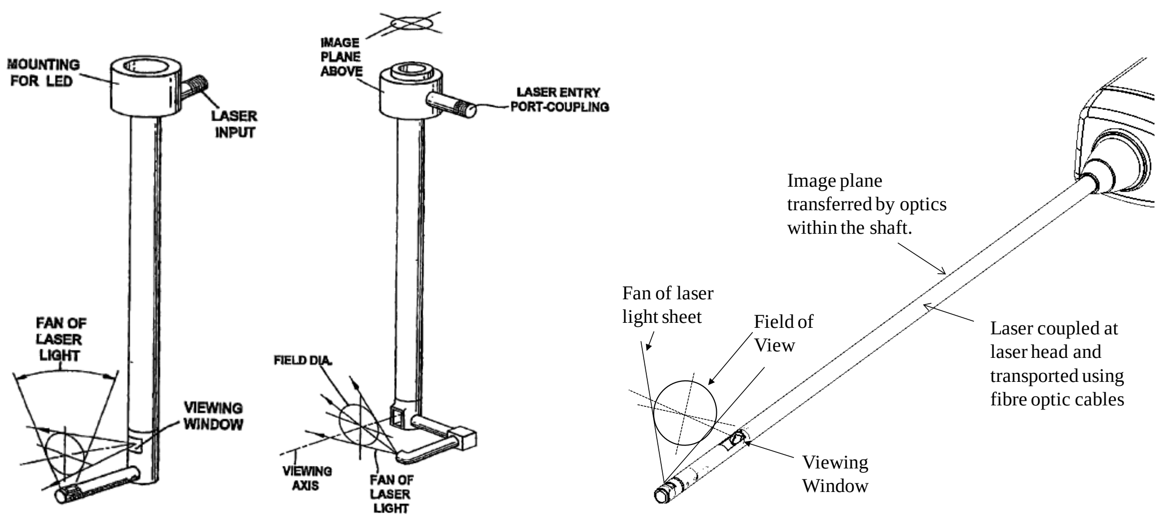

Sketch 1 **Sketch 2** **Sketch 3**

Figure 3.3: Endoscopic PIV designs from a patent by Aroussi and Menacer (2004) seen in sketches 1 and 2. The single stem endoscopic design developed by Olympus is shown in sketch 3.

3.4.1 Illumination

The system functions by transmitting laser energy through a bundle of fibre optic cables. Optical fibre delivery for high power pulses has been documented by a number of authors in the past such as Parry *et al.* (2007), Hand *et al.* (1999), and Stephens (2003). The light produced from a Nd:YAG laser is emitted from the laser head through a series of mirrors and through a harmonic separator to create a λ=532 nm laser beam. From the harmonic separator, the light beam is focused into a fibre optic coupling device that transfers the laser energy down seven flexible optical fibres, arranged in a bundle, to the tip of the rigid endoscopic probe. The open end of the fibre optics is aligned in a [1x7] array and transfers the energy to a series of convex and concave lenses to focus the beam. The beam is then opened up by a sheet optic and then a prism to emit a laser sheet at 45° to the endoscopic probe axis. A schematic of the laser paths from each of the seven fibre optical cables are given in figure 3.4. The various colours represent the illumination paths from each optical cable. The bundle is made up of seven 600 μm sheared optical fibres made from a Silica core and a TEQS (Flouropolymer) cladding which has a fluence of 60 mJ/cm^2. The fibre bundle has a maximum transmission energy of 52 mJ and a transmission energy efficiency of 65% (Gebauer, 2009).

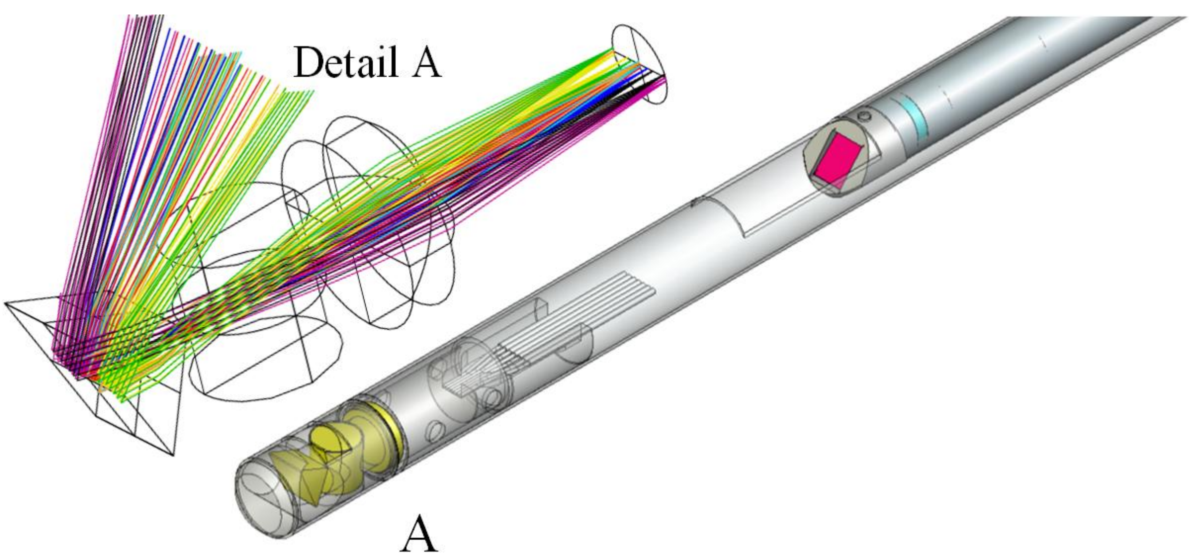

Figure 3.4: Laser paths and sheet optics configuration, post fibre-optic cables. Simulation plotted using Oslo optical software by Ramsbottom *et al*. (2009)

3.4.2 Imaging and optics

The imaging is carried out by a Dantec Nanosense 2M camera that allows 8 Hz double frame imaging. The camera is directly fixed to a coupling device which relays the image through a series of focusing optics down the length of the endoscope. A prism reflects the image 45° to create a Ø56.4 mm circular view field perpendicular to the light sheet. Focusing is performed by adjusting the camera position from the image coupling device. This mechanical focus is then fixed to focus onto the light sheet and is not required to be adjusted again. In figure 3.5, the coloured lines represent field lines of sight of the imaging optics. These have been produced using Oslo optical simulation software by Ramsbottom *et al*. (2009). The software provided an optimum laser and camera layout by adjusting the lens and mirror configuration through the endoscopic PIV probe.

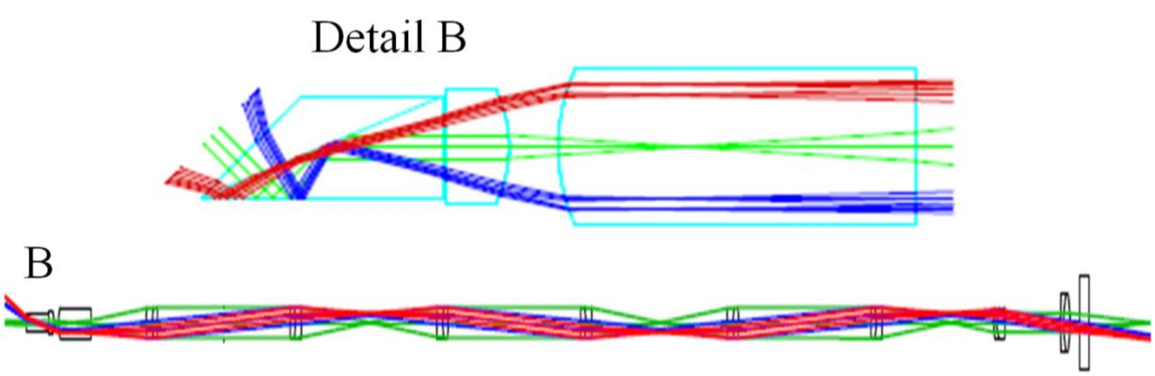

Figure 3.5: Optical configuration of imaging paths to the camera imaging sensor (*right*), coloured lines represent field lines of sight. Simulation plotted using Oslo optical software.

A sample raw image obtained using the SSE-PIV system is shown in figure 3.6. Due to the spherical optics, the image shows noticeable barrel distortion. The image brightness and contrast has been enhanced to emphasise the details within the image. The contrast between light and dark regions in the image is good. This suggests that the illumination from the laser optics is sufficient to illuminate the image area but, due to energy loss within the optical fibres and sheet optics, the illumination intensity is not as high as in a conventional PIV system. There is a noticeable difference in illumination intensity between the top and the bottom of the image, which relate to the furthest and closest position to the source of the laser sheet optics. At the midpoint of the image, in the region of the detail C, the image is in focus, the droplet definition is clear and the droplet displacement can be easily distinguished between frames. Detail D shows a reduction in particle definition at the edge of the image, this is due to a loss of focus. Spherical droplets appear elongated and blurred, due to the curvature of the view field. Droplet displacement in the region of detail D does not provide enough definition to accurately track clusters of particles between two images.

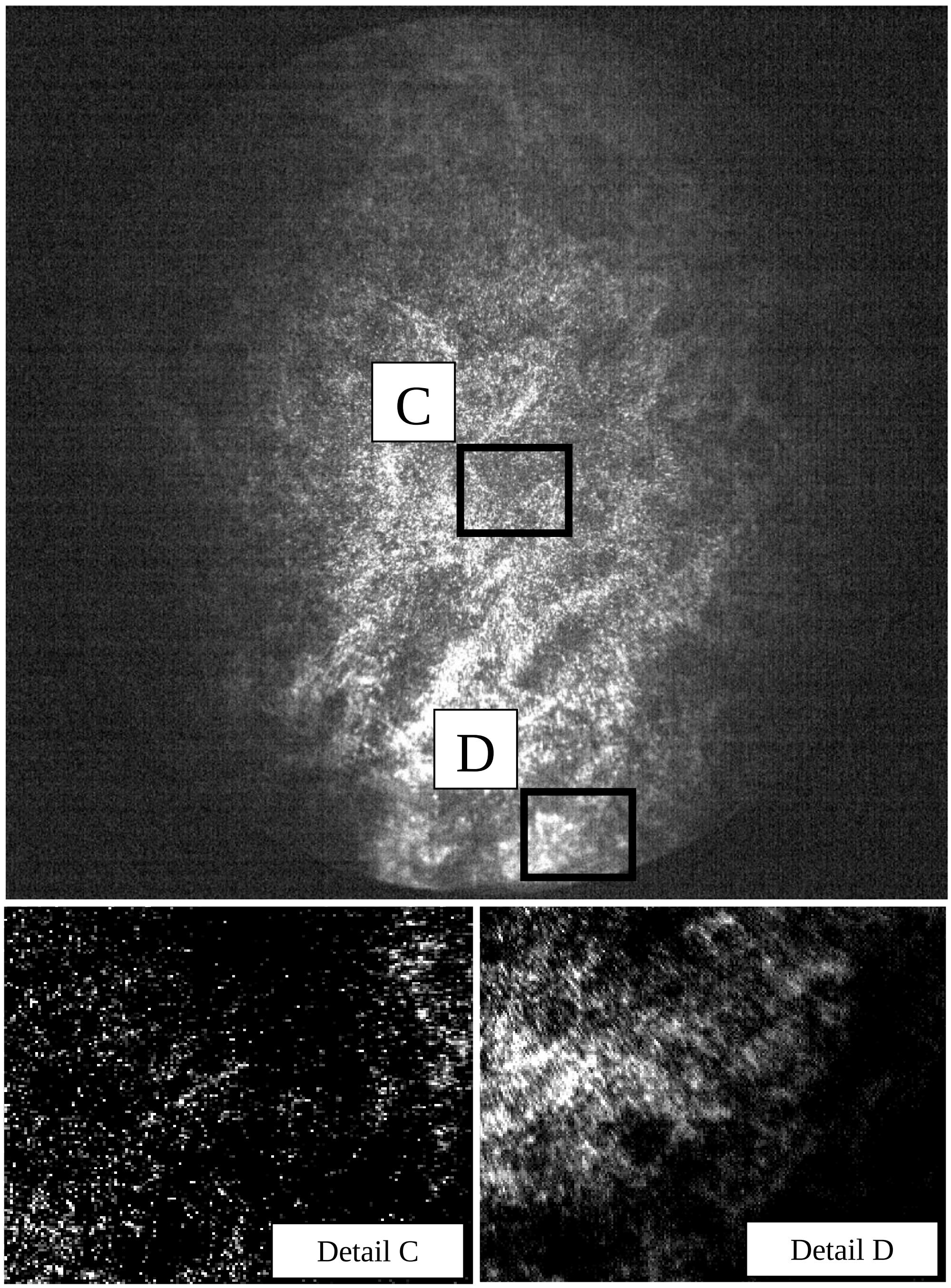

Figure 3.6: Raw image captured by the SSE-PIV system with enlarged details

Using the Oslo optical simulation software the amount of distortion seen on the 5.7128 x 5.7128 mm CCD sensor can be quantified. Figure 3.7 shows the predicted distortion of an image by the barrel distortion effects noticed on the CCD sensor of the imaging device. These curvature and perspective effects have also been noticed in endoscopic images by Reeves and Lawson (2004), Rottier *et al.* (2010), and the authors mentioned in the literature in section 2.3. Figure 3.7 describes the theoretical distortion by simulating light paths travelling through the optics onto the CCD sensor. Axial progression along the CCD sensor shows a maximum distortion value of 300 μm, which corresponds to an 8% barrel deformation of the image at 4mm from the CCD sensor axis. At 2.7 mm from the axis, the distortion is 150 μm and this corresponds to approximately a 3% deformation at the image edge. This 3% folding of the image creates a loss of focus at the view edge, caused by the field curvature, and a change in the image depth of field and in the localised view angle.

Since this study is determining the effectiveness and quantifying the uncertainties of the SSE-PIV system, the tests produced must be carried out with the systems as supplied by Olympus without further digital image enhancement. Image correction or vector correction may be applied in future works.

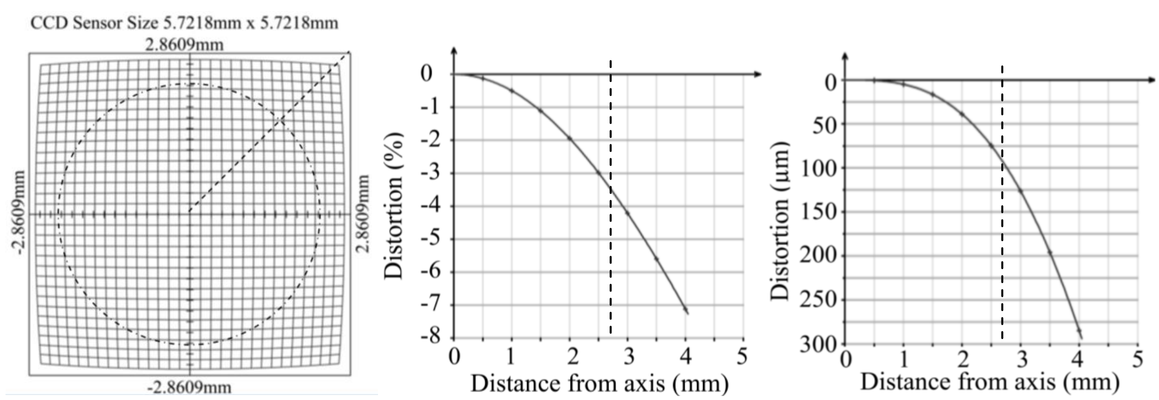

Figure 3.7: Linear plots of distortion from the CCD sensor centre to axis maximum.

The Oslo optical software predicts the deformation of an arbitrary spot within the field of view. An object within an ideal image plane will have similar geometric details as the object. In general, this is not the case and the ray displacement, although independent of the aperture, depends on the object height within the image. As a result the stigmatic image of an object will be displaced from the ideal image, and the image will not be geometrically similar to the object. Figure 3.8 gives an example of how a single particle is imaged using the SSE-PIV system at the centre of the field of view at the optimal focal position. The particle grows in size as the focus is shifted over the range -2.0 mm to 2.0 mm in the z direction. In figure 3.8 the ordinate shows the changes in the particle image from the centre of the CCD array along the increasing object height (OBJ HT) in the SSE-PIV field of view. The centre of the CCD array, labelled as OBJ HT=0 mm and focus shift=0 mm is where the particle is imaged as a perfect circle.

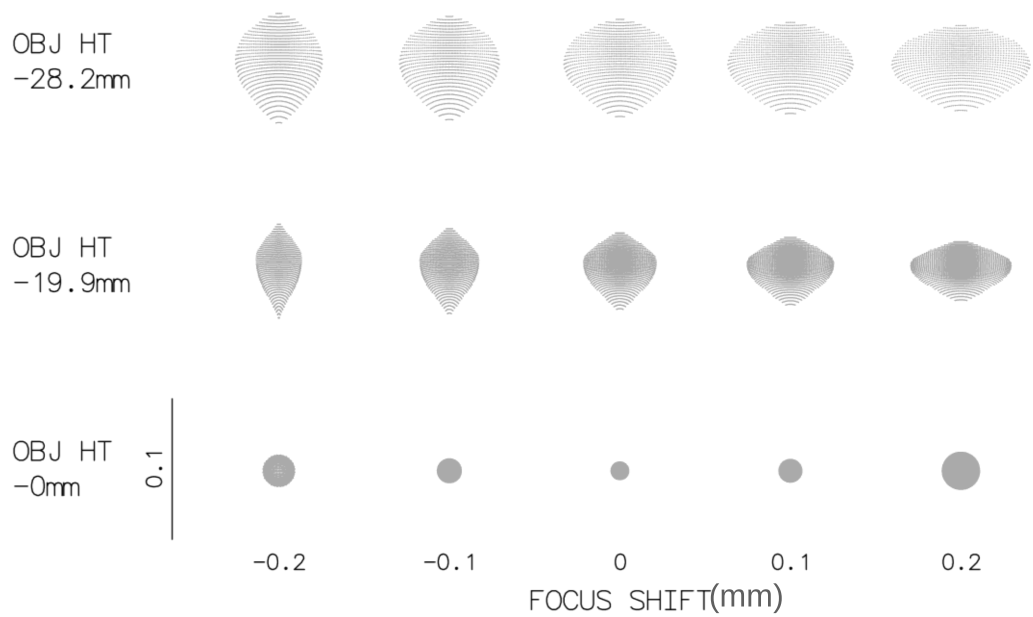

Figure 3.8: A spot shift diagram of a theoretical object within the image area produced by Ramsbottom (2009)

The deformation in figure 3.8 is quite extensive and by comparison with the raw image in figure 3.6 the effects are effectively the same. The object becomes out of focus as it moves away from the centre of the image. By moving the object location ±0.2 mm along the x-axis, the object moves in and out of the focus plane. It is clear that the focus accuracy is important to properly image individual PIV tracer particles. A ±0.2 mm shift in focus position also causes an object to become out of focus, however, since the object remains spherical and only increases in size, the object can still be traced from one frame to the next as long as particle overlap is kept to a minimum. Using out of focus images of particles on PIV (making smaller tracer particles larger) is not uncommon. In figure 3.8, the particle deformation is emphasised as the particle increases in object height (OBJ HT) within the SSE-PIV field of view.

3.5 Recording and processing PIV Images

A detailed mathematical description of PIV image processing statistics is given in Adrian (1988), Adrian (1991), Adrian and Yao (1985), Keane and Adrian (1991), and Keane and Adrian (1992). To date, the most complete description of the numerical processing of digital PIV has been given by Westerweel (1993). This section will focus primarily on the techniques that are used in the experimental procedure described in chapter 4. For this, a simplified mathematical model of the recording and subsequent statistical evaluation of PIV images will be presented. The outlined methods in this section describe the post-processing techniques used for producing velocity information from captured C-PIV and SSE-PIV images.

The two-dimensional spatial estimator for the processing of images into displacement vectors will be referred to as the *correlation*. The literature in this section focuses on the PIV recording technique of a *double frame/ single exposure* method. A schematic of this method is shown in figure 3.9 and figure 3.10.

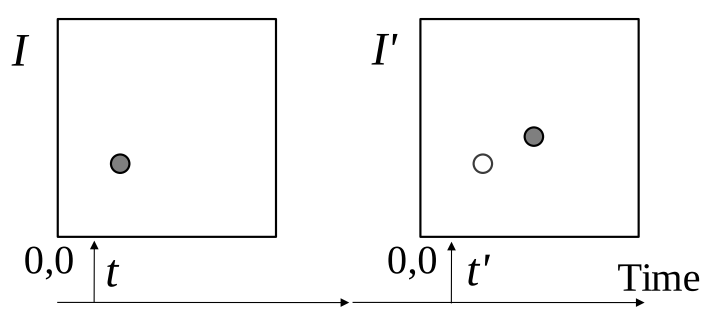

Figure 3.9: Schematic of *double frame/single exposure* PIV recording, reproduced from Raffel *et al.* (2007).

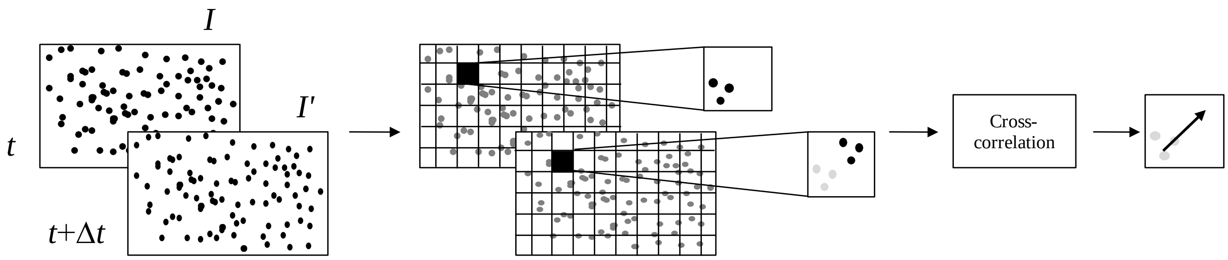

Figure 3.10: Schematic of the *double frame/single exposure* image processing procedure, from Raffel *et al.* (2007).

Typically, PIV recordings are subdivided into interrogation areas, IA, before processing commences. The back projection into the light sheet thickness causes the IA to become an interrogation volume, as given by figure 3.11.

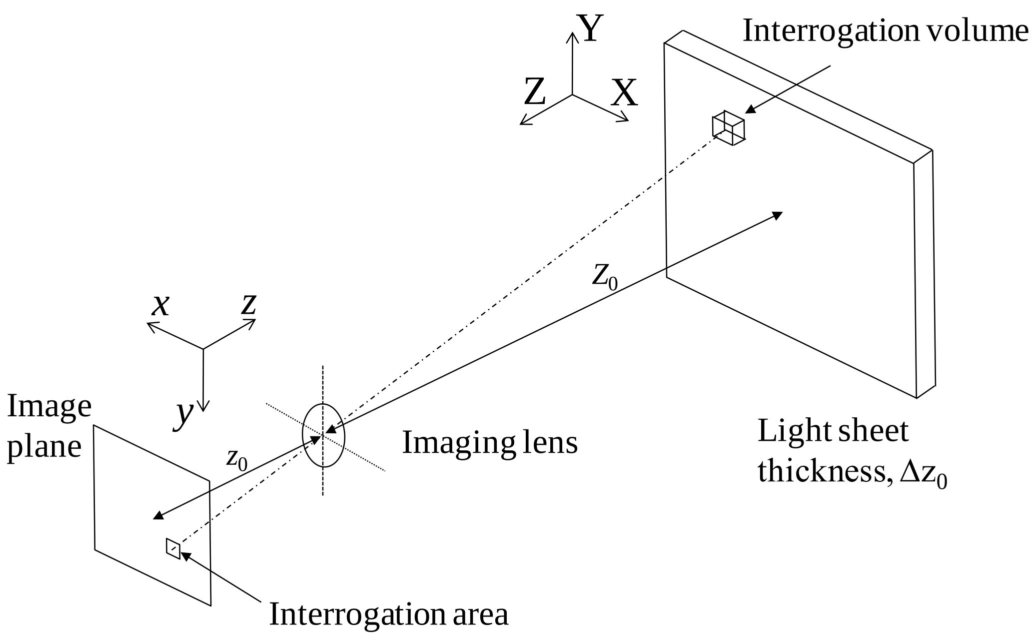

Figure 3.11: Schematic of the geometric relationship between the interrogation volume and its image area on the CCD array.

The image intensity determines the light energy distribution across the image plane. The image intensity field is described in detail and is given a mathematical representation in Raffel *et al.* (2007). The image intensity field is used to determine the exposure time.

3.5.1 Cross-correlation of a pair of two singularly exposed images

PIV images are often evaluated by cross-correlating between two image frames of a single exposure of the tracer particle field. A constant displacement, **D**, of all tracer particles within the interrogation volume is assumed, so that particle locations during the second exposure at time $t'=t+\Delta t$ are given by equation 3.5. Lower case letters refer to the co-ordinates within the image plane.

$$\mathbf{X_i}' = \mathbf{X_i} + \mathbf{D} = \begin{pmatrix} X_i + \mathrm{D}_x \\ Y_i + \mathrm{D}_y \\ Z_i + \mathrm{D}_z \end{pmatrix}, \quad \mathbf{X_i} = \begin{pmatrix} X_i \\ Y_i \\ Z_i \end{pmatrix} \qquad 3.5$$

Where $\mathbf{X_i}'$ is the position vector of a particle i at the time t'. $\mathbf{X_i}$ is the initial particle position vector for the same particle i at time t, **D** is the tracer particle displacement, X_i, Y_i, Z_i and D_x, D_y, D_z are the flow field co-ordinates and displacements in Cartesian co-ordinates. By the optics in figure 3.11, the particle image displacements are given by

$$\mathrm{X_i} = \frac{\mathrm{x_i}}{\alpha}, \qquad \mathrm{Y_i} = \frac{\mathrm{y_i}}{\alpha}, \qquad \mathbf{D_p} = \begin{pmatrix} \alpha \mathrm{D}_x \\ \alpha \mathrm{D}_y \end{pmatrix} \qquad 3.6$$

where $\mathbf{D_p}$ is the particle image displacement and α is the image magnification factor. Equation 3.6 only applies to tracer particles located near the optical axis. The particle image displacement between two frames is identified by I and I' for the first and second frame respectively is shown in figure 3.12.

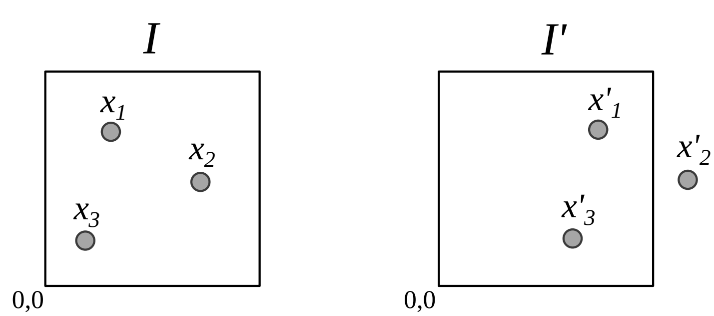

Figure 3.12: The intensity field I recorded at time t and the intensity field I' recorded after a time delay of Δt at t'.

The image intensity field for the first and second exposure can be represented in equation 3.7 and equation 3.8 respectively

$$I(\mathbf{x},\boldsymbol{\Gamma}) = \sum_{\mathbf{i}=1}^{N} V_0\,(\mathbf{X_i})\boldsymbol{\tau}(\mathbf{x}-\mathbf{x_i}), \quad \text{where } \boldsymbol{\Gamma} = \begin{bmatrix} \mathbf{X_1} \\ \mathbf{X_2} \\ . \\ . \\ \mathbf{X_N} \end{bmatrix} \qquad 3.7$$

$$I'(\mathbf{x},\boldsymbol{\Gamma}) = \sum_{\mathbf{j}=1}^{N} V_0{}'\left(\mathbf{X_j}+\mathbf{D}\right)\boldsymbol{\tau}\left(\mathbf{x}-\mathbf{x_j}-\mathbf{d}\right) \qquad 3.8$$

where V_0 $(\mathbf{X_i})$ is the interrogation volume in the first exposure, $V_0{}'$ $(\mathbf{X_j})$ defines the interrogation volume during the second exposure, $\boldsymbol{\Gamma}$ is the state of the ensemble and $\boldsymbol{\tau}$ is the point spread function of the imaging lens, and N is the number of tracer particles inside the interrogation volume. Details of these parameters are described in Raffel *et al.* (2007). By assuming identical light sheets and window characteristics between frames, the cross-correlation function between I and I' can be written as:

$$R_{II'}(\mathbf{s},\boldsymbol{\Gamma},\mathbf{D}) = \frac{1}{a_{\mathrm{I}}}\sum_{\mathbf{i,j}} V_0(\mathbf{X_i})V_0(\mathbf{X_j}+\mathbf{D})\int_{a_{\mathrm{I}}} \boldsymbol{\tau}\,(\mathbf{x}-\mathbf{x_i})\boldsymbol{\tau}(\mathbf{x}-\mathbf{x_j}+\mathbf{s}-\mathbf{D_p})\mathrm{dx} \qquad 3.9$$

where $\mathbf{s}$ is the separation vector in the correlation plane. In equation 3.9, it is possible to separate the $\mathbf{i} \neq \mathbf{j}$ terms, which represent the correlation of different randomly distributed particles and therefore noise in the correlation plane, and the $\mathbf{i} = \mathbf{j}$ terms, which contain the desired displacement information. By this separation, equation 3.9 can be re-written and decomposed into three parts as shown in equation 3.10:

$$R_{II}(\mathbf{s},\boldsymbol{\Gamma},\mathbf{D}) = R_C(\mathbf{s},\boldsymbol{\Gamma},\mathbf{D}) + R_F(\mathbf{s},\boldsymbol{\Gamma},\mathbf{D}) + R_D(\mathbf{s},\boldsymbol{\Gamma},\mathbf{D}) \qquad 3.10$$

where $R_D(\mathbf{s},\boldsymbol{\Gamma},\mathbf{D})$ is the component of the cross-correlation function that corresponds to the correlation of images of particles obtained from the first exposure with images of identical particles obtained from the second exposure (**i** = **j** terms). $R_C(\mathbf{s}, \mathbf{\Gamma}, \mathbf{D})$ is the convolution of mean intensities and $R_F(\mathbf{s}, \mathbf{\Gamma}, \mathbf{D})$ is the fluctuating noise component.

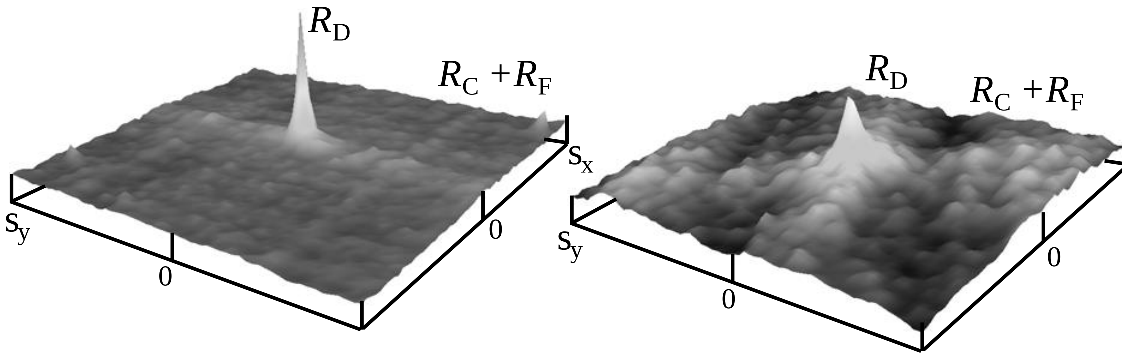

Figure 3.13: Cross-correlation maps of peaks in the cross-correlation function. On the left is a map with high signal to noise ratio, whereas the right map shows a low signal to noise ratio.

For a given distribution of tracer particles inside the flow, the displacement reaches a maximum when $\mathbf{s}=\mathbf{D_p}$. Therefore, the location of the R_{II}' maximum yields the average in-plane displacement, and thus the *u* and *v* components of the velocity inside the flow.

Some measurement systems apply the fast Fourier Transform (FFT) to shorten the computational time to evaluate the cross-correlation as stated in Raffel *et al.* (2007). The distribution of correlation coefficient C_{II}' is obtained by equations 3.11 and 3.12 by means of the FFT operator, $\mathscr{F}$.

$$S_{II'}(\xi, \eta) = \mathscr{F}\{I(x, y)\}\mathscr{F}^*\{I'(x, y)\} \tag{3.11}$$

$$C_{II'}(x, y) = \mathscr{F}^{-1}\{S_{II}(\xi, \eta)\} \tag{3.12}$$

3.5.2 Adaptive Correlation

The adaptive cross-correlation (ACC) is an iterative procedure that is used in PIV to increase the accuracy of the standard cross-correlation method. This technique is attributed to Scarano and Riethmuller (1999), and Scarano and Riethmuller (2000) . The conventional cross-correlation is based on dividing the two images being compared into a number of interrogation windows. The positions of these windows are identical and fixed in both images. Digital image correlation (DIC) is calculated only once to obtain the relative displacement between any two corresponding windows. As a result, the correlated area in any two windows decreases as the displacement increases. However, in ACC, the position and size of interrogation window are continuously refined to obtain the optimal prediction. The accuracy of the cross-correlation function depends on many factors, including the constant wavenumber content of I and I'. This condition is difficult to fulfil in cases where shear layers may be forming and particles are moving in different directions, as shown in Santamarina and Fratta (2005). This difficulty is present in spray flows. The accuracy of image correlation methods increases with the increase in the peak value of the cross-correlation function, as shown by Sjödahl (1998). The peak of the cross-correlation function is proportional to the size of the correlated area between the two interrogated windows, as shown by Hart (2000). The adaptive cross-correlation utilizes IA shifting and IA variable sizing to increase the size of the correlated area.

Increasing the interrogated area size increases the information inside the interrogated window. This increases the peak value of the cross-correlation function and a more accurate prediction of the average velocity vector over the IA can be achieved, as stated in Sadek (2002). In the adaptive cross-correlation, a large interrogation window size is first used to obtain the general direction of flow movement. Next, smaller windows are then used iteratively to better define local displacements.

The procedure for IA shifting involves shifting one of the images in the direction of the particle movement by a number of pixels that best approximates the deformation calculated in the previous iteration. This allows for most of the information in the original window to be included in the second window. There are two ways to shift the interrogation windows in the adaptive cross-correlation. The first is a central difference scheme, by which both IAs are shifted half of required shift but in opposite directions. The second is the forward difference scheme, by which only the second image is shifted by the required shift. A detailed description of window refinement and window shifting as well as of multiple pass interrogation schemes is given in Raffel *et al.* (2007). During the cross-correlation procedure, the PIV software also allows overlapping of the interrogation areas between I and I' by a pre-determined amount. This allows the tracking of tracer particles that are displaced a small amount out of the IA and acts similarly to a window shifting technique. The overlapping can be used in conjunction with window shifting.

3.5.3 Peak detection

Correlation peak-height validation works based on the height of the peaks in the correlation plane. If P_1 is the highest peak and P_2 is the second highest peak, the most common approach, termed the detectability criterion, validates the PIV velocity vectors for which $P_1/P_2 \geq k$, where k is typically around 1.2, Keane and Adrian (1992).

3.5.4 Range Validation

The velocity range validation rejects vectors whose magnitude or components are outside a given range. Normally, the user has an idea about the range of velocities that are physically plausible within the flow field. A criterion for the flow field range can be applied, $L_{\mathrm{min}} \leq |L| \leq L_{\mathrm{max}}$ for length, $u_{min} \leq |u| \leq u_{\mathrm{max}}$ for the x component and $v_{\mathrm{min}} \leq |v| \leq v_{\mathrm{max}}$ for the y component. Hence, if the velocity vector from PIV does not satisfy the above limits, it is rejected.

3.5.5 Moving average

The moving average validation is a special case of the general class of iterative filtered validation described by Host-Madsen and McCluskey (1994). Since the vector field is over-sampled by the PIV technique, there is a correlation between neighbouring vectors, and ideally, there is not too much change from one vector to its neighbours. If the vector deviates too much from its neighbours, it must be an outliner. The moving average validation is performed by analysing the average of the vectors surrounding a given vector.

If the difference is larger than a predefined acceptance factor, the vector is rejected. The rejected vector may be substituted by the local average of the surrounding vectors.

3.5.6 Filtering

Filtering substitutes each vector with the weighted average of the vectors in a neighbourhood of a specified size of $(m \times n)$ vectors. Here, m and n are an odd number of vector cells symmetrically located around each vector. The filter takes out the high frequency fluctuations or jitter in the PIV velocity vector map.

3.6 Summary

This chapter presented a summary of the fundamentals of PIV. The first part of this chapter gave an overview of the PIV hardware and software. The mathematics involved in the recording and correlating PIV images have been explained. This information has been extended to discuss the various filtering and correlation validation schemes that are used to remove unwanted data and thus increase the accuracy of the measurement. Also, within this chapter, the limitations of a conventional PIV system have been identified, in particular, the inability to measure internal flows in non-transparent enclosures. A novel single-stem endoscopic system has therefore been considered to overcome these limitations. The details of the illumination and of the optical arrangement and image resolution of the single-stem endoscope have been described.

CHAPTER 4: EXPERIMENTAL SETUP

4.1 Introduction

In this section experimental setups to obtain velocity measurements of an atomised spray are described. The details of the spray gun, nozzle type and air-water supply is provided in section 4.2. The details of Pitot anemometry hardware setup and calibration details are given in section 4.3. The hardware setup of the conventional PIV system is outlined in section 4.4.1. This section also describes the measurement area and image capture parameters. The details of the setup using the single-stem endoscopic PIV is given in section 4.4.2 and a combined setup to determine the effects of the endoscope shaft on the SSE-PIV field of view is given in section 4.4.3. Section 4.5 summarises the spray and PIV system parameters and also gives details on the calibration images used for PIV and the spray alignment.

4.2 Spray hardware setup

The experimental setup consists of non-swirling air flow that co-flows around the liquid injector. The mixing of the two phases is carried out using an air assist atomising nozzle given schematically in figure 4.1, where u_{gas} is the gas velocity and u_{water} is the liquid velocity. As mentioned in chapter 2, the spray behaviour is more consistent with an air jet since the liquid droplets have little effect on the air phase structure velocity distribution.

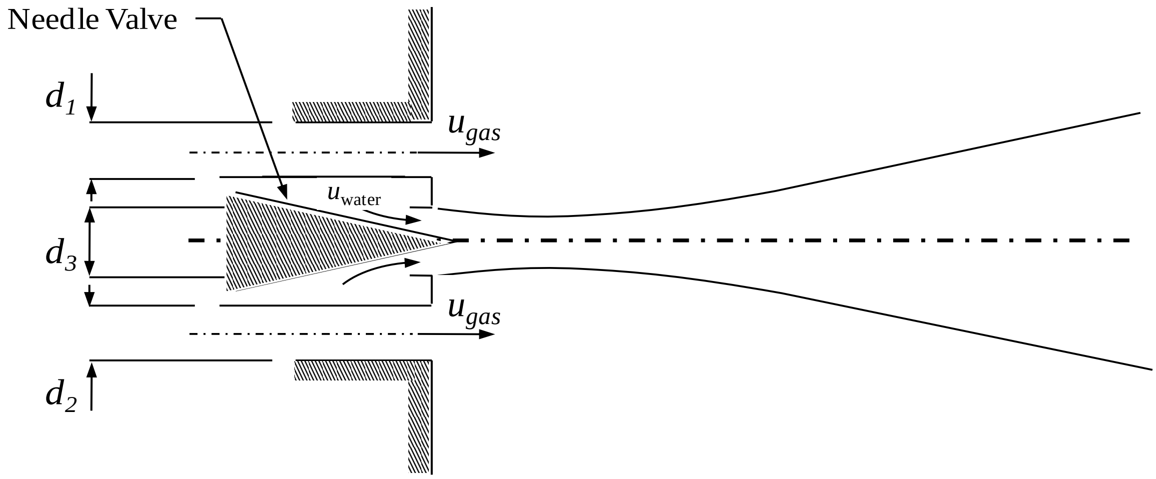

Figure 4.1: Air assist atomiser nozzle used to atomise droplets at the nozzle exit.

The air supply was provided by a compressor, and was regulated at a constant pressure of 7x10^5 Pa. The pressure and mass flow rate of the air supply was monitored during tests to ensure the incoming flow was consistent between experiments. The internal diameter of the pipe connecting to the spray device was 25x10^{-3} m and was fitted with 2 pressure gauges and an orifice plate. The orifice plate has a diameter of 10x10^{-3} m, and was fitted with d, d/2 pressure taps which are directly connected to a U-tube manometer. The air supply to the nozzle is controlled using a regulator and a ball valve. The liquid phase was drawn from a reservoir into the air supply as a result of negative pressure across a T-junction located within the spray gun. The spray gun has the ability to control the liquid and air mass flow rate by adjusting two needle valves located on the body. The mass flow rate of the liquid phase was fixed at 3.5x10^{-3} kg/s for all tests. The liquid agent used within all studies was distilled water which was laden with seeding particles that are neutrally buoyant in water at 290 K. The seeding particles used were hollow glass spheres of an average 50 μm, labelled 'Sphericel'. The nozzle diameter consists of 3 ports, it was therefore more effective for calculating dimensionless parameters and data fitting to use the nozzle equivalent diameter, d_e = 2.87x10^{-3} m, which was computed using equation 4.1.

$$d_e = \sqrt{{d_1}^2 + {d_2}^2 + {d_3}^2} \qquad 4.1$$

The spray was sprayed horizontally to avoid droplets hitting a perpendicular surface and reflecting back upstream. The spray was directed onto a protective screen. The runoff is drained and pumped back into the reservoir. A schematic of the setup is shown in figure 4.6.

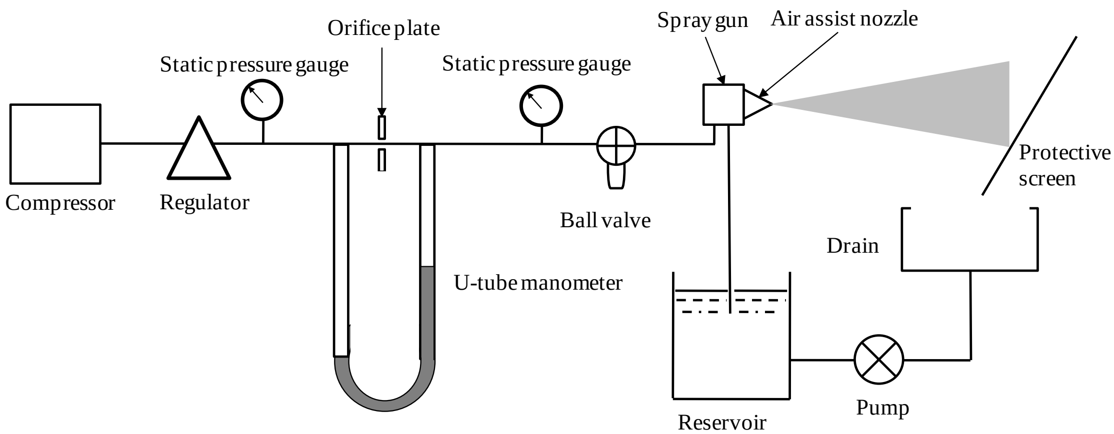

Figure 4.2: Schematic of the spray supply system.

The spray nozzle produces a solid cone of atomised liquid droplets at a 30° angle. Each experimental run was carried out at the same mass flow rate of the air supply and liquid feed rate. The spray flow system was located within a closed laboratory with no windows or external doors. The Laboratory temperature was monitored at 295±3 K. The laboratory was free from drafts and air conditioning as to avoid any spray drift. The liquid reservoir was controlled at a constant 284±3 K.

Dimensionless parameters are calculated to determine the theoretical spray behaviour before any initial testing. These are described in table 4.1, where the parameters were computed at the spray nozzle exit plane, using nozzle equivalent diameter d_e. The dimensionless parameters were kept constant for each test.

Table 4.1: Calculation of dimensionless parameters at the nozzle exit plane.

Dimensionless parameter	**Value**
Reynolds number (*Re*)	1.9×10^{4}
Weber number (*We*)	120
Ohnesorge number (*Oh*)	2.19×10^{-6}
Spray viscosity ratio ($R\mu$)	1.225×10^{-3}
Capillary number (*Ca*)	6.811×10^{-4}

The spray gun was fitted to a Dantec Scheinpflug mount via a pivoting block and two rigidly fixed struts. The mount was fixed on a Dantec 0.09 m x 0.09 m x 1 m profiled aluminium rail using t-slots. The current spray setup was used to allow the spray gun 3 degrees of freedom. That is movement in the yaw, the roll and the pitch angle. The yaw angle of the nozzle can be adjusted to ±120° at 0.25° increments from the rail centreline along the *x*-axis. The pitch and roll angle of the nozzle can be adjusted ±10° at 1° increments. The streamwise spray axis was set to run parallel with the rail centreline axis in the *x* direction. This process was carried out experimentally using Pitot anemometry which measures pressure along a *y* and *z* traverse at increasing axial locations. The setup of the Pitot anemometer will be described in more detail in section 4.3. A schematic of spray gun hardware mounts is shown in figure 4.3.

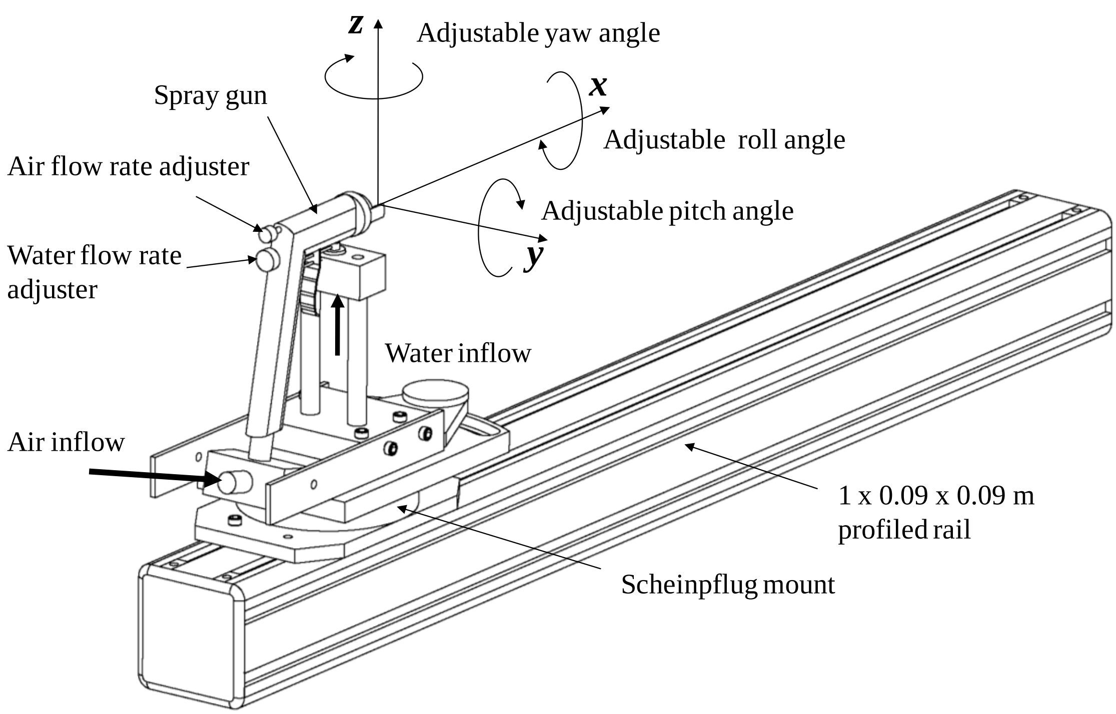

Figure 4.3: Schematic of the hardware mounts used to fix the spray gun to a known axial centreline.

4.3 Spray instrumentation using Pitot anemometry.

A Pitot anemometer measurement was required to initially align the spray axis so that the spray centreline aligned with the x axis and had no deviation in the yaw, pitch or roll angle. It was convenient to align the spray to ensure positional accuracy when obtaining measurements.

The instrumentation of the Pitot anemometer hardware is shown in figure 4.4 and 4.5. A 0.09 x 0.09 m x 1 m profiled rail is fixed parallel to the rail shown in the previous section allowing no degrees of freedom. The secondary rail is fitted which a traversing system via the sliding t-slots located on the rail. This allowed the traverse to move along the streamwise direction and to be secured at a desired position to create no displacement in the roll or pitch angle. The Pitot-static probe has an incremental adjustment in the yaw angle. This was set perpendicular to the profiled rail using a co-ordinate measurement machine. The traverse had 3D movement which allowed 0.8 m at 0.001 m increments in the x direction, 0.26 m at 5×10^{-3} m increments in the y and z direction.

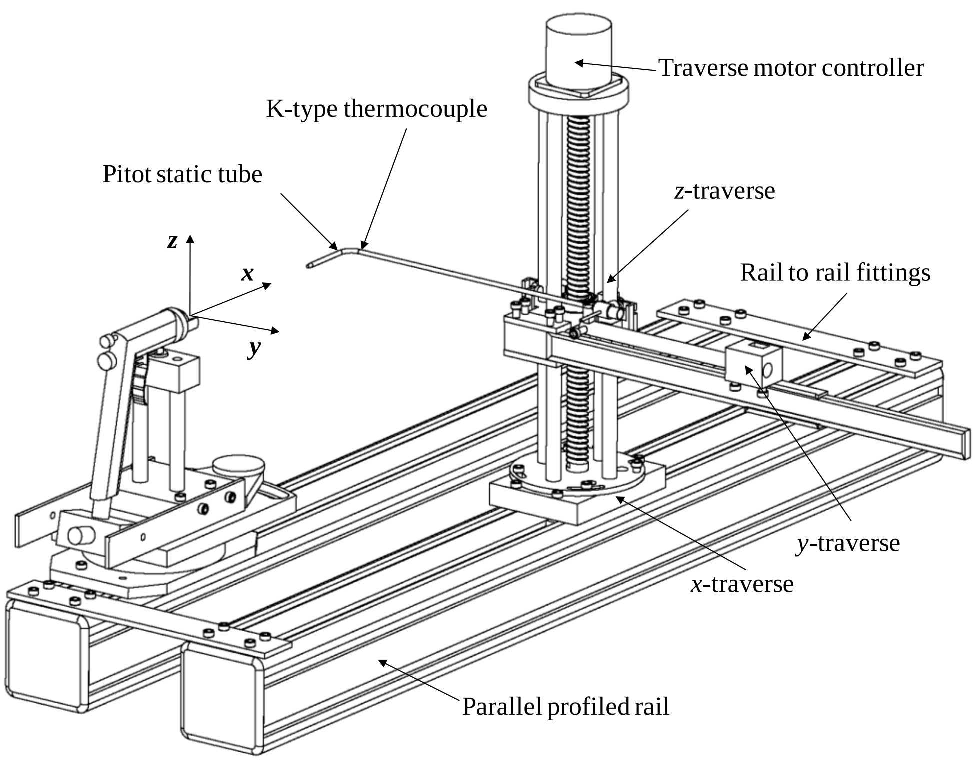

Figure 4.4: Schematic of the Pitot anemometer setup within the spray flow.

Figure 4.5: Image of the Pitot anemometer instrumentation within the spray flow.

The *y* directional traverse is fitted with a clamp to fix a Pitot-static tube. The Pitot-static tube is rotated to align parallel with the *x* axis and the Pitot opening faces the oncoming flow. A K-type thermocouple is located 0.015 m behind the static ports of the Pitot-static tube. The measurement instruments were traversed across the spray in both *y* and *z* directions at increasing streamwise locations. The setup schematic of the Pitot anemometry measurement hardware details are given in figure 4.6.

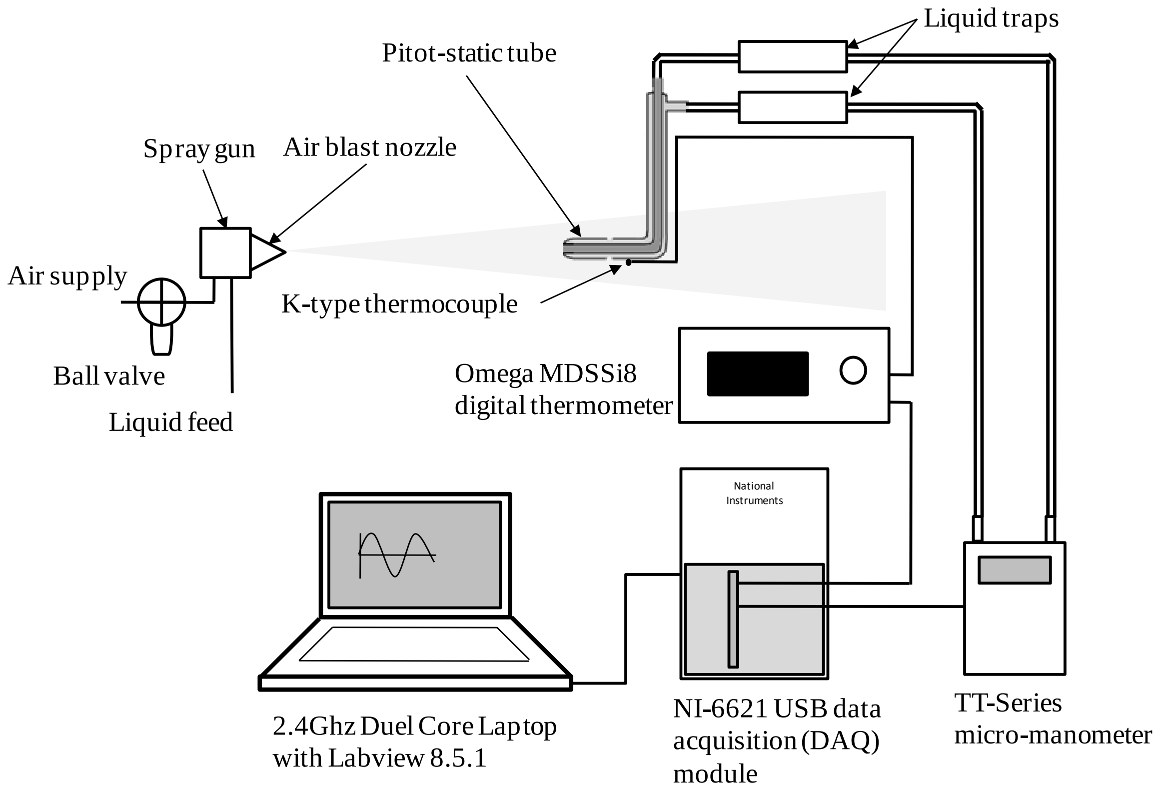

Figure 4.6: Spray rig facility coupled with Pitot-anemometry hardware.

Figure 4.6 shows the data acquisition setup to obtain pressure and temperature information. The Pitot-static tube was connected to a TT-series micro-manometer which has a voltage output ±1 V. The connection is made via 1.5 mm bore surgical tubing to a liquid trap to remove any chance of liquid entering the manometer. The voltage signal is connected to a National Instruments-6621 data acquisition system (DAQ) on channel 1. The pressure signal from the micro-manometer is 1 mV per display count on all manometer ranges. Therefore an output of 874 mV gives a pressure reading of 87.4 pa (on a respective scale). This readout has a ±1% error, the impedance is 2000 Ω. To keep the error to a minimum the connection cable between the micro-manometer and the DAQ card is kept as short as possible.

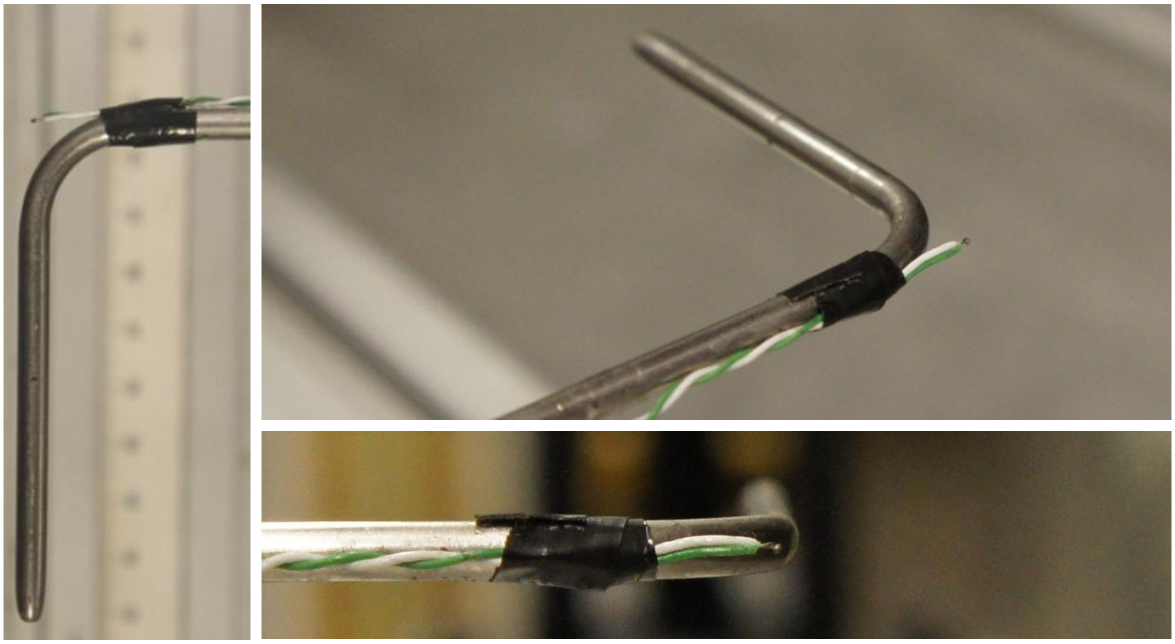

Figure 4.7: Configuration of thermocouple on the Pitot-static probe.

The temperature information was obtained using a class one K-type thermocouple which converts temperature information into a voltage signal. The position of the thermocouple is shown in figure 4.7. The thermocouple was placed 15 mm downstream of the static ports on the Pitot tube. The thermocouple does not make contact with the stainless steel tube. The K-type thermocouple has a tolerance of ±1.5 K between 233 K and 646 K. The voltage signal was connected to a digital thermometer. The thermometer has a reading error from a K-type thermocouple of 0.4 K within the range of 113 K to 1645 K. The digital thermometer was connected to the DAQ card on channel 2. The voltage waveform signal from channel 1 and channel 2 was sent to Labview 8.5.1 post processing software on a Laptop via a USB cable once a set number of samples were collected. The effect of the mass of the liquid droplets on the pressure measurement was determined in Appendix A, where it was determined that the spray transports the liquid homogeneously as a fine mist. Spray computation is carried out using a mixture density, ρ_{mix}. The pressure obtained using the Pitot anemometer was converted to velocity using the equation $\Delta P = \frac{1}{2}\rho_{\mathrm{mix}}u^2$, where ΔP is the dynamic pressure obtained from the measurement, ρ_{mix} is the mixture density at the measured temperature, and u is the streamwise velocity.

The temperature-voltage signal was calibrated using a temperature calibrator which has a calibration accuracy of ±0.05% from the value +0.05% from the range. A range of temperature readings were applied as an input to the digital thermometer using the calibrator. The corresponding voltage reading was taken over a period of 30 Seconds at a 2000 Hz sampling rate. The data collected was averaged to find the voltage value at a known temperature. The temperature increased linearly with respect to voltage at a rate of 0.01 with an initial voltage value of -0.09 V at T=273 K. The calibration plot is given in figure 4.8.

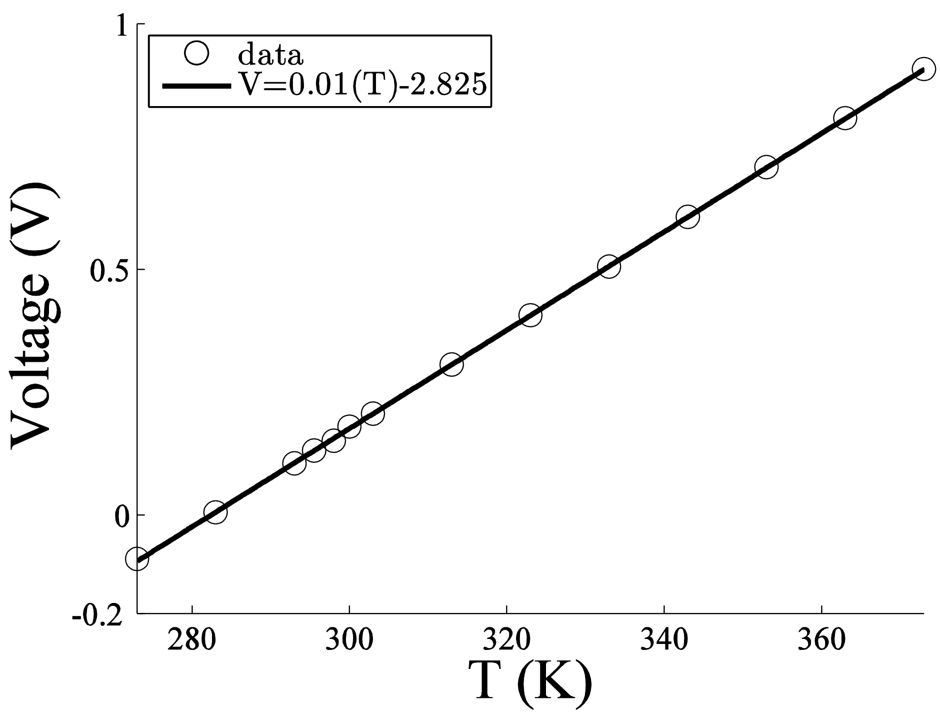

Figure 4.8: Calibration graph for voltage readings using the K-type thermocouple to obtain a temperature value.

4.3.1 Experimental procedure for data capture using the Pitot anemometry

Each test day the laboratory temperature and humidity and the reservoir temperature was recorded. Before each test the water level of the reservoir was set to a starting level to negate any changes in pressure head between runs. The spray device was allowed to run for 30 seconds before data collection to allow any fluctuations in the air supply and liquid feed flow rates to settle. Data was obtained over a time period t=30 seconds at a sampling rate of 2 kHz for each run. The sampling rate and time are both controlled in Labview and the data is automatically written to a text file after the samples are collected. The samples are taken in the radial directions over the range 0 mm<y<260 mm and 0 mm<z<260 mm at 2.5 mm increments. This was then repeated for the axial locations over the range 50 mm<x<350 mm at 50 mm increments. The measurement data was then imported into Matlab 7.6.0 for post processing.

4.4 Spray instrumentation using PIV

A brief review of the PIV hardware and software was described in the literature in chapter 3. In this study a 2D PIV technique for mapping the spray flow field was used. This section provides the details of the conventional PIV and single-stem endoscopic PIV hardware setup within the spray flow regime.

4.4.1 Setup of the conventional PIV system

The C-PIV system uses a Litron Nano L Double pulsed laser to produce a light sheet along the x-y plane. The light sheet has a wavelength of λ=532 nm produced by a Nd:YAG laser which has a max energy output of 400 mJ. The laser beam from the head is converted into a sheet using a 6 mm diameter quartz rod. The sheet emitted has a 70° spread. The laser sheet thickness, Δz_0=1.5 mm, and the focal length Z_0=0.8 m from the laser optics. The position of the laser is mounted on a Dantec 3D traversing system which is controlled by Labview 8.5.1. The laser traverse has a full sweep of 0.8 m, 0.8 m and 1.0 m in the x, y and

z direction respectively. The laser traverse moves at increments of 1×10^{-4} m. The positional accuracy of the laser is therefore defined as $\pm 1 \times 10^{-4}$ m in x, y and z. The laser position is fired along the x-y plane where z=0.

A Dantec Flowsense 4M camera with a 60 mm Nikon macro lens was used to focus on the droplets illuminated by the laser sheet. The working distance from the image sensor to the laser plane is approximately 0.8 m this provides a field of view of approximately 250 mm x 250 mm. The field of view has a magnification factor of $\alpha = l_r . \cos\theta / L_r$ = 0.13389 mm/pixel where l_r and L_r is the distance between reference points in mm and in pixels respectively, and θ is the small uncertainty angle between the image plane and laser plane. To capture the full spray system before evaporation, two images at increased axial location were recorded. The first image captures 30 mm from the nozzle orifice to 280 mm downstream. The second image was captured at 250 mm to 500 mm downstream of the nozzle orifice. The camera has a maximum trigger frequency of 4 Hz and an image resolution of 2048 x 2048 pixels. The camera is mounted perpendicular to the laser sheet and was set to focus on the illuminated droplets and particles on the x-y plane.

The timing of the laser and camera are synchronised using a Dantec timing box, which was controlled by Dynamic Studio v1.45 PIV software. The software is installed on a 2.4 GHz quad-core PC which houses 320 Gb of hard disk space and 3 Gb of memory. The PC is fitted with image acquisition (IMAQ) and data acquisition (DAQ) cards. The hardware setup schematic is given in figure 4.9 and an image of the setup is shown in figure 4.10.

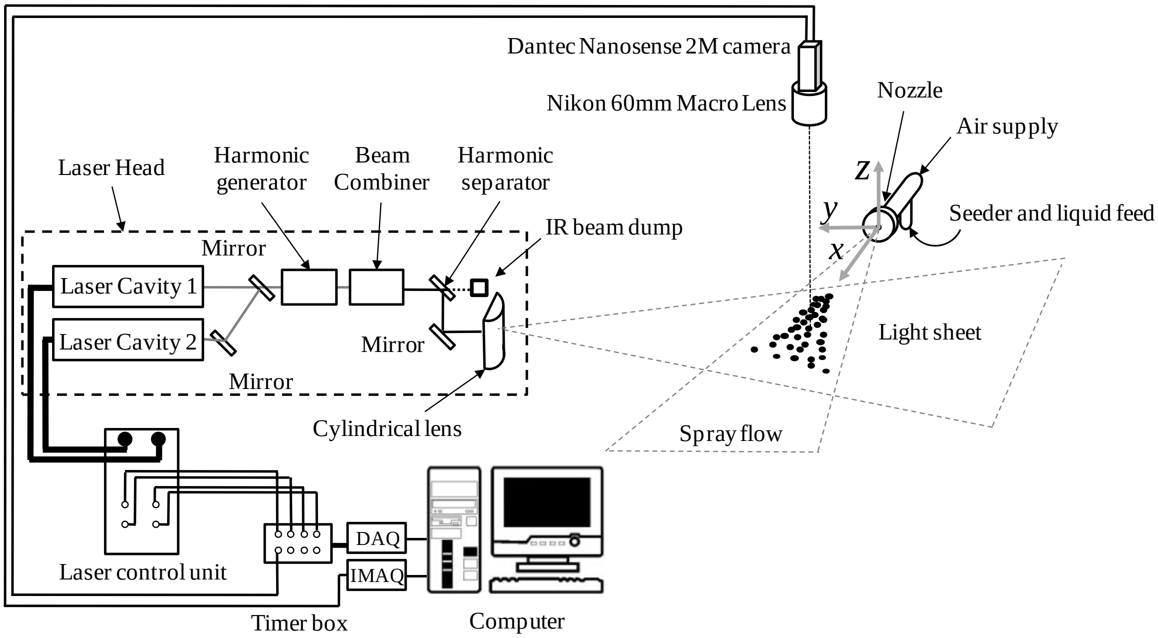

Figure 4.9: Conventional PIV hardware setup schematic.

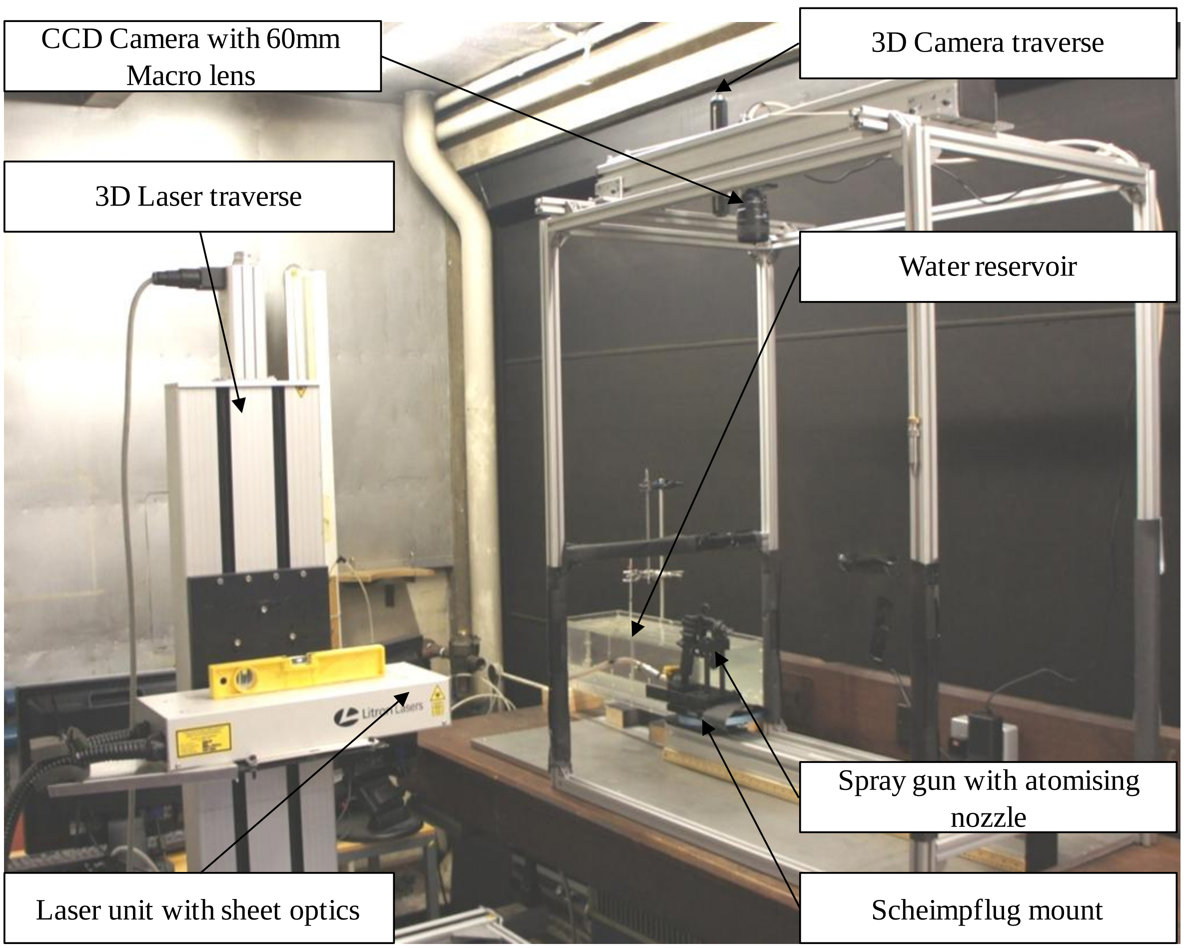

Figure 4.10: Image of the conventional PIV hardware setup.

4.4.2 Setup of the single-stem endoscopic PIV system

The details of laser energy transfer and imaging optics, through the single-stem endoscopic probe, are outlined in chapter 3. This section focuses mainly on the hardware setup of the SSE-PIV system to obtain velocity information of the spray flow regime.

The SSE-PIV system comprises of a newly developed Litron Nd:YAG laser which has an output of 20 mJ per pulse, producing a beam with a wavelength of λ=532 nm and a pulse length of 10 ns. The beam profile is typically Gaussian. The beam is coupled and delivered to the tip of the probe where it is formed into a sheet and projected 45° from the probe as shown in figure 4.11. The endoscopic probe was fixed to the 3D traverse as used by the conventional PIV laser. The endoscopic probe is fixed to a controllable pivot allowing adjustment in the yaw angle. The yaw angle is set to 45° to allow the laser sheet protruding from the endoscope to be parallel to the x-y plane at z=0.

A Dantec Nanosense 2M camera is focused, via optics in the shaft, onto the droplets illuminated by the laser sheet. The field of view captured onscreen is 80 x 60 mm. The actual image captured for PIV use is Ø56.4 mm. An example of the image has been shown in section 3.4.2 and the calibration image is shown in section 4.5.1. The images were recorded at 50 mm increments along the x-axis over the range 50 mm<x<500 mm. The x movement was controlled by the traverse. The camera has a maximum trigger frequency of 8 Hz and an image resolution of 1600 x 1200 pixels. The camera image is also relayed at 45° as shown in figure 4.11. This allows a perpendicular view field to the laser sheet and was set to focus on the illuminated droplets and particles on the x-y plane. The focus position was set by the manufacturer. The predicted *f#* is approximately 8.45 and the working distance is 60.4 mm. Due to the short working distance and the wide field of view the image contains some barrel distortion.

The timing of the laser and camera are synchronised using a Dantec timing box, which was controlled by Dynamic Studio v1.45 PIV software. The software was installed on a 2.4 GHz quad-core Laptop which houses 160 Gb of hard disk space and 2 Gb of memory. The laptop is fitted with a PCI bridge adapter which connects to a DAQ and IMAQ card. The hardware schematic is given in figure 4.12. The entire SSE-PIV system is self-contained requiring only a 24V supply and a small cooling unit. The image schematic of the positional details of the SSE-PIV probe in the spray is given in figure 4.13.

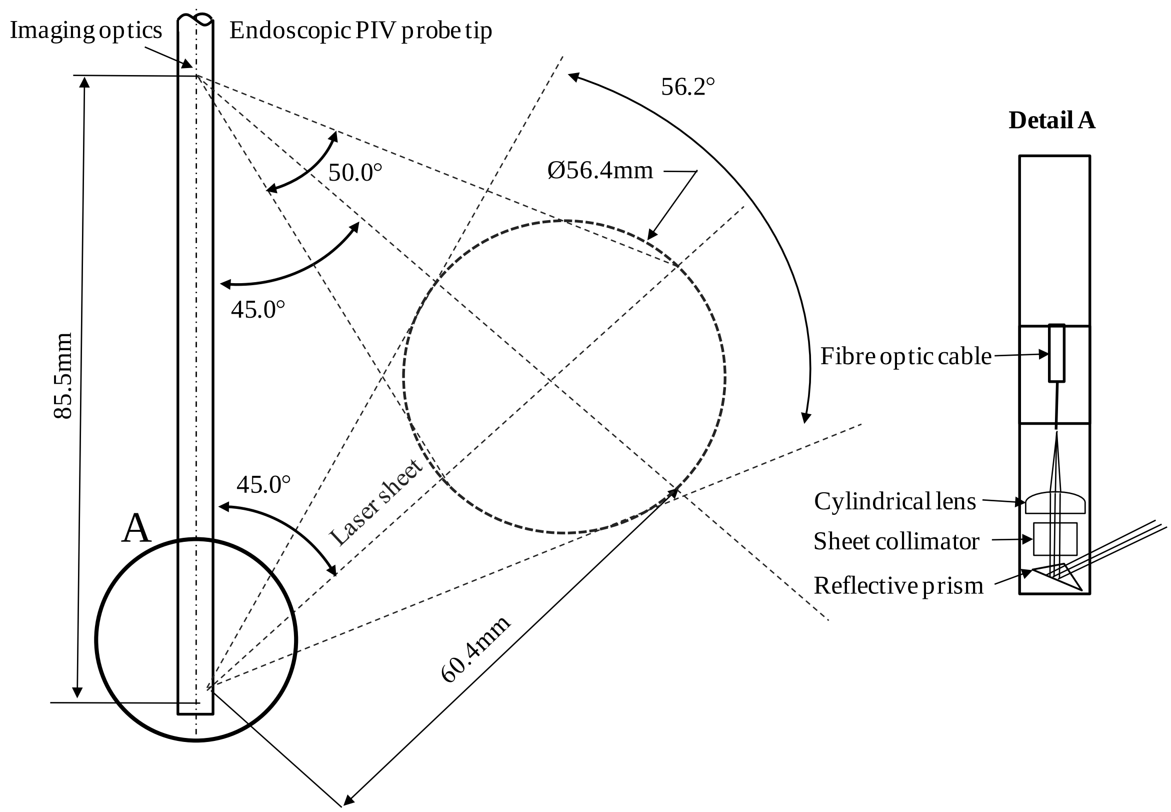

Figure 4.11: Schematic of the laser sheet and imaging window from the single-stem endoscopic probe.

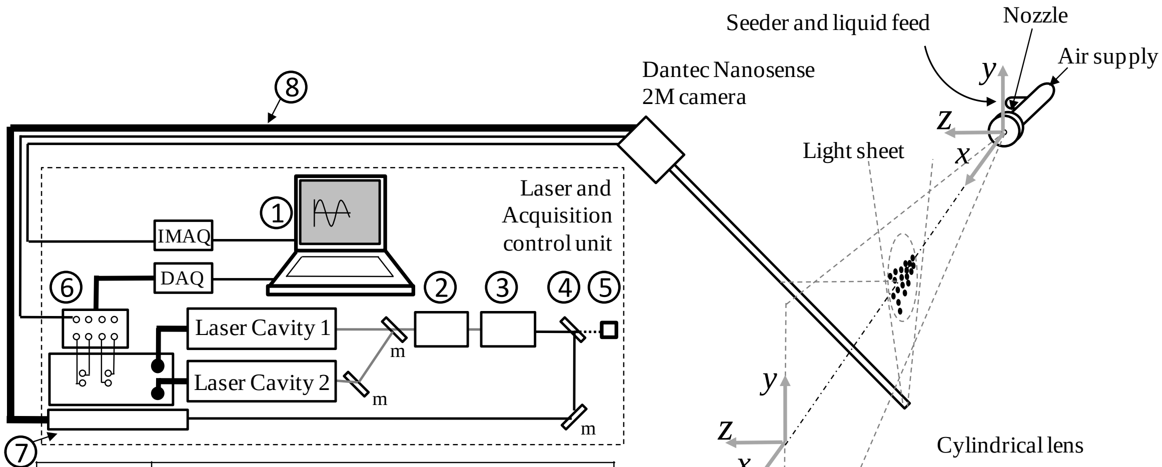

Part No.	Description
1	2.4 Ghz Duel Core Laptop
2	Harmonic Generator
3	Beam combiner
4	Harmonic Separator
5	IR beam dump
6	Timer box
7	Laser beam / fibre optical coupler and interlock
8	Nine core fibre optical cable
m	Laser mirror

Figure 4.12: A hardware schematic of Single-stem endoscopic PIV hardware within the spray flow.

The laser sheet emitted from the SSE-PIV probe is located 7 mm from the top of the shaft. The laser beam travels through the optics within the shaft and is orientated 45° as it is fired and produces a 50° sheet across the *x*-*y* plane. The working distance from the *x*-*y* plane is 60.4 mm as shown schematically in figure 4.13.

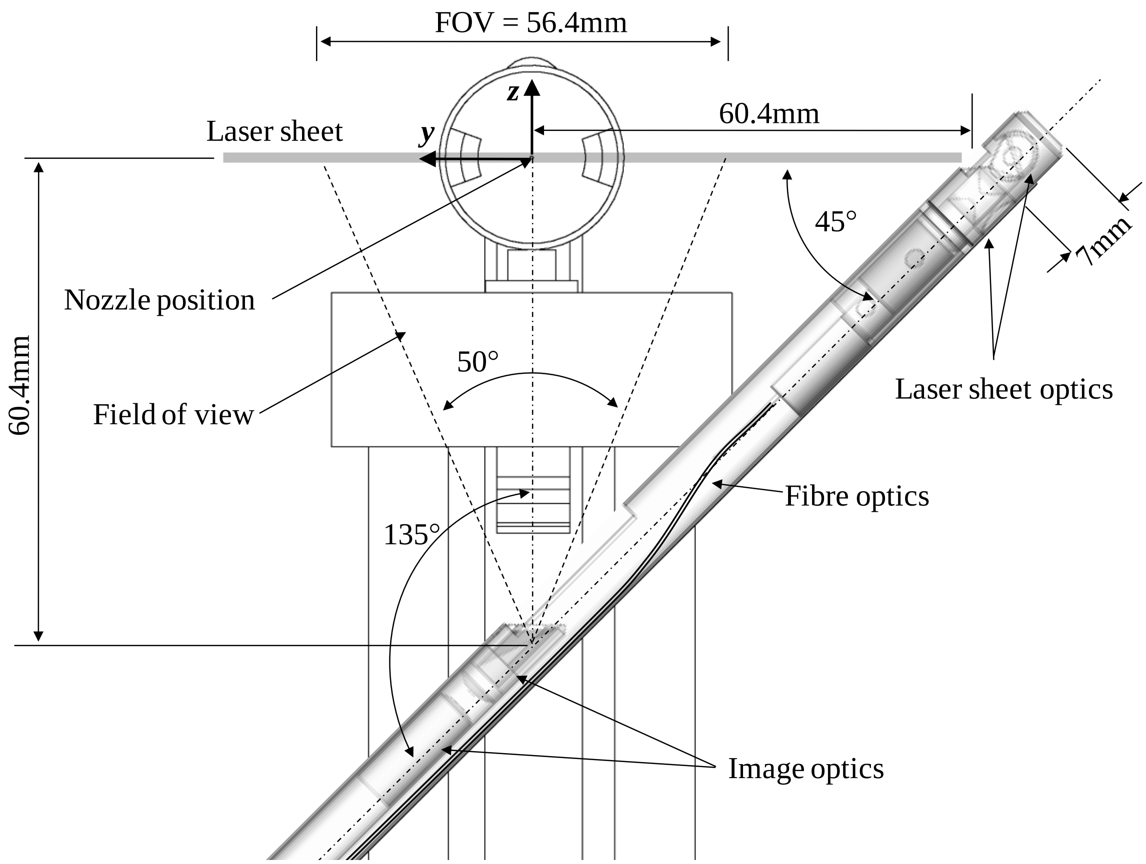

Figure 4.13: A schematic of the positional setup of the single-stem endoscopic PIV in the spray.

4.4.3 Combined setup

An experiment was devised to assess the accuracy of the PIV obtained using the SSE-PIV system. It is assumed that the introduction of the Ø10 mm shaft of the endoscope within the spray flow causes a disturbance to the flow field. To validate the effectiveness of the SSE-PIV system the amount of disturbance that is created by the probe on the field of view must be quantified.

To determine the disturbance in the PIV field of view, a similar setup to that in section 4.4.2 is devised. In this test the endoscope is substituted for a dummy shaft which is a Ø10 mm shaft with a 1 mm, 45° chamfer at the top most edge. This shaft is dimensionally similar to the SSE-PIV probe. The cylinder is held 45° within the spray by an angled block as shown in figure 4.14. The block is fixed to a micro traverse which allows minor movement in the *x*, *y* and *z* direction. The micro traverse has a positional accuracy of 0.05 mm. The entire traverse is fitted to the spray rail via the side T-slots which allow parallel movement in *x* to a maximum of 0.9 m.

The position of the dummy shaft within the spray is exactly the same as that of the SSE-PIV probe mentioned in section 4.4.2. The details of this are seen in figure 4.15. The shaft was set by measuring the position using a laser plumb line against the streamwise axis. The angled block restricts the probe from excessive vibration and displacement in the pitch angle. An image of the probe dummy endoscope can be seen in figure 4.16.

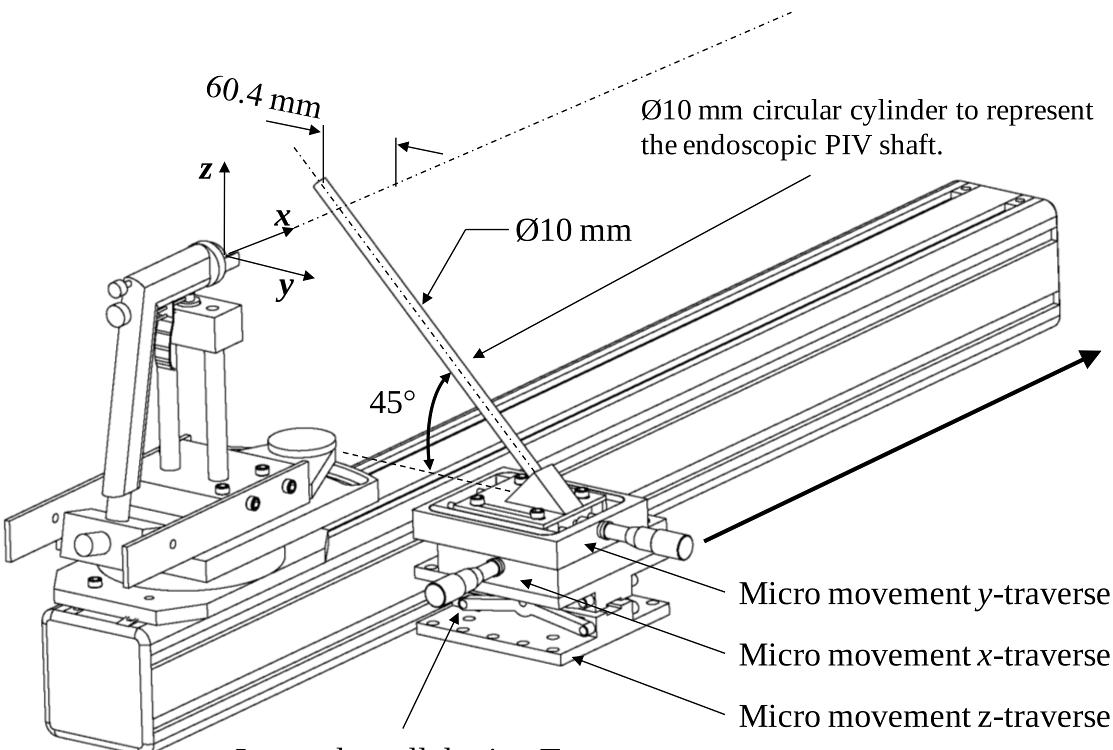

Figure 4.14: The setup of the dummy single-stem endoscopic probe in the spray.

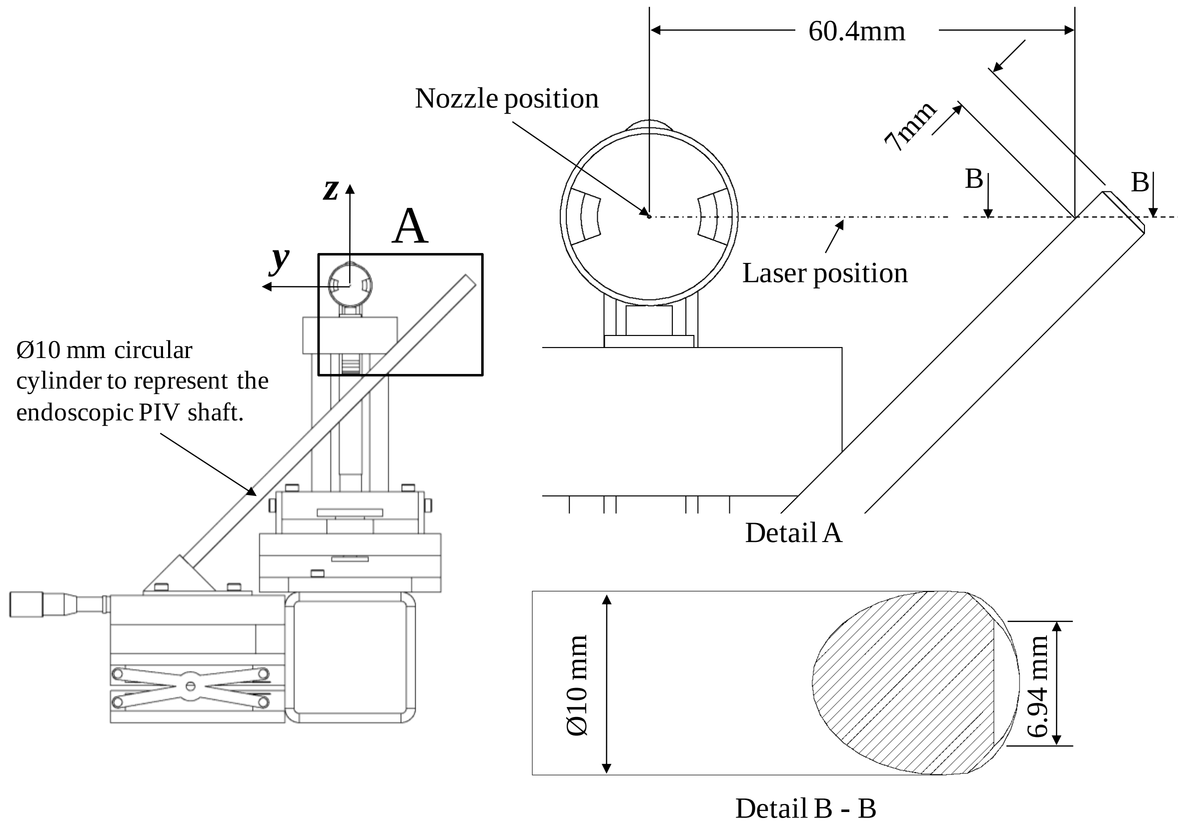

Figure 4.15: Position of the dummy Ø10 mm shaft in the spray and its traversing mount.

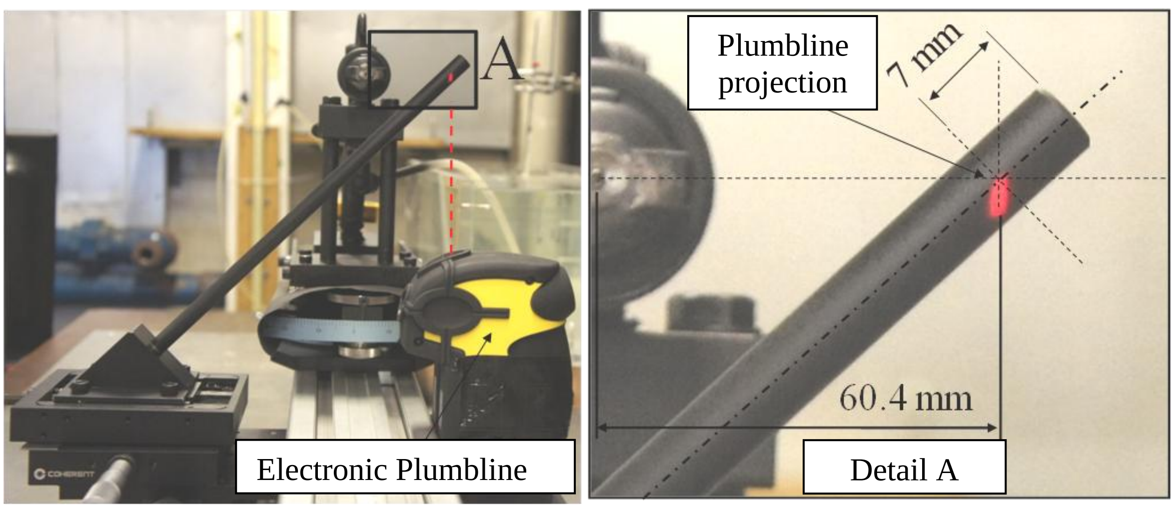

Figure 4.16: Image of the dummy Ø10 mm shaft in the spray and its traversing device. The position is measured using a laser plumb line.

The disturbance caused by the probe was measured using the C-PIV system. The C-PIV is setup as previously described in section 4.4.1. An image of the combined setup is given in figure 4.17. Reflection of the laser energy on the cylinder was minimised by using matt black anti-reflective paint to coat the surface. At 45° the cylinder intrudes the spray. The intrusion is off axis and the cylinder is of finite length. The position of the conventional PIV system laser sheet is along the *x*-*y* plane at *z*=0. This position coincides with the laser position and thus the image plane of the SSE-PIV system setup. The probe at this point has a profile as seen in figure 4.15, detail B-B. The position was measured using an electronic plumb line as shown in figure 4.16. The position of the laser beam to the spray centre axis was measured to be 60.4 mm. The probe was adjusted to meet the positional criterion as shown in figure 4.15 and 4.16. The plumb line is removed before any testing occurs. The PIV recording was repeated for the cylinder position over the range *x*=50 mm to 350 mm at 50 mm increments. An image of the combined setup is shown in figure 4.17 and the streamwise positions in figure 4.18.

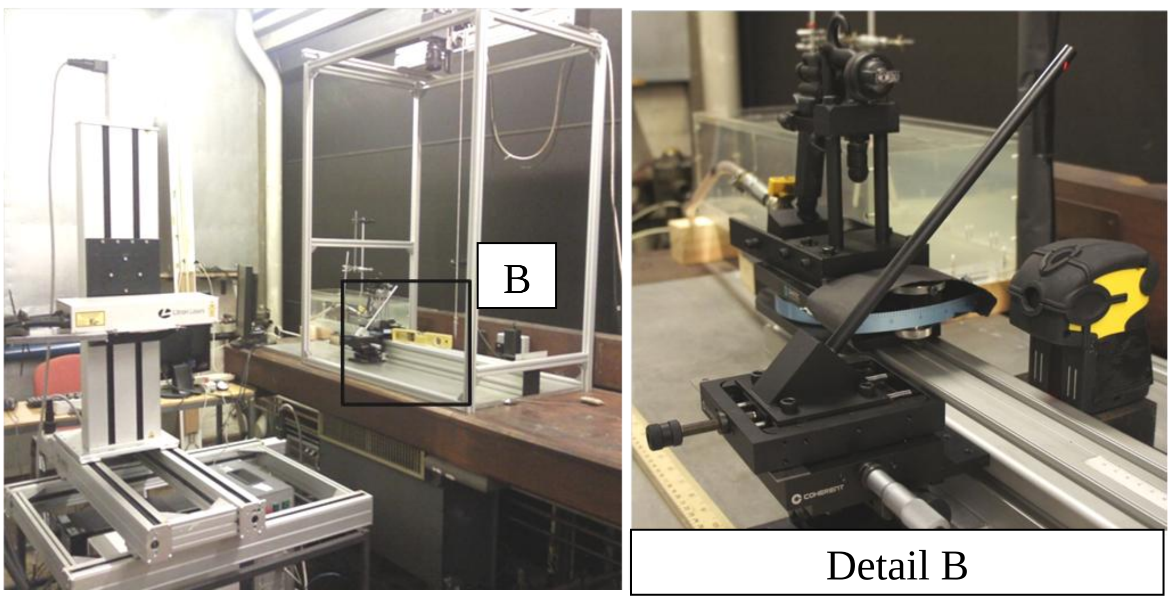

Figure 4.17: An image of the combined setup.

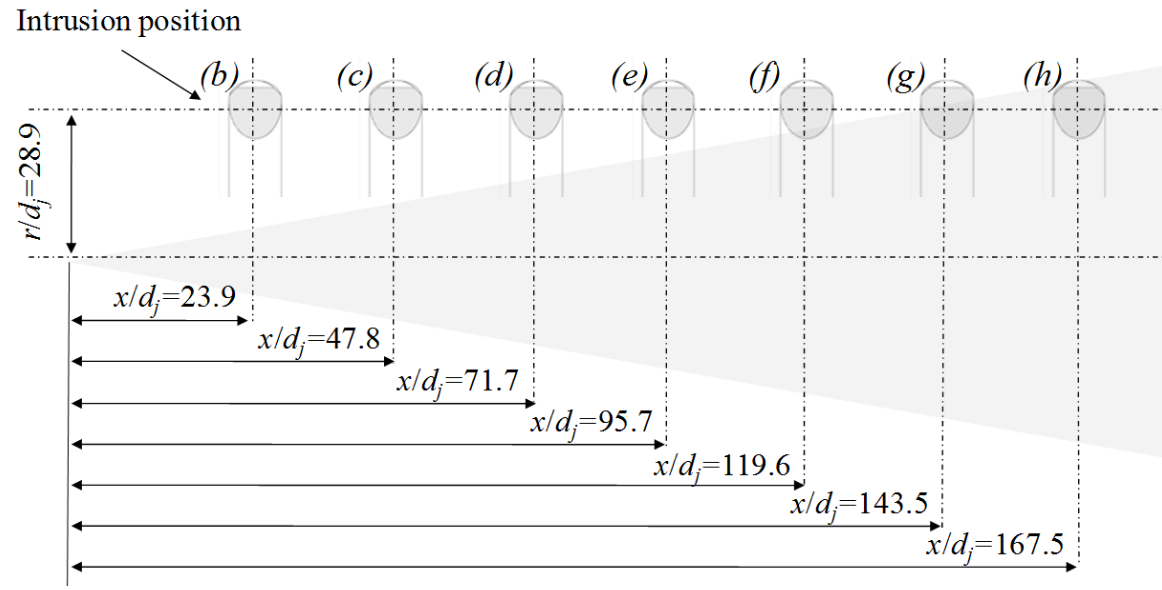

Figure 4.18: Position of the circular cylinder along the streamwise position over the range x=50 mm to 350 mm at 50 mm increments normalised by the jet exit diameter d_j =2.09 mm.

In the PIV image the desired signal and unwanted scatter will be present. Scatter is the result of minor irregularities and characteristics of the system optics and application, including uncontrolled light reflection from the cylinder. To improve the signal component and reduce the noise component, an edge filter is used to block the scattered energy from reaching the detector. With the current setup, the image experiences excess light scatter from the laser reflection on the cylinder as shown in figure 4.19 *(a)*. To increase the spray PIV signal while reducing the light scatter, Rhodamine-B particles of 10-30 μm in diameter are particles are suspended within the spray reservoir. Rhodamine-B particles are fluorescent, and have been used successfully as a laser dye for many laser induced fluorescence (LIF) multiphase applications. Rhodamine-B particles have a max excitation wavelength λ=550 nm and a maximum emission at λ=590 nm. The emission is seen within the orange/red range. An edge filter is placed in front of the camera lens with a dichroic cut-on wavelength λ=570 nm. The filter is 7 mm thick and is backed with an anti reflective coating. This removes the background noise component from the image. There are no additional perspective effects or optical aberrations experienced while using the edge filter. The result of the modified optical setup is shown in figure 4.19 *(b)*.

Rhodamine-B particles have a density of 1190 kg/m^3 and have a refractive index of 1.479. The 30 μm particles are transported independently to the liquid droplets yet still follow the air flow. The gravitational response on the mean particle size, 15 μm, is $u_g = 9.11 \times 10^{-3}$ s, the velocity lag, $u_s = 1.72 \times 10^{-4}$ s and the relaxation time, $\tau_s = 9.30 \times 10^{-4}$ s. The calculations used to obtain these parameters are described in chapter 3.

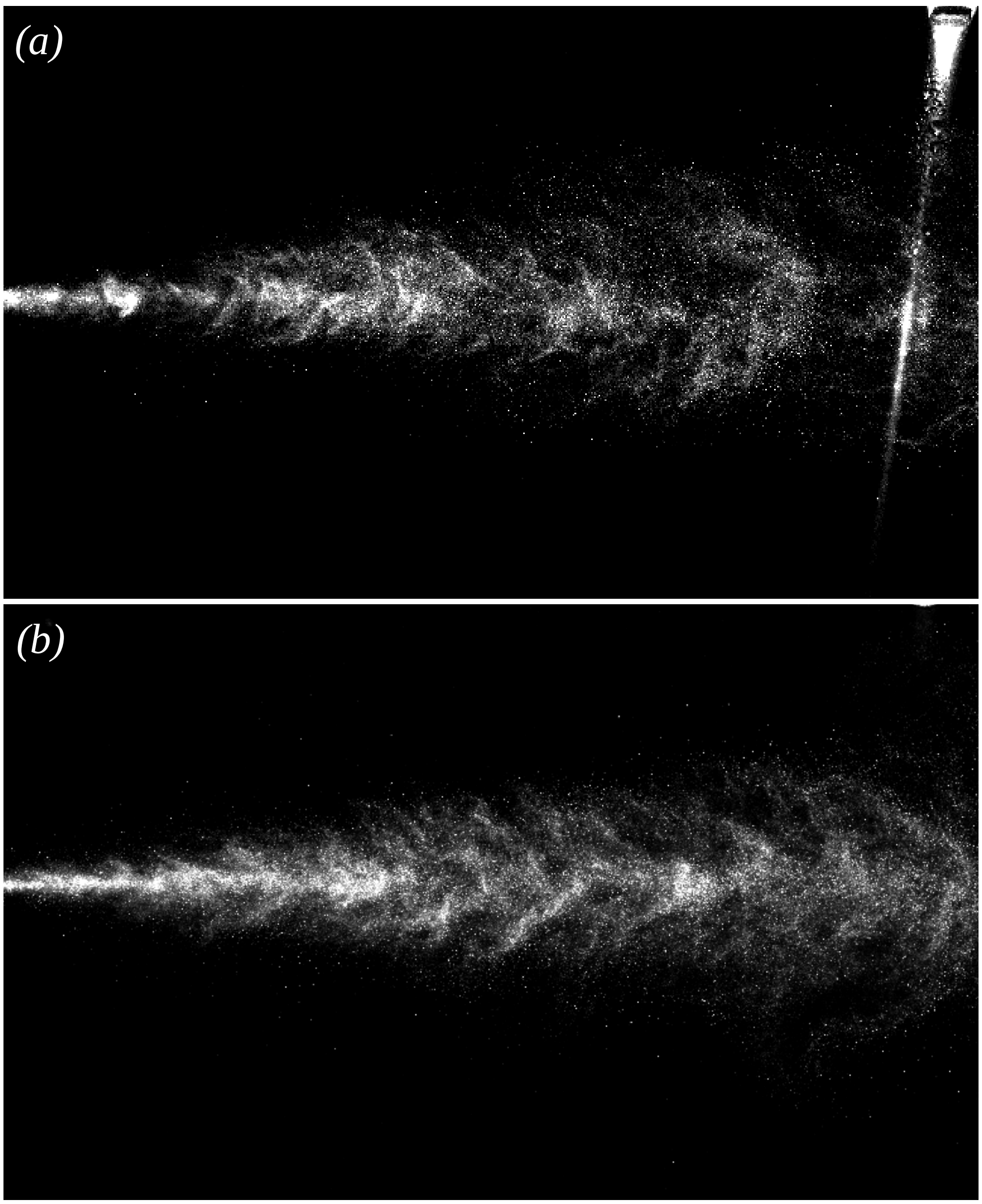

Figure 4.19: *(a)* Original image with light scatter and low signal to noise ratio and *(b)* the corrected image using Rhodamine-B 1-30 μm seeding particles and an edge filter. The contrast and brightness has been increased for visual purposes.

4.5 Processing the PIV images

For both C-PIV and SSE-PIV techniques used in this study; the laser control, laser/camera’s synchronisation, data acquisition and processing was handled by the hardware modules as described in section 4.4 which was all controlled by Dynamic Studio v1.45 software. The summary of the parameters used for C-PIV and SSE-PIV are described in table 4.2.

Table 4.2: Summary of PIV parameter space

Category	C-PIV Parameters	SSE-PIV Parameters
Target Flow of Measurement		
Target flow	Atomised spray flow	Atomised spray flow
Measurement facility	Free stream spray from spray gun	Free stream spray from spray gun
Measurement area	211.5 x 211.5 mm	Ø 58.4 mm
Spray exit velocity (u_e)	50 m/s	50 m/s
Spray exit diameter (d_j)	2.09 mm	2.09 mm
Nozzle equivalent diameter (d_e)	2.87 mm	2.87 mm
Calibration		
Distance of reference points (l_r)	200 mm	56.4 mm
Distance of reference image (L_r)	1493 pixels	1096 pixels
Magnification factor (α)	0.13389 mm/pixel	0.05146 mm/pixel
Flow Visualization		
Tracer particle	Atomised water droplets	Atomised water droplets
Average diameter (d_p)	31.8 μm	31.8 μm
Sauter mean diameter (d_{32})	44.1 μm	44.1 μm
Standard deviation of diameter (s_p)	16.7 μm	16.7 μm
Average specific gravity	1.041	1.041
Light source	Double pulse Nd:YAG laser	Double pulse Nd:YAG laser
Laser power (max)	200 mJ	200 mJ
Thickness of laser light sheet	1.3 mm	1.3 mm
Time between pulses (Δt)	11 ms	16 ms
Image Detection		
Camera	Dantec HISense 4M	Dantec NanoSense 2M
Spatial resolution	2048 x 2048 pixels	1024 x 1024 pixels
Sampling frequency	4 Hz	8 Hz
Gray scale resolution	12 bit	12 bit
Optical system		
Distance from the target (l_t)	800 mm	60.4 mm
Length of focus (F)	60 mm	8.95 mm
f number of lens (f#)	f/2.8	f/8.89
Perspective angle (θ)	19.47°	50°
Data Processing		
Pixel unit analysis	Adaptive correlation method	Adaptive correlation method
Correlation area size	16 x 16 pixels	16 x 16 pixels
Search area size	128 x 128 pixels	128 x 128 pixels
Sub-pixel analysis	3 points Gaussian fitting	3 points Gaussian fitting

4.5.1 Calibration technique

The calibration images are given in figure 4.20. The C-PIV system is calibrated using a scale to give a physical displacement characteristic in mm. The SSE-PIV calibration was carried out by using the known field of view information to provide the physical distance. The image Field of view for C-PIV is 214.45 x 214.45 mm. Figure 4.20 *(b)* shows the on-screen image capture for SSE-PIV. The full field of view is 80 mm x 60 mm. The optical arrangement through the shaft limits the image field of view to Ø56.4 mm. During pre-processing the surrounding blackened region was masked and is neglected from any PIV processing. The magnification factor $\alpha = L_r/l_r = 0.13389$ and 0.05146 mm/pixel for C-PIV and SSE-PIV respectively.

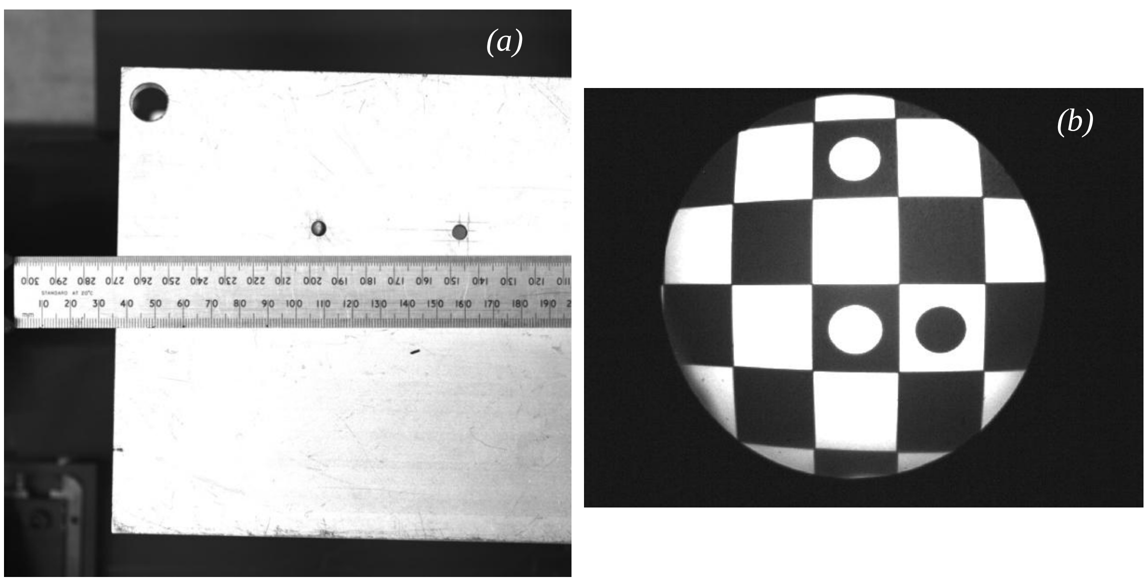

Figure 4.20: *(a)* C-PIV image calibration using a scale and *(b)* SSE-PIV image with a known image field of view diameter.

4.5.2 Processing techniques

The time interval between two laser pulses ranged from 11 to 16 ms which allowed approximately 25% displacement of a particle within a 16 x 16 pixel interrogation window. A masking function was applied to the raw image. This invalidates all areas of the image which have no seeding particles, removing erroneous measurement caused by an ill-defined flow field from the final vector map. The spray has a large velocity variance between maximum velocity at the spray nozzle and minimum occurring downstream and outside the spray shear layer. To increase the detection of tracer particles between frames, recorded images were correlated using an adaptive cross-correlation process as described in chapter 3. Similarly the details of all post processing tools used within this section are described in brief in chapter 3 and in full in Raffel *et al.* (2007). The adaptive cross-correlation involved a multi-gridding method which uses a three step correlation which starts with a larger IA of 64 x 64 pixels and progressively decreases to 16 x16 pixels for both SSE-PIV and C-PIV recordings.

The interrogation area is also correlated using a 50% overlap. This allows particles at a 50% displacement outside the IA to still be traced. The correlation process involves using window offset which uses a central difference scheme. A moving average filtering was applied to the correlation using a 3 x 3 matrix function which has a three pass iteration process and a 1.2 acceptance factor. A smoothing filter was then applied using a 5 x 5 matrix which substitutes average vectors for previously invalidated vectors. The correlated images are then statistically averaged to produce an ensemble mean flow field.

4.5.3 Convergence characteristics

The statistical convergence of the statistical mean flow field has been assessed by considering the statistics of an ensemble mean of 10 to 1000 captured image pairs. The mean RMS of the ensemble mean velocity map was calculated. The differences in calculation of statistical mean RMS from velocity maps between 600 frame and 1000 frame ensembles are less than 3%. Therefore in the tests performed within this study 600 image pairs were captured in each run. The convergence characteristics are shown in figure 4.21. Due to limitations in disk buffer size and speed of the computer only 100 images could be taken successfully. Therefore to achieve 600 images six runs of 100 image pairs were performed back to back. The six ensemble mean plots were then averaged again.

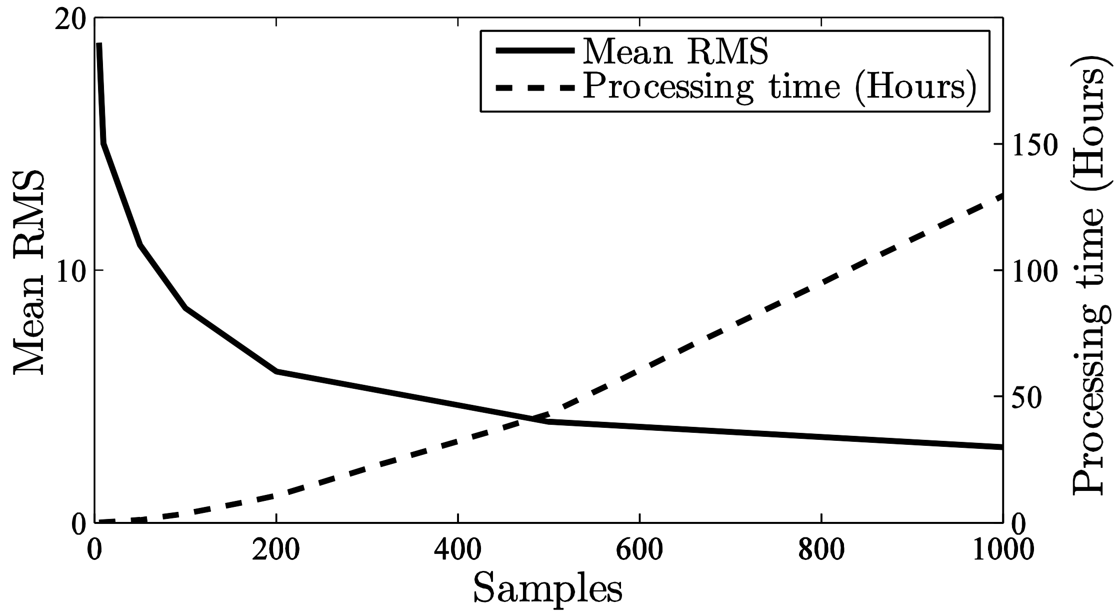

Figure 4.21: Convergence characteristics of the mean RMS from the statistical mean with increasing number of samples with the respective processing time.

4.6 Alignment of the spray centreline axis with an anemometry frame of reference

The spray centreline alignment is carried out using Pitot anemometry, the C-PIV system, and the SSE-PIV system. A series of profiles are obtained along a y and z traverse at increasing stream wise direction, x. The spray is adjusted in the pitch, yaw and roll angle until the spray centreline is aligned to the x axis. This is when the maximum u was measured at u_c when z=0 and y=0 over the range 23.9d_j <x<143.5d_j at x=23.9d_j, where d_j is the jet exit diameter as described in section 5.4.

4.6.1 Spray centreline alignment by Pitot anemometry

Using the setup described in section 4.3 the Pitot-static tube is traversed across the spray along the y an z axis over the range $23.9d_j < x < 143.5d_j$ at $x=23.9d_j$. The process was repeated iteratively until the maximum streamwise velocity was located at $y=0$ and $z=0$. The data from the Pitot anemometry was compared to a whole flow field measurement obtained using the C-PIV system. The conventional PIV system was set to an x-y plane at $z=0$ and streamwise velocity profiles over the range $23.9d_j < x < 143.5d_j$ at $x=23.9d_j$ increments were obtained. The same procedure was carried out using the SSE-PIV system. All techniques are compared at the same position to check alignment coherence between all measurement techniques and are shown in figure 4.22. Figure 4.22 shows the detail of the discrete velocity profile over the range $0.7u_c < u < 1.0u_c$ and $-3.0d_j < r < 3.0d_j$, formed by obtaining streamwise velocity data across the spray radius. Coherence of the spray centreline using y and z traverse data from three different measurement techniques is observed. The maximum streamwise velocity is located at $r/d_j=0$ for all x/d_j positions. The data obtained using the Pitot anemometry and backed up using C-PIV and SSE-PIV techniques. This suggests that the spray centreline pitch angle and centreline yaw angle is aligned to the x axis.

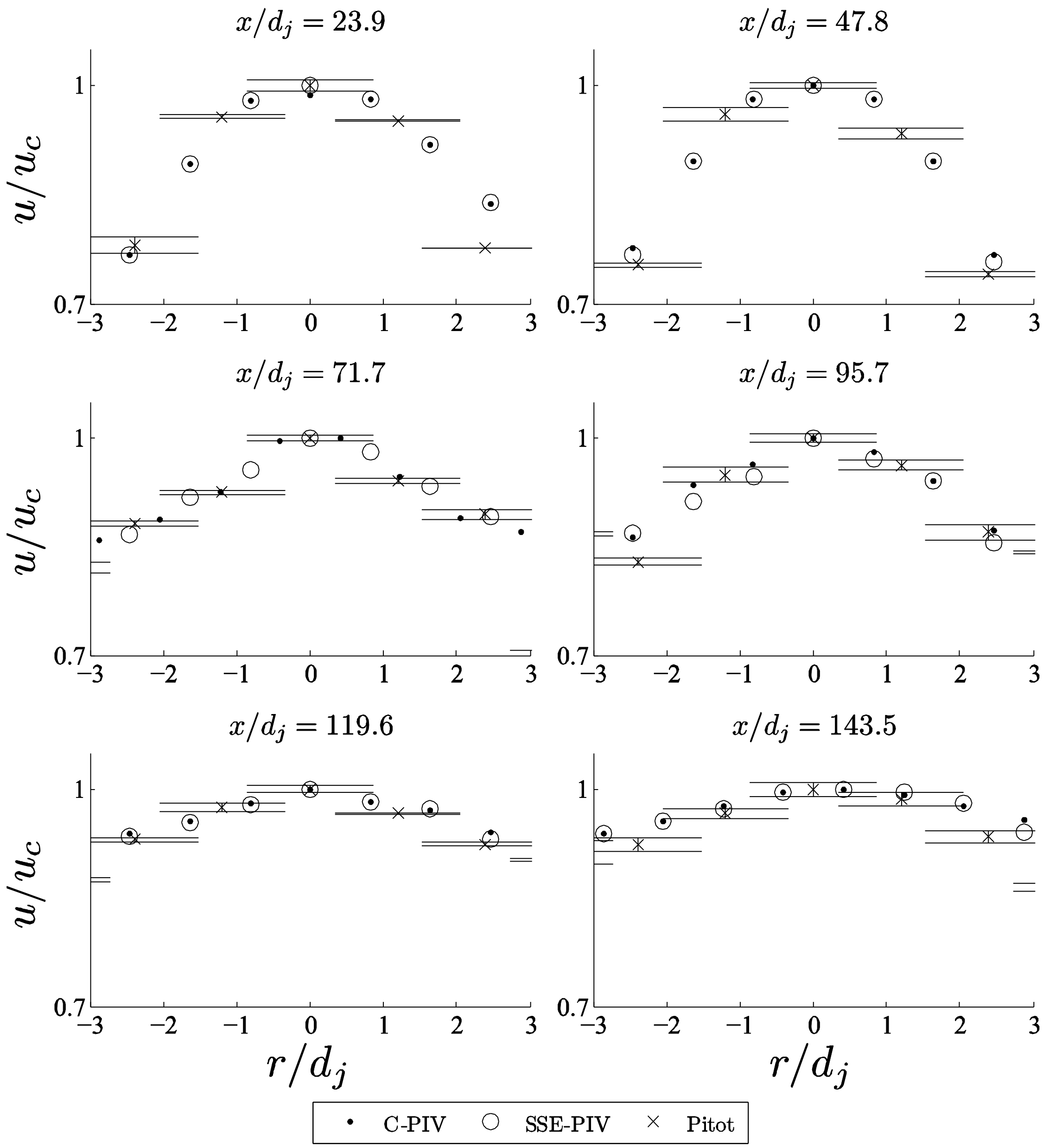

Figure 4.22: Detail of the discrete velocity profile at $0.7u_c < u < 1.0u_c$ and $-3.0d_j < r < 3.0d_j$ obtained by streamwise velocity profiles along y and z directions over the range $23.9d_j < x < 143.5d_j$.

4.6.2 Spray centreline alignment by conventional PIV image capture

The process of alignment is repeated to check pitch and roll angle of the spray, using only the conventional PIV system. The alignment data is obtained by taking a series of x-y plane measurements of streamwise velocity over the range $-11.96d_j<z<11.96d_j$ at increments of $z=2.39d_j$. The results are shown in figure 4.23.

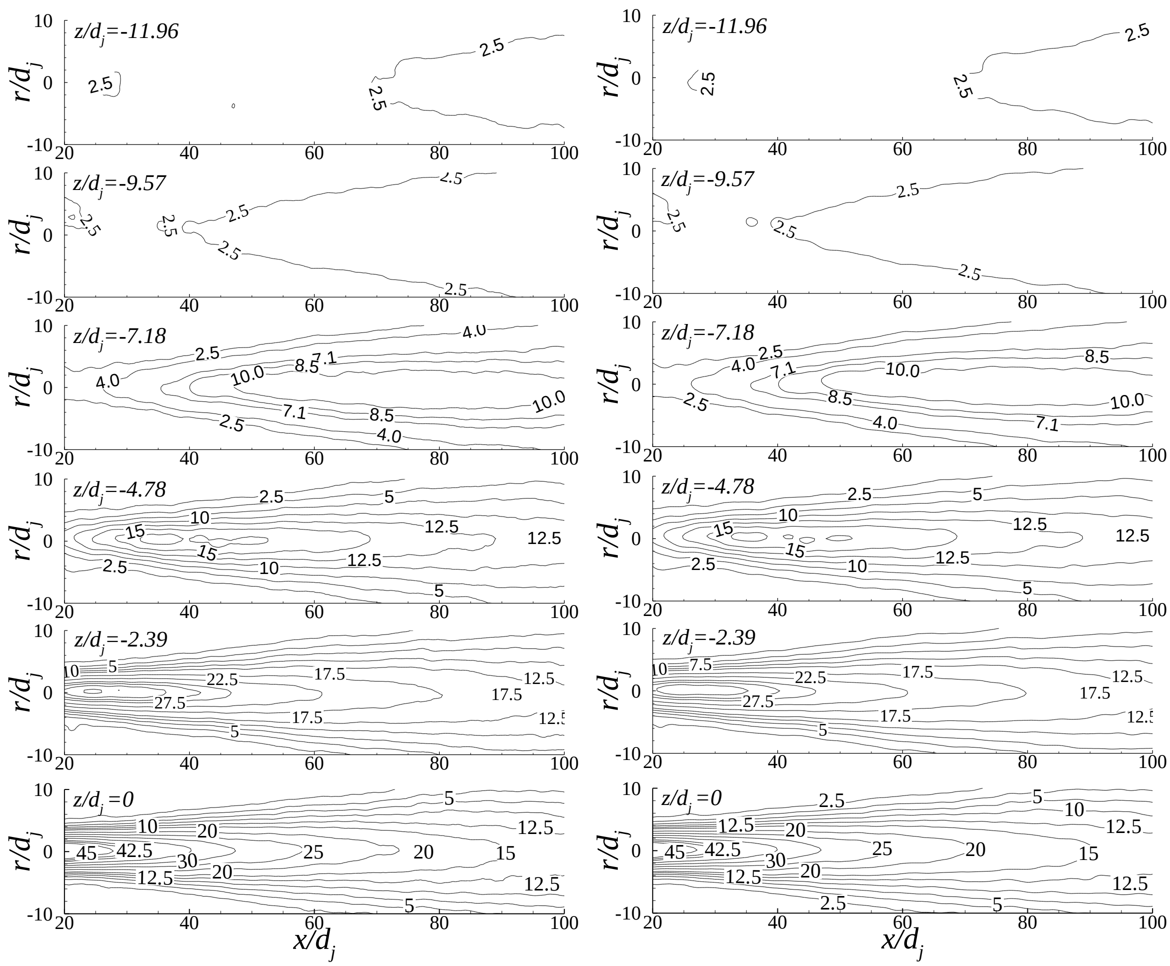

Figure 4.23: C-PIV ensemble mean u velocity on the x-y plane over the range $-11.96d_j<z<11.96d_j$ at increments of $z=2.39d_j$.

By subtracting the streamwise velocity contours of a z/d_j positional plane by a symmetrical plane about z/d_j=0 one can obtain the δu between the two images. Figure 4.24 shows the plots of δu at increasing z/d_j. The maximum velocity variance, δu, between a plane and its symmetrical plane about z/d_j=0 is ±0.02 m/s. It is evident that the mode δu of the contour plots in figure 4.24 is 0 m/s. It is evident that the prevalent positive δu is found between x/d_j =80 and 100. However this error in symmetry propagates and dissipates at random and does not fit a trend of misalignment. To fully understand the alignment properties within the contours of figure 4.24 histograms of δu at increasing z/d_j are produced and presented in figure 4.25. It is clear that there is a predominantly zero value which suggests alignment of the spray centreline in the pitch angle. There is a slight bias towards positive or negative at each z/d_j position. The biasing fluctuates at each z/d_j position and does not show any sufficient trend for mis-alignment. The slight fluctuation may be due to the small changes in incoming pressure and thus the spray exit velocity.

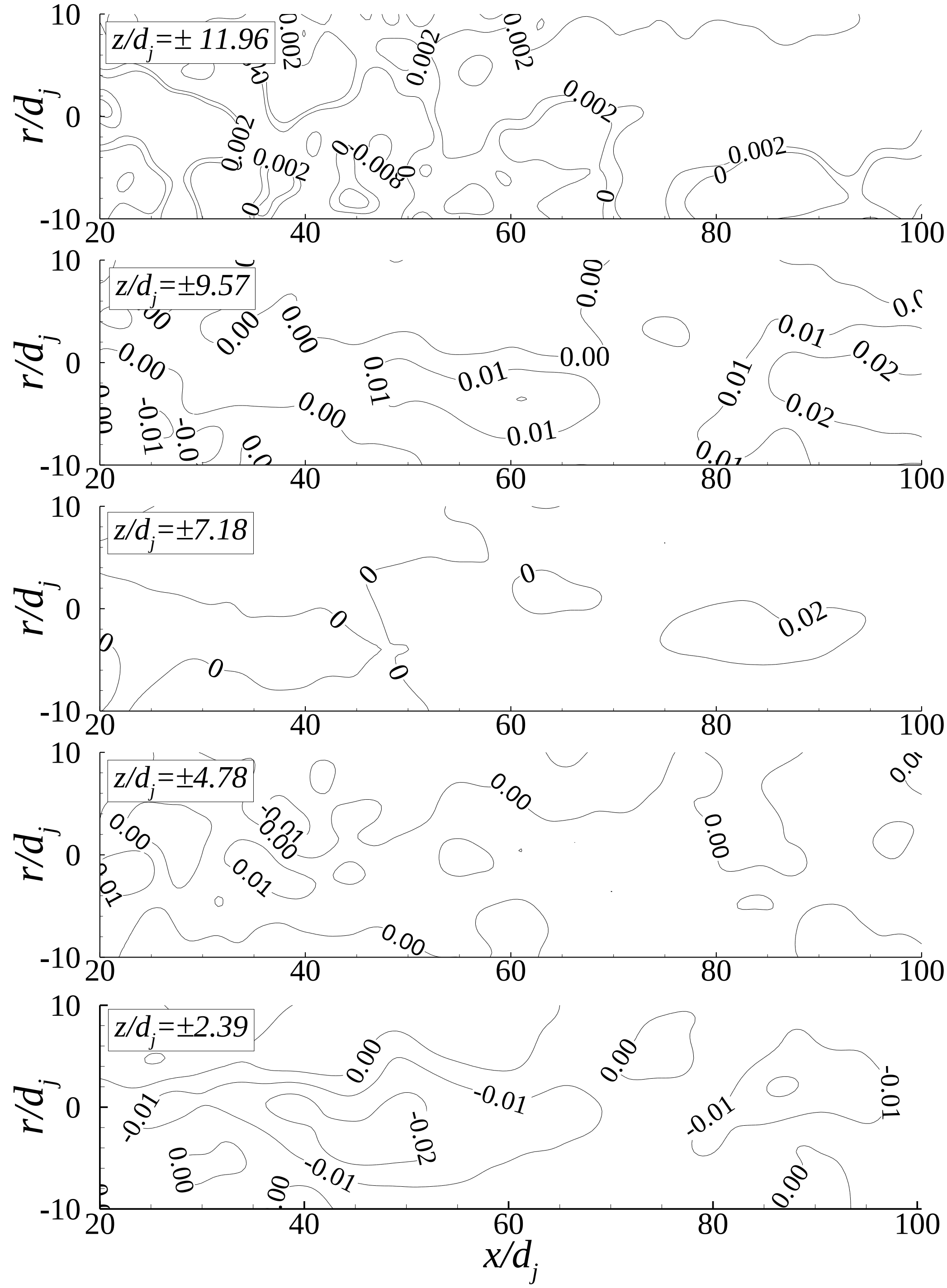

Figure 4.24: Contours of δu on the *x*-*y* plane over the range $-11.96d_j<z<11.96d_j$ at increments of $z=2.39d_j$.

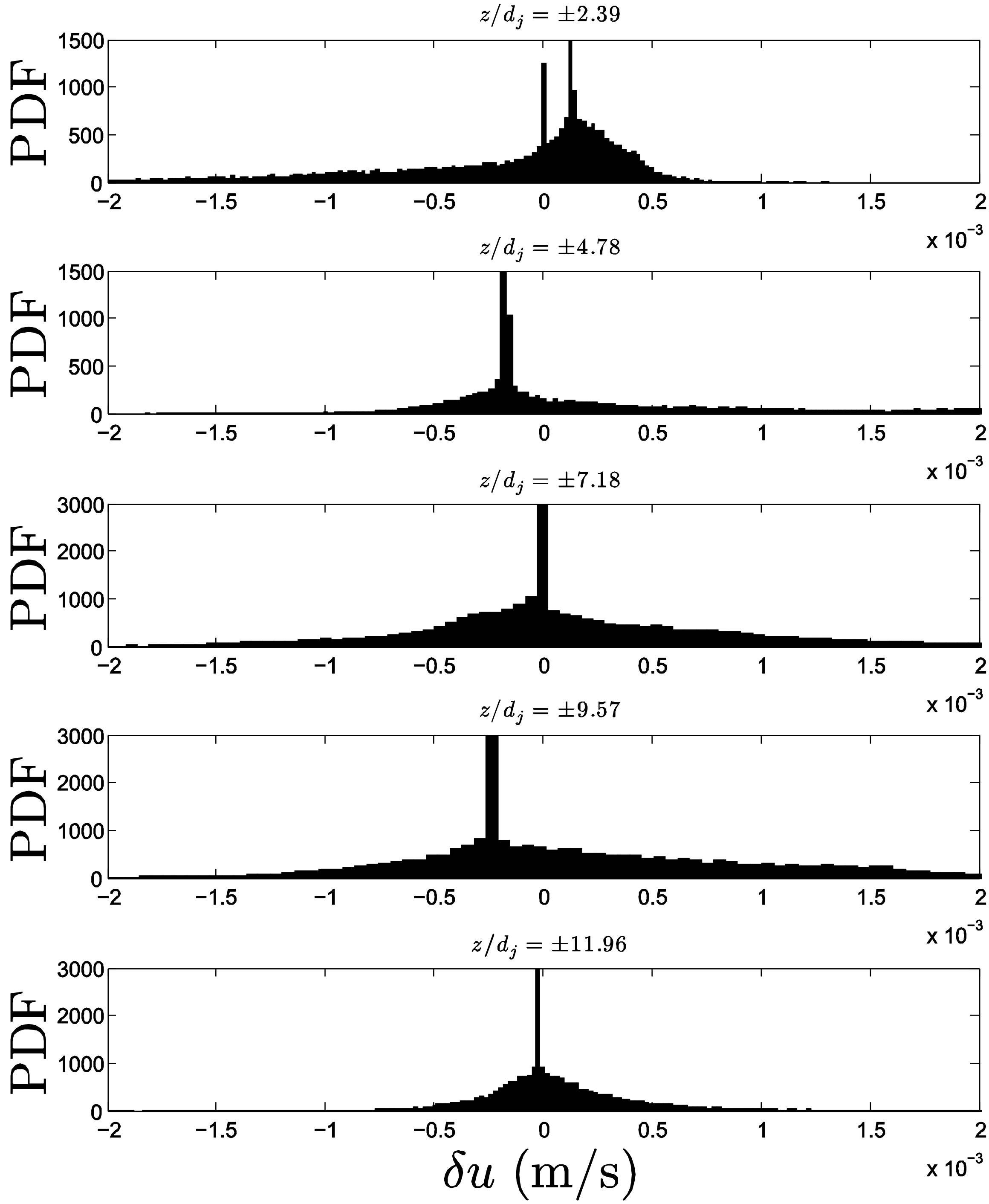

Figure 4.25: The probability density function of δu on the *x*-*y* plane at over the range -11.96d_j<z<11.96d_j at increments of z=2.39d_j.

Probability density function of δu were produced focusing on the first and fourth quartile of the δu contour maps and are presented in figure 4.26. It is evident that in column two there is a positive bias generating within the fourth quartile which would suggest a very small amount of pitch. The third column is a repeated set of data using the same acquisition setup and number of samples. This set of data shows a negative bias. This data compared to that of the previous histogram, in column 2, can conclude the spray centreline is aligned in pitch, yaw and roll angle. Small fluctuations in the streamwise velocity of magnitude $2\text{x}10^{-3}$ m/s may occur due to fluctuations in the incoming air supply and or inherent PIV errors.

Using the data obtained in section 4.6.1 and 4.6.2 one can conclude that the spray centreline is aligned to the streamwise x axis and thus the centreline velocity u_c is located at y=0 and z=0 over the range $23.9d_j < x < 143.5d_j$.

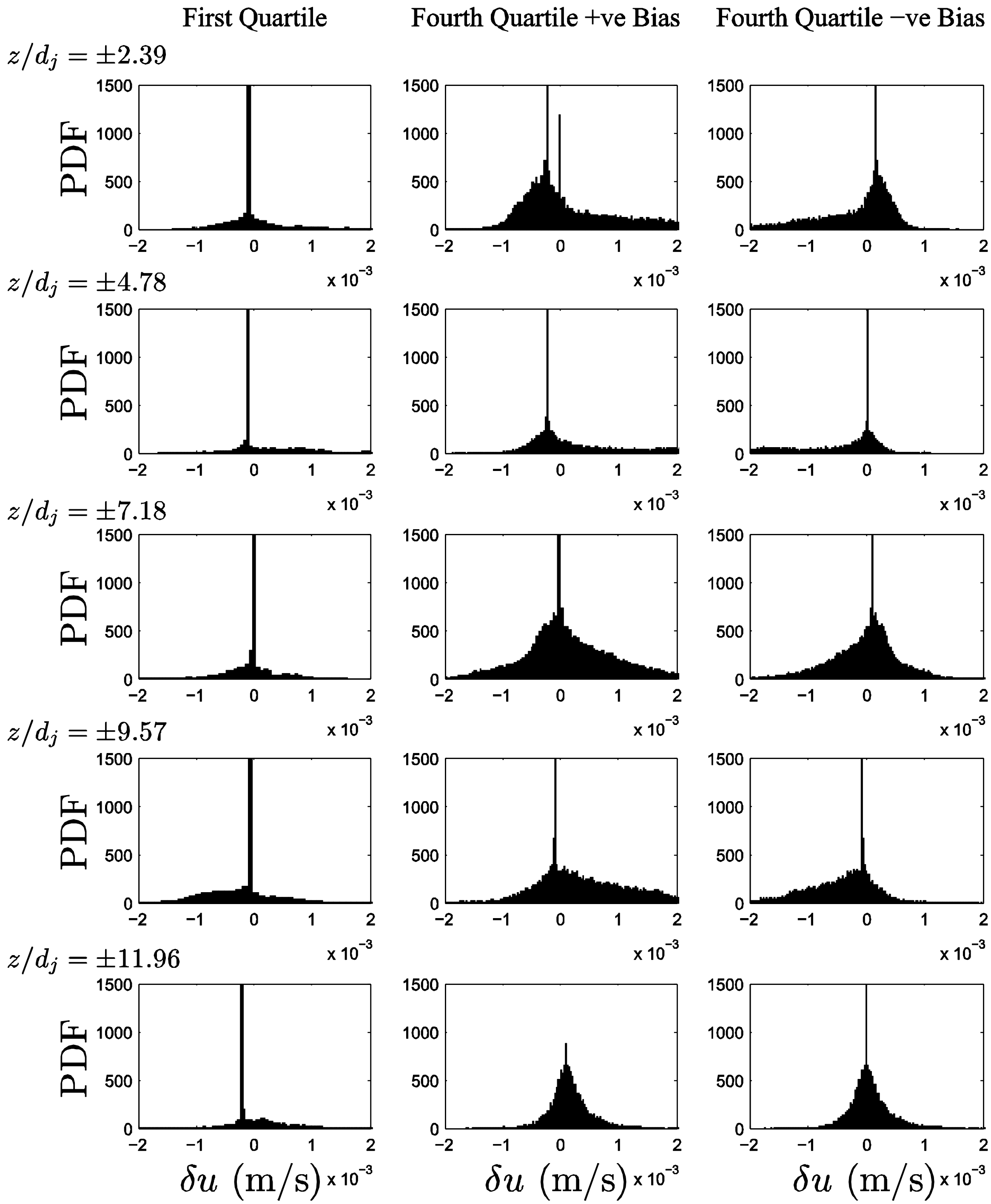

Figure 4.26: First and fourth quartile probability density function of δu on the x-y plane over the range $-11.96d_j<z<11.96d_j$ at increments of $z=2.39d_j$. The fourth quartile is repeated with new samples to show fluctuations in the spray.

4.7 Summary

Within this chapter a detailed description of the instrumentation of the spray is provided. This includes the air water supply and the mounting of the spray device. The setup of the Pitot anemometer, C-PIV, SSE-PIV, and a combined setup are also fully described. The chapter also outlines the spray and PIV measurement parameters. A description of the pre and post processing components used within PIV to obtain mean velocity information of the spray is provided. This includes the calibration details and also the process used to initially align the spray to avoid any positional misalignment in future tests.

CHAPTER 5: ASSESSMENT OF THE MEAN AND TEMPORAL SPRAY CHARACTERISTICS

5.1 Introduction

The primary aim of this experimental study is to validate the measurements recorded by a single-stem endoscopic PIV system (SSE-PIV) to aid its use as a quantitative measurement instrument in open and enclosed flows within industrial applications. To achieve this, the velocity measurements calculated from the SSE-PIV system are directly compared to reference results obtained by the conventional PIV (C-PIV) method and Pitot anemometry.

The assessment of the SSE-PIV system performance is carried out by characterising a fully turbulent atomised free liquid-air spray. This chapter discusses the measured parameters of the jet using C-PIV and SSE-PIV. Section 5.2 presents the ensemble mean velocity flow fields. Sections 5.3 to 5.5 present trends for the mass flow rate, the spray spread rate, and the centreline velocity decay as the spray evolves downstream. The spray time-dependent characteristics captured by C-PIV and SSE-PIV are presented in sections 5.6 and 5.7. The results in this chapter have been published in Lad *et al.* (2011a).

5.2 Ensemble mean flow fields

Figure 5.1 shows the ensemble averaged velocity contours on the meridional plane through the jet axis, obtained from C-PIV. The velocity is normalised by the spray exit velocity u_e, which is computed in section 5.5. Contour maps of u/u_e from the SSE-PIV are overlaid on contour maps of u/u_e from the C-PIV in figure 5.1. The contour plots obtained by the C-PIV system are shown by the solid black lines. The endoscopic images are obtained with the endoscopic probe traversing in the streamwise direction over the range 23.9 $< x/d_j <$ 143.5 at 23.9d_j increments, where d_j is the jet exit diameter defined in section 5.3. This defines six SSE-PIV view fields, labelled as positions P1 to P6 in figure 5.1. The contours of u/u_e from the endoscopic PIV are shown by the dashed lines at the respective position. The endoscopic field of view is 56.4 mm in diameter and thus creates some overlap between successive images. Figure 5.1 *(a)* shows the entire flow field while figure 5.1 *(b)*, *(c)* and *(d)* show the normalised velocity magnitude distribution at increasing x. The radial position r and the axial position x are normalised by the jet exit diameter, d_j=2.09 mm. The contour plots of figure 5.1 *(b)*, *(c)* and *(d)* show that the normalised velocity measured by the SSE-PIV is not matching that from the C-PIV. As r/d_j increases from the centre of the field of view in the SSE-PIV map, u/u_e decreases and the discrepancy between the two measurements becomes more apparent. Each SSE-PIV contour map shows a reduced u/u_e at the maximum and minimum x/d_j locations. This trend is due to the optical distortion and a reduction in illumination that arises from the lens arrangement within the endoscope. As detailed in section 3.5.2, this distortion is of a fish-eye or barrel nature and causes the image to appear curved. This process reduces the depth of field as r/d_j increases from the centre of the image and thus causes the defocusing of the tracer particles and degraded illumination. This was also observed in section 3.5.2

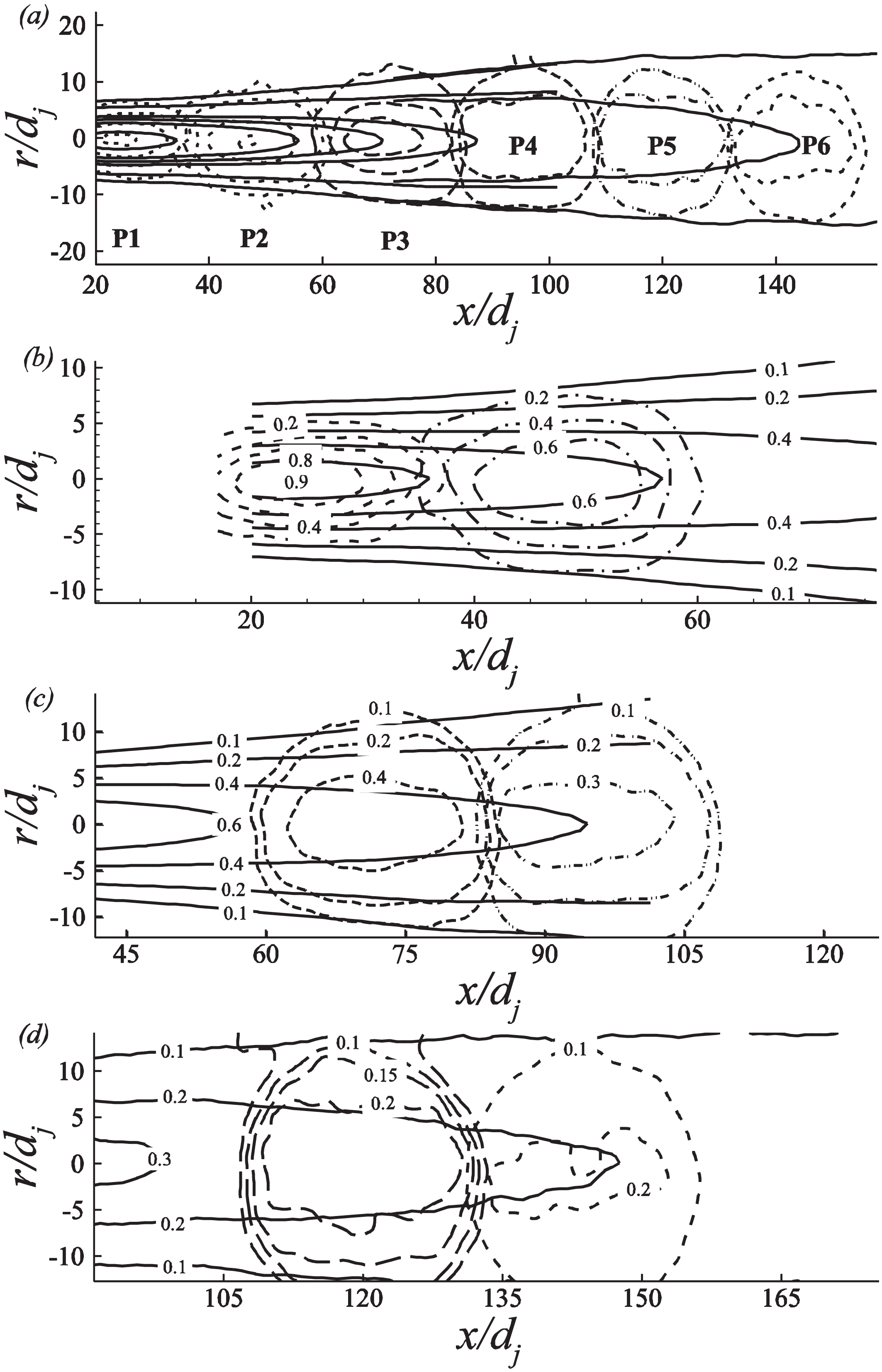

Figure 5.1: C-PIV contour plots of u/u_e overlaid with SSE-PIV.

Spanwise profiles of u/u_c over the range $23.9<x/d_j<143.5$ at $23.9d_j$ increments are shown in figure 5.2. These profiles are radial cross-sections through the centre of each SSE-PIV map, extracted from the SSE-PIV velocity vector map. The error due to field curvature at the centre of the SSE-PIV image plane is at its minimum, therefore the velocity profiles can be compared directly to the ones from C-PIV and Pitot anemometry measurements. The profiles are normalised by the centreline velocity, u_c, and by the jet exit diameter d_j.

The results from Pitot anemometry provide a benchmark result which PIV measurements can be measured against. The shear region of the spray has an increased frequency of flow fluctuation caused by the mixing between layers of the bulk flow of the spray and the surrounding air. The limitation of the Pitot anemometry response time fails to fully record these fluctuations. To overcome the limitation within the Pitot anemometer measurements, each data point is a time average over a sampling time of 30 seconds and a sample rate of 2 kHz. The process for each data point is repeated 5 times to provide an ensemble mean. The normalized axial velocity profiles from the Pitot anemometry in figure 5.2 are bound by error bars, which are sized by the maximum and minimum axial velocity values recorded by the time averaged data. It is evident from figure 5.2 that, as r/d_j increases from the jet centreline to the spray shear region, the uncertainty in the Pitot anemometry measurements increases, as shown by size of the error bars assigned to the Pitot data marker.

The plots in figure 5.2 show that the axial velocity profiles from the SSE-PIV and the C-PIV are similar to the ones from the Pitot anemometry. The SSE-PIV data show some inconsistency in the profile. The inconsistencies are more evident downstream, at increasing x/d_j. As r/d_j increases, there is a large jump towards zero at approximately $r/d_j \approx \pm 12$. The edge of the image is masked. This imposes a value of zero to the velocity vectors in the IA's in the mask and thus the neighbouring IA's are biased towards zero due to neighbourhood averaging. At the position of this jump, the data points are said to be invalid and this data is marked as triangles in figure 5.2.

The profiles also show the δu, (u_{conv}-u_{endo}), between C-PIV and SSE-PIV, marked as diamonds. From the plots in figure 5.2, delta δu is largest at x/d_j=23.9, 119.6 and 143.5. This arises from the different settings of the PIV inter-frame delay Δt between the two techniques. The field of view for C-PIV is much larger than that of the SSE-PIV and therefore has a wider velocity range to capture within the image. The high velocity flow at the nozzle exit plane and the very low velocity downstream in the spray shear region make it difficult to select a common Δt. In this case, a compromise must be considered to ensure the particle image displacement both at the nozzle exit and further downstream is sufficient to allow proper particle tracking. In this sense, the SSE-PIV has a more localised field of view, in which the velocity range is lower, which allows in turn to select a Δt that gives good velocity resolution in the narrower dynamic range of this velocity field. A multi gridding scheme and IA overlapping aid the C-PIV to account for the faster moving flow areas. The resolution of the SSE-PIV and the ability to control the illumination in a localised area allows a better observation of the denser region of the spray, close to the nozzle outlet. At x/d_j=23.9, the δu trend is symmetric about r/d_j=0 and zero at r/d_j=0, which means the measured centreline velocity assumes the same value in both PIV techniques. At x/d_j=119.6 and 143.5, the δu trend is not symmetric about r/d_j=0, which is most probably caused by a small amount of jet axis misalignment in the experimental setup.

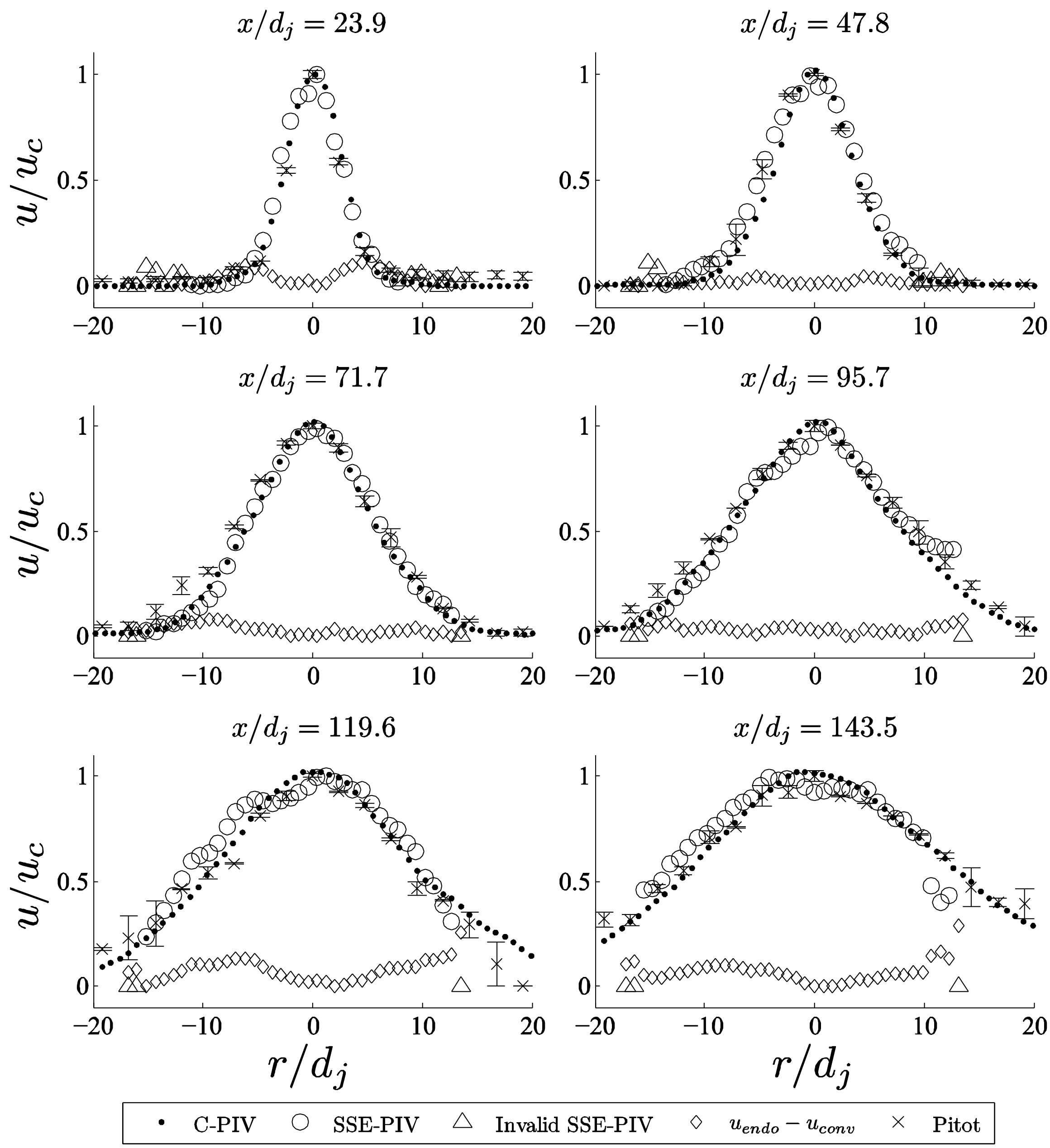

Figure 5.2: Normalized axial velocity profiles obtained from the contour plots using Pitot anemometry, C-PIV and SSE-PIV.

Figure 5.3 shows the ensemble averaged contour plots of u/u_c from C-PIV (*left*) and from SSE-PIV (*right*), plotted side by side. The plots are cropped to show the same axial region from both PIV techniques.

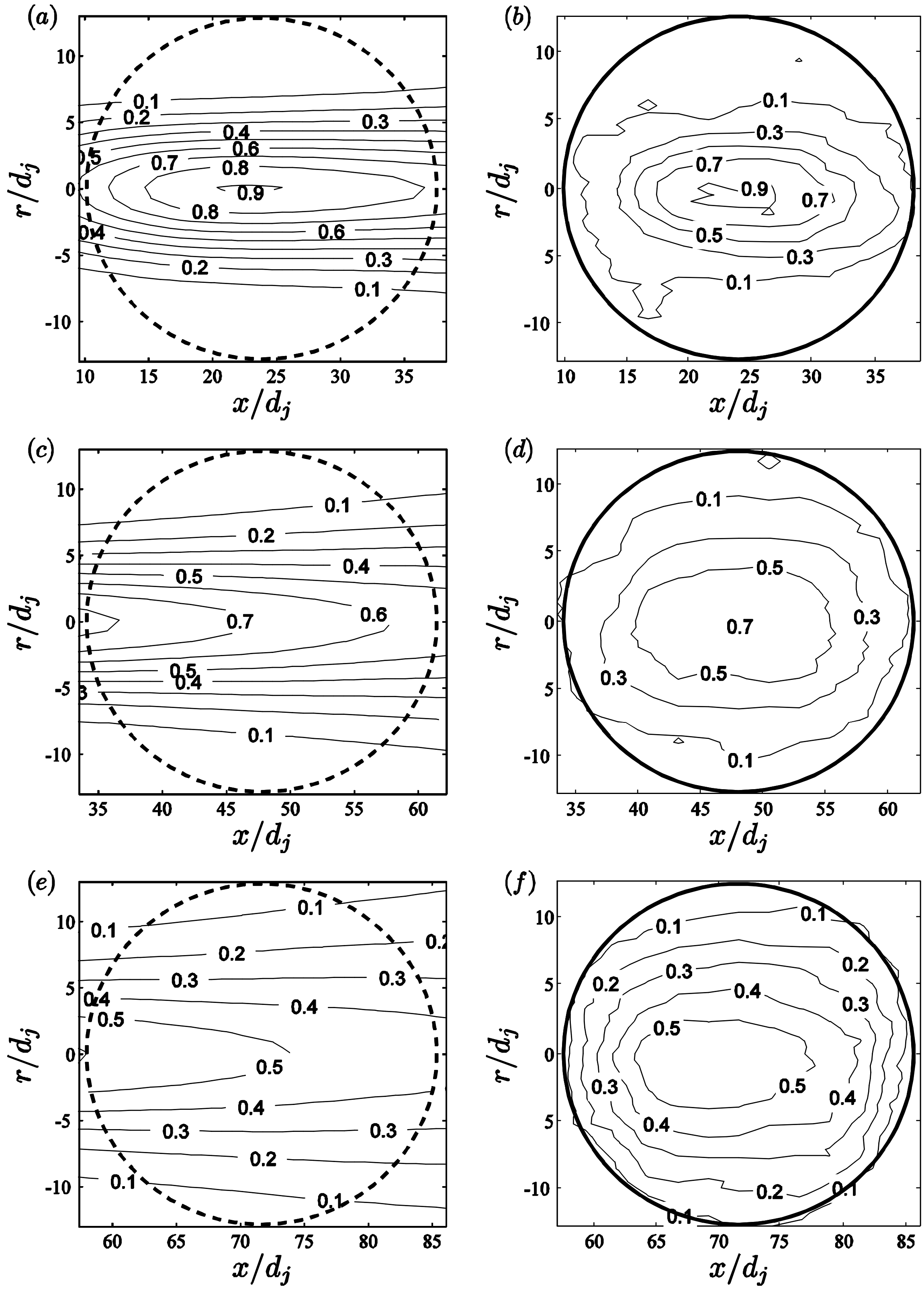
(a)
(b)
(c)
(d)
(e)
(f)
r/d_j
x/d_j
0.1
0.2
0.3
0.4
0.5
0.6
0.7
0.8
0.9

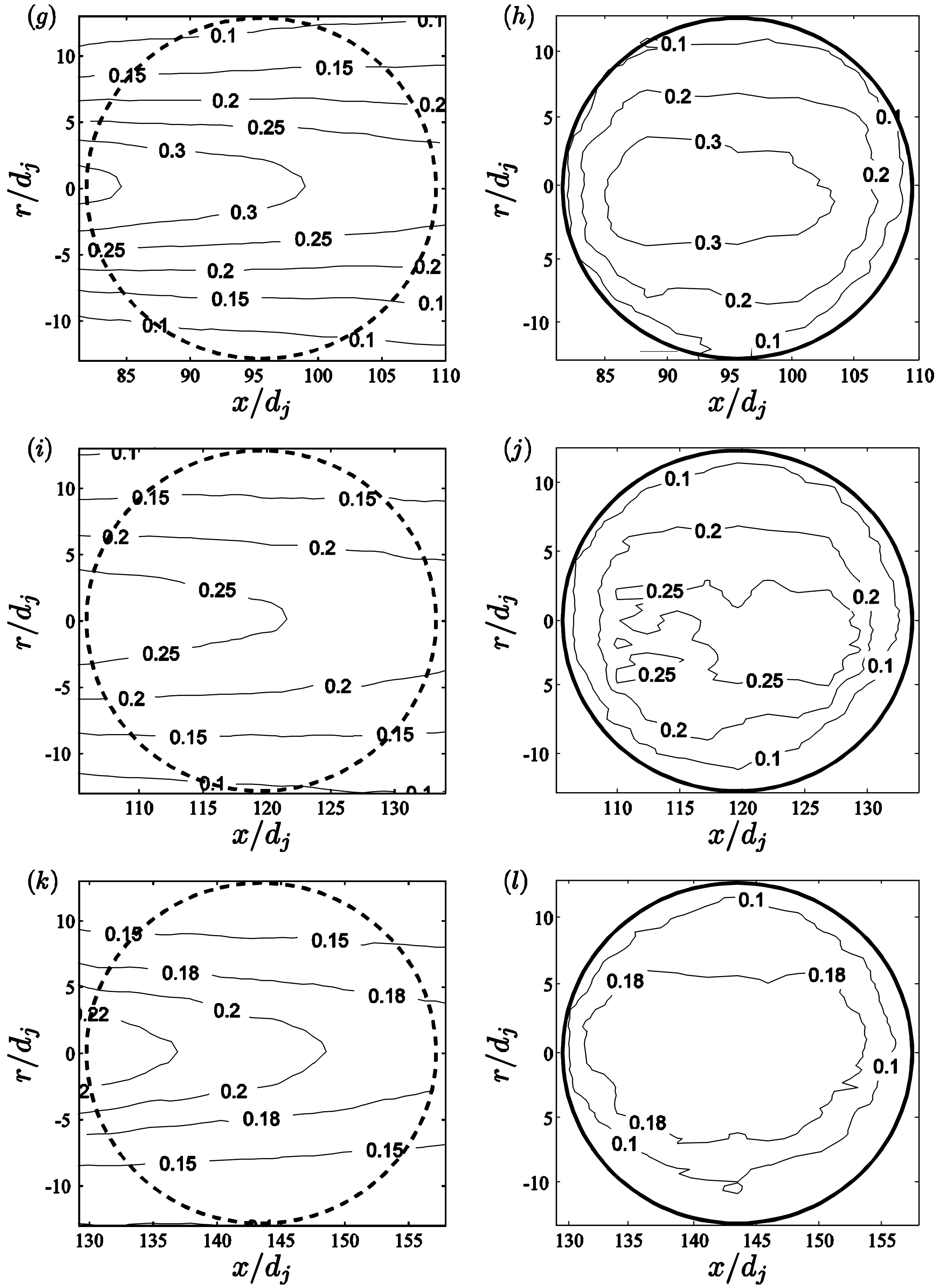

Figure 5.3: Ensemble averaged contours of u/u_e obtained from C-PIV (*left*) and SSE-PIV (*right*).

The plots in figure 5.3 show the position of the SSE-PIV field of view using a solid line circle for actual image boundary and a dashed circle its corresponding position in the C-PIV image. Figure 5.3 *(a)* shows the spray accelerating as x/d_j increases from 10 to 24 before the spray velocity starts to decay. This is a spurious result from the C-PIV measurement, since there is no driving force to justify the observed flow acceleration downstream of the nozzle exit plane. The spray within the region before x/d_j =23.9 is very dense. The raw image in chapter 4 section 4.4.3 also shows excess light scatter and no real tracer droplet definition due to this dense region in the spray. It is acceptable to believe that this spurious axial velocity increment is due to tracer particle mismatching, since each IA is over-saturated with particles and has too much noise to detect any single particle. By comparing side by side each image pair in figure 5.3, the SSE-PIV contours show velocity trends similar to the C-PIV images.

From figure 5.3 there is an obvious is discrepancy of momentum continuity within the SSE-PIV velocity contours. At each SSE-PIV position the contour plots suggests that the velocity of the jet accelerates and then decelerates as the axial position within the plot increases. These plots suggest a decrease in accurate velocity correlation as the position from the centre of the SSE-PIV field of view increases. The correlation between a reduction in accuracy and distance from the field of view centre arises due to the increase in optical distortion. In chapter 3 it was mentioned that the theoretical droplet deforms and increases in size and reduces in clarity as it moves further away from the centre of the field of view due to the optical configuration of the endoscope. This effect is due to the particle being viewed from highly curved optics, particles at the centre of the image are in focus, and particles at the edge of the field of view are out of focus. The change in droplet definition leads to particle mis-matching and an increase in loss of particle pairs. This in turn leads to false velocity data. Also as the droplets become more out of focus the subsequent energy scatter from the droplet is reduced and may not be picked up by the PIV correlation algorithm or removed using the PIV validation methods. A further description on the noticed effects due to the optical distortion and the reduction in illumination intensity on velocity data can be found in chapter 6.

The biasing towards zero of the measured axial velocity along the boundary of the SSE-PIV field of view is clearly visible on all SSE-PIV contours in figure 5.3. This causes a slight under prediction in the spray spread rate characteristics as x/d_j increases, as documented in section 5.4. The contour spill-over observed in *(d)*, *(f)* and *(h)* are due to averaging neighbourhood IAs. The region in which the axial velocity measured by SSE-PIV is reported incorrectly as near zero at $r/d_j > \pm 10$ in figure 5.2 is displayed in figure 5.3 as a ring of near-zero velocity at the perimeter of the SSE-PIV field of view. The velocity jump observed in figure 5.2 translates into the packing of the normalized velocity contour lines in figure 5.3 *(d)*, *(f)* and *(h)* around the perimeter of the SSE-PIV image. As mentioned previously, this is due to the combination of two sources of error. The first is the increased curvature effects of the optical setup and the second is a bias towards zero as the average filter performs neighbourhood average of IAs close to a masked region. As the streamwise location increases, the bias towards zero becomes more apparent as the jet shear layer extends beyond the limits of the SSE-PIV field of view.

Figure 5.4 shows the contour maps of $\delta u/u_e$, which are computed by subtracting between the velocity fields of the side by side contour maps in figure 5.3. It is evident from figure 5.4 *(a)* and *(b)* that areas of 50% error between the two PIV measurement techniques are present at the left and right hand side of the endoscopic image. This large uncertainty is due to the biasing towards zero within areas of high axial velocity and a lack of illumination as described in more detail in chapter 6. The $\delta u/u_e$ value at $r/d_j=0$ is maximum and the minimum $\delta u/u_e$ of each field of view decreases as the image location increases in the streamwise direction. As x/d_j increases, u of the real jet tends towards zero and thus the δu between the C-PIV and SSE-PIV within the invalid region also tends towards zero. Therefore, the overall $\delta u/u_e$ between the contour maps of C-PIV and SSE-PIV is shown to reduce as the endoscope is moved further along in the positive x/d_j direction.

As r/d_j tends to zero in each contour map, the $\delta u/u_e$ between C-PIV and SSE-PIV reduces to 10% near the centre of the SSE-PIV field of view. The reduction in $\delta u/u_e$ as r/d_j tends to zero is due to the reduction in curvature effects within the field of view. As the curvature effects from optical distortion are reduced, the particle image within each IA is more defined and thus traceability between frames is more accurate. All plots in figure 5.4 show $\delta u/u_e$=0 when r/d_j=0 on the meridional plane, along the x/d_j axis. This suggests that the prediction of the peak centreline velocity is measured as the same by both PIV techniques.

It is clear that much of the variance in $\delta u/u_e$ in figure 5.4 is due to the optical distortion and reduction in illumination intensity as the radial distance increases from the centre of the field of view in each SSE-PIV captured image.

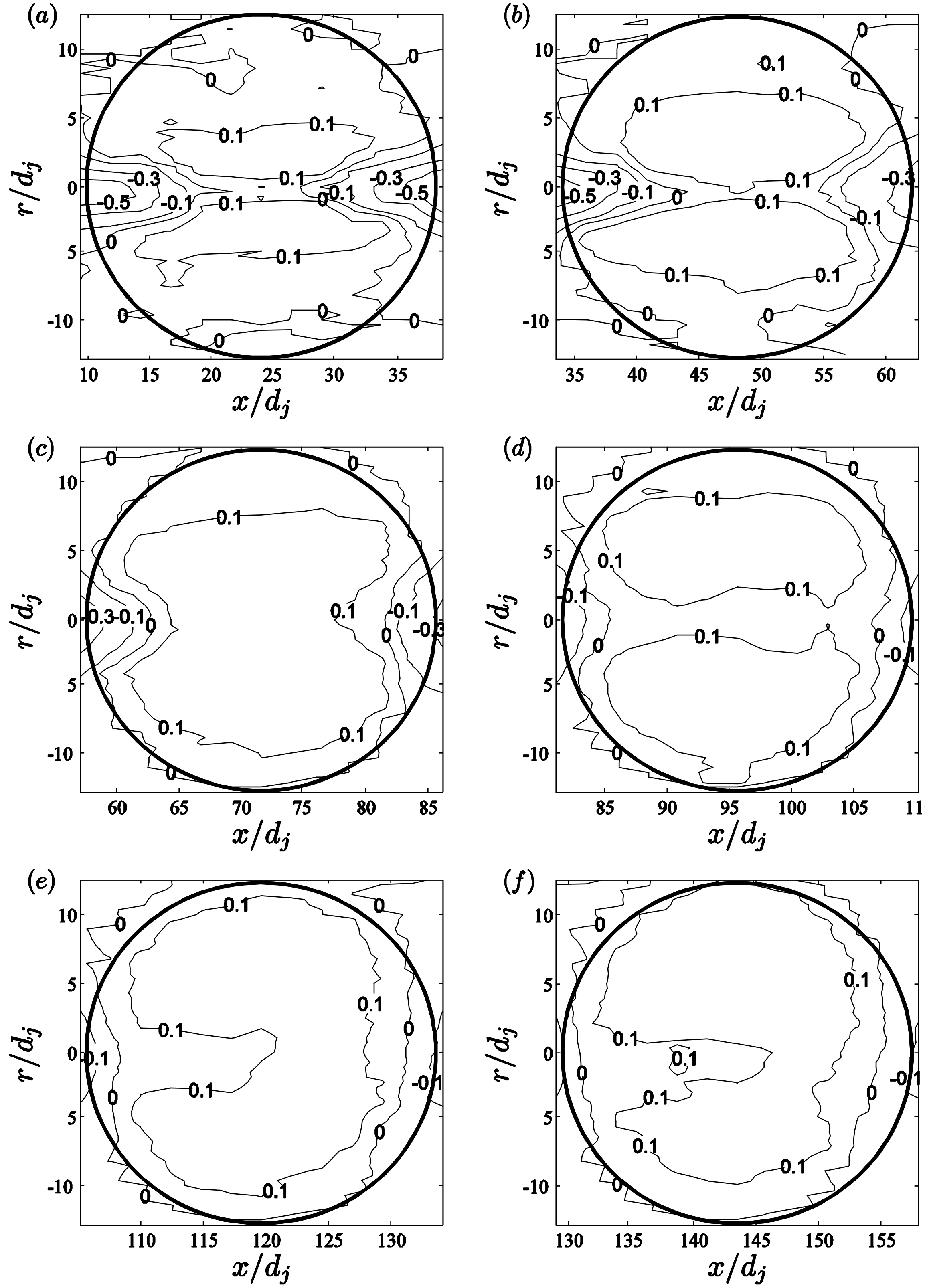

Figure 5.4: Contours of $\delta u/u_e$, describing the normalized velocity difference between C-PIV and SSE-PIV within the SSE-PIV field of view.

5.3 Mass flow rate

The spray used to compare the SSE-PIV and the C-PIV measurement techniques has a water phase that is premixed with air upstream of the nozzle. The water is atomised upon ejection and transported downstream by the air flow. The mass flow rate of the spray has been computed at $23.9 < x/d_j < 143.5$ at $23.9d_j$ increments. Statistical mean velocity profiles of u were obtained at the above locations. C-PIV and SSE-PIV profiles were extracted from the contour maps shown in section 5.1. In the case of SSE-PIV, one profile is extracted from the meridional location of each contour map. The mass flow rate is computed using equation 5.1

$$\dot{m}_{mix} = 2\pi\rho_{mix}\int_{r=0}^{r=r_{max}} u(r)r.\,dr \qquad 5.1.$$

where $\dot{m}_{mix}$ is the mass flow rate of the spray mixture, r is the radial distance from the jet axis, and $u(r)$ is the streamwise velocity u at r. The integral in equation 5.1 was evaluated in discrete form using the trapezoidal integration rule. ρ_{mix} is the mixture density of the spray mixture. The spray flow has a typically a fine mist of fluid within the airstream. This study assumes that the flow is homogeneous and a series of computations where carried out as described by Whalley *et al*. (2006) and is shown in appendix A. The mixture density was determined to be approximately 1.34 kg/m^3 at $x/d_j \approx 20$. With the entrainment of the surrounding air within the spray becomes diluted and the mixture density reduces and asymptotes to the density of air, as shown in appendix A. Since the variation in mixture density is very low within the measurement range, the current procedure for the computation of mass flow rate is acceptable to quantify the difference $\dot{m}_{mix}$ between instrumentation. The process was repeated for each measurement technique. The results in this section are published in Lad *et al.* (2011a). The calculation for mixture properties of the spray can be seen in the Appendix A. The mass flow rate of the water is calculated by the change in volume, ΔV, in the water reservoir over a period of time, t, which can be written as $\dot{m}_l = \rho_l(\Delta V/t)$. It is assumed that $\dot{m}_l$ is conserved as the spray propagates in the positive axial direction.

It is important to note that, due to the laser light reflection from the dense spray from the nozzle, the PIV data close in the region x/d_j <23.9 is unreliable and thus it is not used for the analysis of the mass flow rate nor to compute other spray time-mean statistics in sections 5.4 to 5.6.

Figure 5.5 shows the computed mass flow rate of the spray as the x/d_j increases from the nozzle exit. The mass flow rate increases linearly with increasing axial position due to the fluid of the surrounding air being drawn radially inwards towards the sprays conical surface causing entrainment, as discussed in Ricou and Spalding (1961). Figure 5.5 shows the mass flow rate that is calculated from C-PIV, SSE-PIV and Pitot anemometry profiles taken along y and z directions over the range $23.9 < x/d_j < 143.5$ at $23.9d_j$ increments. The same linear trend is obtained from C-PIV, SSE-PIV, and the Pitot anemometry measurements. At x/d_j=23.9 the mass flow rate computed from the C-PIV measurements is under predicted with respect to that from the Pitot and the SSE-PIV data. This is due to the measurement uncertainty in the C-PIV technique where the spray is dense and there is a high amount of noise when attempting to correlate peaks between frames. The SSE-PIV system overcomes this by having a higher resolution in a localised image of the spray.

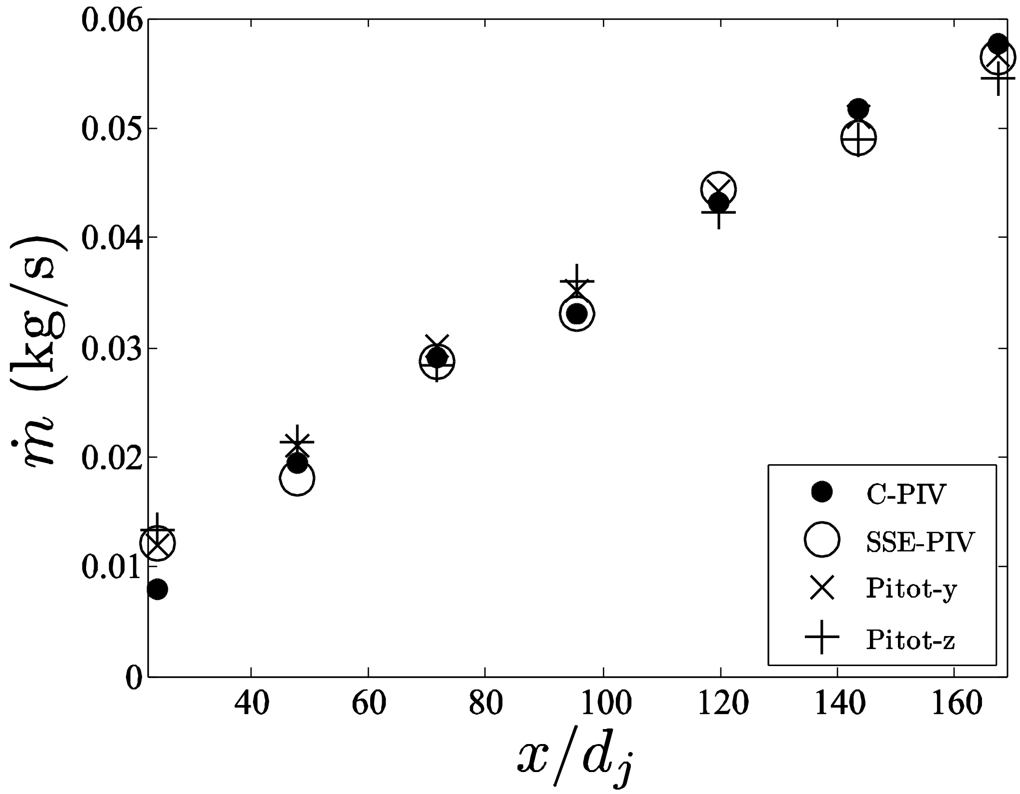

Figure 5.5: Mass flow rate obtained from C-PIV, SSE-PIV, and Pitot anemometry.

Figure 5.6 shows the mass flow rate data obtained by C-PIV with a linear regression. The plot shows, overlaid, the 65% confidence interval band of the mass flow rate from the Pitot anemometry *y* and *z* traverses. As the C-PIV and SSE-PIV were both obtained along the *x*-*y* plane, the associated mass flow rates should be compared to that from Pitot traverses in *y*. The confidence bands from Pitot-*y* and Pitot-*z* traverses are represented by dash-dash and dash-dot lines respectively.

The confidence interval bands are used to determine the uncertainty of the mass flow rate axial distribution computed from the three different anemometrical surveys. The prediction bounds were computed using equation 5.2

$$(a, b) = \hat{y} \pm t_{\mathrm{CI}/2, n-2}\left(\frac{\sigma}{\sqrt{n}}\right) \qquad 5.2.$$

where ŷ is the y-value predicted for x using the regression equation, $t_{CI/2,n-2}$ is the value from the t-table corresponding to half the desired confidence interval, CI, at $n - 2$ degrees of freedom, and n is the size of the sample, the number of x, y data points. The standard deviation, σ, is the standard deviation of the sample defined as

$$\sigma = \sqrt{\frac{1}{n}\sum_{i=1}^{n} x_i^2 - \bar{x}^2} \qquad 5.3.$$

The slope of the predicted mass flow rate from the Pitot and C-PIV data varies slightly. The mass flow rates obtained from these techniques display a better agreement among one another at higher x/d_j locations. The under prediction of the mass flow rate from the C-PIV at x/d_j =23.9 causes a bias in the regression, which creates a lower initial $\dot{m}$ which rises quicker in the positive axial direction at a rate of $d\dot{m}/d(x/d_j)$=3.4x10^{-4}, suggesting more fluid entrainment from the surroundings in the spray. The confidence interval bands show that the predicted mass flow rate from the Pitot-y data is within the uncertainty limits of the Pitot-z data.

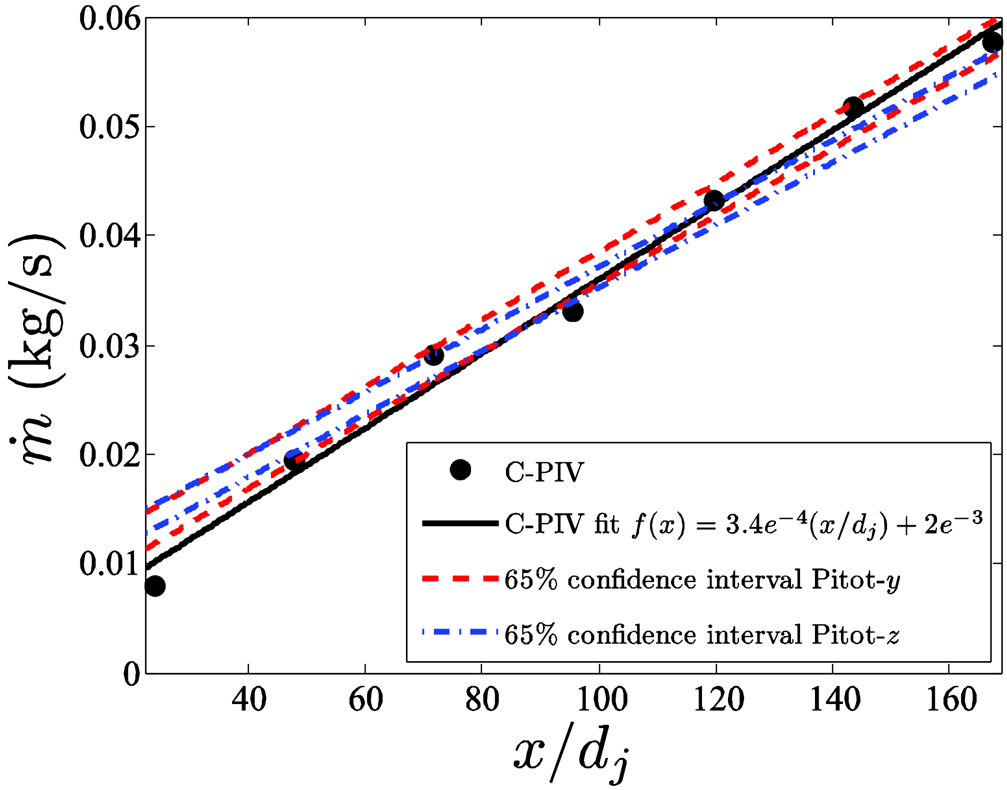

Figure 5.6: Mass flow rate obtained from C-PIV and Pitot anemometry.

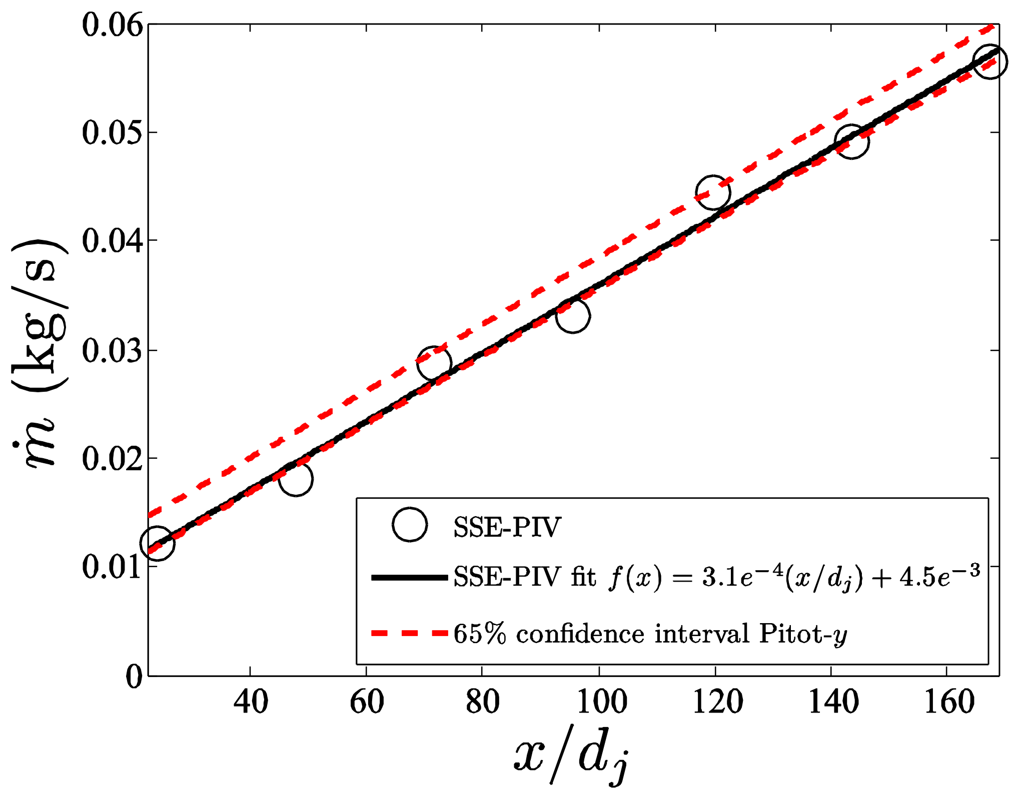

Figure 5.7: Mass flow rate obtained from SSE-PIV, and Pitot anemometry.

Figure 5.7 shows $\dot{m}$ data computed using SSE-PIV velocity profiles against the Pitot-y data. The linear growth of mass flow rate is shown using the black line and the 65% confidence interval band is shown by the red dashed lines. The SSE-PIV linear fit falls within the uncertainty band of the Pitot-y data and shows a better fit than that from the mass flow rate estimated from the C-PIV. The mass flow entrainment rate is approximately $d\dot{m}/d(x/d_j)$ =3.1x10^{-4} which is 0.3x10^{-4} less than from the regressed mass flow rate from the C-PIV. The trend for the SSE-PIV shows a consistently lower $\dot{m}$ value. This shows that the SSE-PIV under predicts the value of $\dot{m}$ which results from not fully describing the Gaussian distribution of the profile due to the narrower field of view compared to C-PIV and also from under predicting the velocity at the perimeter of the field of view. Figure 5.8 shows the comparison of the uncertainty bands of C-PIV and SSE-PIV. Figure 5.8 shows that both entrainment rates are well within 1σ spread of the uncertainty bands. The difference in entrainment rates described previously is shown in figure 5.8 by a difference in gradient between the blue and the red lines.

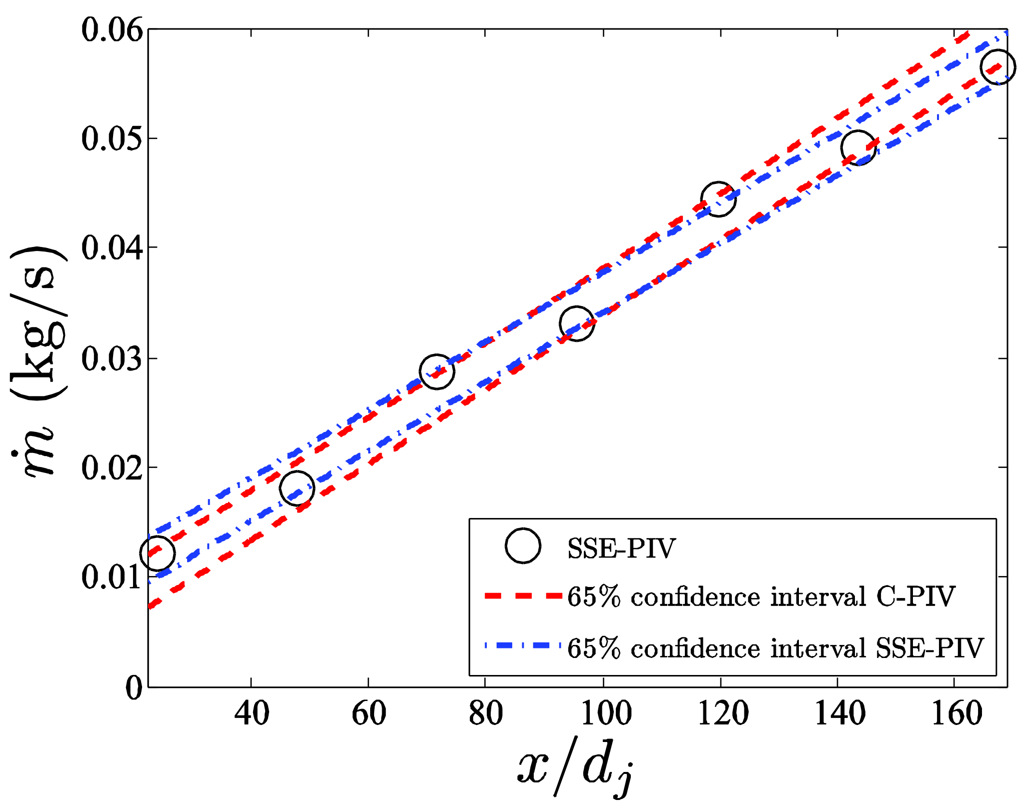

Figure 5.8: Mass flow rate obtained from C-PIV and SSE-PIV.

5.4 Spray spreading rate

Self-similar velocity profiles for fully turbulent jets have been used in the past to determine the spreading rate of a jet. These were described in section 2.2.1. With increasing distance from the nozzle exit, the jet centreline velocity decreases asymptotically to zero. The axial momentum, net of the mixing losses, is conserved in the streamwise direction by the increasing spray cross-section as axial distance increases. From similarity considerations, an axi-symmetric spray spreads laterally at a linear rate while its centreline velocity, u_c, varies inversely with axial distance. The fully developed flow of a spray produces a Gaussian axial velocity profile as shown by Seiner and Ponton (1985). They studied the time-averaged axial velocity profile of high Reynolds number supersonic jets and found it to be self-similar in the axial direction in the form of the half-Gaussian curve of equation 5.4

$$\frac{u}{u_c} = e^{\left(-\ln(2)\eta^2\right)} \quad , \quad \eta = \frac{r-h}{b} \qquad 5.4.$$

where u is the velocity at radial position r, the spray centreline velocity is u_c, the velocity profile half-width is b, and the radius of the potential core is h. Since in this study the Reynolds number is within the subsonic range, the potential core can be neglected making $\eta = r/b$. A schematic of the streamwise evolution of the spray streamwise velocity profile, described by equation 5.4, is shown in figure 5.9. The half width is determined by the position of r at which u=0.5u_c.

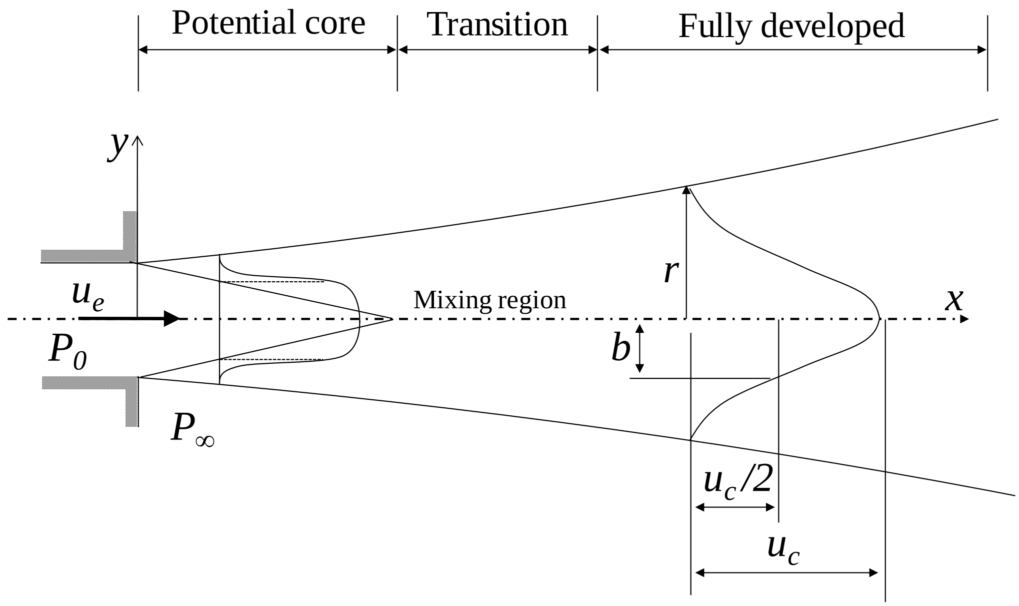

Figure 5.9: A schematic for the spray structure describing the position of the jet half width.

The jet half width in equation 5.4 is estimated from the same velocity profiles used for determining the streamwise distribution of the jet mass flow rate in section 5.3. Each velocity profile is fitted to equation 5.4 using a least square fit. Using the Newton Raphson technique for data regression, it is possible to determine numerically *b* for both C-PIV and SSE-PIV. Specifically, the least squares error and its derivative with respect to *b* are defined by equations 5.5 and 5.6

$$\sigma_{i=} \sum_{j=0}^{n} \left[\left(\frac{u}{u_c} \right)_j - e^{-ln2.\eta_{ij}^2} \right]^2 \qquad 5.5.$$

$$\frac{\partial \sigma}{\partial b} = \sum_{j=0}^{n} 2 \left(\left(\frac{u}{u_c} \right)_j - e^{-ln2.\eta_{ij}^2} \right) \left(2\eta_{ij}(ln2) e^{-(ln2)\eta_{ij}^2} \right) \left(-\frac{r_j}{b_i^2} \right) \qquad 5.6.$$

where n is the number of velocity measurement points across a single traverse from the jet axis, at which j=0, to the edge of the PIV field of view, in the radial direction and b_i is the i-th guess of b. Solve b_{i+1}=$-\sigma_i/(d\sigma/db)_{i-1}$ until convergence. There are two issues with this method. The first issue is that the function assumes that the residual least squares error tends to zero. The second issue is that the Newton Raphson algorithm is exact for a rational function but is not exact once a sum operator is introduced. To remove this problem an arbitrary small constant, a, of the order $0.05b$ has been used in equation 5.7.

$$b_i = b_{i-1} - a\left(\frac{\sigma_{i-1}}{\left(\frac{\partial\sigma}{\partial b}\right)_{i-1}}\right) \qquad 5.7.$$

Equation 5.7 typically converges in less than 200 iterations. The solutions for b at different axial locations were calculated from equation 5.7 using Matlab. The results in this section were published in Lad *et al.* (2011a).

Figure 5.10 shows the variation of the jet half-width b along the jet axis. Both values for b and x are normalised by the jet exit diameter d_j. Figure 5.10 shows that the spray width increases linearly as the x/d_j increases. This agrees with the measurements by Pavlova *et al.* (2008b) and Pavlova *et al.* (2008a) and is also consistent with findings from Faeth *et al.* (1995), Karpetis and Gomez (1999) and Cossali (2001). The regressed values of b from Pitot-y and Pitot-z traverses are shown separately to show the spreading of the spray width in both the y and z directions. C-PIV data x/d_j<38 is excluded from the plot as the data points are not consistent with the linear nature of the spread rate and affect the regression of the jet exit diameter presented in the next paragraph. The uncertainty at x/d_j<38 is due to the large amount of PIV uncertainty in the first quartile of the C-PIV vector map described previously in section 5.1, figure 5.3. This uncertainty was not observed to be as significant with SSE-PIV.

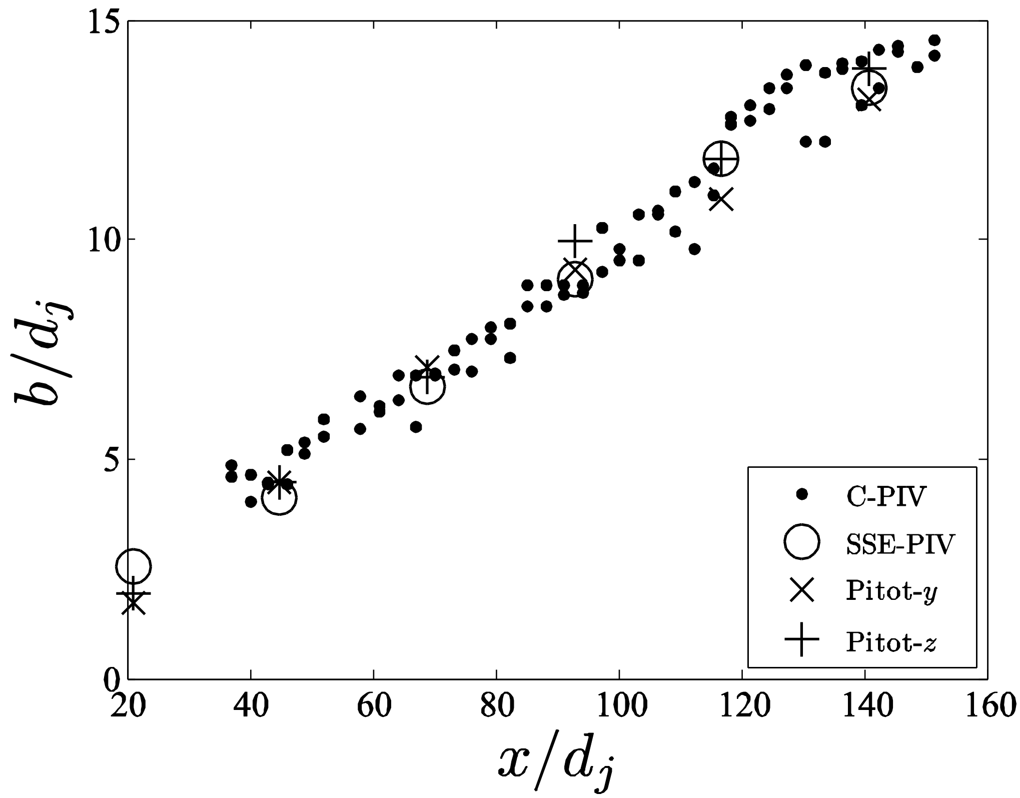

Figure 5.10: Spray spread rate obtained from C-PIV, SSE-PIV, and Pitot anemometry.

Figure 5.11 shows the linear relationship of the spray width using C-PIV. The spread rate was computed at $6.1\text{x}10^{-2}$. The initial jet diameter, d_j, used to normalize lengths in this thesis is computed from the linear regression stated in the legend of figure 5.11. This gives d_j=2.09 at x/d_j=0. Figure 5.11 shows the C-PIV spreading computation to be consistent with the Pitot anemometry and sits comfortably within the 65% confidence interval band of the both Pitot-*y* and Pitot-*z* data.

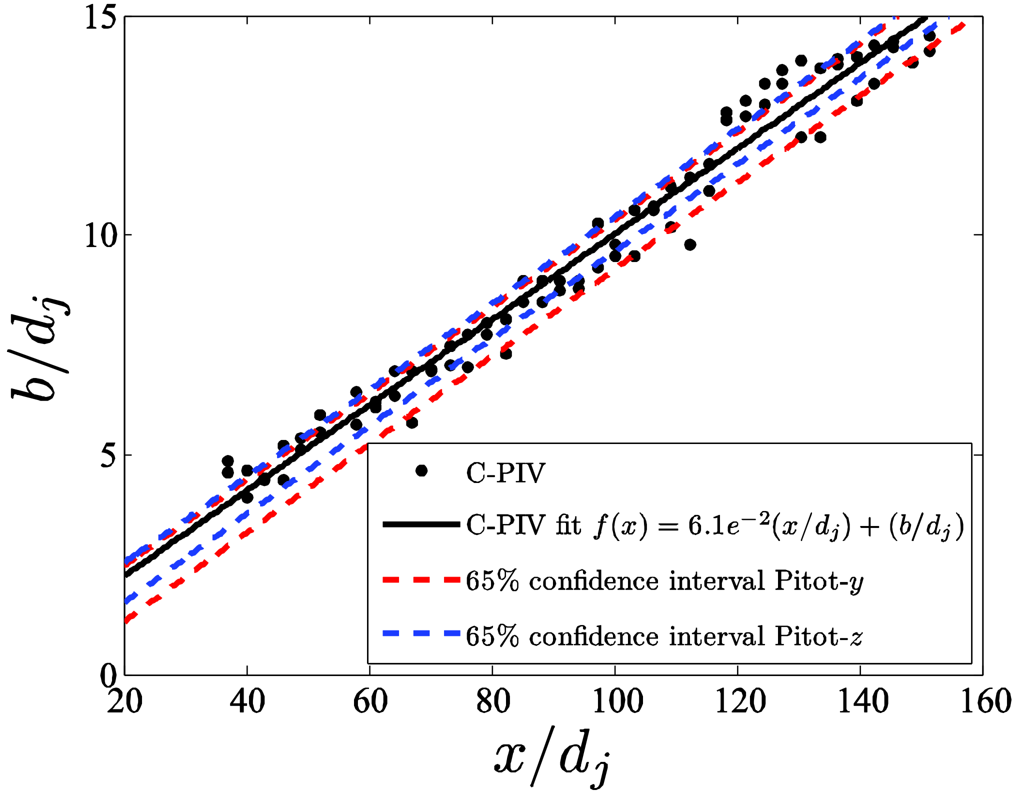

Figure 5.11: Spray spread rate obtained from C-PIV and Pitot anemometry with 65% CI bands.

Figure 5.12 shows the spreading characteristics obtained using the SSE-PIV records plotted with the 65% confidence interval band from *b* from the Pitot anemometry. Much like the C-PIV, the two sets of data are in agreement. The SSE-PIV spread rate is computed to be $6.5\text{x}10^{-2} d_j$ and predicts a d_j of 2.07 at x/d_j=0.

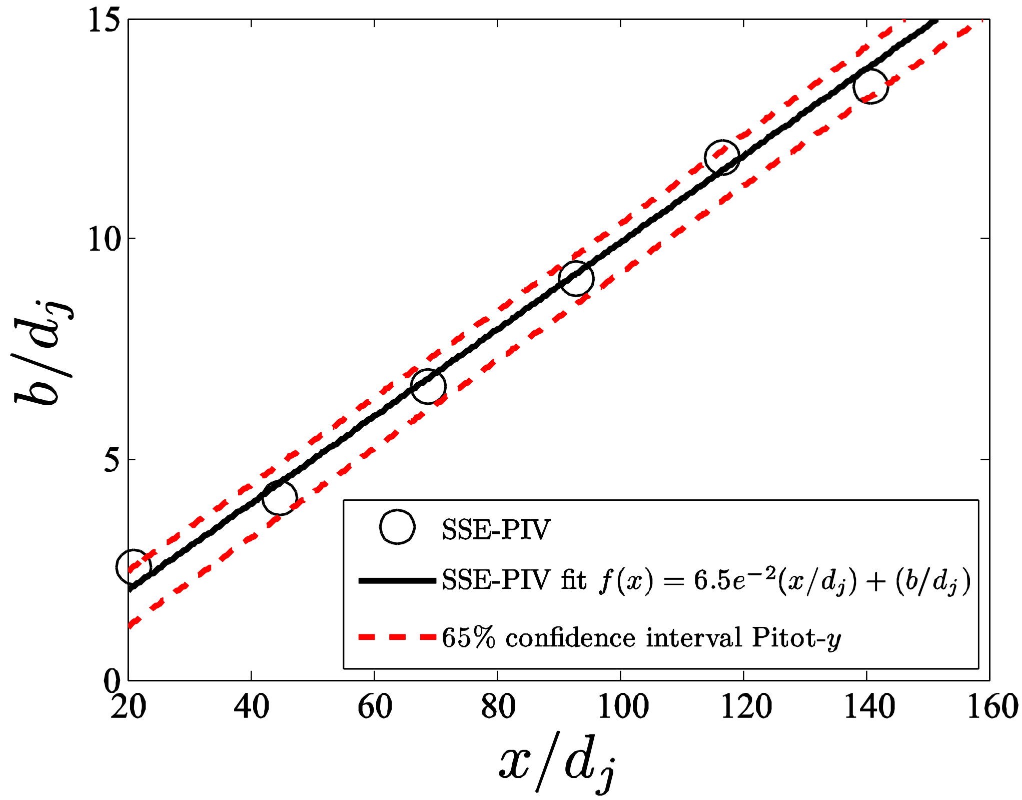

Figure 5.12: Spray spread rate obtained from SSE-PIV and Pitot anemometry with 65% CI band.

Figure 5.13 shows the comparison between the 65% CI bands for the jet half-width estimated from the C-PIV and SSE-PIV traverses. Figure 5.13 shows very little difference between the two bands. Both sets of data are in agreement and the 65% CI overlap. There is an overall under prediction in b/d_j in the SSE-PIV data that is due to the under prediction of u in the contour maps as shown in the contour maps in section 5.1. To appreciate this, the velocity decay will be discussed within the next section.

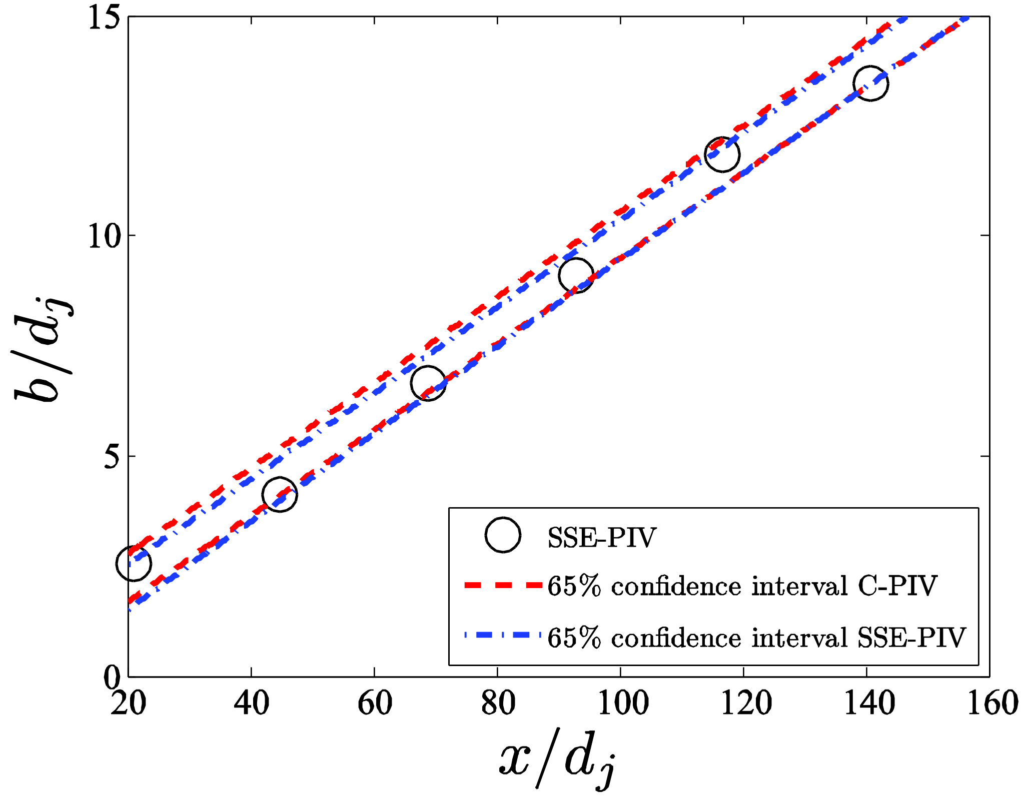

Figure 5.13: Spray spread rate obtained from C-PIV and SSE-PIV with 65% CI bands.

5.5 Centreline velocity decay

Figure 5.14 shows the downstream evolution of the centreline velocity, u_c, and its decay characteristics as axial location increases from the nozzle exit plane. The C-PIV data is obtained by extracting a single profile of u at r=0 from $0<x/d_j<185$ from the C-PIV time-averaged vector map that was used to generate the contours described in section 5.1. This is repeated three times to check for the repeatability of the spray decay characteristics among tests. The profile is shown in figure 5.14 by the black dots. The data for SSE-PIV cannot be taken in the same way due to the degradation of the velocity magnitude as r increases from the centre of the field of view. The u value at r=0 is extracted from the centre of the SSE-PIV field of view over the range $23.9<x/d_j<143.5$ at $23.9d_j$ increments. Similarly, the centreline velocity from each Pitot traverse is plotted in figure 5.14.

The error bars for the centreline velocity distribution from the Pitot anemometry are computed using the difference in the measured u_c between the x-y plane and x-z plane. The

Pitot anemometry values are found using $\frac{1}{2}[u_c(x,y)+ u_c(x,z)]$ with the uncertainty component being $\pm[u_c(x,y) - u_c(x,z)]$. The centre-line velocity is also validated using an analytical approach by Whalley (1996), which is the procedure described in Appendix A. The results in this section are published in Lad *et al.* (2011a).

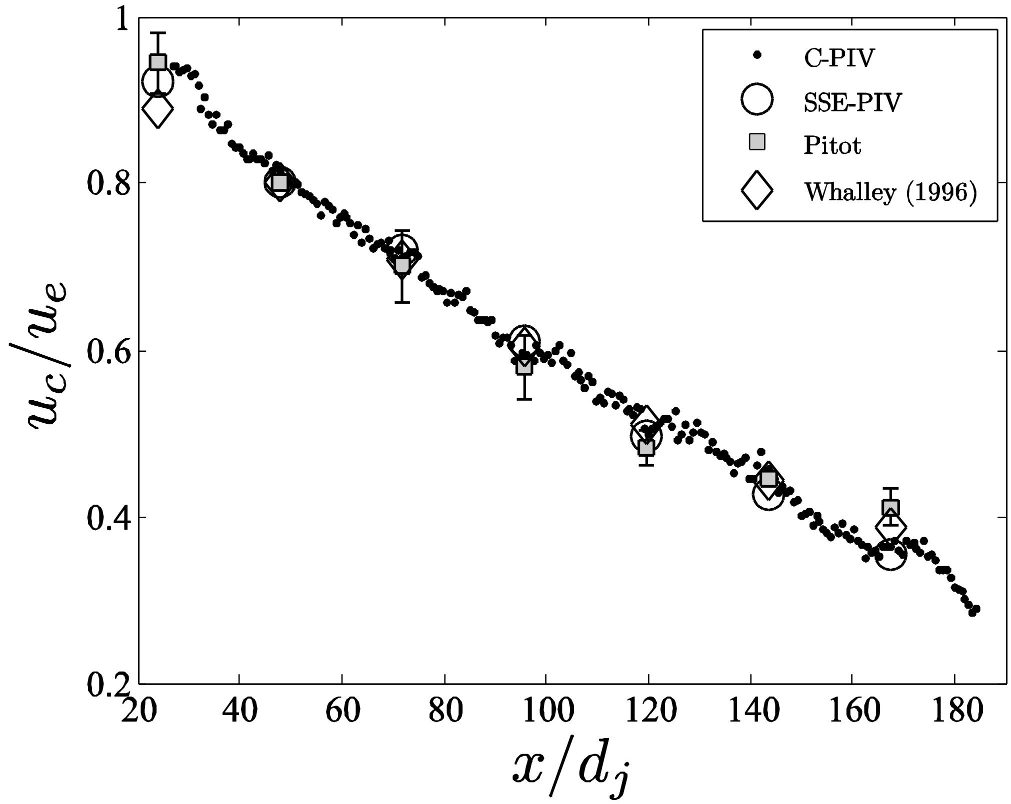

Figure 5.14: Velocity decay obtained by C-PIV, SSE-PIV, Pitot anemometry, and analytically by Whalley (1996).

Figure 5.15 compares the measured centreline velocity decay from the C-PIV against the Pitot anemometry measurements. The linear regression of the C-PIV data fits within the 65% CI of the Pitot data. From figure 5.15, it is also evidential that the variance between the data points and the mean regression increases when x/d_j<40 and x/d_j>180. This is most likely due to the large velocity range across the C-PIV field of view. The selection of Δt is based on the majority of the image having 25% particle image displacement within each IA. Although this theory was applied successfully, the measurement uncertainty increases as the distance from the centre of the image increases. The sudden increase in velocity seen at x/d_j<40 is also due to the uncertainty caused by increased light reflection as the spray becomes dense. This is not the case with the SSE-PIV, as shown in figure 5.14. The data point at x=23.9d_j is closer to the analytical value computed using the procedure outlined by Whalley (1996), as shown in figure 5.14.

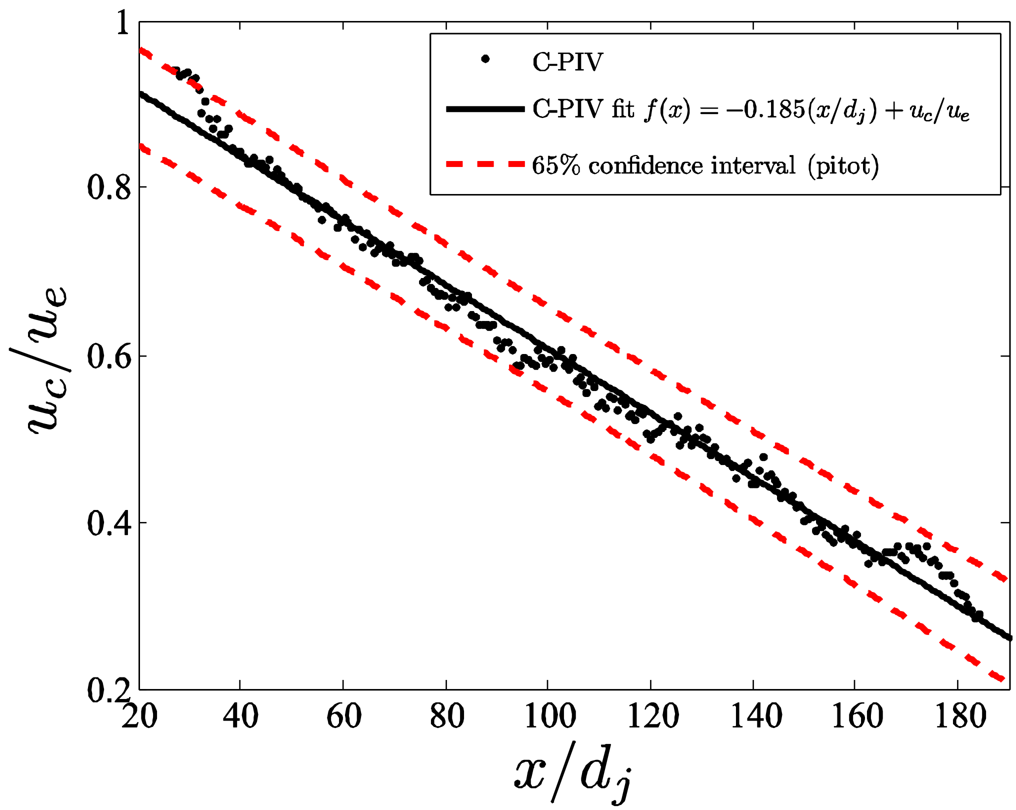

Figure 5.15: Centreline axial velocity decay obtained from C-PIV and Pitot anemometry with 65% CI band.

Comparing figure 5.15 to figure 5.16 shows that the streamwise decay of the axial velocity along the jet centreline from the C-PIV measurements is more consistent with that from Pitot anemometry in spite of the increased amount of uncertainty at x/d_j<40 and x/d_j>180 in the C-PIV data compared to the SSE-PIV measurements.

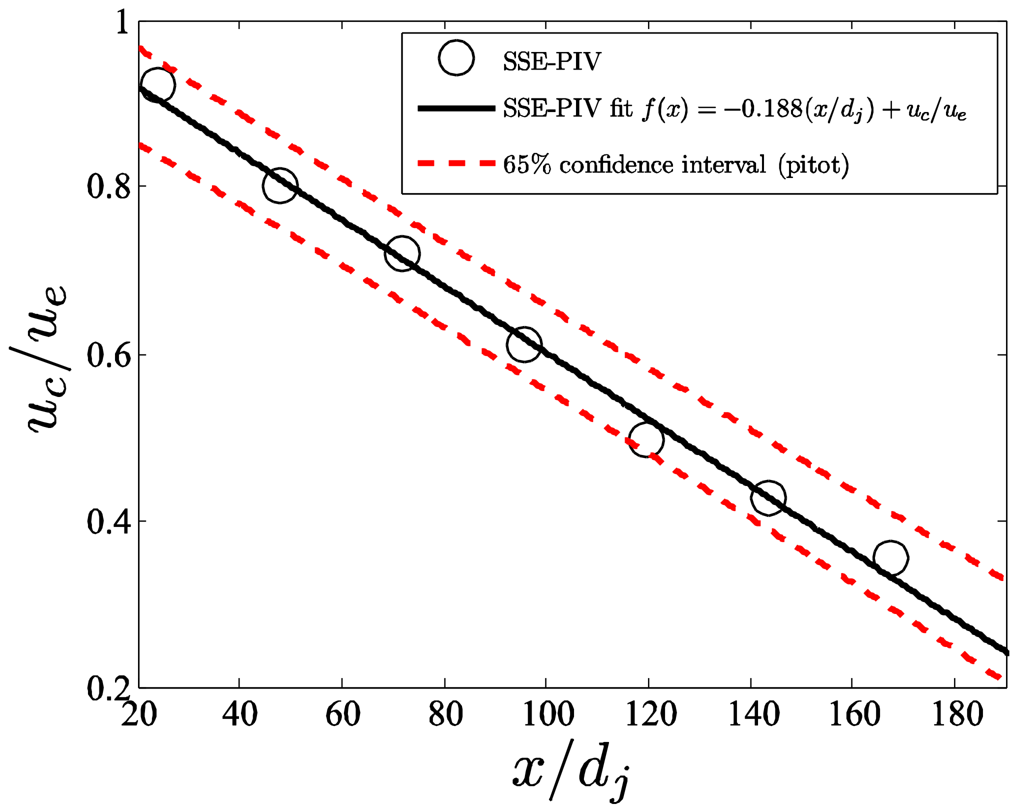

Figure 5.16: Centreline axial velocity decay obtained from SSE-PIV and Pitot anemometry with 65% CI band.

Figure 5.17 shows overlaid the 65% confidence interval bands of the jet centreline velocity distribution along the jet axis from the C-PIV and the SSE-PIV. The decay rates from the SSE-PIV and the C-PIV, which are -0.185d_j and -0.188d_j, give 65% confidence interval bands with a substantial overlap between them. There is a slight departure from this overlap as x/d_j increases. The reason for the increased decay rate of SSE-PIV is due to the illumination. Much of the laser intensity is lost through the coupling devices, the fibre optic cables and the sheet lenses. This, along with the reduction in tracer particles as the spray spreads radially downstream, causes an increased amount of uncertainty in the measured velocity by the SSE-PIV as flow features are not properly resolved.

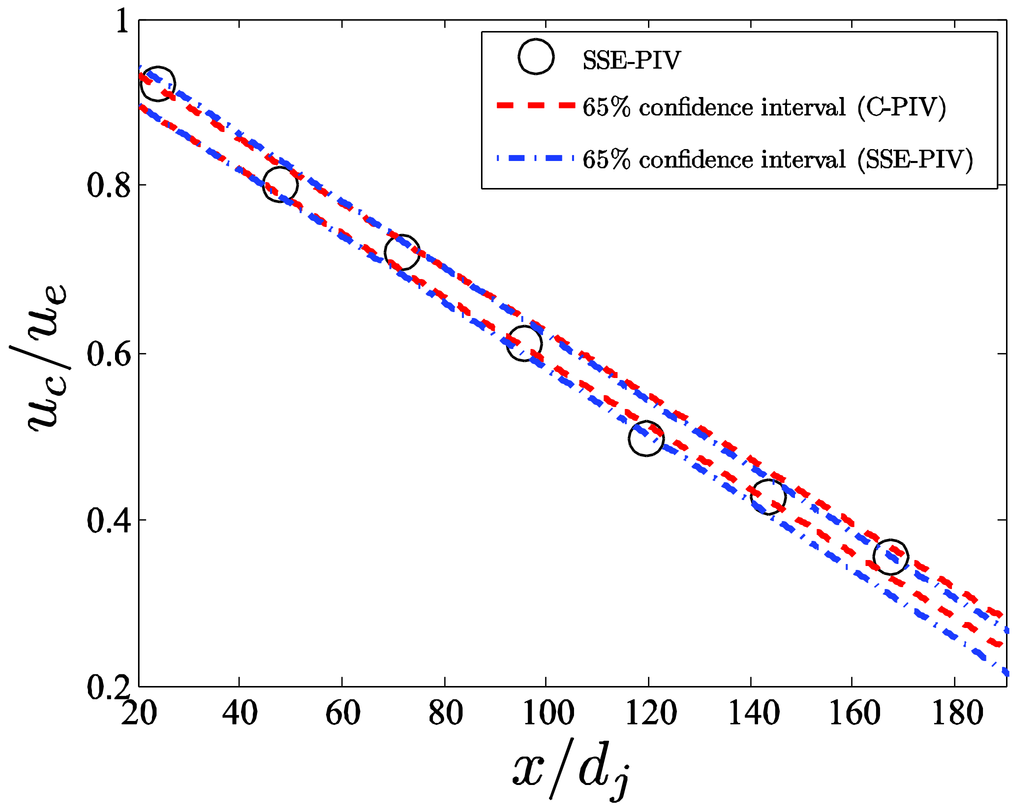

Figure 5.17: Centreline axial velocity decay obtained from C-PIV and SSE-PIV with 65% CI bands.

5.6 Unsteady characteristics

In this section, the axial velocity spectrum of the subsonic free spray is estimated at different axial positions from C-PIV and SSE-PIV velocity measurements. The instantaneous axial velocity profile at different streamwise locations is extracted and the velocity spectrum obtained by Discrete Fourier Transform to estimate the streamwise variation of the dominant wavenumber in the spray. This is used to estimate the dominant frequency, the Strouhal number, of the spray, under the frozen turbulence approximation. The frozen turbulence approximation is now presented in more details.

A set of instantaneous profiles of u were obtained using C-PIV along $-r<y<r$ in the x-y plane over the range $23.9<x/d_j<143.5$ at $11.95d_j$ increments. A sample of 600 instantaneous profiles was captured at each location at a capture rate of 4 Hz. This was repeated using SSE-PIV over the range $23.9<x/d_j<143.5$ at $23.9d_j$.

Townsend (1976), states that turbulent flows with a dominant velocity component, such as a spray, have eddies that usually propagate downstream. The propagation velocity is assumed to be close to the local average flow velocity and is referred to as the convective velocity, u_{conv}. A schematic of u_{conv} is seen in figure 5.18.

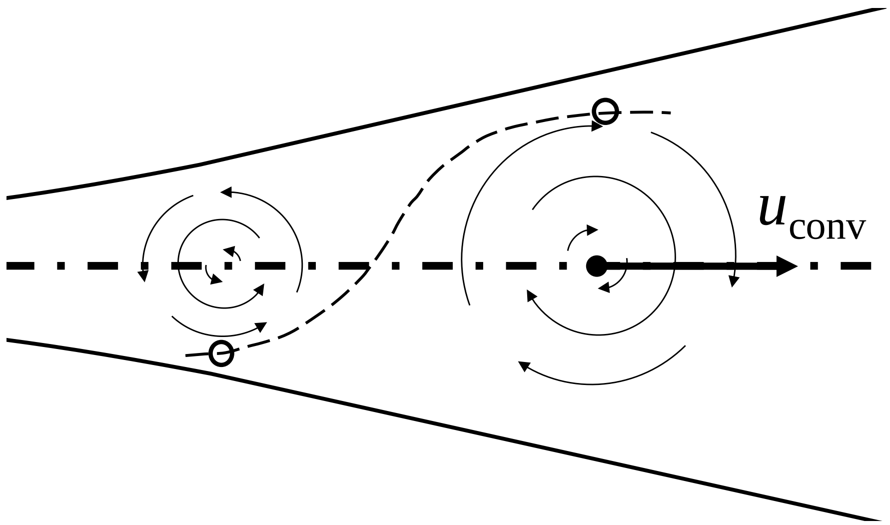

Figure 5.18: Schematic of convective velocity in eddy propagation.

The convective velocity is often used in experiment by applying Taylor's frozen turbulence approximation, Taylor (1938). An estimation of turbulent convection velocities and corrections to Taylor's approximation was given by Álmaco and Jiménez (2009). It is understood that the prediction of u_{conv} using Taylor's approximation does not take into account the eddy size and in certain flows can lead to large errors in the interpretation of large-scale turbulence in jets. However, for benchmarking between two measurement techniques, the theory is quite adequate, in the sense that the comparison between the two experimental results is performed under the same approximation, which makes the outcome of the comparative analysis acceptable.

Finding vorticity structures within temporal contour maps involves extracting the convectional velocity from the ensemble of instantaneous profiles and is shown in equation 5.8

$$u_{\mathrm{conv}} = \frac{1}{n}\sum_{j=1}^{n}\left[\frac{1}{m}\sum_{i=1}^{m} u(r)_i\right]_j \qquad 5.8.$$

where n is the number of snapshots and m is the number of PIV vectors from the axis to the edge of the PIV field of view. The convective velocity is applied as shown in figure 5.19 to estimate the instantaneous radial distribution of axial velocity in the Langrangian frame of reference.

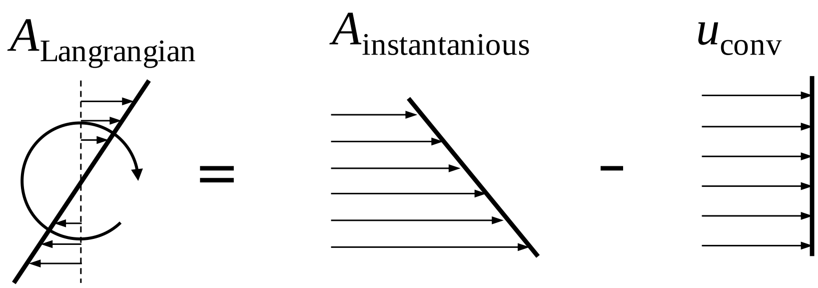

Figure 5.19: Application of convective velocity to obtain frozen fluctuating structures from temporal profiles.

Applying the Discrete Fourier transform to the radial profile of axial velocity in the Langrangian frame of reference gives equation 5.9.

$$\mathrm{U}(k,t) = \sum_{m=0}^{n-1} u'\,(m\,\Delta r, t)e^{-j\frac{2\pi}{m}km\Delta r} \qquad 5.9.$$

where u' is the instantaneous velocity profile in the Langrangian frame of reference, k is the wavenumber, r is the radial coordinate and t is the acquisition time of the PIV data. By making use of the 4 Hz constant frame rate of the PIV data, $t=m\Delta t$, where $\Delta t=0.25$ seconds. The discrete time averaged axial velocity spectrum $\overline{\mathrm{U}}'(k)$ is given by equation 5.10.

$$\frac{1}{\mathrm{T}}\int_{0}^{\mathrm{T}} \mathrm{U}'(k,t)\,dt \;\approx \frac{1}{n}\sum_{m=1}^{n} \mathrm{U}'\,(k\,,m\Delta t)\,\Delta t \qquad 5.10.$$

where n is the number of PIV velocity vector maps and m is the number of data samples .

Figure 5.20 and figure 5.21 show the DFT of u' of a profile at a particular x/d_j position. Time is normalised by d_j/u_e. The axis tu_e/d_j is limited to 169 to increase visibility of plot details. Whereas equation 5.9 gives the continuous wavenumber spectrum of the relative axial velocity, figures 5.20 and 5.21 show discrete spectra in which $k_l=l\Delta k$, where $\Delta k=\mathrm{T}^{-1}$ and $0<l<m$.

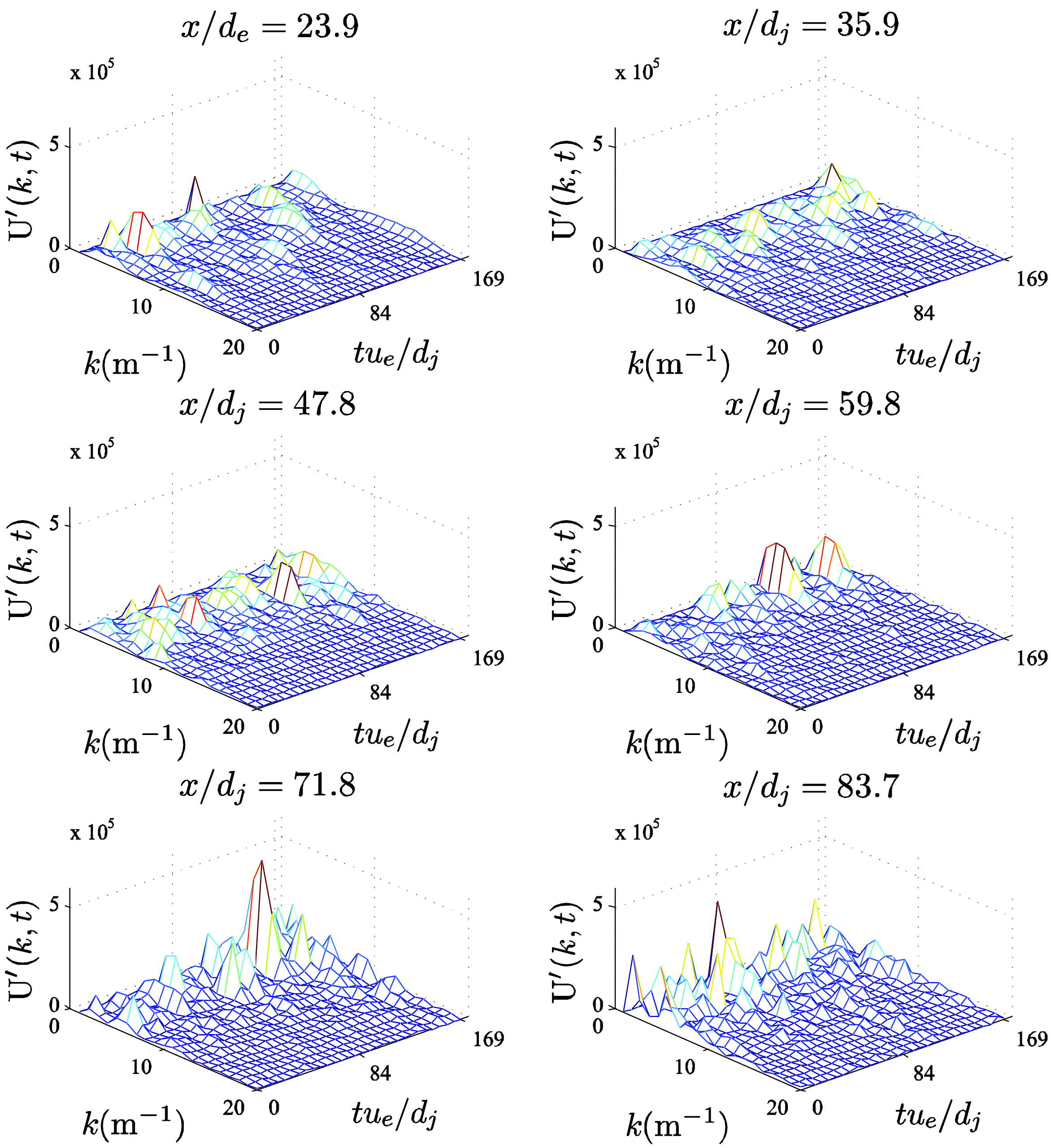

Figure 5.20: Discrete Fourier transform of u'. t and u are normalised by d_j. k is the physical wave number

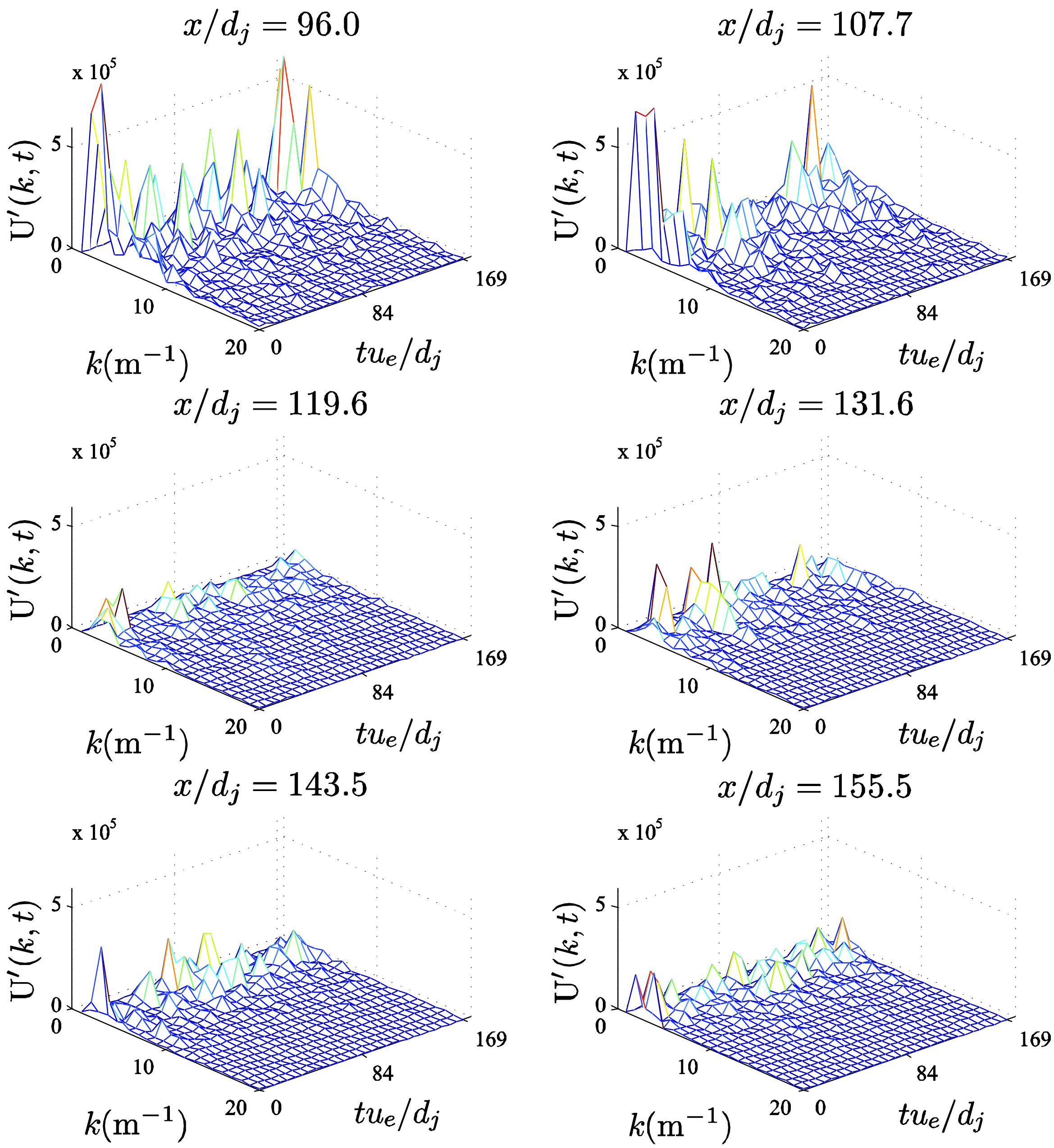

Figure 5.21: Discrete Fourier transform of u'. t and u are normalised by d_j. k is the physical wave number

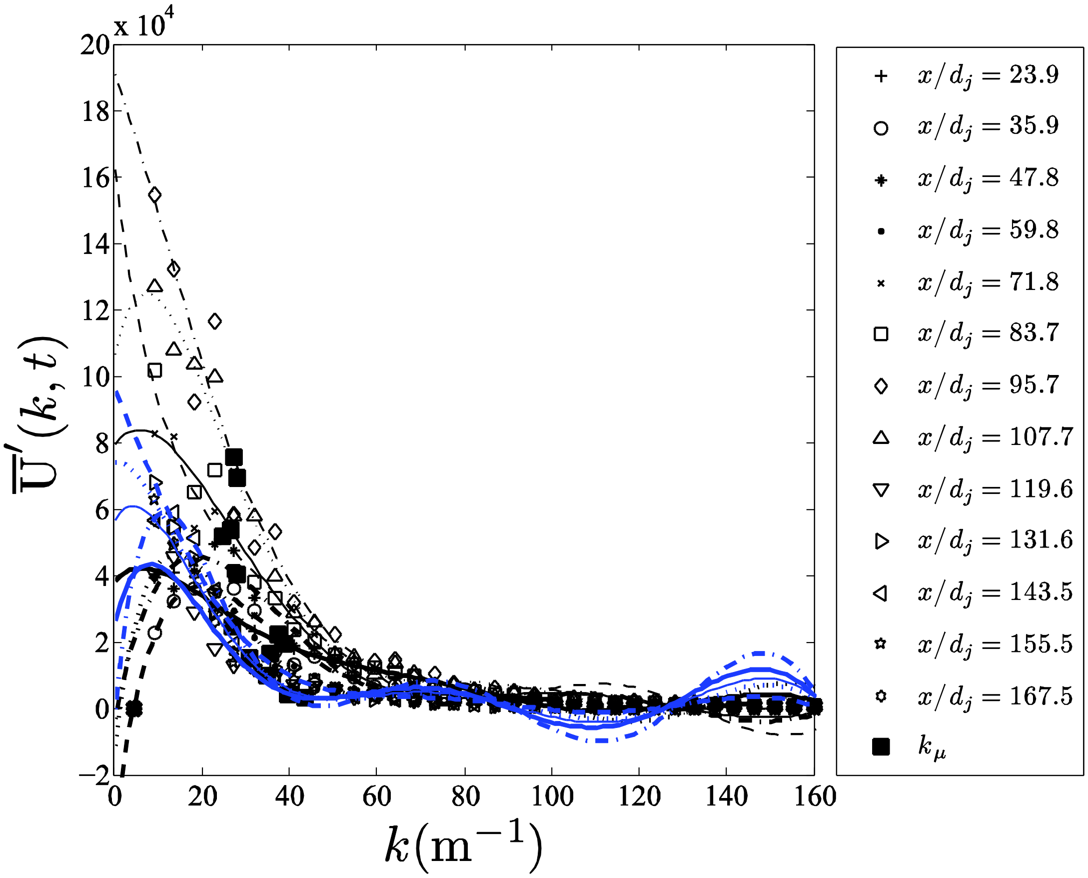

Figure 5.22: Time-averaged discrete Fourier transform of u' at each x/d_j position. k_μ is the dominant wave number.

Figure 5.22 shows the time-averaged Fourier transform of u' at increasing x/d_j positions. Each discrete spectrum is interpolated by a 9th order polynomial. From figure 5.22, there is a dominant contribution to the time-averaged spectrum by the zero wavenumber component, corresponding to a uniform velocity bias in the convective velocity. The dominant wave number cannot be found by simply selecting the maximum observed value of k. The dominant wavenumber is therefore obtained by finding the x-centroid of the area beneath each polynomial fit. The x-centroid is the statistical mean of the area beneath the polynomial fit which locates the dominant k value in a fully developed turbulent jet. The dominant wavenumber at each position is denoted by k_μ and is plotted in figure 5.22 as black squares. Figure 5.22 shows that the dominant k is within the range of $25 < k < 45$ for all x/d_j locations.

The streamwise variation of the Strouhal number associated to the dominant wavenumber in the jet is determined using equation $St=fd_j/u_e$ where $f=u_c/l$ and $l=1/k$. For clarity, the k value computed from the time-averaged Discrete Fourier transform is the physical wavenumber as opposed to the circular wavenumber. Figures 5.23 and 5.24 show the resulting streamwise distribution of the Strouhal number from the PIV measurements

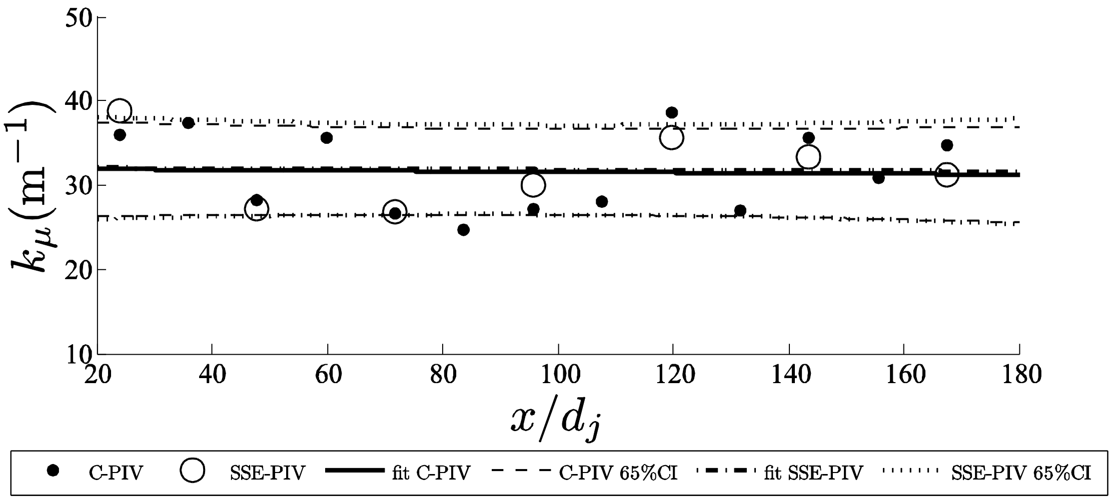

Figure 5.23: Streamwise variation of normalised dominant wavenumber k_μ along the jet.

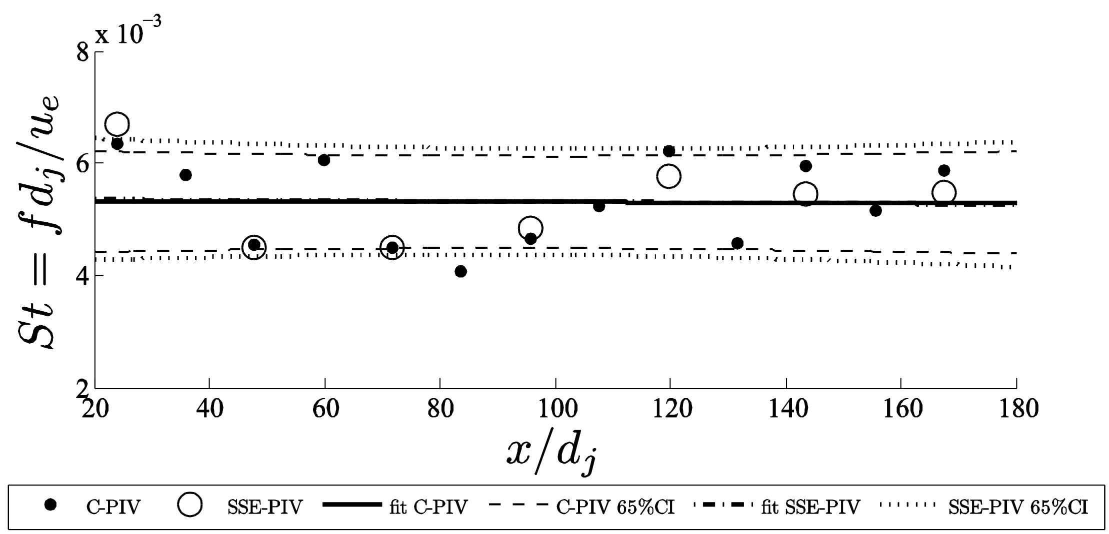

Figure 5.24: Streamwise variation of the dominant Strouhal number along the jet.

Figure 5.24 shows that the dominant Strouhal number decreases very slightly with increasing distance from the nozzle exit, from a value of 0.005319 and 0.005374 at x/d_j=0 for C-PIV and SSE-PIV respectively. These values have a variation of 1%. The streamwise rate of decay of St as x/d_j increases is -1.37x10^{-7} and -5.91x10^{-7}for C-PIV and SSE-PIV respectively. The overlap between 65% CI bands from each St streamwise distribution shows that the two estimates for Strouhal number are very similar.

5.7 Fluctuation of velocity of the spray

The PIV vector maps taken at progressing time are used to determine whether the spray flow is steady or unsteady. This allows one to validate the use of ensemble mean techniques when discussing flow features. The steadiness of the spray is evaluated from the RMS of the axial velocity which is computed by equation 5.11.

$$u_{\mathrm{RMS}} = \sqrt{\frac{1}{(n-1)}\left(\sum_{i=1}^{n} {u'_i}^2 - {u_i}^2\right)} \qquad 5.11.$$

where u'_i is the instantaneous axial velocity and u is the ensemble mean axial velocity. The contours of u_{RMS}/u_e from the C-PIV are presented in figure 5.25 *(b)* and 5.25 *(d)*. Figure 5.25 *(a)* and *(c)* show the C-PIV ensemble mean streamwise velocity contours.

Figure 5.25 *(b)*, shows that the magnitude of the streamwise u_{RMS} velocity increases to 8% around the jet axis, within the approximate range r/d_j= ±4.5, up to x/d_j =50. This increase in u_{RMS} is common as r approaches the spray shear layer and is well documented in the literature. At a radial distance greater than the jet shear layer the value of u_{RMS}/u_e reduces rapidly to 5%, then slowly to 1% as r/d_j increases further. The RMS level outside the jet shear layer decreases with increasing distance from the nozzle outlet plane, until, after x/d_j≈50. The RMS velocity increases above the free stream level at the radial boundary of the PIV field of view. Beyond $x/d_j \approx 50$, the presence of the jet is felt through an increase in the u_{RMS} level radially across the full field of view of the C-PIV image. The shear layer mean velocity profile is shown, in figures 5.25 *(a)* and *(c)*, to spread at a comparatively lower rate with u remaining below $0.1u_e$ at $x/d_j \approx 100$. It is believed that the atomiser nozzle of the spray helps the flow to become fully developed over a short distance from the nozzle exit thus giving a self-similar velocity profile after $x/d_j \approx 50$. At $x/d_j > 80$ the spray characteristics become similar to that of a mist, as the RMS velocity fluctuation within the spray becomes substantially uniform in the radial direction as shown in figure 5.25 *(d)*.

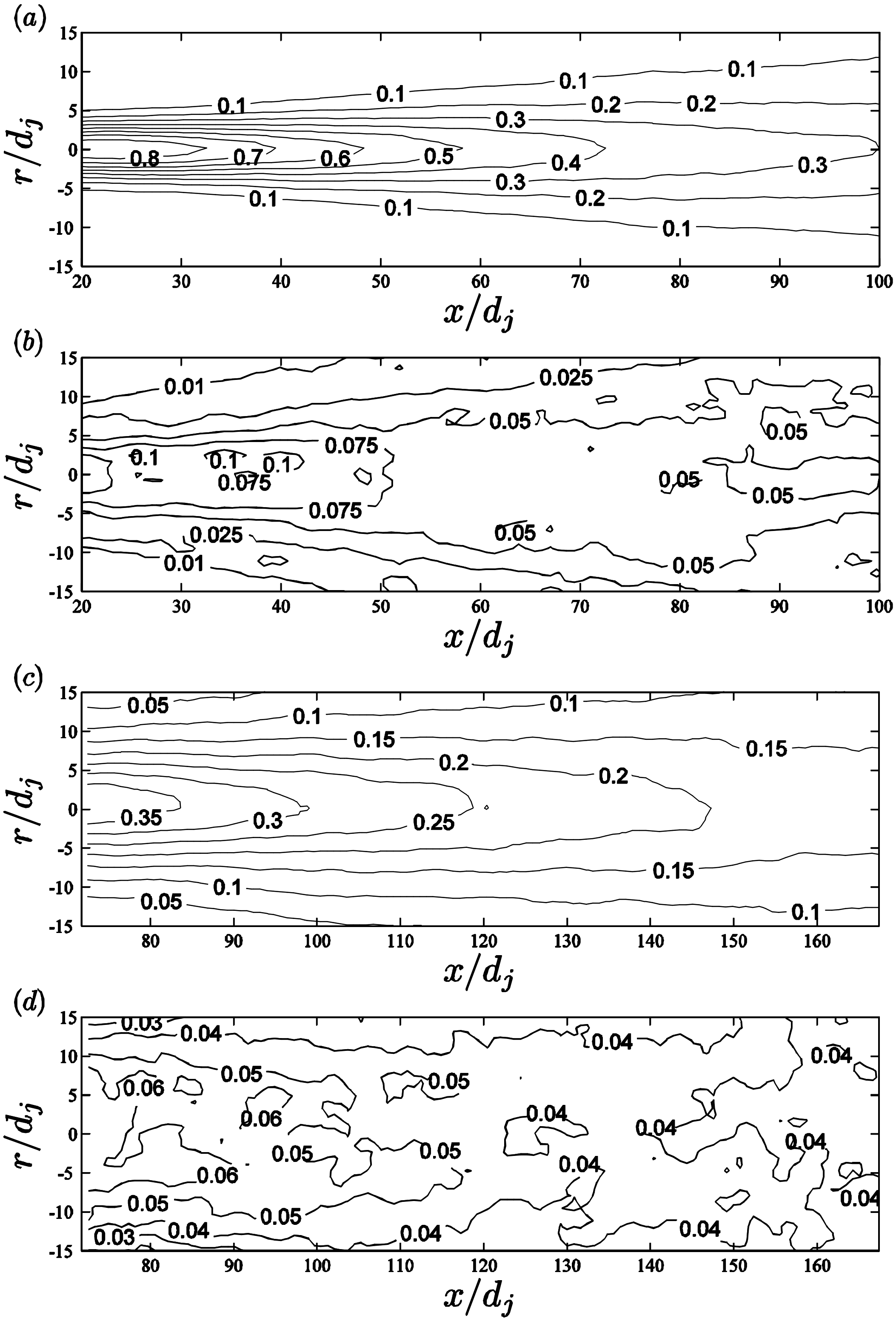

Figure 5.25: Plots of u/u_e of the jet from C-PIV over the range *(a)* $20<x/d_j<100$, *(c)* $80<x/d_j<170$, and plots of u_{RMS}/u_e over the range *(b)* $20<x/d_j<100$, *(d)* $80<x/d_j<170$.

Figure 5.26 shows u_{RMS}/u_e computed from equation 5.11 for C-PIV (*left*) and SSE-PIV (*right*). Both sets of contour maps are limited to the field of view of the SSE-PIV with the single-stem endoscope located six positions as outlined previously in section 5.2. The area of SSE-PIV plots *(b)*, *(d)*, *(f)*, *(h)*, *(j)* and *(l)* is outlined using a solid thick black line; the same field of view is identified on the C-PIV field of view with a dashed line on figures 5.26 *(a)*, *(b)*, *(e)*, *(g)*, *(i)* and *(k)*. In the case of SSE-PIV, the contour levels spill-over the field of view boundaries. This is a spurious numerical effect from the post processing graphical package. In figure 5.26 *(a)*, the u_{RMS}/u_e value at x/d_j=25 is approximately 12%. This is twice as high as the u_{RMS}/u_e observed within the jet shear layer at x/d_j=25. The fluctuation at x/d_j<23.9 is not a physical flow feature but a measurement error. The increase in fluctuation is due to the excess light reflection in the denser part of the spray. As discussed in section 5.2, within this region, the velocity recorded is false, and measurements within the limit x/d_j<23.9 should be neglected.

The SSE-PIV contours presented in figure 5.26 are very noisy. The contour boundaries become increasingly irregular as r/d_j increases. The irregularity arises due to the curvature of the endoscopic lens. As previously described in section 5.2 the optical quality of the image captured by SSE-PIV decreases as the radial distance from the centre of the image increases. This is due to the optical distortion by the optical configuration in the endoscope. This increases the amount of background noise masking the signal of the u_{RMS}. In figure 5.26 the u_{RMS} level in the region close to the field of view edge of all SSE-PIV images is seen to be very unstable. This is not a true depiction of the spray turbulent qualities and should be noted as such. The fluctuation at the field of view edge is approximately 10% in figure 5.26 *(b)*. This value increases as the image position progresses in the streamwise direction to 30%, as seen in figure 5.26 (*l*). Plots at lower x/d_j show 10% u_{RMS}/u_e at the radial position of the SSE-PIV field of view at r>10d_j and r<-10d_j. This results from high cross-correlating noise components, since very few tracer particles are available to track. As the spray diffuses and increases in r, tracer particles start appearing within the distorted part of the image. These tracer particles appear out of focus and distorted and have very little to no traceability. In this region there is an increase in the noise components in the SSE-PIV vector maps, hence an increase in u_{RMS}/u_e at the image edge.

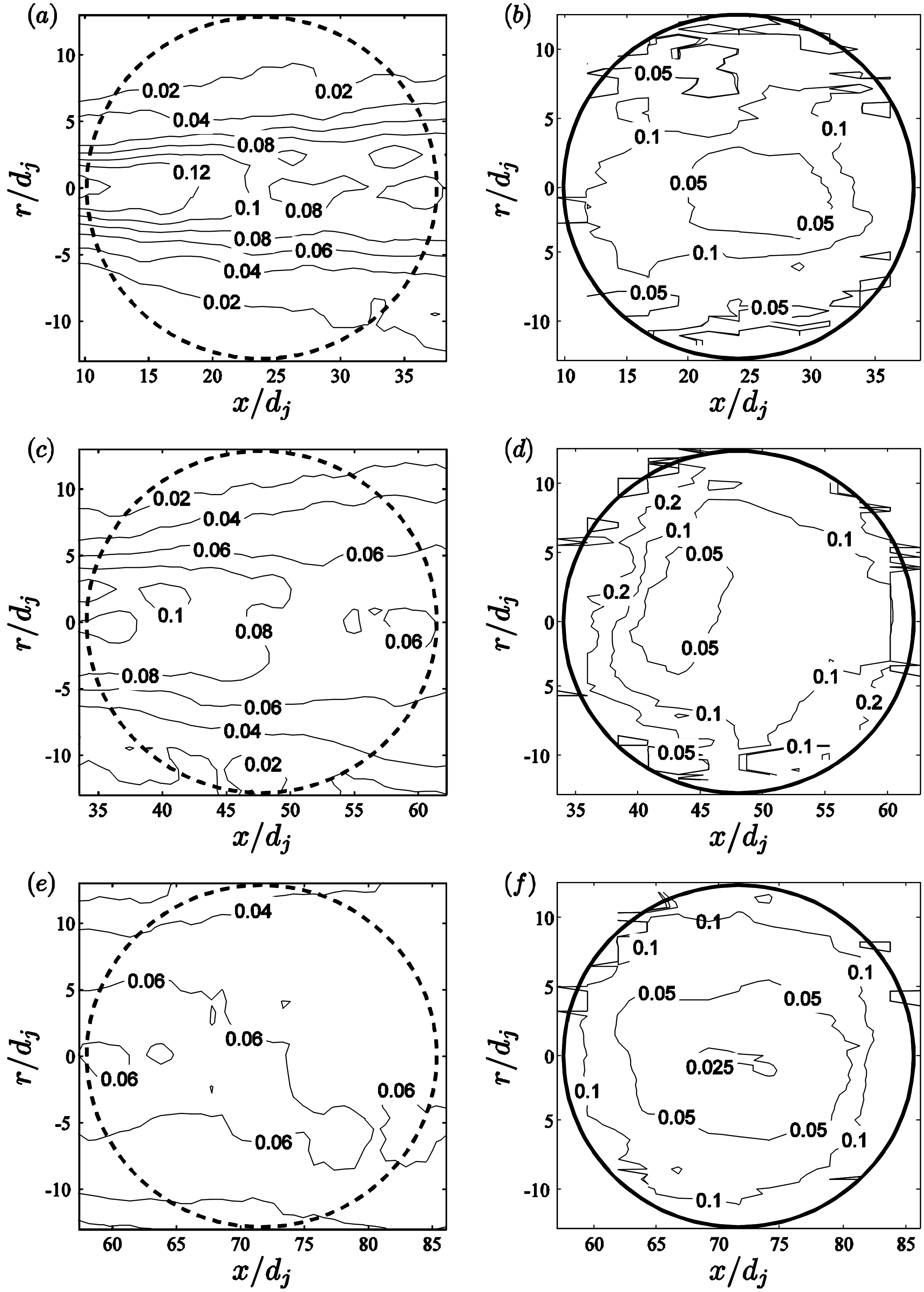
(a)
0.02
0.02
0.04
0.08
0.12
0.1
0.08
0.08
0.06
0.04
0.02
(b)
0.05
0.1
0.1
0.05
0.05
0.1
0.05
0.05
(c)
0.02
0.04
0.06
0.06
0.1
0.08
0.06
0.08
0.06
0.04
0.02
(d)
0.2
0.1
0.05
0.1
0.2
0.05
0.1
0.2
0.1
0.05
0.1
(e)
0.04
0.06
0.06
0.06
0.06
0.06
(f)
0.1
0.1
0.1
0.05
0.05
0.025
0.1
0.05
0.05
0.1
0.1
r/d_j
x/d_j

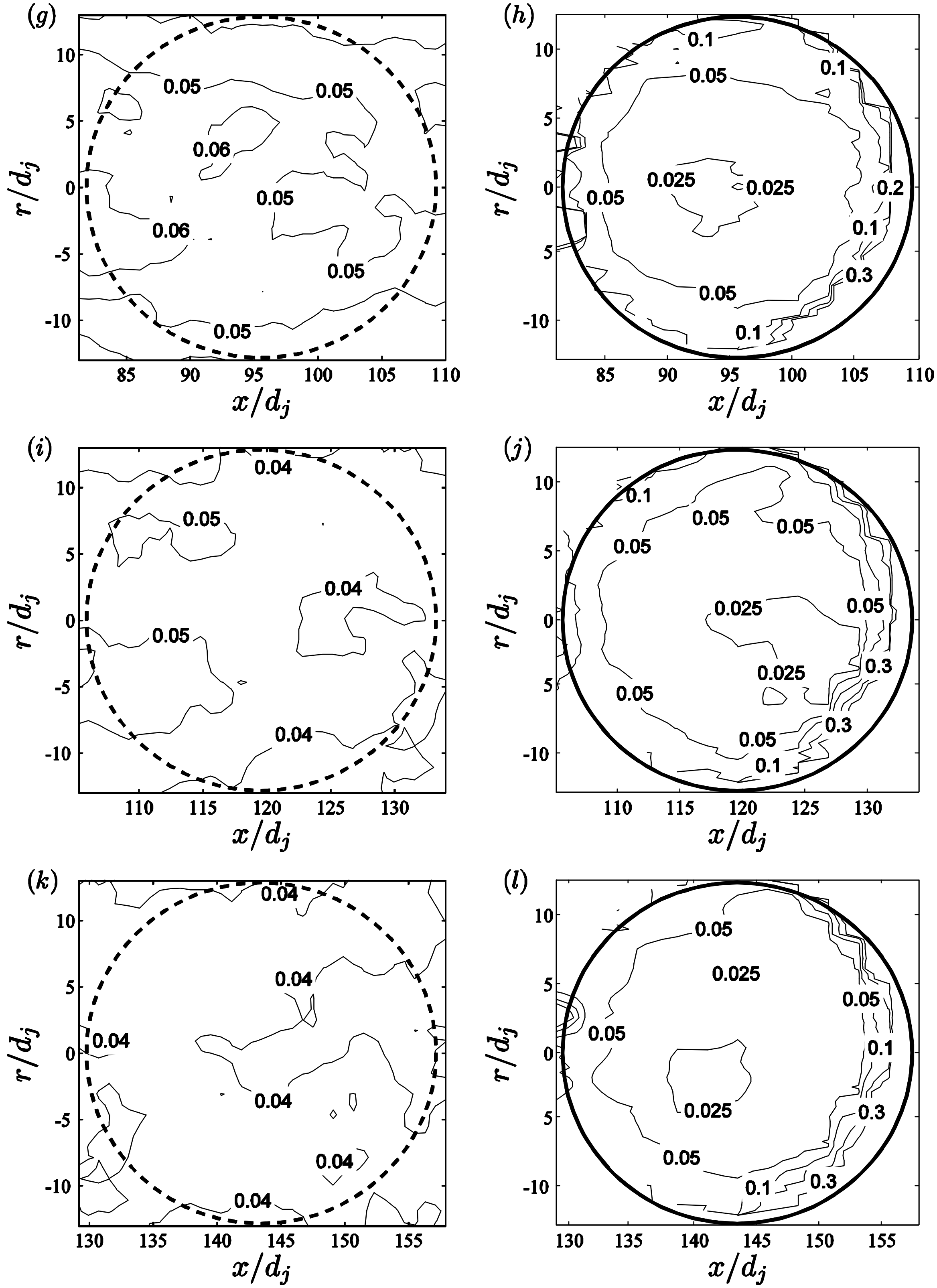

Figure 5.26: Plots of u_{RMS}/u_e of the spray using C-PIV (left) and SSE-PIV (right) at increasing x/d_j. All plots are limited to the the SSE-PIV field of view.

5.8 Summary

In this chapter the mean flow fields and the unsteady statistical components of the spray were presented using conventional PIV, the single-stem endoscopic PIV and Pitot anemometry. The data obtained shows the similarity of the velocity vector fields between techniques from which the mass flow rate, the spray spreading rate, the velocity centreline decay, the dominant wave number and the Strouhal number were extracted. This chapter also presented natural fluctuation of the jet which was obtained experimentally using the conventional PIV and single-stem endoscopic PIV. The measurement uncertainty described in this chapter is discussed in greater detail within chapter 6.

CHAPTER 6: ASSESSMENT OF ACQUISITION AND MEASUREMENT UNCERTAINTY

6.1 Introduction

In the previous chapter, the ensemble mean profiles and the unsteady characteristics obtained by C-PIV and SSE-PIV were compared. This chapter focuses on estimating the amount of uncertainty in the SSE-PIV measurements and compares it against the benchmark result from C-PIV. Section 6.2 determines the amount of uncertainty inherent to the SSE-PIV system. This includes the system and acquisition uncertainty due to the optical, illumination, and image calibration arrangement. The assessment of the measurement uncertainty due to the number of samples and image processing parameters are discussed in section 6.8. The assessment of the amount of intrusion caused by the PIV probe of Ø10 mm and the effect of the finite length on the SSE-PIV viewing window is discussed in section 6.9.

6.2 System and acquisition uncertainty

The measurement position and time in PIV are defined by equations 6.1 and 6.2. In equation 6.1, $\boldsymbol{X_0}$ indicates the location of the origin on the image plane and $\boldsymbol{X_s}$ and $\boldsymbol{X_e}$ show the starting and ending positions of the correlation area. The physical location can be obtained by the use of the magnification factor, α. The locations of $\boldsymbol{X_s}$ and $\boldsymbol{X_e}$ are usually defined by the centre positions of the correlation area. The measurement time is defined by the mean value of the pulse time of the laser light sheet as shown by equation 6.2, where t_s and t_e are the first and second pulse times. The PIV measurement variables u, x, t that define each single vector $u(x,t)$ in the PIV image are the subjects of uncertainty analysis and they are analysed independently in this section.

$$x = \alpha[(\boldsymbol{X_s} + \boldsymbol{X_e})/2 - \boldsymbol{X_0}] \quad 6.1.$$

$$t = (t_s + t_e)/2 \quad 6.2.$$

To find the uncertainty within the PIV systems, it is prudent to develop an error model. By developing an error model, one can acknowledge each factor that influences a measured value and that constitutes a potential source of error and is therefore a source of measurement uncertainty. The contribution of each error source to the total uncertainty is governed by the coefficient that weights the contribution of each source to the total uncertainty. These coefficients are determined from the measurement error model. In this study, the error model applied by Park *et al.* (2008) will be used. This model uses the law of combined uncertainty to provide an independent combined uncertainty as stated in equation 6.3 and equation 6.4,

$$\varepsilon^2 = \sum_{i=1}^{N} (\partial f/\partial \delta i)^2\, {\delta_i}^2 \quad 6.3.$$

$$\varepsilon^2 = \sum_{i=1}^{N} [c_i \delta_i]^2 \quad 6.4.$$

where ε is the uncertainty and c_i is the sensitivity coefficient of a given error source δ_i. The sensitivity coefficient is obtained by $c_i \equiv \partial f/\partial \delta_i$. The standard uncertainty, δ_i, is obtained by measurement and/or by reference to the published literature. Both C-PIV and SSE-PIV techniques estimate the in-plane velocity vector based on the measured displacement $\Delta\boldsymbol{X}$ of the seeding particles over time Δt. This gives $u=\alpha(\Delta\boldsymbol{X}/\Delta t)+\delta u$, where α is the optical magnification of the PIV lenses and δu is the error due tracer particle lag in the spray. The equation $u=\alpha(\Delta\boldsymbol{X}/\Delta t)+\delta u$ can be used to calculate the sensitivity coefficients $(\partial u/\partial \alpha)$, $(\partial u/\partial \Delta\boldsymbol{X})$, $(\partial u/\partial \Delta t)$, and $(\partial u/\partial \delta u)$ for α, $\Delta\boldsymbol{X}$, Δt, and δu respectively. The equation 6.4 can be expanded into its constituents as shown in equations 6.5 to 6.11. This technique combines the factors of uncertainty to find the combined uncertainty for the targets of u, x and t, shown in equations 6.9 to 6.11. The uncertainty in velocity is based on the velocity magnitude. The uncertainties of u, x and t are combined in equation 6.12 to find the combined uncertainty, σ_u, from each PIV system.

The uncertainty due to the optics is given by

$$\varepsilon_\alpha = \frac{\partial u}{\partial \alpha}.\left[\left(\frac{\partial \alpha}{\partial L_r}\delta_1\right)^2 + \left(\frac{\partial \alpha}{\partial l_r}\delta_2\right)^2 + \left(\frac{\partial \alpha}{\partial L_r}\delta_3\right)^2 + \left(\frac{\partial \alpha}{\partial L_r}\delta_4\right)^2 + \left(\frac{\partial \alpha}{\partial L_t}\delta_5\right)^2 + \left(\frac{\partial \alpha}{\partial \theta}\delta_6\right)^2\right]^{\frac{1}{2}} \quad 6.5.$$

In equation 6.5, δ is the estimated error source and the numeric subscripts 1 to 6 represent the error due to the reference image, physical distance, image distortion by the optics, image distortion by the CCD calibration board position, and by the calibration board offset, respectively.

The uncertainty due to the particle displacement $\varepsilon_{\Delta \boldsymbol{X}}$ is given by

$$\varepsilon_{\Delta \boldsymbol{X}} = \frac{\partial u}{\partial \Delta \boldsymbol{X}}.\left[\left(\frac{\partial \boldsymbol{X}}{\partial x}\delta_7\right)^2 + \left(\frac{\partial x}{\partial \boldsymbol{X}}\delta_8\right)^2 + \left(\frac{\partial \alpha}{\partial \theta}\delta_9\right)^2 + (\delta_{10})^2 + (\delta_{11})^2\right]^{\frac{1}{2}} \quad 6.6.$$

The numeric subscripts 7 to 11 in equation 6.6 represent the error due to laser power fluctuation, the image distortion by CCD, the normal view angle, the mis-matching error, and the sub-pixel analysis. Combining the estimated error sources with the respective sensitivity coefficients in equation 6.6, the uncertainty due to particle position, $\varepsilon_{\Delta \boldsymbol{X}}$, is obtained.

The uncertainty, $\varepsilon_{\Delta t}$, due to the tracer particle travel time, Δt is given by

$$\varepsilon_{\Delta t} = \frac{\partial u}{\partial \Delta t}.[(\delta_{12})^2 + (\delta_{13})^2]^{\frac{1}{2}} \quad 6.7.$$

δ_{12} and δ_{13}, in equation 6.7 represent the errors inherent in the delay generator and the pulse time, respectively. Combining these standard errors with the respective sensitivity coefficients in equation 6.7, the uncertainty due to time, $\varepsilon_{\Delta t}$, can be obtained.

The error due to the seeding particle lag, that is, due to the difference between the seeding particle displacement and the surrounding fluid displacement is given by

$$\varepsilon_{\delta u} = \frac{\partial u}{\partial \delta u}.\left[(\delta_{14})^2 + (\delta_{15})^2\right]^{\frac{1}{2}} \qquad 6.8.$$

δ_{14} and δ_{15} in equation 6.8 represent the error due to the seeding particle trajectory deviating with respect to that of the flow and the out of plane motion or the 3D particle–flow effect, respectively. Combining these standard errors with the respective sensitivity coefficients in equation 6.8, the uncertainty due to velocity magnitude, $\varepsilon_{\delta u}$, can be obtained.

The magnification factor, particle displacement, time and seeding velocity uncertainty all contribute to the uncertainty in target velocity, ε_u, as per equation 6.9.

$$\varepsilon_u = \left[(\varepsilon_\alpha)^2 + (\varepsilon_{\Delta \boldsymbol{X}})^2 + (\varepsilon_{\Delta t})^2 + (\varepsilon_{\delta u})^2\right]^{\frac{1}{2}} \qquad 6.9.$$

The measured velocity magnitude u in $u=\alpha(\Delta \boldsymbol{X}/\Delta t)+\delta u$ refers to the velocity vector u with origin at x in the flow field at time t

The uncertainty in the vector position, ε_x, is affected by the digital error, δ_{16}, by the non-uniformity of the seeding particle distribution, δ_{17}, by the origin correlation, δ_{18}, and by the magnification factor, δ_{19}. ε_x is determined as shown in equation 6.10.

$$\varepsilon_x = \left[\left(\frac{\partial x}{\partial \boldsymbol{X}}\delta_{16}\right)^2 + \left(\frac{\partial x}{\partial \boldsymbol{X}}\delta_{17})\right)^2 + \left(\frac{\partial x}{\partial \boldsymbol{X}}\delta_{18}\right)^2 + \left(\frac{\partial x}{\partial \alpha}\delta_{19}\right)^2\right]^{\frac{1}{2}} \qquad 6.10.$$

The uncertainty in the target time, ε_t, is affected by the delay generator, δ_{12}, and the pulse time, δ_{13}, as shown in equation 6.11.

$$\varepsilon_t = [(\delta_{12})^2 + (\delta_{13})^2]^{\frac{1}{2}} \qquad 6.11.$$

The error sources for the dependant variables *u*, *x* and *t* are combined using equation 6.12 to determine the combined uncertainty of the PIV systems. A coverage factor, *k*=1, is used in this uncertainty analysis that corresponds to the 65% confidence interval band. This gives

$$\sigma_u = \sqrt{(\varepsilon_u)^2 + (\varepsilon_x\, \partial u/\partial x)^2 + (\varepsilon_t\, \partial u/\partial t)^2} \qquad 6.12.$$

6.2.1 Application of uncertainty analysis to conventional and endoscopic PIV systems

Table 4.2 in section 4.5, shows the principal dimensions of the PIV measurement systems, which consist of the following sub-systems: (1) Calibration, (2) Flow Visualization, (3) Image Detection, and (4) Data Processing. The target flow field is the 2D cross-section on the *x*-*y* plane of an air jet laden with atomised water droplets. The measurement area is 211.5 mm x 211.5 mm, which is determined by the arrangement of the camera and of optical systems and that also depends on the laser pulse energy for illumination. The calibration was conducted by the insertion of a calibration board at the same position as the laser light sheet. The distance of the reference point, l_r, and its distance on the image plane, L_r, were used to determine the magnification factor, α, by equation 6.13

$$\alpha = l_{\mathrm{r}} \cos\theta / L_{\mathrm{r}} \approx l_{\mathrm{r}}\, (1 - \theta^2/2)/L_{\mathrm{r}} \qquad 6.13.$$

where L_r was obtained by detecting the calibration board reference points in pixel units and θ is a small angle between the light sheet and the calibration board. This is the simplest method for the calibration of the magnification factor, α. The setting up, acquisition, image pre/post-processing and validation for C-PIV and SSE-PIV has been previously described in chapter 4.

The flow chart of the PIV measurement procedure is shown in figure 6.1. The measurement starts from the digital image of the visualised flow field, obtained by the imaging hardware, the pulsing time of the laser illumination, and the information from the calibration procedure that uses the calibration board. The outputs from the PIV measurement are the flow velocity vectors, each velocity vector position, and the velocity vector time. The identified error sources in this measurement process are shown in figure 6.1. The errors propagate from the input data to the output measurements as shown in the data flow of figure 6.1.

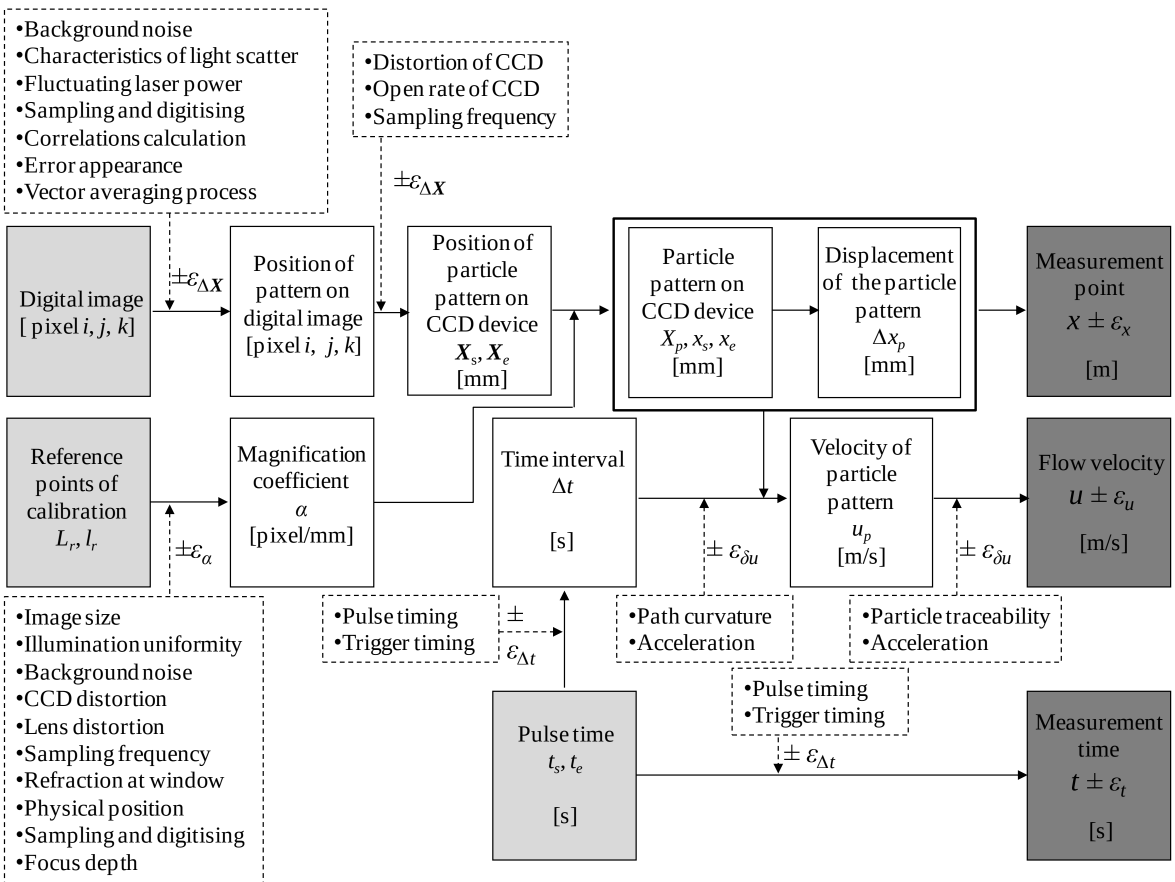

Figure 6.1: Data flow of PIV measurement and propagation of uncertainty.

6.2.2 Identification of the sensitivity factors

Uncertainty in reference position L_r, derived from equation 6.13.

$$\partial\alpha/\partial L_r = -l_r/L_r^2 \text{ [mm/pixel}^2\text{]} \qquad 6.14.$$

Uncertainty in physical position l_r, derived from equation 6.13.

$$\partial\alpha/\partial l_r = 1/L_r \text{ [1/pixel]} \qquad 6.15.$$

Uncertainty in image distortion is the same sensitivity as equation 6.14.

The uncertainty in the position of the calibration board (reference board position)a pinhole camera model is assumed. When $\alpha = l_r/L_r = l_t/f$, where l_t and f show the distance from the target and the focus length in pixel unit respectively. The difference between planes is Δz_0 and the sensitivity coefficient is obtained as equation 6.16, as the reduction equation is linear for l_t.

$$\partial\alpha/\partial l_t = l_r/(L_r.l_t) \text{ [1/pixel]} \qquad 6.16.$$

Uncertainty in the calibration board offset from the image plane (parallel board) and the change in angle from the ideal normal view angle can be found by differentiation of equation 6.13 to create the sensitivity factor equation 6.17.

$$\partial\alpha/\partial\theta = -l_r\,.\theta_1/L_r \text{ [mm/pixel]} \qquad 6.17.$$

The uncertainty in the laser power fluctuation affects the location of a particle within the IA and therefore affects both the physical and digital particle position the sensitivity is as per equation 6.18 which is derived from equation 6.1.

$$\partial X/\partial x = 1/\alpha \text{ [pixel/mm]} \qquad 6.18.$$

The uncertainty observed at the CCD by distortion, the non uniformity of tracer particles, the correlation of the origin and centre position of the IA is affected by the uncertainty in the uncertainty in the observation of the physical and digital image position of the particle. The sensitivity is as per equation 6.19 and is derived from equation 6.1.

$$\partial x/\partial X = \alpha \ \text{[mm/pixel]} \qquad 6.19.$$

The uncertainty in the magnification factor is primarily due to the physical measurement used for calibration. This has a direct affect on the uncertainty observed on the digital position. The sensitivity factor is shown in equation 3.12 and is derived from equation 6.1.

$$\partial x/\partial \alpha = X \ \text{[pixel]} \qquad 6.20.$$

The sensitivity factors shown in this section are each multiplied by the respective uncertainty δ_i that is defined in sections 6.3.1 to section 6.3.5.

6.3 Quantification of uncertainty sources in the system and acquisition

6.3.1 The magnification factor α

The calibration board has two primary sources of error. These are the quantisation of the reference positions in pixels and the determination of the physical length between these positions. The distance of the reference points in pixels, L_r, were measured along the image plane in C-PIV and SSE-PIV. The position of the reference points was detected from a 2D image using two points and calibrating the distance between them. The quantisation error band of this type of method along the pixel scale is approximately ±0.7 pixels, which gives a statistical uncertainty of δ_1=±0.7 pixels, as determined by Park *et al.* (2008). Using equation 6.13, the contribution of δ_1 to the uncertainty in α is obtained.

The uncertainties in the physical length, l_r, of the PIV calibration reference points affects the accuracy of the magnification factor and thus the calibration. The error in stating l_r

affect the measurements of velocity, u, and of the velocity vector position, x. A well-deployed calibration board has less than a ±20 μm error. Therefore δ_2= ±20 μm. The sensitivity coefficient for α is due to the scaling from pixels to meters in the PIV image. Equation 6.14 gives the uncertainty contribution of δ_2 to the uncertainty of α.

The optical system is commonly affected by optical distortion effects. A larger view angle can cause a barrel distortion and a non-perpendicular setup can give perspective effects. It is important to quantify the image distortion in C-PIV and SSE-PIV. This distortion affects the measurement of the vector location of particles at their start position, $\boldsymbol{X_s}$, and end position, $\boldsymbol{X_e}$. The large view angle and short working distance of the SSE-PIV system creates a larger amount of barrel distortion within the image compared to the C-PIV. This distortion was estimated using the Oslo Optical simulation software by Ramsbottom (2009) as presented in chapter 3. The distortion of the image affects the magnification factor. A high perspective angle and the short working distance, of the SSE-PIV system causes the image plane to be curved. The maximum amount of distortion or out of focus effect is at the edge of the field of view. The amount of curvature is not proportional to the radius. The change in the image curvature starts to appear more prominent when r/d_j<10 and r/d_j>10. The amount of uncertainty associated at the maximum field of view of the SSE-PIV system is approximately 0.5 mm and therefore the uncertainty due to this optical distortion for SSE-PIV δ_3= ±10 pixels for SSE-PIV. From Park *et al.* (2008) and Raffel *et al.* (2007), the distortion of the C-PIV image is estimated to be 0.5% of Reference length, L_r. The uncertainty due to this optical distortion for C-PIV is δ_3=0.005l_t = ±4.11 pixels for C-PIV.

The distortion and other error factors from the CCD could cause errors of image detection. The tolerance band caused by the accuracy of CCD is usually small, and it is therefore neglected, Park *et al.* (2008).

The calibration phase in the experimental setup plays a large role in the measurement accuracy. The position of the reference board for calibration and the laser light sheet may be offset to the laser sheet and/or non-parallel, as schematically shown in figure 6.2. The calibration setup directly impacts on the magnification factor, since the calibrated plane can differ from the measurement plane, which causes an uncertainty in the final value of α. The

SSE-PIV system has a mechanically fixed laser and camera position to ensure the view angle is always normal to the light sheet and the image plane is parallel and focused onto the light sheet. This fixed position has an uncertainty due to the manufacturing tolerance of the lens mounts inside the endoscope shaft. According to the endoscope machining specification provided by Olympus, the machining tolerance is ±0.5 mm. This ±0.5 mm tolerance is cumulative along the image lens track and in the optical arrangement for the laser sheet formation. The maximum statistical difference between the camera focus plane and the laser sheet plane for the SSE-PIV system is δ_5=±5 mm positional shift and a δ_6=±2°=±0.035 radians parallelax angle.

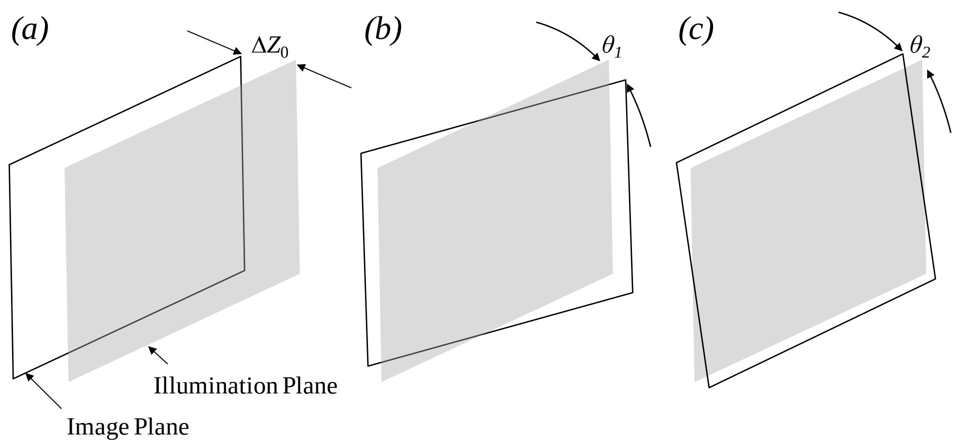

Figure 6.2: Uncertainty of image plane and illumination alignment for the calibration board *(a)* parallel offset, *(b)* yaw angle, and *(c)* roll angle offsets.

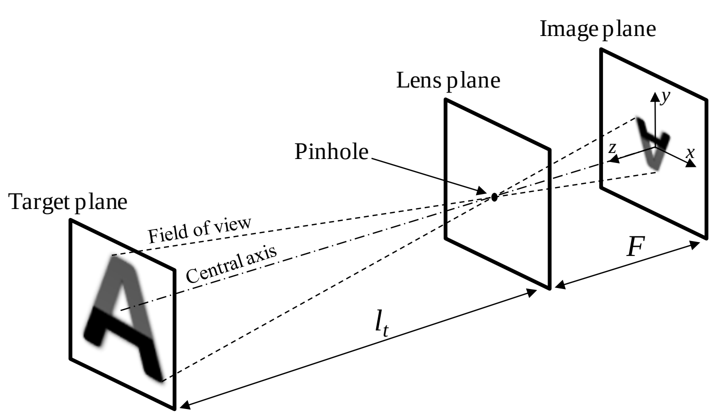

Figure 6.3: Sketch of a pinhole camera.

To find the uncertainty due to the offset between the image plane and the laser plane, a pinhole camera layout is assumed, as shown schematically in figure 6.3, in which α can be described $\alpha = l_r/L_r = l_t/F$, where l_t and F are, respectively, the distance from lens plane to the target plane and the focus length from the pin hole to the image plane in pixel units. It is first assumed that the two planes are parallel. The light sheet thickness is taken as $\Delta z_0 = 5$ mm. The sensitivity coefficient for α due to l_t is $1/F$. This relationship assumes the calibration board is parallel to the laser light sheet. However, an exact parallelism is not achievable in practice. It is assumed that, when using a well-controlled calibration technique, the angle between the laser plane and calibration board may deviate at most $\delta_6=\theta_1 = \pm 2° = \pm 0.035$ radians from parallel as stated in Park *et al*. (2002) for both PIV techniques. If the image plane is at a high yaw angle θ_1 from the illumination plane, there is the possibility of uneven laser intensity across the image. The lack of alignment will also increase in the loss of particle traceability and introduce an amount of perspective effect. The sensitivity coefficient for α due to yaw angle is shown in equation 6.17 in section 6.2.2.

6.3.2 Displacement of particle image $\Delta \boldsymbol{X}$

An alternative approach to assessing the measurement precision in PIV evaluation can be based on a numerical simulation which is an approach taken by a number of researchers for example, Westerweel (1993), Keane and Adrian (1990), Keane and Adrian (1991), Keane and Adrian (1992), Cowen and Monismith (1997), and Keane *et al.* (1995). These past studies involved varying a single PIV parameter at a time, artificial particle image recordings of known content was generated, evaluated and compared to with the known result. This type of simulation is known as the Monte Carlo simulation, and the details of which are given in Raffel *et al.* (2007). By using the application examples of the models outlined in Raffel *et al.* (2007) Ch. 5.5, one can apply the measurement uncertainty models to this spray application to evaluate the measurement uncertainty in $\Delta \boldsymbol{X}$.

The spatial and temporal fluctuations in laser power intensity directly affect the detection of the particle image position. The maximum uncertainty is associated to the estimate of the particle diameter. If the experimental condition is well-controlled, this uncertainty is approximately 1/10 of the nominal particle diameter. The particle size affects the ability of the PIV system to detect moving particles in the flow. Specifically, the PIV system detects the Mei-scattered light from the moving particles. The apparent particle diameter from the Mei-scattering principle is $q=\pi d_p/\lambda$, where q is the Mei scattering normalised diameter, d_p, is the nominal particle diameter in mm and λ is the illumination wavelength, which in both SSE-PIV and C-PIV is 532 nm. In the PIV images captured using both PIV techniques the droplet energy scatter observed was approximately 2-4 pixels. At a flow speed of ≈50 m/s, the pulse time is approximately 11 ms to obtain an approximate 4 pixel displacement between image pairs in the C-PIV system and 16 ms for the SSE-PIV system. Raffel *et al*. (2007) presented by RMS the uncertainty of the particle image displacement in pixels for different sized interrogation areas, IA. The uncertainty was noted to be constant except for when the particle image displacement is less than 0.5 pixels. For a particle displacement greater than 0.5 pixels, a linear relationship is obtained. This behaviour can also be observed in the experimentally obtained error estimates in Willert and Gharib (1991). A theory provided by Westerweel *et al*. (1997) may be used to explain this behaviour. The particle displacement of each PIV image in the current study was approximately 25% of the IA side length with a 16 x 16 IA. According to Raffel *et al*. (2007) and Park *et al*. (2003), a 4 pixel energy scatter with a 4 pixel displacement in $\Delta\boldsymbol{X}$ has an uncertainty of ±0.5 pixels, which in this case, is equivalent to δ_7=0.0071 mm and δ_7=0.02573 mm for C-PIV and SSE-PIV respectively. The sensitivity coefficient for $\Delta\boldsymbol{X}$ due to laser power fluctuation is shown in equation 6.18 in section 6.2.2.

The uncertainties arising from image detection are due to the configuration of the optical system, the amount of distortion of the CCD array, and the angle at which the camera is from the normal position, as defined in figure 6.2, diagram C. The image distortion caused by lens aberration can affect the detection of the tracer particle position and can result in a false $\Delta\boldsymbol{X}$. However, this factor is already accounted for by the uncertainty in the magnification of the optical system, defined in section 6.2.3.

The distortion observed at the CCD sensor has the same error source as the one in the calibration of the optical system presented in section 6.2.3. The typical amount of error on a conventional PIV system due to the image distortion by the CCD is δ_8=±0.0056 pixels as determined by Park *et al.* (2008). The error may be different cell by cell. The SSE-PIV system has a 3% increase in CCD distortion at the edge of the CCD as described in chapter 3 and therefore the assumed uncertainty for SSE-PIV due to the image distortion by the CCD is δ_8=±0.05768 pixels. The resulting uncertainty on $\Delta\boldsymbol{X}$ due to δ_8 is given by equation 6.19.

As per figure 6.2*(c)* the normal or perpendicular view angle may differ from the illumination plane. The increase in roll angle has the same effect as an increase in yaw angle described in section 6.3.1. A highly accurate setup may still inherent a roll angle which is estimated as θ_2 = ±2° = ±0.035 radians (Raffel *et al.* (2007)) for both C-PIV and SSE-PIV. Therefore for both PIV techniques the uncertainty due to the normal view angle δ_9= ±0.035 radians. The resulting uncertainty in $\Delta\boldsymbol{X}$ acquisition due to δ_9 is shown in equation 6.17 in section 6.2.2.

The uncertainties in image post-processing are defined by the mis-matching of droplets within the image pairs and also by interpolation errors in the subpixel analysis. In the pixel unit analysis, the mis-matching of a pair of particle images could happen due to the wrong selection of the IA, a poorly selected Δt, and the mis-alignment of the image and illumination planes. Any large localised error can be detected by comparing the candidate velocity vector with the surrounding ones, but small errors of mis-matching cannot be detected easily. PIV recordings obtained from a quiescent flow were used in determining the measurement uncertainty in the cross-correlation evaluation of single exposed particle pairs by Willert and Gharib (1991), and Willert *et al.* (1995) and a similar investigation for double exposed images by Willert (1996). The error due to post-processing was tested by post-processing an artificial image by Okamoto *et al.* (2000) and Nishio and Murata (2003). Using an artificial image enables the detection of the measurement error directly. The uncertainty band of the particle position in pixel units due to mis-matching can be estimated statistically and is approximately ±0.2 pixels for both the C-PIV and the SSE-PIV systems. The uncertainties of sub-pixel analysis depend on many factors, such as the diameter of tracer particle, the image noise level, and the particle concentration. The system error of sub-pixel analysis can be estimated by means of an artificial image (Okamoto *et al.* 2000) and is approximately ±0.03 pixels. Therefore the uncertainty in $\Delta\boldsymbol{X}$ due to processing mis-matching is δ_{10}= ±0.2 pixels and uncertainty in sub-pixel analysis is δ_{11}= ±0.03 pixels for both C-PIV and SSE-PIV systems.

Other error sources from image analysis may exist, which affect the measurement results, but these errors are less amenable to being modelled, based on the description of the PIV hardware and software of figure 6.1. They are application-specific and are specific to the experimental procedure. For instance, in some flows, the statistical uncertainty can be reduced by ensemble averaging the results.

6.3.3 Δt between pulses.

The time between pulses is set by the user and controlled by the timing box, which relays information to the laser Q-Switch and the camera trigger. The Δt pulses are set at approximately 11 ms and 16 ms for C-PIV and SSE-PIV respectively. This Δt is set to allow approximately 25% of particle image displacement within a 16 x 16 pixel IA. The delay generator controls the pulse timing that operates to ±200 ps, which is obtained from the Litron Nano L user manual. The laser itself has an uncertainty for the pulse timing of ±500 ps, which is also obtained from the user manual. Keeping the two uncertainty sources independent the uncertainty due to the delay generator is δ_{12}= ±200 ps and the uncertainty due to the pulse time is δ_{13}= ±500 ps.

6.3.4 δu of experiment.

The seeding (atomised water droplets) trajectory depends on the acceleration of flow field. Atomised droplets under 34 μm within air jets have usually very low velocity lag in the accelerating fluid (Raffel *et al.* (2007)). In this application, it can be assumed that the flow is homogeneous and that u_g=u_l assuming negligible slip velocity and hence very little velocity lag. This is assumption is based on the homogeneous flow computations in Appendix A. Raffel *et al.* (2007) and Park *et al.* (2008) state that with a good choice of flow seeder the velocity lag due to particle trajectory is less than 0.01% of the localised flow velocity. Therefore, the uncertainty due to particle trajectory δ_{14}= 5 mm/s

The particle out-of-plane velocity component affects the in-plane measured value. In the case of a jet flow, droplets moving through the PIV plane are quite common. The droplets moving out of the PIV plane reduce the correlation peak signal strength. Three methods exist to compensate for this out of plane motion. Firstly, the Δt between image pairs can be reduced, which reduces the dynamic range of the velocity within the image. Secondly, the light sheet thickness can be increased to accommodate the out of plane motion within a given pulse time. This does however prove difficult, since the energy of the laser sheet diminishes proportionally to an increase in its thickness. Thirdly, the mean out of plane velocity component can be accommodated using a parallel offset of the light sheet between the illumination pulses in the direction of the flow. The amount of uncertainty in the in-plane mean velocity vector, caused by out of plane motion of the tracer particle can be given by Park *et al*. (2008) and shown in equation 6.2.1

$$u_m = u + w.\tan\theta_p \qquad 6.21.$$

where w is the normal velocity component and $w \cdot \tan\theta_p$ indicates the error component due to out of plane motion. The perspective angle θ_p can be estimated by the distance from the target plane and the size of measurement area. The maximum error associated to out of plane motion is estimated by using the maximum measured velocity of the jet, which is $u_e \approx 50$ m/s at $x/d_j=0$. The PIV correlation uses a 50% overlap and a 3 step refinement to search signals between frames. This process, along with a short Δt, allows only a 2-4 pixel displacement of droplets between frames, limiting the error due to out of plane motion to 0.5% of the mean local velocity. The perspective angle θ can be estimated by the distance from the target plane and the size of measurement area. When the out of plane component of velocity is assumed as 0.5% of the mean uniform flow velocity, the error is estimated as $\delta_{15}=\pm 0.577$ mm/s and ± 2.037 mm/s for the C-PIV and SSE-PIV systems respectively.

6.3.5 Measurement position: *x*

The measurement position and particle image displacement is measured using the PIV plane origin, $\boldsymbol{X_0}$, the particle start position $\boldsymbol{X_s}$, and end position $\boldsymbol{X_e}$. These factors have a combined uncertainty that affects the correlation accuracy. Keane and Adrian (1990) used an analytical model and Monte-Carlo simulations to determine the effects of experimental parameters to optimise PIV performance. From their investigation, it was found that the double-pulsed laser systems displayed their best performance when the interrogation area has a seeding density of 10-20 particles. The primary source of error in 2-D PIV is background noise that has a negative effect on the detection of the particle image displacement. Westerweel (2000) and Foucaut *et al.* (2004) provide a table with PIV control parameters. The parameters discuss the limits of α, $\Delta\boldsymbol{X}$, u, Δt and d_p. It was observed that, if the control parameters are within the limits, then the RMS of the measured particle image displacement has approximately a 0.1 to 0.5 pixels uncertainty in digital error which is similar to what was stated by Park *et al.* (2008). Therefore uncertainty due to digital error $\delta_{16} = \pm 0.5$ pixels.

Uncertainties arise in the correlation distance $\Delta\boldsymbol{X}$ when the particle distribution is not uniform in the IA. The non-uniformity of the seeding within a captured image causes the central position of the IA within the measured velocity field to be displaced from its original position. This kind of biasing is noticeable at the edge of the jet, within shear regions, where the bulk flow is densely populated by seeding particles and the entrained flow can show one or two seeding particles at best. PIV in the jet is performed using water droplets that are atomised on ejection and transported with the air flow. The atomized water droplet size was measured at 50 mm, 200 mm, and 350 mm from the nozzle, using LabView Vision Studio software by the shadow imaging technique. The particle sizing technique is described in Appendix B. The median droplet size, 34 μm, is of the same order of magnitude of the nominal seeding particle size of 50 μm. Therefore, both water droplets and solid particles participated to creating the Mei scatter on the PIV images. There is no seeding in the laboratory air that is entrained in the jet downstream of the nozzle, therefore the velocity field measured by PIV is limited 80% of the jet radius as determined by the jet shear layer vorticity thickness, sketched in figure 6.4. In the outer 20% of the jet shear layer, the low particle count introduces the possibility of a bias in the correlation distance $\Delta\boldsymbol{X}$. This bias is due to the peak in the auto-correlation being driven by the $\Delta\boldsymbol{X}$ of the greater number of the displaced particles towards the jet axis in the two-dimensional IA.

This bias will be at most 50% of the IA, which is 8 pixels within a 16 x 16 correlation grid. The uncertainty due to non-uniform tracer particle distribution δ_{17}=8 pixels for both C-PIV and SSE-PIV techniques.

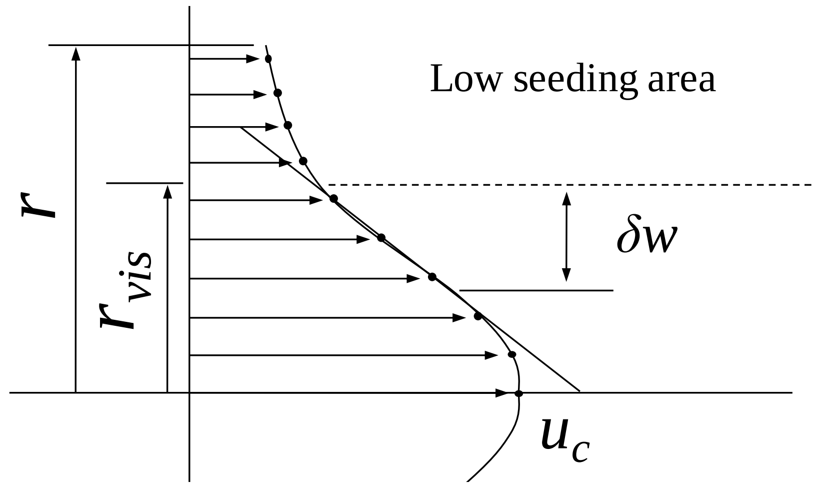

Figure 6.4: Schematic of jet half profile with low seeding in the outer layer.

An additional source of error is the difference in origin between the physical space and the image plane. $\boldsymbol{X_0}$ indicates the location of the origin on the image plane. The correlation between the physical space and the image plane is given by the definition of the coordinate system. This type of correlation can inherent up to 2 pixels of uncertainty, due to the bias shifting and uncertainty in the original calibration magnification factor. This gives the uncertainty due to correlation of the origin δ_{18}=±2 pixels. The sensitivity coefficient for the centre position for correlation, non-uniformity of tracer particles and the origin correlation all have sensitivity factors derived from equation 6.1 and the sensitivity coefficient for the centre position is as per equation 6.19 in section 6.2.2. The uncertainty in the measurement position, *x*, due to the magnification factor is $4.1\text{x}10^{-4}$ and $5.2\text{x}10^{-4}$ for C-PIV and SSE-PIV systems respectively ($\sqrt{\sum \varepsilon_i{}^2}$ from table 6.1). The results of this uncertainty analysis are summarised in tables 6.1-6.4. Tables 6.1-6.4 report the error sources that contribute to the uncertainty of the PIV velocity measurements $u(x,t)$, and t in $u=(\Delta \boldsymbol{X}/\Delta t)+\delta u$.

Parameter	Category	Error sources	δ_i	unit	c_i	unit	$c_i\,\delta_i$	ε
α (mm/pixel)	Calibration	δ_1 Reference image	0.7 (0.7)	pixel	8.97E-05 (4.65E-05)	mm/pixel^2	6.28E-05 (3.26E-05)	0.000417 (0.000522)
		δ_2 Physical distance	0.02 (0.02)	mm	6.70E-04 (9.12E-04)	1/pixel	1.34E-05 (1.82E-05)	
		δ_3 Image distortion by lens	4.11 (15)	pixel	8.97E-05 (4.65E-05)	mm/pixel^2	3.69E-04 (6.97E-04)	
		δ_4 Image distortion by CCD	0.0056 (0.0057)	pixel	8.97E-05 (4.65E-05)	mm/pixel^2	5.02E-07 (2.65E-07)	
		δ_5 Parallel board	0.5 (5)	mm	1.67E-04 (4.69E-05)	1/pixel	8.35E-05 (2.35E-04)	
		δ_6 Board position	0.035 (0.035)	rad	4.69E-03 (4.69E-05)	mm/pixel	1.64E-04 (1.64E-04)	
$\Delta\boldsymbol{X}$ (pixel)	Acquisition	δ_7 Laser power fluctuation	0.0070 (0.0071)	mm	0.13389 (0.0515)	pixel/mm	9.51E-04 (3.66E-04)	0.00568 (0.00571)
		δ_8 Image distortion by CCD	0.0056 (0.0057)	pixel	1 (1)		5.60E-03 (5.70E-03)	
		δ_9 Normal view angle	0.035 (0.035)	rad	4.69E-03 (4.69E-05)	mm/pixel	1.64E-04 (1.64E-06)	
	Processing	δ_{10} Mis-matching error	0.2 (0.2)	pixel	1 (1)		0.2 (0.2)	0.20224 (0.20224)
		δ_{11} Sub-pixel analysis	0.03 (0.03)	pixel	1 (1)		0.03 (0.03)	
Δt (s)	Acquisition	δ_{12} Delay generator	2.00E-09 (2.00E-09)	s	1 (1)		2.00E-09 (2.00E-09)	5.39E-09 (5.39E-09)
		δ_{13} Pulse time	5.00E-09 (5.00E-09)	s	1 (1)		5.00E-09 (5.00E-09)	
δu (mm/s)	Experiment	δ_{14} Particle trajectory	5 (5)	mm/s	1 (1)		0.05 (0.05)	5.0314 (5.3990)
		δ_{15} 3-D effects	0.577 (2.037)	mm/s	1 (1)		0.577 (2.037)	

Table 6.1: The combination of component errors for the C-PIV and SSE-PIV configurations. SSE-PIV figures are in brackets.

Parameter	Category	Error Sources	ε	unit	c_i	unit	$c_i\,\varepsilon$	unit
α		ε_α Magnification Factor	0.00041708 (0.000522)	mm/ pixel	3.63E-05 (4.00E-05)	pixel/s	1.52E+02 (2.09E+02)	mm/s
ΔX		$\varepsilon_{\Delta X}$ Image displacement	0.20791997 (0.2079492)	pixel	12.16 (11.71)	mm/pixel/s	2.53 (2.44)	mm/s
Δt		$\varepsilon_{\Delta t}$ Image interval	5.39E-09 (5.39E-09)	s	0.5355 (0.75)	mm/s^2	2.88E-09 (4.04E-09)	mm/s
δu		$\varepsilon_{\delta u}$ Experiment	5.0331 (5.3990)	mm/s	1 (1)	mm/s	5.0331 (5.3990)	mm/s
						$\varepsilon_u =$	1.52E+02 (2.09E+02)	mm/s

Table 6.2: Combination of component errors to determine ε_u for the C-PIV and SSE-PIV configurations. SSE-PIV figures are in brackets

Parameter	Category	Error Sources	δ_i	unit	c_i	unit	$c_i\,\delta_i$	unit
$\boldsymbol{X_s, X_e}$	Acquisition	δ_{16} Digital error	0.5 (0.5)	Pixel	0.13389 (0.0515)	mm/pixel	6.69E-02 (2.58E-02)	mm
		δ_{17} Non-uniformity of distribution	8 (8)	Pixel	0.13389 (0.0515)	mm/pixel	1.07 (0.412)	mm
$\boldsymbol{X_0}$	Calibration	δ_{18} Origin Correlation	2 (2)	Pixel	0.13389 (0.0515)	mm/pixel	0.268 (0.103)	mm
α		δ_{19} Magnification factor	0.00041708 (0.000522)	mm/ pixel	1024 (28.2)	pixel	0.427 (0.00147)	mm
						$\varepsilon_x =$	(1.190) (0.426)	mm

Table 6.3: Combination of component errors to determine ε_x for the C-PIV and SSE-PIV configurations. SSE-PIV figures are in brackets.

Parameter	Category	Error Sources	δ_i	(unit)	c_i	unit	$c_i\ \delta_i$	unit
t_s, t_e		δ_{12} Delay Generator	2.00E-09 (2.00E-09)	s	1 (1)	s	2.00E-09 (2.00E-09)	s
		δ_{13} Pulse Time	5.00E-09 (5.00E-09)	s	1 (1)	s	5.00E-09 (5.00E-09)	s
						ε_t =	5.39E-09 (5.39E-09)	s

Table 6.4: Combination of component errors to determine ε_t for the C-PIV and SSE-PIV configurations. SSE-PIV figures are in brackets.

6.3.6 Ranking of the error sources

Table 6.1 shows that the SSE-PIV system has a large amount of lens distortion. This was previously noticed in the raw images in chapter 3, section 3.5.2. The average uncertainty due to lens distortion is ±4.11 pixels and ±10 pixels for C-PIV and SSE-PIV respectively. These values correspond to a $\pm 3.69\text{x}10^{-4}$ and $\pm 4.65\text{x}10^{-4}$ mm/pixel uncertainty in calibration due to lens and optical distortion. Lens distortion is the largest source of uncertainty in the velocity measurement in this application of SSE-PIV.

The next largest sources of error in the C-PIV and SSE-PIV systems are due to the positioning of the calibration board. This includes the uncertainties of the parallel offset and the angular difference between the laser plane and the image plane. The uncertainty is calculated at $\pm 8.35\text{x}10^{-5}$ and $\pm 2.35\text{x}10^{-4}$ mm/pixel for C-PIV and SSE-PIV respectively. Although the endoscope has a factory set laser /camera position, a ±5 mm uncertainty in positioning still arises due to the machining tolerance of each lens mount. The combined uncertainty due to the individual error sources for calibration is $\pm 4.17\text{x}10^{-4}$ and $\pm 5.22\text{x}10^{-4}$ mm/pixel. Even though the SSE-PIV has an advantage with laser camera alignment and selection of reference points in the calibration, the effects due to lens distortion have a larger weight on the total calibration uncertainty.

The particle image displacement, $\Delta\boldsymbol{X}$, is affected by the laser intensity fluctuation, image distortion, image quality, and the image digital auto-correlation technique. The image displacement uncertainty due to the acquisition system, $\Delta\boldsymbol{X}$, is $\pm 5.68\text{x}10^{-3}$ and $\pm 5.71\text{x}10^{-4}$ pixels for C-PIV and SSE-PIV respectively. The largest sources of error for $\Delta\boldsymbol{X}$ are derived from mis-matching and sub-pixel analysis with a corresponding uncertainty of ±0.2 and ±0.03 pixels, respectively. By combining these error sources, the total seeding particle uncertainty for $\Delta\boldsymbol{X}$ is ±2.079 mm for both C-PIV and SSE-PIV.

The uncertainty with respect to Δt is due to the pulse timing and the delay generator. These uncertainties are determined by the laser hardware. The variation in Δt is evaluated as $\pm 5.39\text{x}10^{-9}$ seconds. Both C-PIV and SSE-PIV systems share the same laser and timing box hardware and therefore have the same variation in Δt.

The combined uncertainty for δu is based on incorporating out of plane particle motion and is evaluated as ±0.5767 mm/s and ±2.037 mm/s for C-PIV and SSE-PIV respectively. The out of plane motion affects the SSE-PIV system to a greater extent than the C-PIV system is due to its large perspective angle and short focal length. The barrel distortion effect on the SSE-PIV reduces the depth of field and thus causes more particles to be imaged out of plane.

6.3.7 Combined velocity measurement uncertainty

Table 6.1 describes the uncertainties of individual errors, δ_i, inherent in the C-PIV and SSE-PIV setups. Using equations 6.5 to 6.11, these uncertainties δ_i are combined with the sensitivity parameters, c_i, to obtain the measurement uncertainties of α, $\Delta \boldsymbol{X}$, Δt and δu, listed in table 6.2. The uncertainty values in the velocity in the streamwise direction $u(x,t)$ vector position x and time t listed in tables 6.2, 6.3, and 6.4 respectively

These combined uncertainty values for α, $\Delta \boldsymbol{X}$, Δt and δu are used to estimate the error in velocity measurement, ε_u, position, ε_x, and time, ε_t by equation 6.9 to equation 6.11 respectively. The ε_u, ε_x, and ε_t estimates for C-PIV and SSE-PIV are shown in tables 6.2, 6.3 and 6.4 respectively. It is can be seen from table 6.2 that the total uncertainty for ε_u is ±152 and ±209 mm/s for C-PIV and SSE-PIV respectively.

From table 6.3, the total uncertainty ε_x is ±1.190 mm for C-PIV and ±0.426 mm for SSE-PIV. The velocity vector position uncertainty is reduced in the case of SSE-PIV. The better resolution in the SSE-PIV image increases the identification of tracer particles and more accurately tracks them between frames. The greater tracer particle positional accuracy resulting from the lower magnification factor in the SSE-PIV is reflected in the ε_x estimate. The largest source of uncertainty contribution to ε_x in the C-PIV system is α, with an uncertainty of ±0.427 mm. In the SSE-PIV system, the velocity vector position uncertainty due to α is slightly lower, at ±0.426 mm.

The uncertainty in Δt, shown in table 6.4, is determined by the laser system and is comparatively small compared to the uncertainty in $\Delta \boldsymbol{X}$. It is important to note that the uncertainty in Δt does not include the effect of the selection of the pulse width between frames.

The errors ε_u, ε_x, and ε_t can be combined, as described in equation 6.22, to provide the total uncertainty inherent in the setup of the hardware and software of the PIV systems.

$$\sigma_u = \sqrt{\varepsilon_u^2 + (\varepsilon_x \partial u/\partial x)^2 + (\varepsilon_t \partial u/\partial t)^2} \qquad 6.22.$$

The combined total error, σ_u, at the maximum measured velocity is calculated at ±151.75 mm/s and ±209.19 mm/s for C-PIV and SSE-PIV respectively. This value for the SSE-PIV system is determined using the maximum distortion characteristics where r is maximum, at the boundary of the SSE-PIV field of view where r=28.2 mm. A plot of the mean velocity profiles fitted with the tolerances computed using equation 6.22 is shown in figure 6.5.

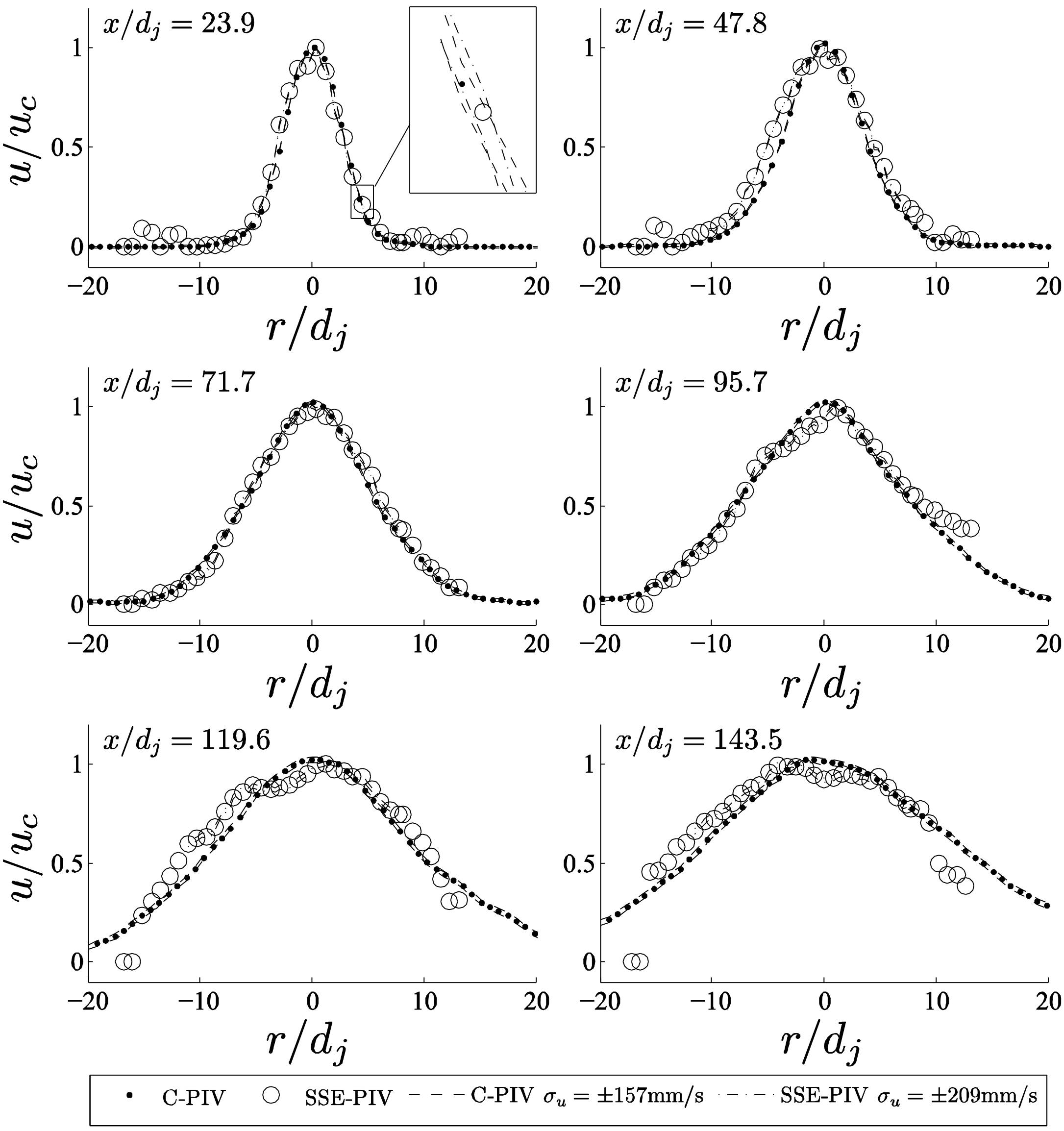

Figure 6.5: Normalised time averaged axial velocity profiles u/u_c along r over the range $23.9<x/d_j<145.5$ at $23.9d_j$ increments (symbols). 63% confidence interval bands from σ_u of equation 6.22 (lines).

As r/d_j tends towards zero the amount of distortion due to the lens curvature decreases. This is better appreciated from the graph in figure 6.6, where the variation of the normalised uncertainty of u/u_c with normalised radial distance shows a minimum of σ_u/u_e at r/d_j=0. The uncertainty band in the mean velocity profile of figure 6.6 is rather narrow with respect to the u/u_c variation with r/d_j. In figure 6.6, a significant change in the mean u/u_c is shown with x/d_j, which is greater than the uncertainty band σ_u.

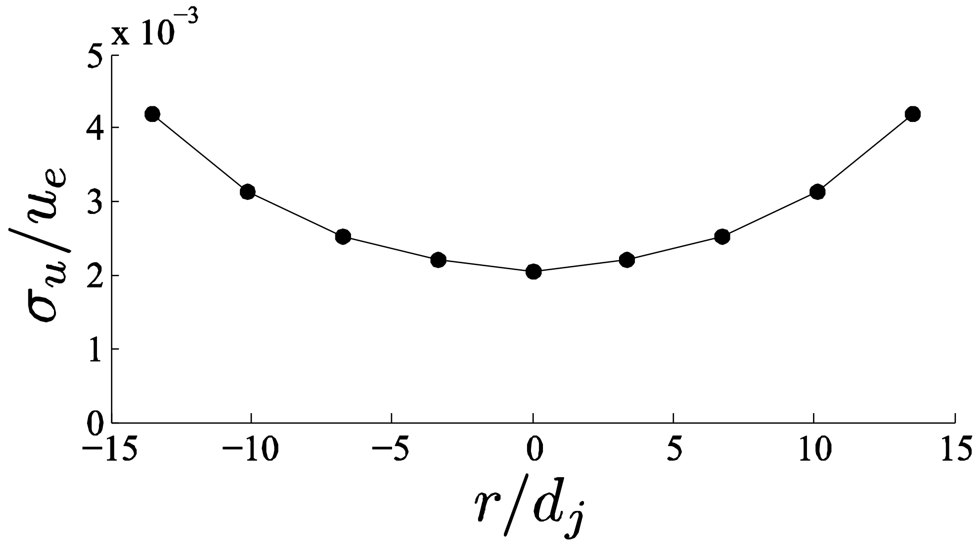

Figure 6.6: Variation of the uncertainty in the axial velocity profile with radial position *r* across the jet.

6.3.8 Illumination uncertainty

As mentioned previously, the curvature within the field of view affects the depth of field at which the camera is focused. As the curvature of the image increases, the out of focus effects are greater, causing out-of-focus particles, and also a reduction in illumination intensity.

The streamwise variation of the illumination intensity or pixel peak intensity of the SSE-PIV images is presented in figure 6.7. The pixel peak intensity is associated to the luminosity, that is, how bright the particle is in the flow. The CCD array instead returns the value of the contrast, which is a greyscale value between 0 and 255. At 255 the level of luminosity saturates the CCD array, and 1 is the lowest luminosity level detectable by the CCD array. Figure 6.7 shows the instantaneous image intensity on the left, in figure 6.7 *(a)*, *(c)*, *(e)*, *(g)*, *(i)* and *(k)*, and ensemble mean pixel intensity on the right, in figure 6.7 *(b)*, *(d)*, *(f)*, *(h)*, *(j)* and *(l)*. The illumination intensity has a clear reduction as the distance increases from the centre of the image to the image perimeter.

As mentioned in section 5.2, the illumination delivered by the endoscope became an issue as the streamwise location increased. The laser was set to its maximum energy output for all SSE-PIV measurements. One of the problems with laser delivery via optical fibre optic cables is a severe loss in laser intensity for illumination through the optics. It is evident from figure 6.7 that as the x/d_j increases the general image peak intensity decreases. This is due to the spray becoming sparse and thus reducing the amount of reflecting droplets. In an ideal image, one would expect the mean image pixel peak intensity to be constant throughout the image. It is interesting that this is not the case within the SSE-PIV. As x/d_j increases, the lack of illumination is more apparent. This is also shown in figure 6.7 *(h)*, (*j)* and *(l)* that the image pixel peak intensity is higher as r/d_j tends towards zero. This is not due to alignment but simply to how the laser sheet is formed by the endoscopic optics. The reason for the pixel peak intensity drop off as r increases in the streamwise location is most probably due to the Gaussian shape of the beam profile before it is converted into a sheet. The endoscope has no optics to even out the laser intensity at its axis centre than at its diverging edge. The lack of an even illumination of the SSE-PIV field of view clearly has an effect on the uncertainty of the velocity vectors predicted off the image central axis.

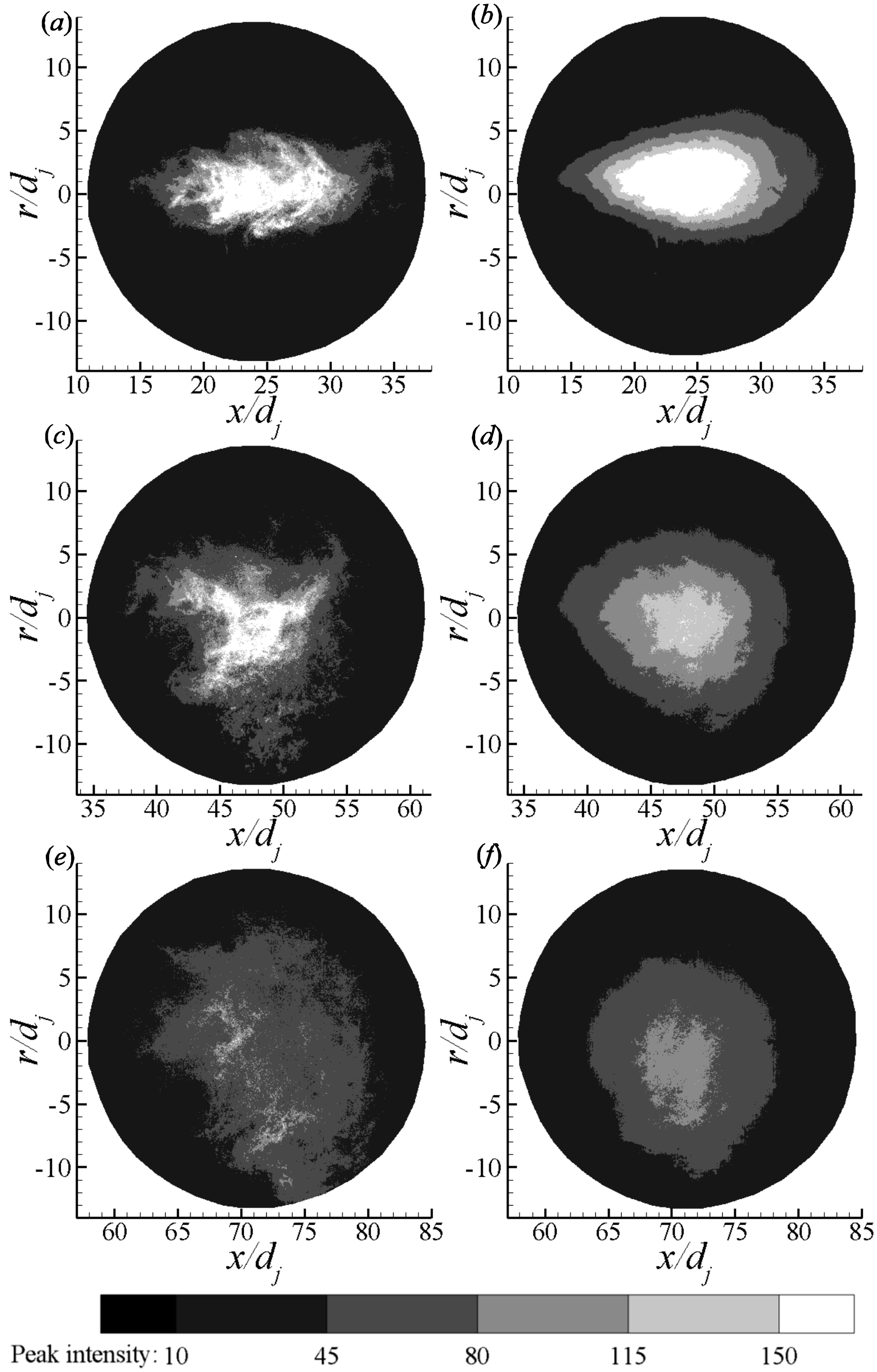

(a)
(b)
(c)
(d)
(e)
(f)
r/d_j
x/d_j
10
5
0
-5
-10
10 15 20 25 30 35
35 40 45 50 55 60
60 65 70 75 80 85
Peak intensity: 10 45 80 115 150

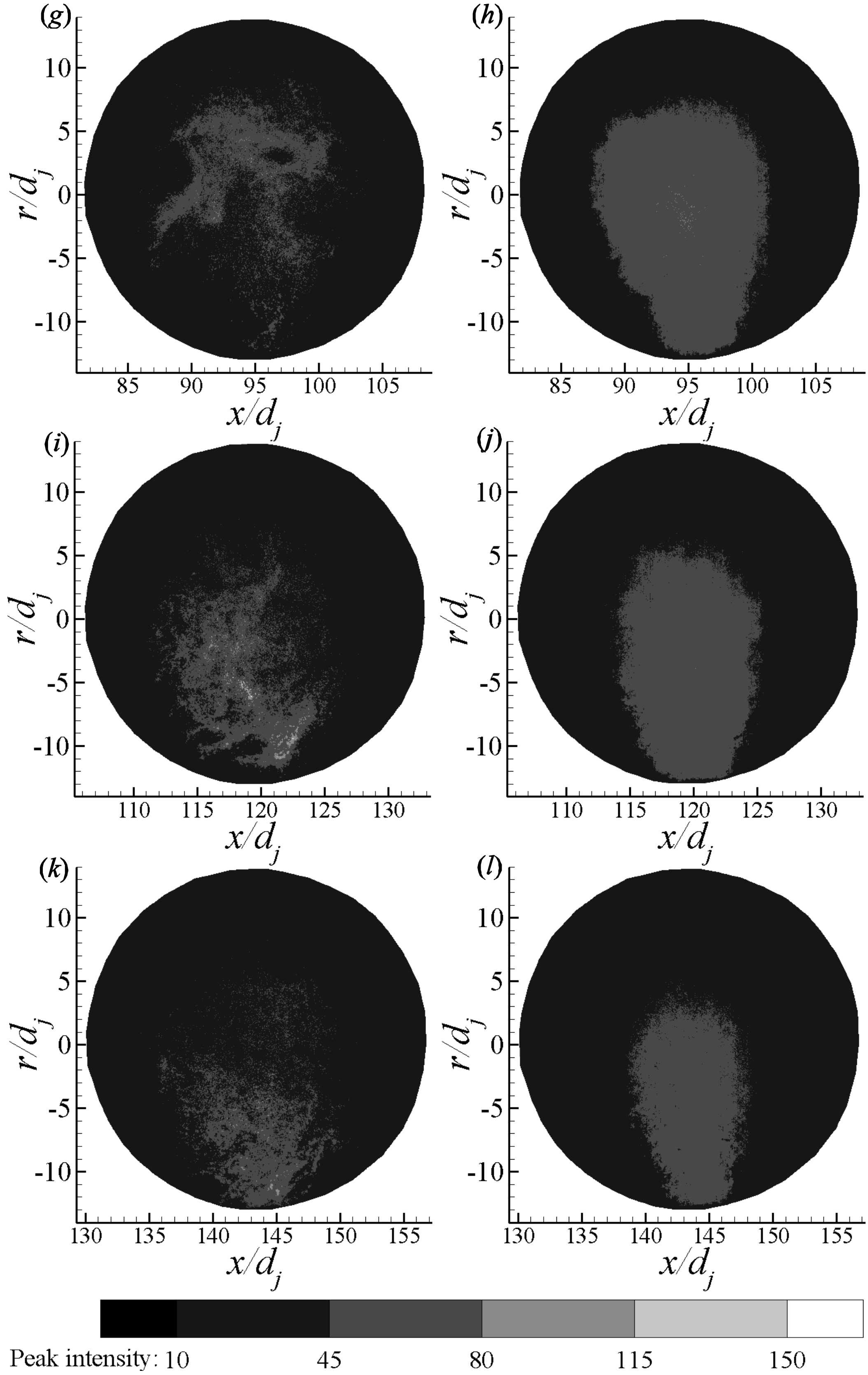

Figure 6.7: SSE-PIV contours of instantaneous image pixel peak intensity *(a), (c), (e), (g), (i), (k),* and ensemble mean image pixel peak intensity, *(b), (d), (g), (h), (j), (l),* over the range 10< x/d_j <158. The level 255 is the recorded luminosity that saturates the CCD array, and 1 is the lowest luminosity level detectable by the CCD array.

6.4 Assessment of the intruded flow field

In sections 6.1 and 6.2 the amount of uncertainty within SSE-PIV has been analysed using the hardware setup and image pre- and post-processing. Within this section the author has extended the investigation to determine if the intrusive action of inserting an endoscope into a spray will have an effect on the spray flow within the region of the viewing window. By doing so, this study separates the measurement error in SSE-PIV associated with intrusion from the measurement uncertainty associated with the hardware and software.

It is important to note that a full characterisation of the changes in the spray flow field due to the presence of the SSE-PIV endoscope is not performed, but the analysis is limited to whether any significant change occurs in the field of view of the SSE-PIV endoscope field of view only. This is simply because, characterising such a flow system is very difficult. The probe cylindrical body is placed within the spray off axis, at a 45°, and is also of finite length. To fully resolve the three-dimensional flow past the cylinder including the surface boundary layer and the end effects at the shaft tip will require more resources and a large amount of time. Therefore this study is limited to addressing the effect of the cylinder on the flow at the viewing window of the SSE-PIV endoscope.

The setup of the test is as per chapter 4 section 4.4.3. Two back to back tests are performed without and with the cylindrical probe model in place. The axial position of the probe is placed over the range $23.9<x/d_j<167.5$ at $23.9d_j$ increments. Each incremental position is labelled by the letters *(b)* through to *(h)*. The label *(a)* refers to the un-intruded spray, which is the spray without the cylindrical probe, and is used for all tests with probe as the benchmark result for comparison purposes. Velocity vector measurements are obtained using C-PIV along the x-y plane at z=0. The PIV measurements have the same field of view as the setup in chapter 4, section 4.4.1.

Figure 6.8 shows the mean streamwise velocity contours, u, normalised by the jet exit velocity, u_e over the range $20<x/d_j<100$ and $-15<r/d_j<15$. The contours in figure 6.8 *(b-e)* show no appreciable change in the spray flow field when compared to figure 6.8 *(a)*.

Figure 6.9 presents u/u_e over the range $80<x/d_j<170$ and $-25<r/d_j<25$. The mean velocity contours of figure 6.9 *(f-h)* again show no appreciable change in the spray flow field when compared to figure 6.9 *(a)*, even as the jet width increases and starts to impinge directly onto the cylinder.

Studies have been performed by Aroussi *et al*. (2010), Lad *et al*. (2011c) and Lad *et al*. (2010) on the interaction of a cold atomised spray onto a 10 mm circular cylinder which represents an endoscopic probe. All the research carried out used a probe which was arranged at 250 mm from the spray nozzle and was placed directly on the spray centreline axis. The studies showed time average statistics of the near wake flow field due to the spray-structure impingement.

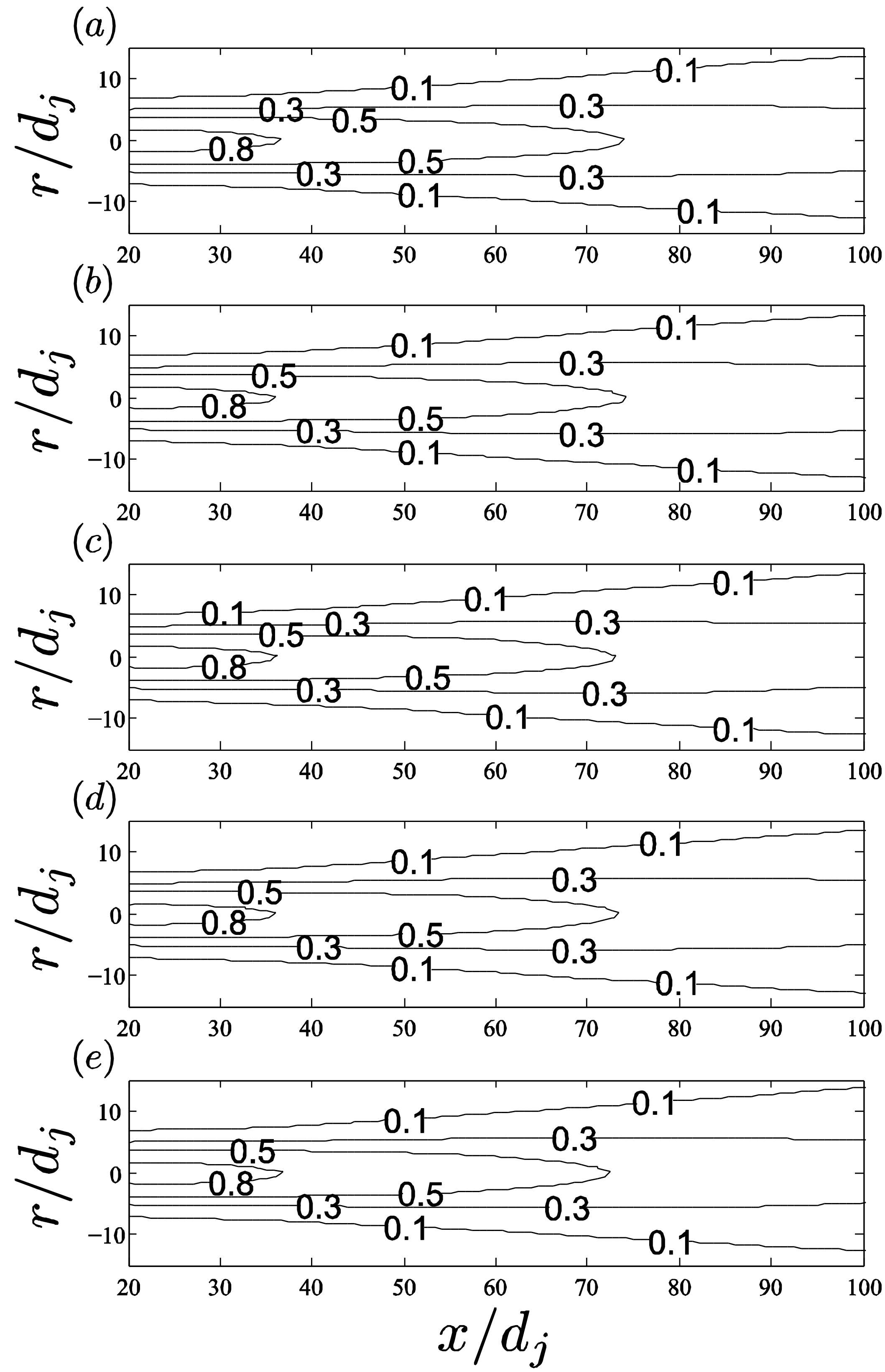

Figure 6.8: C-PIV Contours of u/u_e over the range $20<x/d_j<100$ and $-15<r/d_j<15$. *(a)* without cylindrical probe, *(b-e)* with cylindrical probe.

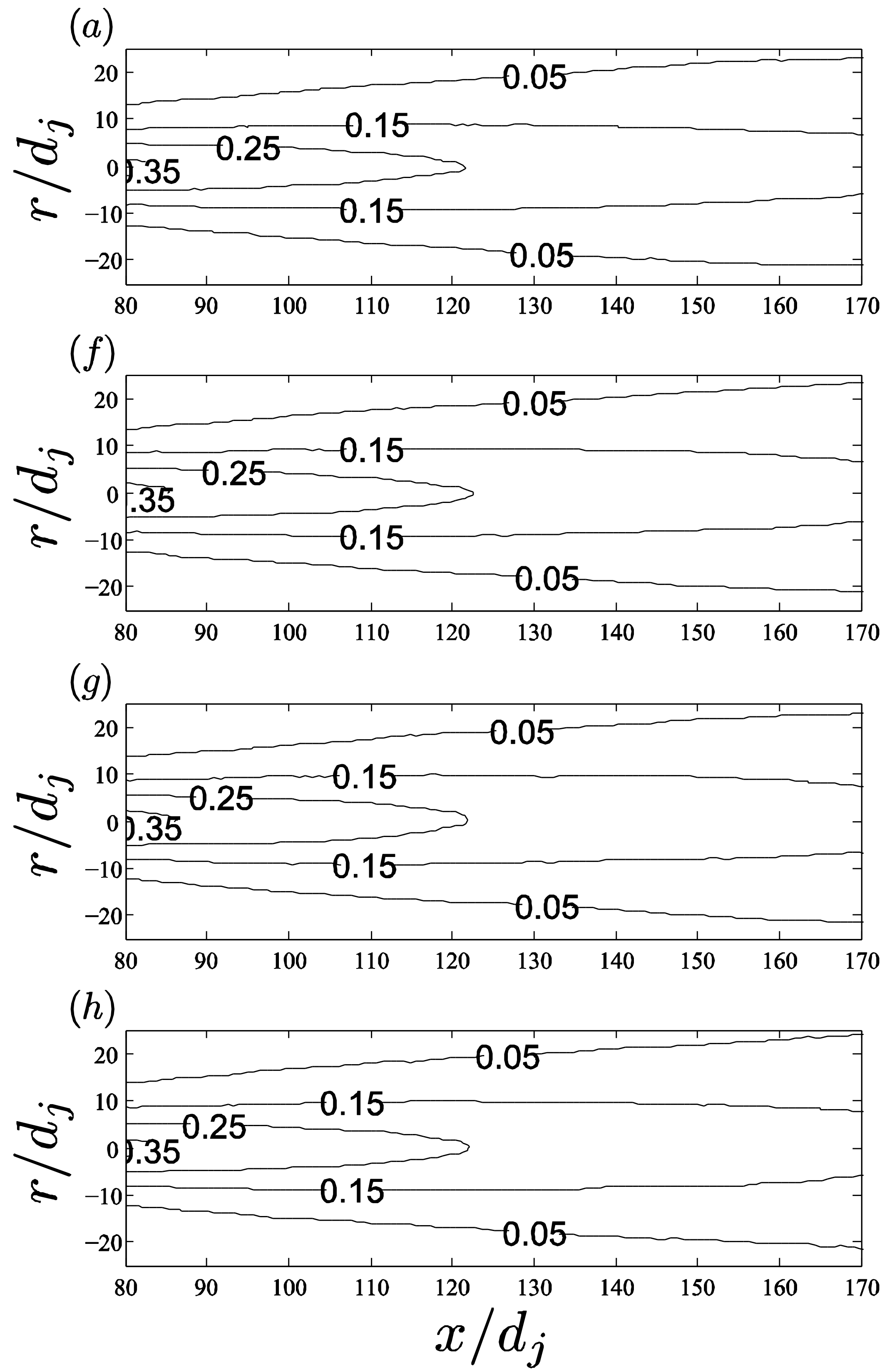

Figure 6.9: C-PIV contours of u/u_e over the range $80<x/d_j<170$ and $-25<r/d_j<25$. *(a)* without cylindrical probe, *(f-h)* with cylindrical probe.

To estimate the error in the SSE-PIV measurements due to the intrusiveness of the endoscopic probe one must first determine the uncertainty of the C-PIV measurements. By doing so, any flow feature which extends beyond the measurement uncertainty can be attributed to the presence of the cylindrical probe.

The C-PIV uncertainty is computed by finding the standard deviation of the C-PIV measurements. This quantifies statistically the difference between the instantaneous C-PIV measurement and the C-PIV measurement ensemble mean, taken at the same flow condition, for instance, without probe. In this analysis, the spray is assumed statistically stationary, which is a condition commonly referred to as that of turbulent, steady flow. The standard deviation is computed using equation 6.23.

$$\sigma_u = \sqrt{\frac{1}{n-1}\sum_{i=1}^{n}(u_i' - u)^2} \qquad 6.23.$$

where n is the number of C-PIV vector maps, taken at constant geometry and flow conditions, which in this test is 600, u_i' is the instantaneous contour map of the streamwise velocity and u is the ensemble mean velocity contour map. The normalised axial velocity standard deviation contours in the spray meridional plane are shown in figure 6.10 and 6.11. Figure 6.10 displays σ_u over the range $20<x/d_j<100$, which is the same field of view as in figure 6.8. Figure 6.11 displays σ_u over the range $80<x/d_j<170$, which is the same field of view as figure 6.9. The contours of σ_u are normalized by $\sqrt{n}$ and u_e and are amplified by a factor of 1000. The normalisation by $\sqrt{n}$ allows to re-interpret σ_u as the 68% confidence interval band of the ensemble averaged normalised velocity distributions of figure 6.8 and figure 6.9. This information is used in figure 6.12 and figure 6.13 to determine whether any difference between the velocity field with and without the SSE-PIV model probe is statistically significant.

The maximum $\sigma_u/u_e\sqrt{n}$ shown in the figure 6.10 is $1.5\text{x}10^{-3}$ at $x/d_j=20$ on the spray axis. The amount of measurement uncertainty reduces to $1\text{x}10^{-3}$ as x/d_j increases. The measurement uncertainty also rapidly decreases as r/d_j increases and $\sigma_u/u_e\sqrt{n} \approx 0.5\text{x}10^{-3}$ in the spray shear layer. One would expect the uncertainty in the shear layer to be higher than the uncertainty seen at the spray centreline. One possible reason to this may be attributed to the spray shear layer having a low seeding concentration. This has been described in section 6.3.5 previously as the visible spray *r* being only 80% of the actual spray *r*, and therefore the mixing region of the spray is not properly resolved. Figure 6.11 shows a trend that supports this influence.

The maximum deviation reported in figure 6.11 is 0.9×10^{-3}, which occurs at x/d_j<100 along the jet axis. $\sigma_u/u_e\sqrt{n}$ reduces to 0.7×10^{-3} over the range 100<x/d_j<150 and 0.5×10^{-3} at x/d_j>150.

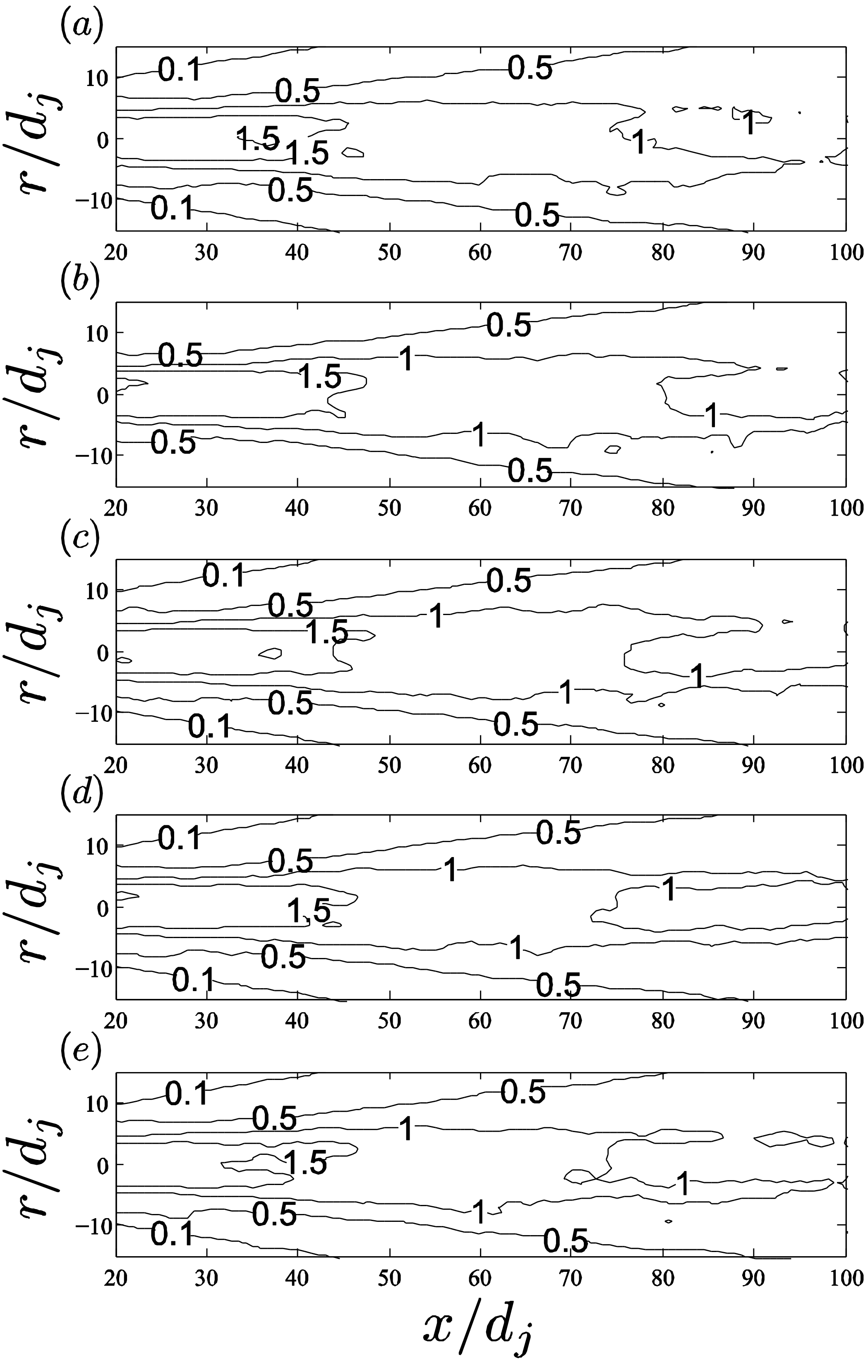

Figure 6.10: C-PIV contours of $(\sigma_u/u_e\sqrt{n}) \times 10^{-3}$ over the range 20<x/d_j<100 and -15<r/d_j<15. *(a)* spray without SSE-PIV model probe, *(b-e)* spray with model probe.

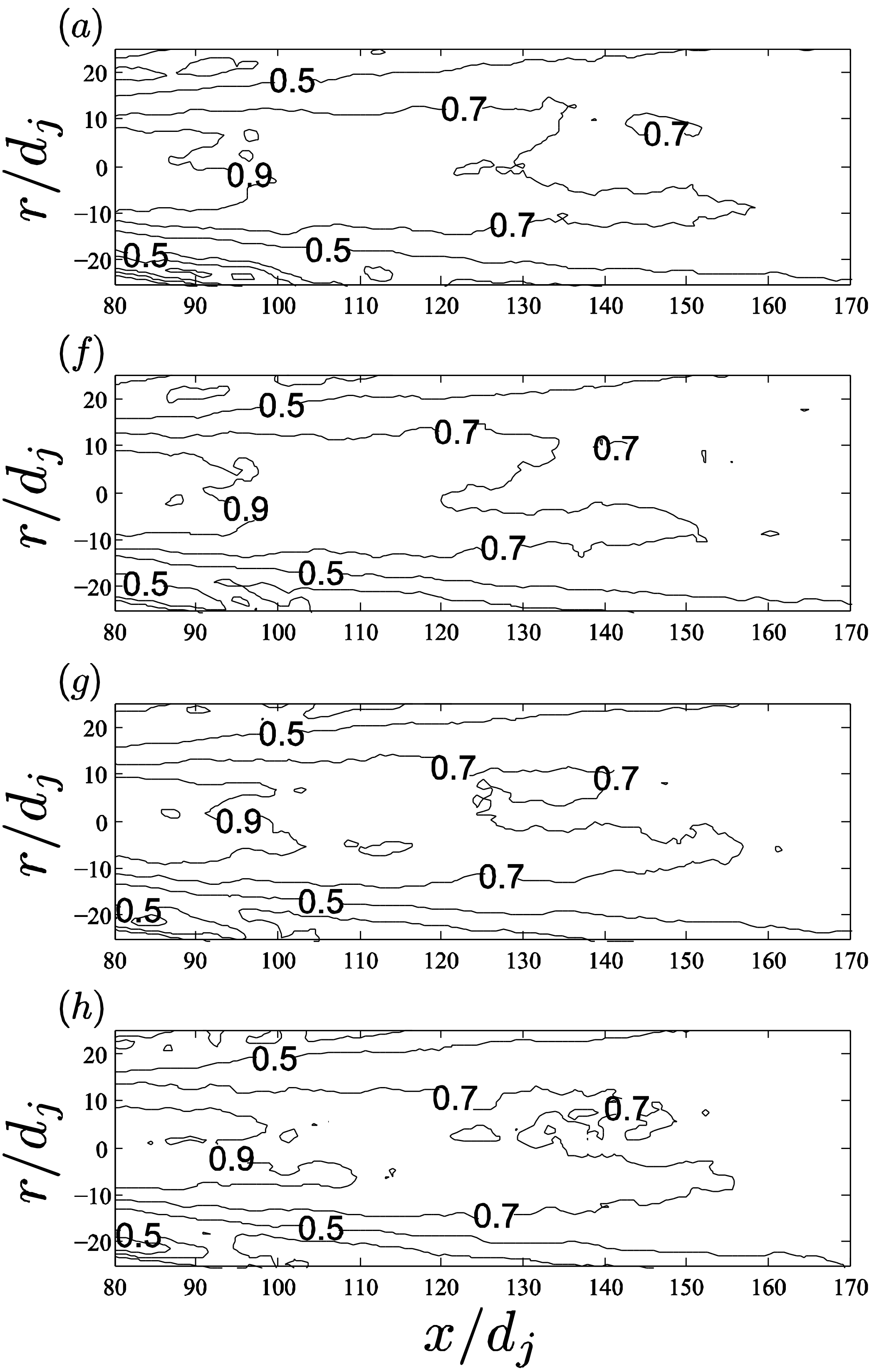

Figure 6.11: C-PIV of $(\sigma_u/u_e\sqrt{n}) \times 10^{-3}$ over the range $80<x/d_j<170$ and $-25<r/d_j<25$. *(a)* spray without SSE-PIV model probe, *(f-h)* spray with model probe.

Figure 6.13 shows the results of subtracting the normalised mean axial velocity measurements of figures 6.8 *(b-e)* from the mean axial velocity measurements of figure 6.8 *(a)*. Similarly, figure 6.13 shows the difference in the normalised axial velocity of figure 6.9 *(f-h)* from the measurement of figure 6.9 *(a).* The subtraction provides a contour plot of the variance between the two flow fields termed δu. This difference aims to show the effect of the presence of the model SSE-PIV probe on the mean velocity field as measured by C-PIV. In ideal conditions, the δu between flow fields is zero, suggesting no probe interference effect is present in the measurements. However, experimentally, some measurement uncertainty exists as shown previously in figure 6.10 and 6.11. It is argued that if $\delta u/u_e > \sigma_u/u_e\sqrt{n}$, then the C-PIV measurements indicate a probe intrusive effect greater than that of the measurement uncertainty. This would conclude that the intrusion has a negative effect on SSE-PIV measurement by affecting the flow velocity at the SSE-PIV measurement plane.

Figure 6.12 shows the contour maps of $\delta u/u_e$ over the range $10<x/d_j<100$ and $-15<r/d_j<15$. Similarly Figure 6.13 over the range $80<x/d_j<170$ and $-25<r/d_j<25$. Figure 6.12 *(b)* shows the maximum $\delta u/u_e$ to be $\pm 0.25\text{x}10^{-3}$ which is located at $x/d_j \approx 40$ along the spray axis. The axial location of this error is $\approx 20d_j$ away from the model probe position and this $\delta u/u_e$ value is only ≈17% of $\sigma_u/u_e\sqrt{n}$ at the same position in the meridional plane in figure 6.8 *(b).* At x/d_j =60 and 85, $\delta u/u_e$ is ±0.15. This is ≈15% of $\sigma_u/u_e\sqrt{n}$ at the same position in the meridional plane in figure 6.8 *(b)*. Figure 6.12 *(c)* to *(e)* also show lower $\delta u/u_e$ than the corresponding values of $\sigma_u/u_e\sqrt{n}$. The contours show $\delta u/u_e$ is random in nature and does not show any specific trend that can be associated to intrusion due to the probe.

The same trend is also observed from figure 6.13. In figure 6.13 *(f)*, the maximum $\delta u/u_e$ is $0.25\text{x}10^{-3}$ which is approximately 35% of the $\sigma_u/u_e\sqrt{n}$ computed at the same location on the meridional plane in figure 6.9 *(f)*. This relative increase in $\delta u/u_e$ with the streamwise direction is due to the increase in $\sigma_u/u_e\sqrt{n}$ as x/d_j increases. Similar results are obtained in figure 6.13 *(g)* and *(h)*.

This suggests that, in this application of the SSE-PIV endoscope, the probe influence effect on the measured axial velocity at the measurement plane is smaller than the measurement uncertainty. It can be seen from figure 6.12 and 6.13 that, as the measurement uncertainty reduces, the $\delta u/u_e$ value becomes larger. By reducing the measurement uncertainty further, the intrusive effect due to the SSE-PIV model probe may become significant. However, the measurement uncertainty used in this study, as a reference, to determine the significance of the SSE-PIV probe intrusiveness are representative of the measurement uncertainty used in conventional particle image velocimetry applications. It is therefore argued that, by a proper design of experiment, a SSE-PIV endoscope can provide useful velocity measurements that have an acceptably low error due to the intrusiveness of the probe in a free spray.

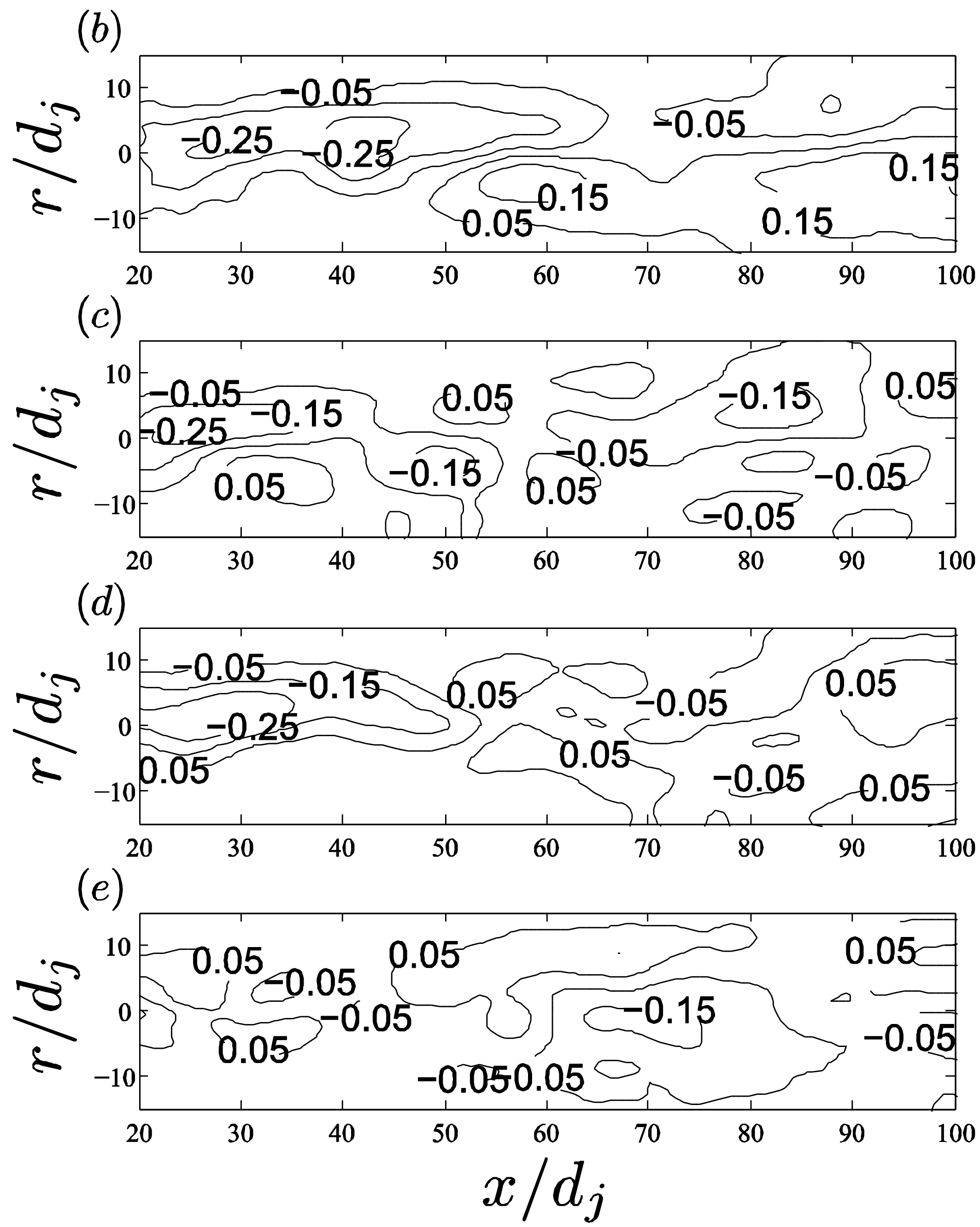

Figure 6.12: C-PIV contours of $(\delta u/u_e) \times 10^{-3}$ over the range 20<x/d_j<100 and -15<r/d_j<15.

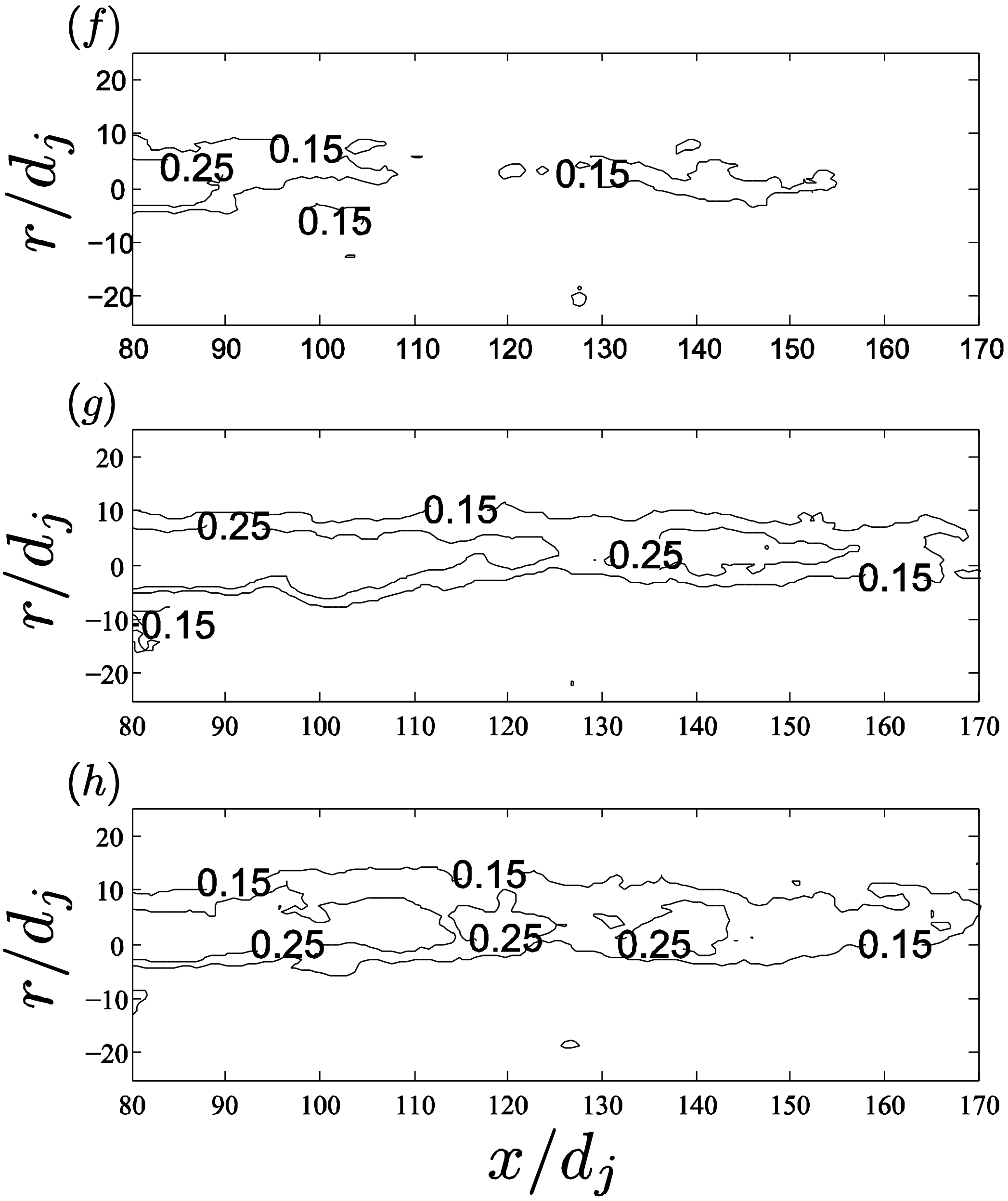

Figure 6.13: C-PIV contours of $(\delta u/u_e) \times 10^{-3}$ over the range 80<x/d_j<170 and -25<r/d_j<25.

6.5 Summary

In this chapter, the uncertainty sources inherent within the SSE-PIV system has been identified and quantified. The largest sources of uncertainty are primarily due to two components. The first component is the main source of uncertainty in SSE-PIV, which is the illumination of the image. The second component is the optical aberration, which leads to image defocusing and a reduction in particle identification. An additional uncertainty factor may arise due to the endoscope intruding the flow. However, within this study, it was found that the amount of intrusion uncertainty was lower than the overall measurement uncertainty of the spray.

CHAPTER 7: CONCLUSIONS & FUTURE WORK

7.1 Conclusions

This research gave a systematic metrological assessment of a single-stem endoscopic PIV system applied to an atomised turbulent free jet. The SSE-PIV measurements were benchmarked against conventional PIV and Pitot anemometry. The comparison among the measurements was supported by a systematic measurement uncertainty estimate.

From the results presented in chapter 5 and chapter 6, successful areas and areas for improvement in the current single-stem endoscopic PIV system are identified.

1) This is the first assessment of the single-stem endoscopic PIV system within an industrial flow system which in this case (test case 1) is a turbulent free spray which represents diesel spray applications.

2) The SSE-PIV data provides results comparable to the ones from conventional PIV and Pitot anemometry in a free spray. With the development areas identified from this study the use of the SSE-PIV can be extended to test cases 1-4 identified within the context in section 1.1.

3) The smaller field of view of the SSE-PIV reduces the velocity range in the image and makes it easier to select an optimum Δt between laser pulses.

4) The use of a fixed laser and camera position in SSE-PIV allows an easy setup that requires no focusing. The position of the laser is determined by the position of the probe. Likewise, the position of the CCD camera is determined by the position of the probe. This fixes the SSE-PIV magnification coefficient and removes the requirement for using a calibration board in the test set-up procedure.

5) The parallel studies identified a laser illumination plane and image capture position to reduce the amount of disturbance the probe has on the flow within the measurement field of view. The amount of intrusion by the probe on the flow experienced within this test case can be reduced below the measurement noise threshold by a judicious placement of the SSE-PIV probe. The effect of the intrusiveness.

6) The design of the optics and lenses within the shaft of the endoscope provide a clear field of view that is accurately focused onto the illuminating laser sheet. However, only 3/4*r* of the field of view is usable in SSE-PIV, due to optical distortion effects. The effects of the distortion are also observed along the minimum and maximum axial regions on the horizontal central axis of the image.

7) The SSE-PIV image optics cause barrel distortion across the field of view. It was noticed that this effect causes tracer particles close to the outer perimeter of the field of view to be distorted and become out of focus. If the particles are densely populated within this region, particle mismatching is almost certain. The optical configuration of the lenses within the endoscope probe needs to be addressed to greatly reduce the observed barrel distortion. This will then reduce particle mismatching at increasing *r* within the image and also increase the accuracy of data within field of view allowing more of the data within the field of view to be used.

8) The largest source of uncertainty in the SSE-PIV measurements is due to the uneven illumination of the field of view, with noticeable degradation at the field of view perimeter. The illumination balance is also biased to region closest to the source. These effects are primarily due to the transmission losses of laser energy within fibre optic cables and coupling devices. Development of the illumination transport and sheet optics must be carried out in the next generation SSE-PIV system. The need for an evenly distributed laser light across the field of view is necessary for more of the field of view to be used. The intensity of the

illumination must also be greatly increased to account for the intensity reduction in the out of focused areas.

9) This study has validated the use of a single-stem endoscopic PIV system in test case 1, a free spray, so that the system can be used in similar industrial flows, outside the laboratory environment.

7.2 Future recommendations

The research carried out within this thesis has identified areas for improvement, as outlined in section 7.1, for the next generation single-stem endoscopic PIV system. The work is carried out in this study is part of an iterative process to assist in developing the SSE-PIV. The testing of the SSE-PIV system within other test cases (1-3) will commence after the successful integration of the elements outlined for development within this study. Further work should include:

1) Introduce an optical image correction in the SSE-PIV image acquisition sub-system to reduce the amount of distortion observed at increasing r within the field of view, thus leading to more in focus particles and a larger usable field of view. This would also reduce the uncertainty due to particle mismatching;

2) Improve laser delivery via fibre optic cables to illuminate the entire image plane evenly with no drop-off at the image edge this would create an improvement of the identification of individual particles especially within the out of focused areas;

3) After addressing points 1) and 2) the SSE-PIV system can be applied to test case 2 as outlined within the context. This is the quantification of the SSE-PIV data taken within an annular flow regime which represents flows which appear in areas such as bearing chambers and turbomachinery. These flows are re-circulating and disturbances caused downstream of the probe will appear upstream thus leading to uncertainty in the data capture. The development and

application of the universal passive control techniques outlined within the studies identified in chapter 1 will need to be carried out;

4) Test the SSE-PIV system in test cases 3 and 4 in both cases provided a detailed analysis of the data and thus highlighting the areas of further development. By doing this the SSE-PIV system will be a marketable product which can claim usability in many industrial style flow applications.

APPENDIX A

Homogeneous flow calculations

The Pitot-static tube measures the dynamic pressure of the jet flow. The dynamic pressure can be converted into the mixture mean velocity within a multiphase jet if the mass fractions of the liquid phase and of the air phase are known. Within this study, the liquid phase is premixed with air upstream of the nozzle as water is atomised upon ejection.

The mass flow rate of each phase was calculated experimentally. For the purpose of calculations of the air mass flow rate, integration was performed on velocity profiles at increasing streamwise locations obtained by the means of Pitot-Static data, equation A.1

$$\dot{m}_g = 2\pi\rho_g \int_{r=o}^{r=r} u_{(r)} r.\, dr \qquad \text{A.1.}$$

The mass flow rate of air increases along the streamwise position due to the entrainment of laboratory air. The mass flow rate of the water is calculated by the change in volume (ΔV) in the water reservoir over a period of time (t), $\dot{m}_l = \rho_l(\Delta V/t)$. $\dot{m}_l$ is unchanged as the jet flow progresses.

The total mass flux of the jet at a point is the total mass flow rate of both gas and liquid phases within a cross section at that point. The mass flux is calculated from equations A.2 and A.3 where subscripts g and l represent gas and liquid states, A is the cross sectional area and $\dot{m}$ is the mass flow rate (kg/s).

$$G = \text{Total mass flux (kg/m}^2\text{)} = \frac{\dot{m}_g + \dot{m}_l}{A} \qquad \text{A.2.}$$

$$G_g = \frac{\dot{m}_g}{A} \quad , \quad G_l = \frac{\dot{m}_l}{A} \qquad \text{A.3.}$$

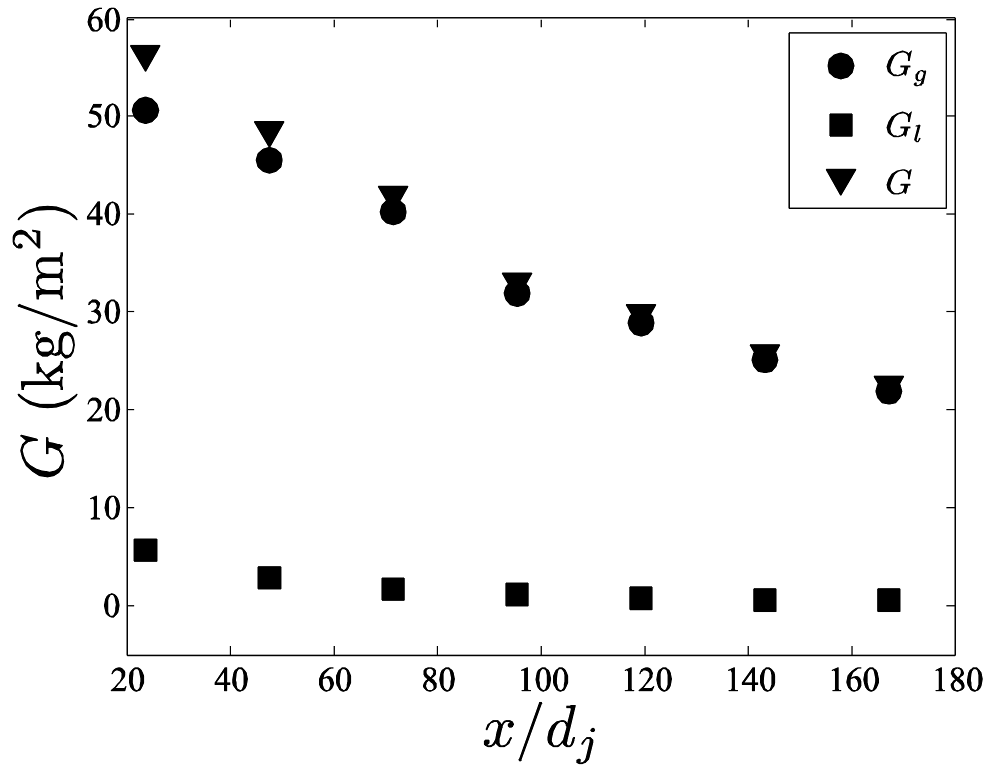

Figure A.1: Mass flux with respect to jet axial position noramised by the spray exit diameter.

Figure A.1 shows the streamwise variation of the measured mass flux of the jet at various axial positions. These results were obtained following the procedure in section 5.3. As water is added to the jet at the nozzle, the mass water mass flow rate is essentially constant. As the jet cross-sectional area grows in the streamwise direction, the water phase mass flux reduces in the streamwise direction. The jet entrains the laboratory air as it expands. This causes an increase in air mass flow rate with streamwise direction. As the jet cross-sectional area grows, the net effect is a reduction in mass flux with streamwise direction. Figure A.1 shows that the mass flux of the liquid phase is considerably lower than the gas phase and therefore gives a smaller contribution to the total mass flux of the jet.

Using the mass flux information the mass dryness fraction (ζ) can be calculated using equation A.4. The streamwise variation of the mass dryness fraction with streamwise distance is shown in figure A.2. It is evident that that at $x/d_j \approx 23$ and $\zeta \approx 0.9$. This value rises hyperbolically and asymptotes to an almost constant value $x/d_j \approx 140$. This means that at $x/d_j > 140$, the contribution by the liquid phase to the jet mass flux becomes negligible.

$$\zeta = \frac{G_g}{G} \tag{A.4.}$$

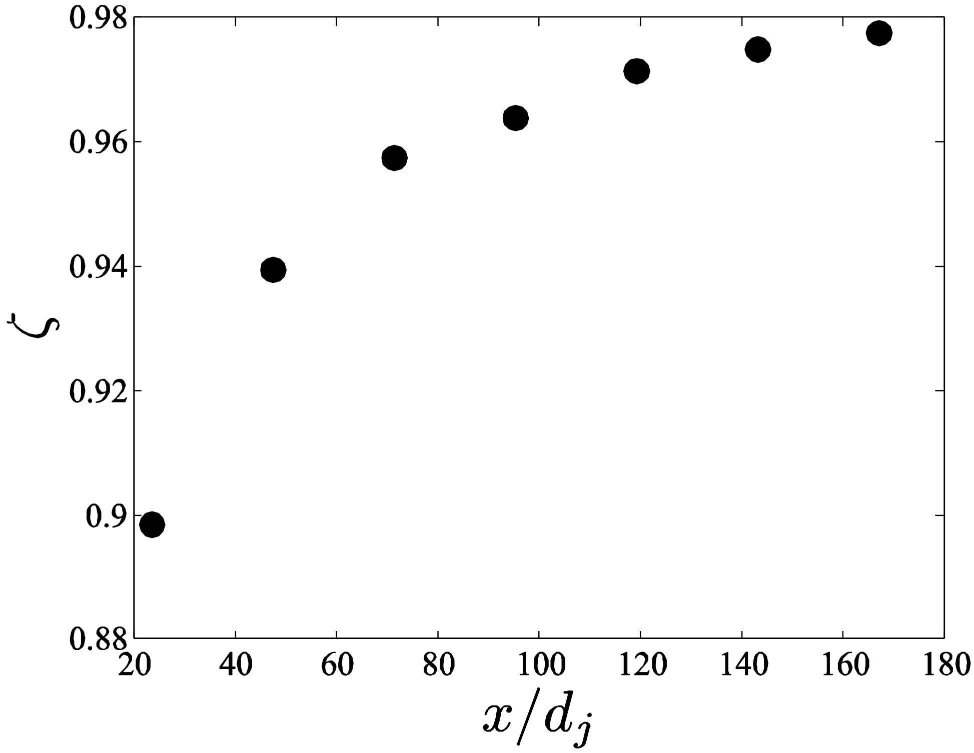

Figure A.2: Mass dryness fraction with respect to jet axial distance normalised by the spray exit diameter.

The superficial velocity (V) is the velocity of each phase as if it were flowing as a single phase. This value is determined by equation A.5 and the data is plotted in figure A.3.

$$V_g = \frac{G_g}{\rho_g} \quad , \quad V_l = \frac{G_l}{\rho_l} \tag{A.5.}$$

Figure A.3 shows the superficial gas velocity of the gas and liquid phases of the jet. It is clear that the liquid has very little superficial velocity of its own even at the nozzle end. The jet characteristics are entirely dependent by the air phase and thus one can assume that the liquid is evenly dispersed and entrained within the jet and the two phases act as a single homogeneous fluid.

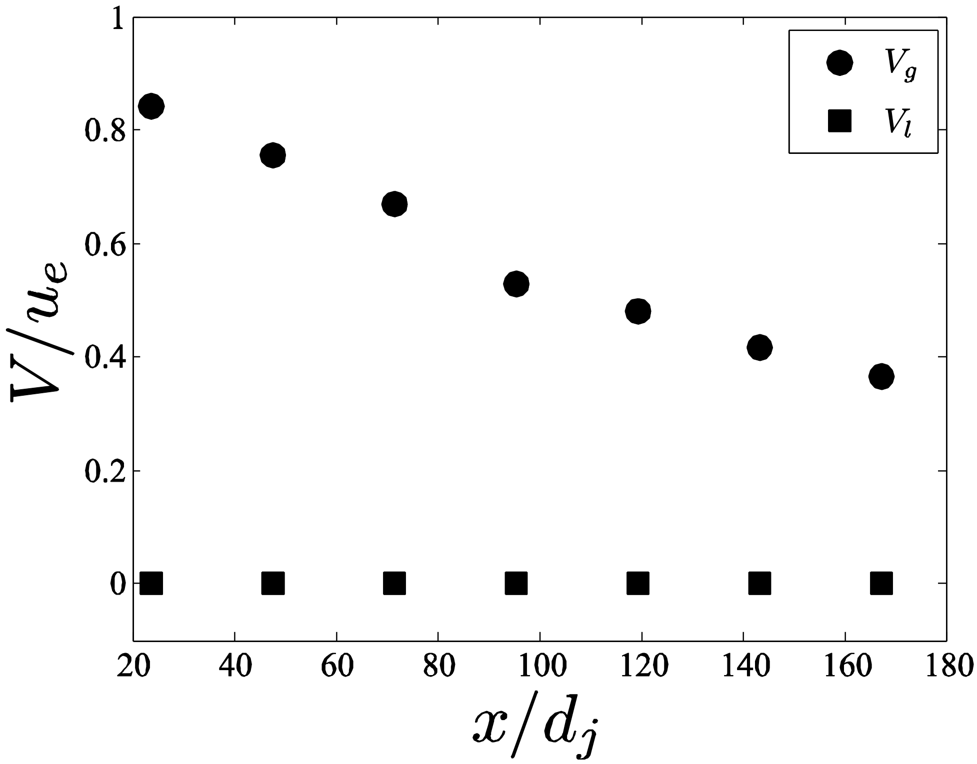

Figure A.3: Superficial velocity with respect to jet axial distance normalised by spray exit diameter.

The jet is therefore characterized by an air flow, which is the dominant phase, in which the water, the secondary phase, is evenly dispersed, to create a homogeneous mixture. Using the homogeneous flow model, a common density and viscosity can be calculated.

The void fraction (β) is the time averaged fraction of cross-sectional area. This is the volume which is occupied by gas it can be found using equation A.6, where A_g is the time averaged cross sectional area occupied by gas.

$$\beta = \frac{A_g}{A} \tag{A.6.}$$

Equation A.6 defines void fraction in its simplest terms. However, within a jet, it is difficult to measure the portion of the jet cross-sectional area occupied by gas. So by using the equation of continuity, equation A.7, the homogeneous void fraction can be derived.

$$\dot{m}_g = AG_g = AGx = \rho_g u_g A_g = \rho_g u_g \beta A \qquad \text{A.7.}$$

$$\dot{m}_l = AG_l = AG(\zeta - 1) = \rho_l u_l A_l = \rho_l u_l (\beta - 1)A \qquad \text{A.8.}$$

$$\beta = \frac{1}{1 + \left[\frac{u_g}{u_l} \cdot \frac{1-\zeta}{\zeta} \cdot \frac{\rho_g}{\rho_l}\right]} \qquad \text{A.9.}$$

Within a homogeneous flow model, it is assumed u_g = u_l, so, equation A.7 becomes equation A.8 and equation A.9. The data is plotted on figure A.4. The void fraction increases due to the constant mass flow rate of liquid phase and the increasing jet diameter and mass flow rate of the gas phase due to entrainment.

$$\beta_{mix} = \frac{1}{1 + \left[\frac{1-\zeta}{\zeta} \cdot \frac{\rho_g}{\rho_l}\right]} \qquad \text{A.10.}$$

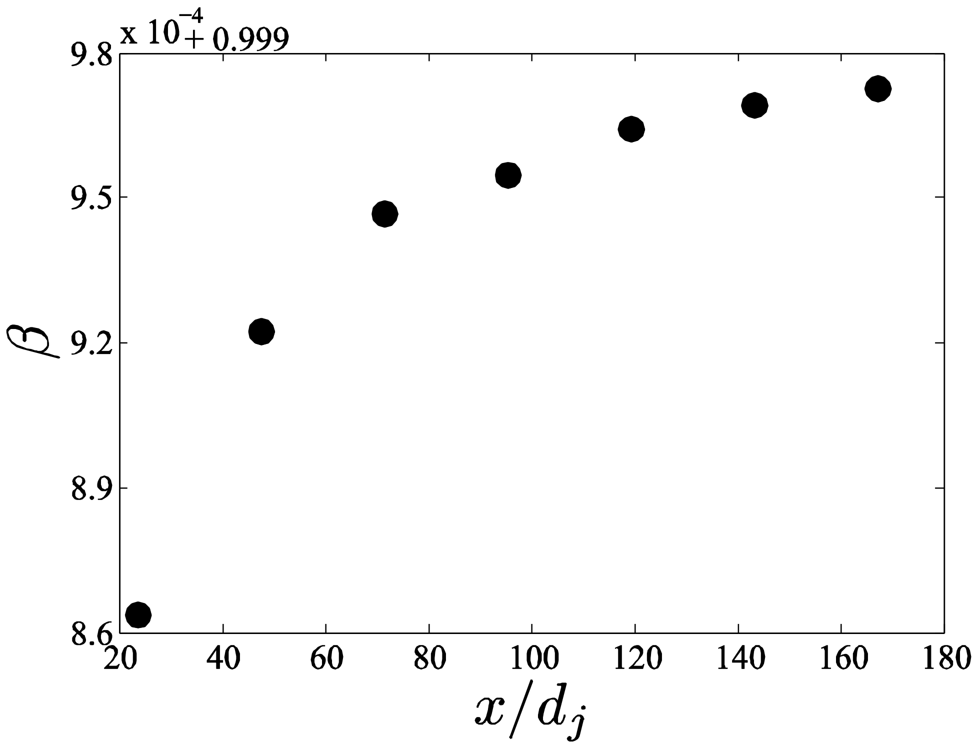

Figure A.4: Void fraction with respect to jet axial distance normalised by spray exit diameter.

From the void fraction, the theoretical true gas velocity can be deduced using equation A.11.

$$u_g = \frac{V_g}{\beta} \quad , \quad u_l = \frac{V_l}{1-\beta} \qquad \text{A.11.}$$

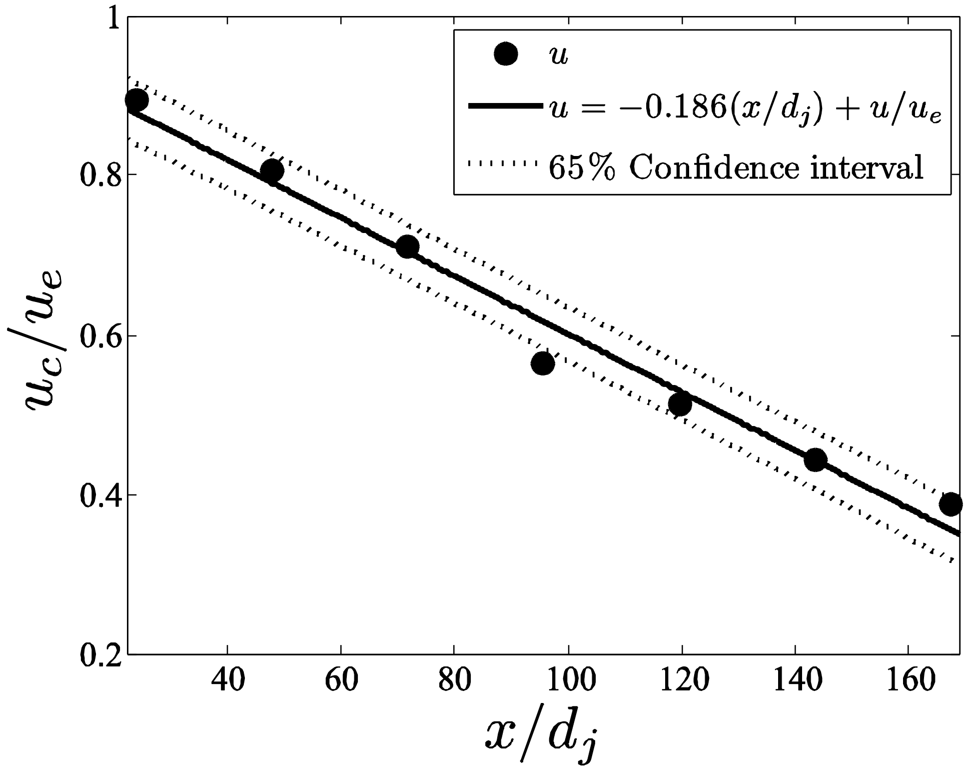

Figure A.5: Computation of the centreline velocity decay normalised with the spray exit velocity

The theoretical gas velocity obtained from mass flow rate information produces very similar decay rates and max *u* values to that observed by both the PIV and SSE-PIV experiments. Similarly, as the flow is assumed to be homogeneous, there is also a mixture density and a mixture viscosity that are calculated using equations A.13 and A.14.

$$\rho_h = \rho_g \beta_{mix} + \rho_l (1 - \beta_{mix}) \qquad \text{A.12.}$$

$$\frac{1}{\rho_{mix}} = \frac{\zeta}{\rho_g} + \frac{1-\zeta}{\rho_l} \qquad \text{A.13.}$$

$$\frac{1}{\mu_{mix}} = \frac{\zeta}{\mu_g} + \frac{1-\zeta}{\mu_l} \qquad \text{A.14.}$$

The homogenous density is calculated to be 1.34 kg/m^3 at $x/d_j \approx 23$. This value decreases to 1.23 kg/m^3 at $x/d_j \approx 167$ and asymptotes to ρ_g at $x/d_j > 167$. The plotted data can be seen on figure A.6. With the addition of the liquid phase, the density increases very little. This is due to the low amount mass per unit volume of liquid introduced upstream of the nozzle. Since the mass flow rate of liquid is fixed and the mass flow rate of air is increasing due to entrainment, the liquid phase starts dense and then become sparse. This is the cause of the reduction in density as the jet expands downstream.

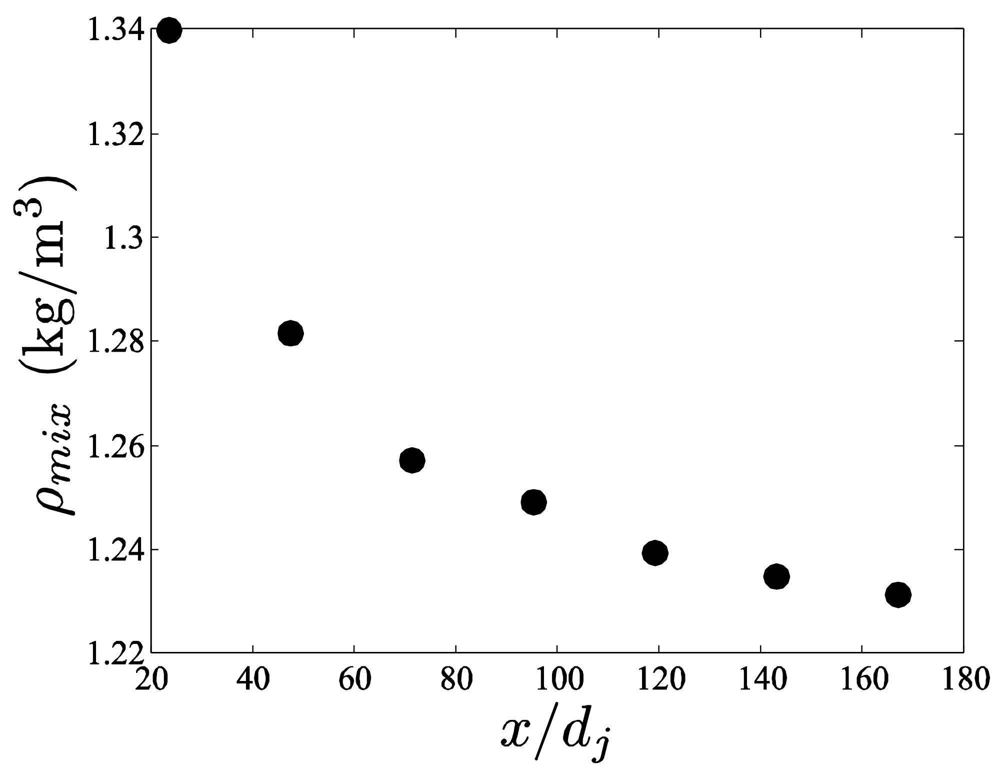

Figure A.6: Mixture density with respect to jet axial distance normalised by spray exit diameter.

The homogenous viscosity is calculated at 6x10^{-6} kg/ms at $x/d_j \approx 23$. This value decreases to 12x10^{-6} kg/ms at $x/d_j \approx 167$ and asymptotes to μ_{mix}. The plotted data can be seen on figure A.7. The increase in void fraction drives the increase of homogeneous viscosity.

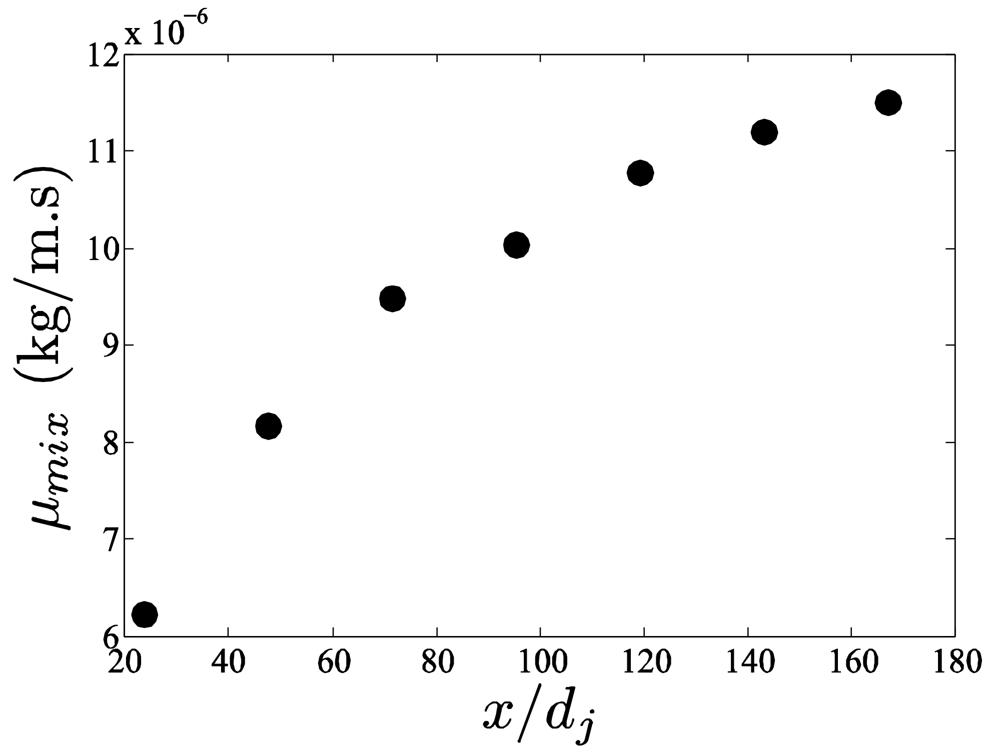

Figure A.7: Homogeneous viscosity with respect to jet axial distance normalised by spray exit diameter.

Using the homogenous flow model and the calculated mixture density and viscosity, the mixture effects on the local Reynolds number is obtained by equation A.15,

$$Re_{mix} = \frac{Gd}{\mu_{mix}} \qquad \text{A.15.}$$

where d is the jet diameter at each axial position. The local Reynolds number describes the flow state at a given cross-flow plane. Figure A.8 describes the decrease of local Reynolds number in the streamwise direction. The local Reynolds number decreases from $1.5\text{x}10^5$ at $x/d_j \approx 23$ to $1.1\text{x}10^5$ at $x/d_j \approx 167$. The decay of local Reynolds number is fairly linear and would suggest a maximum local Reynolds number of approximately $1.6\text{x}10^5$ at the nozzle exit.

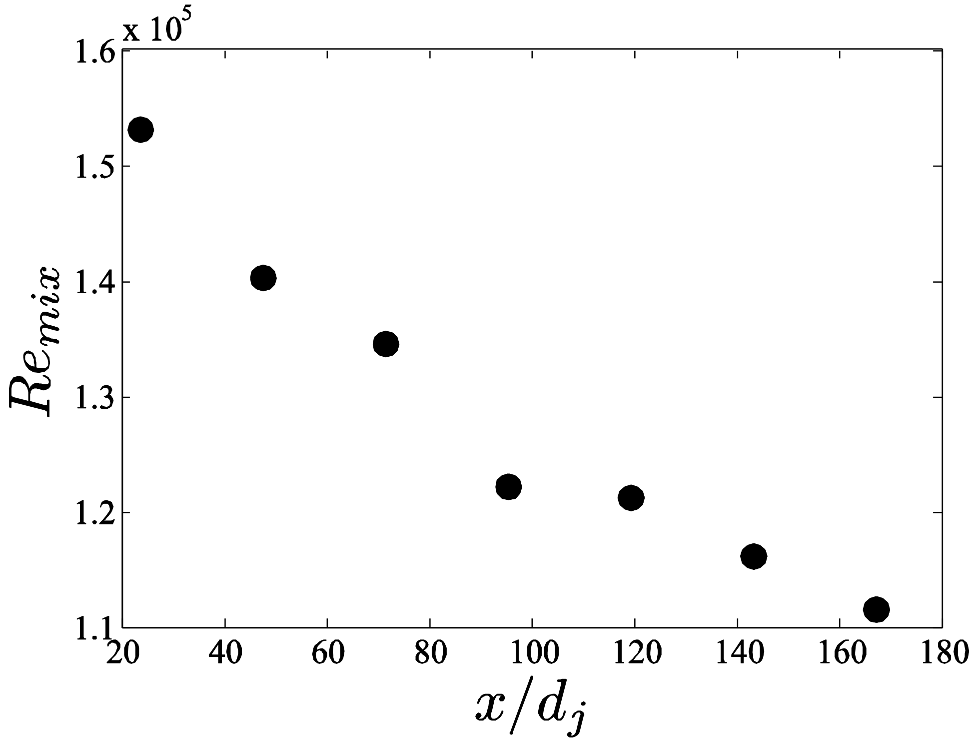

Figure A.8: Variation of local Reynolds number with streamwise position normalised by the spray exit diameter.

APPENDIX B

Introduction to droplet sizing

In order to measure the droplet size in the current spray flow regime a direct image analysis technique was applied. The details of this technique are given in Lad *et al*. (2011). There are several difficulties in obtaining accurate droplet size due to the spray behaviour is given in Lefebvre (1989). These include the higher concentration of drops in a spray, the high and changing velocity of the drops, the wide range of drop sizes and the changes of drop size with time through evaporation and coalescence processes.

The accuracy of a digital image analysis (DIA) technique is for spray droplet characterisation is found comparable with other known devices such as the PDA given in Blaisot and Yon (2005) and Kashdan *et al.* (2003).

Application of the DIA technique

Lad *et al.* (2011b) carried out a study using an in house DIA particle sizing technique developed by Muhamad (2011). The DIA technique has been developed for the automated determination of the properties of droplets such as its size. It uses a 8-bit digital shadow image of the spray.

Experimental setup

The DIA technique is based on the extraction of information from the digital images. In order to acquire these images, several components or equipments have been utilised. The following sub-topics describe the function of each component and also explain about the DIA system setup.

Components of the DIA system

There are three main components used in the development of DIA system, they include a laser, a digital camera and a computer as shown in Figure B.1. The analysis software was developed by Muhamad (2011).

Figure B.1 shows a basic schematic for the hardware setup. A more detailed description is shown in Lad *et al.* (2011b). The pulsed laser backlit a screen to produce shadows of droplets to be captured using a CCD camera. The maximum output of the laser was 200 mJ and it produced a pulsed beam of wavelength 532 nm. The laser beam was converted to a laser cone using a concave lens, and then it was diffused by a diffusive screen. The laser system has produced a trigger signal and it occurred at about 2 μs before the laser pulsed. This trigger signal was used to synchronise the detection of the digital camera. The output of the signal is +5V TTL and is a positive edge.

Digital camera was used to capture shadow images of the droplets which were back-lighted by the diffused light. The DIA technique was applied to process and analyse the images to determine droplet size distribution in real-time using custom developed software. A FireWire type camera was selected as part of the DIA system development. It equipped with IEEE1394-b connectors to allow high image transfer speed. This monochrome camera has a resolution up to 1280x960 pixels. It also has an ability to receive an external triggering signal for synchronization with the pulsed laser.

The purpose of DIA system was to characterise small particles or droplets in the range of micron sizes. Thus, it was important to have a higher magnification of image. Therefore, a 200 mm micro-lens equipped with a spacer or bellow was used in this study. As a result, field of view (FOV) of the image with a resolution of 1280 x 960 pixels was at 1.82 mm x 1.36 mm. The optical configuration of this current setup has produced a magnification factor of 2.6 and having a 250 mm working distance.

The DIA system was equipped with a computer for controlling the laser and the camera. The developed software was installed in this computer and used as a platform for synchronisation between the pulsed laser and the camera. A monitor of the computer was used to display on-line results. These results were obtained from the developed software where the software automatically processed and analysed the acquired images and plotted them into graphs.

Working principle of the DIA system

In this experiment, the DIA system was applied to perform an on-line characterisation of spray droplets. A schematic diagram of the system setup was depicted in Figure B.1.

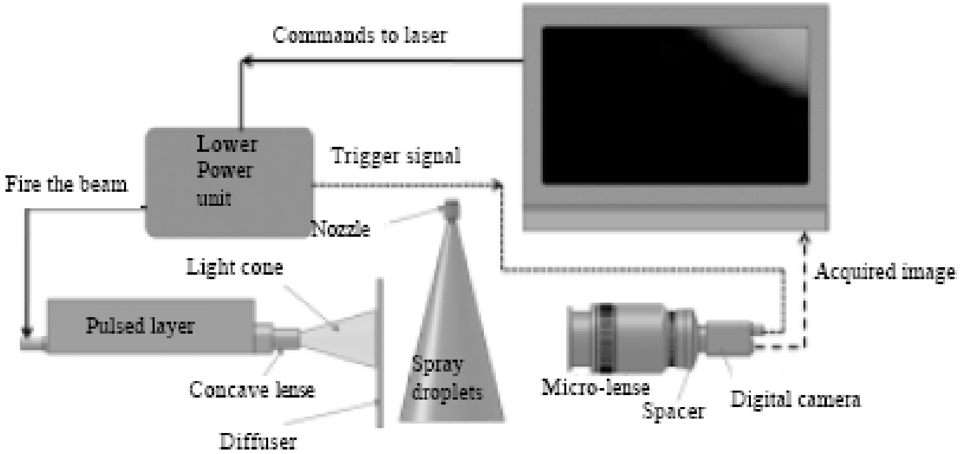

Figure B.1: Schematic of the droplet sizing hardware setup sourced from Lad *et al.* (2011b).

A computer was used to send commands to the laser to fire the beam at required light intensity. The commands were written using windows hyperterminal program and sent to a laser power supply via serial RS-232 cable. Once the commands were entered, the pulsed beam was fired from the laser unit and converted to laser cone by a concave lens. The repetition rate and duration of this pulsed were about 0.5 Hz and 5 μs, respectively. The droplets were back-lighted with a light source and the camera acquired the shadow image of the drops in a sequence of frames.

At about 2 μs before the laser pulsed, a trigger signal was produced from the laser power supply unit. This signal was then triggered the camera to acquire a raw image of the drops. The resolution of acquired image was at 1280 x 960 pixels. The working distance between the drops and a focal lens was about 250 mm. The image was then directly transferred from the camera to a memory of computer via IEEE-1394b

FireWire cable for instant processing. The image was processed and analysed using the developed software in order to obtain the droplet size distribution and the mean size.

Digital image processing and analysis: The DIA technique was applied to extract valuable information from an image. The analysis of captured a captured image is fundamentally carried out in four stages. The captured image is enhanced, segmented, the statistical results are presented in the software and then the statistical results are analysed and plotted. Details of these processes are given in Muhamad (2011) and the raw image to processed image is shown in figure B.2.

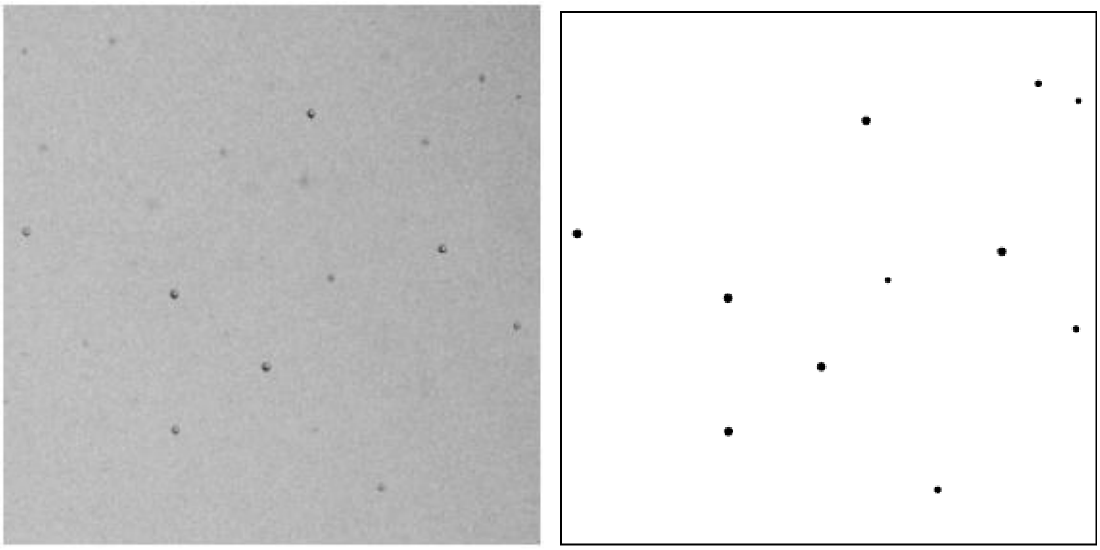

Figure B.2: Example of a captured raw image on the left and processed image on the right.

The algorithm also determined the number of spray droplets per image. The algorithm of result presentation was created to calculate the droplets diameter based on the area of the drops given in equation B.1

$$D_p = 2\sqrt{\frac{A_p}{\pi}} \qquad \text{B.1.}$$

where, D_p was the equivalent droplet diameter and A_p was the area of the drop. This developed software has identified every drop in the image and maintained a list of data that contains information regarding each of the drops.

The results of the droplet sizing are shown in figure B.3 to figure B.5. Figure B.3 to figure B.5 shows the droplet sizing statistical distributions as the spray axial location is increased. The results show that the mean droplet size decreases to 33.4 μm, 31.8 μm, and 29.9 μm at axial locations x/d_j =23, x/d_j =95, and x/d_j =167 respectively. The Sauter mean diameter (SMD) is measured to be 52.0 μm, 44.1 μm, and 40.9 μm at axial locations x/d_j =23, x/d_j =95, and x/d_j =167 respectively.

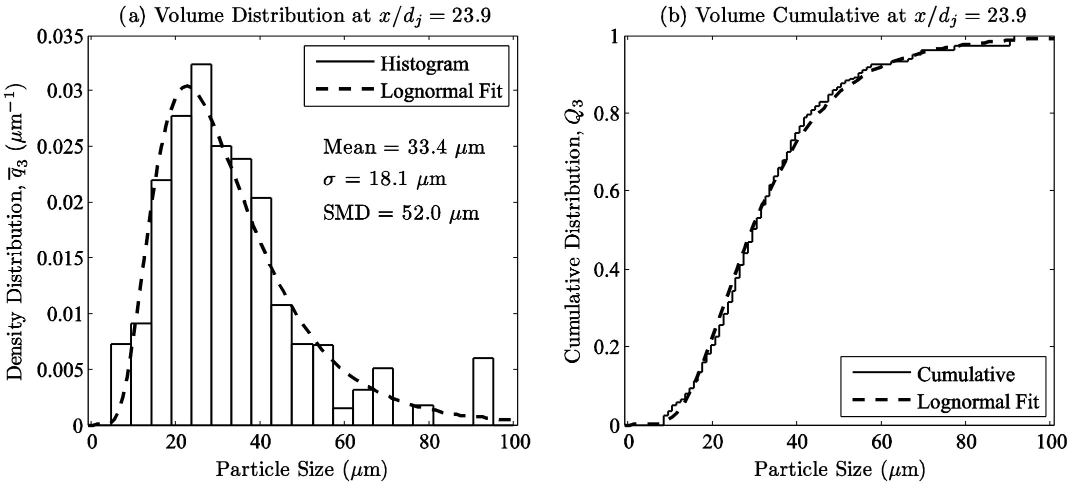

Figure B.3: Statistical mean of droplet sizing and distribution (*a*) and the cumulative distribution (*b*) at x/d_j=23.

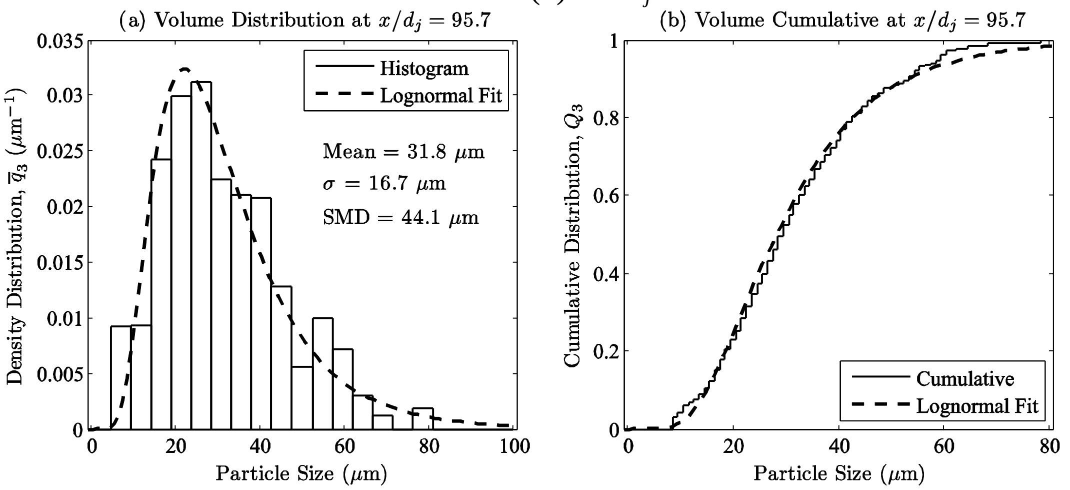

Figure B.4: Statistical mean of droplet sizing and distribution (*a*) and the cumulative distribution (*b*) at x/d_j=95.

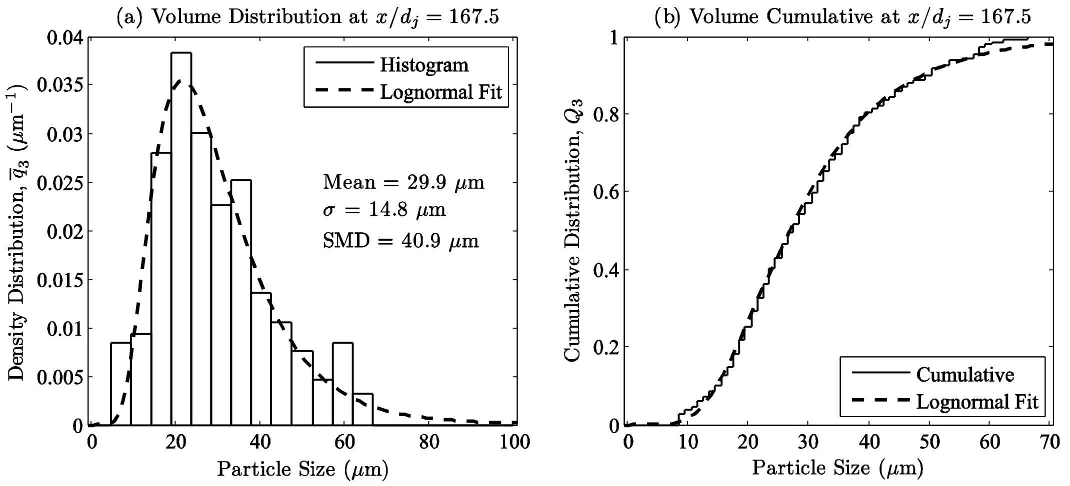

Figure B.5: Statistical mean of droplet sizing and distribution (*a*) and the cumulative distribution (*b*) at x/d_j=167.

REFERENCES

ABRAMOVICH, G. N. (1963) *The theory of turbulent jets*, Cambridge, M.I.T. Press.

ADEBAYO, D., LAD, N. & AROUSSI, A. (2008a) Passive control techniques of flow around an endoscopic PIV probe, *International conference on computational heat and mass transfer*, Guangzhou, China, May 18-21, 2009.

ADEBAYO, D., AROUSSI, A. & LAD, N. (2008b) Flow control of an annular cylinder with a circular probe, *International conference of hydrocarbon and chemistry*, Ghardaia, Algeria, April 21-24, 2008.

ADEBAYO, D., AROUSSI, A. & LAD, N. (2009) Characterisation of annular flow in turbomachinery applications, *4th Congres Algerien de genie des procedes*, Alger, Algeria, May, 04-06, 2009.

ADEBAYO, D., AROUSSI, A. & LAD, N. (2010a), The instability of fluid motion in an annular cavity with various width gap, *International symposium of hydrocarbon systems*, Algeria, May 23-15 , 2010.

ADEBAYO, D., AROUSSI, A. & LAD, N. (2010b) Experimental investigation of flow around an endoscopic probe in rotating machinery, *14th International symposium of flow visualisation*, Daegu, Korea, June 21-24, 2010.

ADRIAN, R. J. (1988) Double exposure, multiple-field particle image velocimetry for turbulent probability density, *Optics and Lasers in Engineering*, **9**, pp. 211-228.

ADRIAN, R. J. (1991) Particle-imaging techniques for experimental fluid mechanics, *Annual Review of Fluid Mechanics*, **23**, pp. 261-304.

ADRIAN, R. J. & YAO, C. S. (1985) Pulsed laser technique application to liquid and gaseous flows and the scattering power of seed materials, *Applied Optics*, **24**, pp. 44-52.

ALBERTSON, M. L., DAI, Y. B., JENSEN, R. A. & ROUSE, H. (1950) Diffusion of submerged jets, *Trans. A.S.C.E*, **115**, pp. 639-664.

ÁLMACO, J. C. D. & JIMÉNEZ, J. (2009) Estimation of turbulent convection velocities and correction to Taylor's approximation, *Journal of Fluid Mechanics*, **640**, pp. 5-26.

AROUSSI, A. & MENACER, M. (2004) Planar light sheet probes. *patent: US 6,762,827 B2.* The University of Nottingham.

AROUSSI, A., LAD, N. & ADEBAYO, D. (2008) Characterisation of flow around a cylindrical probe, *International conference of hydrocarbon and chemistry*, Ghardaia, Algeria, April 21-24, 2008.

AROUSSI, A., LAD, N. & ADEBAYO, D. (2009a) Intrusive effects of a circular obstacle in a particulate laden flow, *4th Congres Algerien de genie des procedes*, Alger, Algeria, May, 04-06, 2009.

AROUSSI, A., LAD, N. & ADEBAYO, D. (2009b) An experimental scrutiny of the factors influencing an effective mineral separation in froth flotation, *4th Congres Algerien de genie des procedes*, Alger, Algeria, May, 04-06, 2009

AROUSSI, A., LAD, N., MUHAMAD SAID, M.F., ADEBAYO, D. & AL-ATABI, M. (2010) The interaction of a cold atomised spray with a circular cylinder, *Journal of Engineering Science and Technology*, **5**, 3, pp. 161-372.

AROUSSI, A., ADEBAYO, D. & LAD, N. (2010a) The effect of cyclone in a particulate laden gas distribution in a power plant, *International symposium of hydrocarbon systems*, Algeria, May 23-15 ,2010

AROUSSI, A., LAD, N. & ADEBAYO, D. (2010b) Enclosed atomised spray flow mapping using a novel quantitative endoscopic laser measurement system, *International symposium of hydrocarbon systems*, Algeria, May 23-15 ,2010.

BAKKE, P. (1957) An experimental investigation of a wall jet, *Journal of Fluid Mechanics*, **2**, pp. 467-472.

BASARAN, O. A. (2002) Small-scale free surface flows with breakup: Drop formation and emerging applications, *American Institute for Chemical Engineers Journal*, **48**, pp. 1842-1848.

BECKER, H. A., HOTTEL, H. C. & WILLIAMS, G. C. (1967) The nozzle-fluid concentration field of the round, turbulent, free jet, *Journal of Fluid Mechanics*, **30**, pp. 285-303.

BELTAOS, S. & RAJARATNAM, N. (1973) Plane turbulent impinging jets, *IAHR Journal of Hydraulic Research*, **11,** pp. 29-59.

BELTAOS, S. & RAJARATNAM, N. (1974) Impinging circular turbulent jets, *ASCE Journal of Hydraulic Engineering*, **100**, pp. 1313-1328.

BIRKHOFF, G. & ZARANTONELLO, E. H. (1957) *Jets, wakes, and cavities*, New York, Academic Press

BLAISOT, J. B. & YON, J. (2005) Droplet size and morphology characterization for dense sprays by image processing: Application to the diesel spray, *Experiments in Fluids*, **39**, pp. 977-994.

BOGUSLAWSKI, L. & POPIEL, C. O. (1979) Flow structure of the free round turbulent jet in the initial region, *Journal of Fluid Mechanics*, **90**, pp. 531-539.

BRADBURY, L. J. S. (1965) The structure of a self-preserving turbulent plane jet, *Journal of Fluid Mechanics*, **23**, pp. 31-64.

BRAHMA, R. K., FARUQUE, O. & ARORA, R. C. (1991) Experimental investigation of mean flow characteristics of slot jet impingement on a cylinder, *Heat and Mass Transfer*, **26**, pp. 257-263.

CECCON, S., AUTERI, F., BARON, A., BELAN, M., GILBERTINI, G. & QUADRIO, M. (2006) Turbulent flow in a helically coiled pipe: An endoscopic PIV study, *DIA-SR 06-09*, Politecnico di Milano, Dipartmento di Ingegneria Aerospaziale.

CHHABRA, S., SHIPMAN, T. N. & PRASAD, A. K. (2005) The entrainment behaviour of a turbulent axisymmetric jet in a viscous host fluid, *Experiments in Fluids*, **38**, pp. 70-79.

CHOU, Y.-W., HSIAO, F.-B., HSU, C.-C. & HUANG, J.-M. (2002) Vortex dynamics and energy transport of a plane jet impinging upon a small cylinder, *Experimental Thermal and Fluid Science*, **26,** pp. 445-454.

CHOU, Y. W., CHENG, C. K., SHEU, S. S. & HSIAO, F. B. (1996) Self-sustained oscillating vorticies of a planar jet impinging upon a small cylinder, *6th International Symposium on Flow Modelling and Turbulence Measurements*, pp. 133-140.

COSSALI, G. E. (2001) An integral model for gas entrainment into full cone sprays, *Journal of Fluid Mechanics*, **439,** pp. 353-366.

COUTIER-DELGOSHA, O. & DEVILLERS, J. F. (2003) Experimental and numerical study of the cavitating flow on a hydrofoil, *American Society of Mechanical Engineers Conference Proceedings***,** pp. 1365-1371.

COWEN, E. A. & MONISMITH, S. G. (1997) A hybrid digital particle tracking velocimetry technique, *Experiments in Fluids*, **22,** pp. 199-211.

CROWE, C. T., SOMMERFIELD, M. & TSUJI, Y. (1998) *Multiphase Flows with Droplets and Particles*, Boca Raton, USA., CRC Press.

DIERKSHEIDE, U., MEYER, P., HOVESTADT, T. & HENTSCHEL, W. (2001) Endoscopic 2D-PIV flow field measurements in IC engines, *4th International Symposium on Particle Image Velocimetry*, Gottingen, Germany.

DIERKSHEIDE, U., MEYER, P., HOVESTADT, T. & HENTSCHEL, W. (2002) Endoscopic 2D particle image velocimetry (PIV) flow field measurements in IC engines, *Experiments in Fluids*, **33,** pp. 794-800.

DONALDSON, C. D. & SNEDEKER, R. S. (1971) A study of free jet impingement. Part 1. Mean properties of free and impinging jets, *Journal of Fluid Mechanics*, **45,** pp. 281-319.

DONALDSON, C. D., SNEDEKER, R. S. & MARGOLIS, D. P. (1971) A study of free jet impingement. Part 2. Free jet turbulent structure and impingement heat transfer, *Journal of Fluid Mechanics*, **45,** pp. 477-512.

EVERITT, K. W. & ROBINS, A. G. (1978) The development and structure of turbulent plane jets, *Journal of Fluid Mechanics*, **88,** pp. 563-583.

FAETH, G. M. (1987) Mixing, transport and combustion in sprays, *Progress in Energy and Combustion Science*, **13,** pp. 293-345.

FAETH, G. M. (1991) Structure and atomization properties of dense turbulent sprays, *Symposium (International) on Combustion*, **23,** pp. 1345-1352.

FAETH, G. M. (1996) Spray combustion phenomena, *International Symposium on Combustion*, **26,** pp. 1593-1612.

FAETH, G. M., HSIANG, L. P. & WU, P. K. (1995) Structure and breakup properties of sprays, *International Journal of Multiphase Flow*, **21,** pp. 99-127.

FLECKHAUS, D., HISHIDA, K. & MAEDA, M. (1987) Effect of laden solid particles on the turbulent flow structure of a round free jet, *Experiments in Fluids*, **5,** pp. 323-333.

FORTHMAN, E. (1936) Turbulent Jet Expansion, *NACA Tech. Memo. No.789*, Washington, USA.

FOUCAUT, J. M., MILIAT, B., PERENNE, N. & STANISLAS, M. (2004) Characterization of different PIV algorithms using the EUROPIV synthetic image generator and real images from a turbulent boundary layer, *Proceeding of the EUROPIV 2 workshop on particle image velocimetry*, Springer, Berlin Heidelberg New York, pp.163–186

GAUNTNER, J., LIVINGOOD, N. B. & HRYCAK, P. (1970) Survey of literature on flow characteristics of a single turbulent jet impinging on a flat plate, *NASA TN D-5652*, Lewis Research Centre, USA.

GEBAUER, H. (2009) Fibre delivery of 50 mJ, *DEL-2.6-LHZ*, PROVAEN (Process Visualisation and Analysis Endoscope System), STREP 032669, European Commission, 6th Framework.

GEIS, T., ROTTENKOLBER, G., DITTMANN, M., RICHTER, B., DULLENKOPF, K. & WITTIG, S. (2002) Endoscopic PIV-measurements in an enclosed rotor-stator system with pre-swirled cooling air, *11th International Symposium on Applications of Laser Techniques to Fluid Mechanics*, Lisbon, Portugal.

GINDELE, J. & SPICHER, U. (1998) Investigation of in-cylinder flow inside IC engines using PIV with endoscopic optics, *9th Int. Symposium on Application of Laser Techniques to Fluid Mechanics*, **31**.

GLAUERT, M. B. (1956) The wall jet, *Journal of Fluid Mechanics*, **1,** pp. 625-643.

GORDON, R. & AKFIRAT, J. C. (1965) The role of turbulence in determining heat transfer characteristics of impinging jets, *International Journal of Heat and Mass Transfer*, **8,** pp. 1261-1272.

GUTMARK, E., WOLFSHTEIN, M. & WYGNANSKI, I. (1978) The plane turbulent impinging jet, *Journal of Fluid Mechanics*, **88,** pp. 737-756.

HAND, D. P., ENTWISTLE, J. D., MARIER, R. R. J., KUHN, A., GREATED, C. A. & JONES, J. D. C. (1999) Fibre optic beam delivery system for high peak power laser PIV illumination, *Measurement Science and Technology*, **10,** pp. 239-245.

HART, D. P. (2000) PIV error correction, *Experiments in Fluids*, **29,** pp. 13-22.

HOST-MADSEN, A. & MCCLUSKEY, D. R. (1994) On the accuracy and reliability of PIV measurements, *7th International Symposium on Application of Laser Techniques to Fluid Mechanics*, pp. 214-226.

HSIAO, F.-B., HSU, I. C. & HUANG, J.-M. (2004) Evolution of coherent structures and feedback mechanism of the plane jet impinging on a small cylinder, *Journal of Sound and Vibration*, **278,** pp. 1163-1179.

HSIAO, F. B., CHOU, Y. W. & HUANG, J. M. (1999) The study of self-sustained oscillating plane jet flow impinging upon a small cylinder, *Experiments in Fluids*, **27,** pp. 392-399.

KANG, S. H. & GREIF, R. (1992) Flow and heat transfer to a circular cylinder with a hot impinging air jet, *International Journal of Heat and Mass Transfer*, **35,** pp. 2173-2183.

KARPETIS, A. N. & GOMEZ, A. (1999) Self-similarity, momentum scaling and Reynolds stress in non-premixed turbulent spray flames, *Journal of Fluid Mechanics*, **397,** pp. 231-258.

KASHDAN, J. T., SHRIMPTON, S. & WHYBREW, A. (2003) Two-phase flow characterization by automated digital image analysis. Part 1: Fundamental principles and calibration of the technique, *Particle and particle systems characterisation*, **20**, pp. 387-397

KEANE, R. D. & ADRIAN, R. J. (1990) Optimization of particle image velocimeters part 1: Double pulsed systems, *Measurement Science and Technology*, **1,** pp. 1202-1215.

KEANE, R. D. & ADRIAN, R. J. (1991) Optimization of particle image velocimeters, II. Multiple pulsed systems, *Measurement Science and Technology*, **2,** pp. 963-974.

KEANE, R. D. & ADRIAN, R. J. (1992) Theory of cross-correlation analysis of PIV images, *Applied Scientific Research*, **49,** pp. 191-215.

KEANE, R. D., ADRIAN, R. J. & ZHANG, Y. (1995) Super-resolution particle image velocimetry, *Measurement Science and Technology*, **6,** pp. 754-768.

KEGALJ, M. & SCHIFFER, H.-P. (2009) Endoscopic PIV measurements in a low pressure turbine rig, *Experiments in Fluids*, **47,** pp. 689-705.

KLAR, M., JEHLE, M., JAHNE, B., DETERT, M., JIRKA, G. H., KOHLER, H. J. & WENKA, T. (2004) Simultaneous 3-D PTV and micro-pressure sensor equipment for flow analysis in a subsurface gravel layer, In: Greco M, Carravetta A, Della Morte R (eds), *Proceedings of the 2nd International Conference on Fluvial Hydraulics*, Napoli, Italy.

KLEINSTREUER, C. (2003) *Two-phase flow: theory and applications*, New York, USA., Taylor & Francis Books.

KOSASIH, P. B., TIEU, A. K. & LI, E. B. (2001) PIV study of lubricant flow in journal bearing supply pocket, *14th Australasian Fluid Mechanics Conference*, Australia, pp. 481-484.

KOTSOVINOS, N. E. (1976) A note on the spreading rate and virtual origin of a plane turbulent jet, *Journal of Fluid Mechanics*, **77,** pp. 305-311.

LAD, N., AROUSSI, A. & ADEBAYO, D. (2008b) Flow visualisation of flow around an endoscopic PIV probe, *International conference of hydrocarbon and chemistry*, Ghardaia, Algeria, April 21-24, 2008.

LAD, N., AROUSSI, A. & ADEBAYO, D. (2008a) Flow visualisation inside a lab scale flotation cell using CFD and experimental techniques, *International conference of hydrocarbon and chemistry*, Ghardaia, Algeria, April 21-24, 2008.

LAD, N., AROUSSI, A. & ADEBAYO, D. (2009) Visualisation of process flows with a novel laser sheet endoscopic system, *4th Congres Algerien de genie des procedes*, Alger, Algeria, May, 04-06, 2009.

LAD, N., AROUSSI, A. & ADEBAYO, D. (2010) Experimental and computational characterisation of atomised spray flow around a circular cylinder, *Progress in Computational Fluid Dynamics*, **10**, 4, pp. 232-238.

LAD, N., AROUSSI, A. & ADEBAYO, D. (2010b) Effective mineral and ore recovery from waste slurry using flotation technology, *International symposium of hydrocarbon systems*, Algeria, May 23-15 ,2010

LAD, N., AROUSSI, A.& ADEBAYO, D. (2010c) Near wall spanwise PIV measurement of technique of fluid structure interaction within an atomised spray, *World engineering and science and technology congress* (ESTCON), Kuala Lumpur, Malaysia June 15-17, 2010.

LAD, N., AROUSSI, A., MUHAMAD SAID, M.F., ADEBAYO, D. & AL-ATABI, M. (2010d) The interaction of a cold atomised spray with a circular cylinder, *Journal of Engineering Science and Technology*, **5**, 3, 161-372.

LAD, N., AROUSSI, A. & ADEBAYO, D. (2010e) Flow mapping of multiphase flows using a novel single stem endoscopic PIV Instrument, *14th International symposium of flow visualisation*, Daegu, Korea, June 21-24, 2010.

LAD, N., AROUSSI, A. & ADEBAYO, D. (2011a) Flow mapping of multiphase flows using a novel single-stem endoscopic particle image velocimetry instrument. *Measurement Science and Technology*, **22,** 064003 (9 pp.).

LAD, N., AROUSSI, A. & MUHAMAD SAID, M. F. (2011b) Droplet size measurement for liquid spray using digital image analysis technique, *Journal of Applied Sciences*, **11,** pp. 1966-1972.

LAD, N., AROUSSI, A., ADEBAYO, D. & AL-ATABI, M. (2011c) Characterisation of multiphase fluid-structure interaction using non-intrusive optical techniques, *Journal of Engineering Science and Technology*, **6**, 2, pp. 131-145.

LEE, J. H. W. (2003) *Turbulent Jets and Plumes: A Langrangian Approach*, The Netherlands, Kluwer Academic Publishers Group.

LEFEBVRE, A. H. (1989) *Atomization and Sprays*, New York, Hemisphere Publishing Company.

MARTIN, H., JAMES, P. H. & THOMAS F. IRVINE, JR. (1977) Heat and Mass Transfer between Impinging Gas Jets and Solid Surfaces, *Advances in Heat Transfer*, Elsevier.

MCNAUGHTON, K. J. & SINCLAIR, C. G. (1966) Submerged jets in short cylindrical flow vessels, *Journal of Fluid Mechanics*, **25,** pp. 367-375.

MIIKKULAINEN, P., JÄRVINEN, M. & KANKKUNEN, A. (2000) Black liquor spray properties in operating recovery boiler furnaces, *5th European Conference on Industrial Furnaces and Boilers*, Porto, Portugal.

MIIKKULAINEN, P., KANKKUNEN, A. & JÄRVINEN, M. P. (2004) Furnace endoscope-measuring fuel spray properties in hot and corrosive environments, *Experiments in Fluids*, **37,** pp. 910-916.

MUHAMAD SAID, M.F., LAD, N., AROUSSI, A. (2009) Impingement of a liquid spray on a convex surface, *4th Congres Algerien de genie des procedes*, Alger, Algeria, May, 04-06, 2009

MUHAMAD SAID, M. F. (2011) Development of particle sizing based on dynamic image analysis, *PhD Thesis*, Department of Engineering, University of Leicester, UK.

NAUWERCK, A., GINDELE, J. & SPICHER, U. (2000) Investigation of the transient in-cylinder flow inside a two-stroke engine with particle image velocimetry, *SAE Technical Paper*, Series 2000-01-09-02.

NISHIO, S. & MURATA, S. (2003) A numerical approach to the evaluation of error vector appearance possibility in PIV, *Proceedings of 5th International Symposium on Particle Image Velocimetry***,** pp. 3321.1-3321.9.

OKAMOTO, K., NISHIO, S., SAGA, T. & KOBAYASHI, T. (2000) Standard images for particle-image velocimetry, *Measurement Science and Technology*, **11,** pp. 685-691.

PAI, S. (1952) Axially symmetrical jet mixing of a compressible fluid, *Quarterly of Applied Mathematics*, **10,** pp. 141–148.

PARK, J. T., AOUAT, A. D., WU, B. & NISHIO, S. (2008) The specialist committee on uncertainty analysis, *Proceedings of 25th International Towing Tank Conference*, **2,** pp. 433-469.

PARRY, J. P., SHEPHARD, J. D., THOMSON, M. J., TAGHIZADEH, M. R., JONES, J. D. C. & HAND, D. P. (2007) Optical fibre array for the delivery of high peak-power laser pulses for fluid flow measurements, *Applied Optics*, **46,** pp. 3432-3438.

PAVLOVA, A. A., OTANI, K. & AMITAY, M. (2008a) Active control of sprays using a single synthetic jet actuator, *International Journal of Heat and Fluid Flow*, **29,** pp. 131-148.

PAVLOVA, A. A., OTANI, K. & AMITAY, M. (2008b) Active performance enhancement of spray cooling, *International Journal of Heat and Fluid Flow*, **29,** pp. 985-1000.

POLAT, S., HUANG, B., MUJUMDAR, A. S. & DOUGLAS, W. J. M. (1989) Numerical flow and heat transfer under impinging jets: A review, **2**, pp. 157-197.

POREH, M., TSUEI, Y. G. & CERMAK, J. E. (1967) Investigation of a turbulent radial wall jet, *Journal of Applied Mechanics*, **34,** pp. 457-463.

QUÉRÉ, D. (1999) Coating of a Fibre, *Annual Review of Fluid Mechanics*, **31,** pp. 347-384.

RAFFEL, M., WILLERT, C., WERELEY, S. & KOMPENHANS, J. (2007) *Particle Image Velocimetry: A Practical Guide*, Springer Berlin.

RAJARATNAM, N. (1976) *Turbulent Jets (Developments in Water Science),* Amsterdam, Elsevier Scientific Publishing Company.

RAMSBOTTOM, A. (2009) Design of Optics through endoscope, *DEL-4.2-OLYUMPUS*, PROVAEN (Process Visualisation and Analysis Endoscope System). Project No: STRP 032669.

REEVES, M. & LAWSON, N. J. (2004) Evaluation and correction of perspective errors in endoscopic PIV, *Experiments in Fluids*, **36,** pp. 701-705.

REICHARDT, H. (1951) Vollständige Darstellung der turbulenten Geschwindigkeitsverteilung in glatten Leitungen, *ZAMM - Journal of Applied Mathematics and Mechanics / Zeitschrift für Angewandte Mathematik und Mechanik*, **31,** pp. 208-219.

RICOU, F. P. & SPALDING, D. B. (1961) Measurements of entrainment by axisymmetrical turbulent jets, *Journal of Fluid Mechanics*, **11,** pp. 21-32.

ROCKWELL, D. & NAUDASCHER, E. (1979) Self-sustained oscillations of impinging free-shear layers, *Annual Review of Fluid Mechanics*, **11,** pp. 67-94.

ROTTIER, C., GODARD, G., CORBIN, F., BOUKHALFA, A. M. & HONORÉ (2010) An endoscopic particle image velocimetry system for high-temperature furnaces, *Measurement Science and Technology*, **21**, 115404 (9 pp.).

RUFF, G. A., BERNAL, L. P. & FAETH, G. M. (1991) Structure of the near-injector region of a non-evaporating pressure-atomized sprays, *Journal of Propulsion and Power*, **7,** pp. 221-230.

RUFF, G. A., SAGAR, A. D. & FAETH, G. M. (1988) Structure and mixing properties of pressure-atomized sprays, *American Institute of Aeronautics and Astronautics*, paper no: 10198-831, 26th Aerospace Sciences Meeting**,** Reno, NV, Jan. 11-14, pp. 11.

RUFF, G. A., WU, P.-K., BERNAL, L. P. & FAETH, G. M. (1992) Continuous- and dispersed-phase structure of dense non-evaporating pressure-atomised sprays, *Journal of Propulsion and Power*, **8,** pp. 280-289.

SADEK, S. (2002) Soil structure interaction in transparent synthetic soils using digital image correlation, *PhD Thesis.* New York, Polytechnic University

SANTAMARINA, J. C. & FRATTA, D. (2005) *Introduction discrete signals and inverse problems: An introduction to engineers and scientists*, Chichester, West Sussex, John Wiley & Sons Ltd.

SCARANO, F. & RIETHMULLER, M. L. (1999) Iterative multigrid approach in PIV image processing with discrete window offset, *Experiments in Fluids*, **26,** pp. 513-523.

SCARANO, F. & RIETHMULLER, M. L. (2000) Advances in iterative multigrid PIV image processing, *Experiments in Fluids*, **29,** pp. S051-S060.

SCHAUER, J. J. & EUSTIS, R. H. (1963) The flow development and heat transfer characteristics of plane turbulent impinging jet, *Technical report 3*, California, USA., Stanford University.

SCHLICHTING, H. (1968) *Boundary Layer Theory (Sixth Edition)*, McGraw-Hill

SEINER, J. M. & PONTON, M. K. (1985) Acoustic data for high Reynolds number supersonic axisymmetric jets, *NASA TM-86296.*

SJÖDAHL, M. (1998) Some recent advances in electronic speckle photography, *Optics and Lasers in Engineering*, **29,** pp. 125-144.

STEPHENS, T. J. (2003) Fibre-optic delivery of high peak power laser pulses for flow measurement, *PhD Thesis*, Edinburgh, Heriot-Watt Univerity.

STIESCH, G. (2003) *Modelling Engine spray and combustion processes*, Springer.

TABRIZI, S. P. A. (1996) Jet impingement onto a circular cylinder, *PhD Thesis*, University of Liverpool, Liverpool, UK.

TAYLOR, G. I. (1938) The spectrum of turbulence, *Proceedings of the Royal Society London*, **164,** pp. 476-490.

TOLLMIEN, W. (1945) Calculation of Turbulent Expansion Processes, *Technical report A120108.*

TOWNSEND, A. A. (1976) *The structure of turbulent shear flows*, *2nd Edition*, Cambridge University Press.

VAN DER HEGGE ZIJNEN, B. (1958) Measurements of the velocity distribution in a plane turbulent jet of air, *Applied Scientific Research*, **7,** pp. 256-276.

VATTULAINEN, J., NUMMELA, V., HERNBERG, R. & KYTÖLÅ, J. (2000) A system for quantitative imaging diagnostics and its application to pyrometric in-cylinder flame-temperature measurements in large diesel engines, *Measurement Science and Technology*, **11,** pp. 103-119.

VEN DE HULST, H. C. (1957) *Light scattering by small particles*, New York (re-published 1981 NY Dover publications. New York), John Wiley & Sons, Inc.

WERNET, M. P. (2000) Application of DPIV to study both steady-state and transient turbomachinery flows, *Optics and Lasers Technology*, **32,** pp. 497-525.

WESTERWEEL, J. (1993) Efficient detection of spurious vectors in particle image velocimetry data, *Experiments in Fluids*, **16,** pp. 236-247.

WESTERWEEL, J. (2000) Theoretical analysis of the measurement precision in particle image velocimetry, *Experiments in Fluids*, **20,** pp. 165-177.

WESTERWEEL, J., ADRIAN, R. J., EGGELS, J. G. M. & NIEUWSTADT, F. T. M. (1992) Measurements with PIV in fully developed pipe flow at low Reynolds number, *Proceedings of the Sixth International Symposium on Applications of Laser Technique to Fluid Mechanics*, Lisbon, Portugal, July 20-23.

WHALLEY, P. B. (1996) *Two-Phase flow and heat transfer*, Oxford University Press, USA (July 18, 1996).

WILLERT, C. (1996) The fully digital evaluation of photographic PIV recordings, *Applied Scientific Research*, **56,** pp. 79-102.

WILLERT, C. & GHARIB, M. (1991) Digital particle image velocimetry, *Experiments in Fluids*, **10,** pp. 181-193

WILLERT, C., STASICKI, B., RAFFEL, M. & KOMPENHANS, J. (1995) A digital video camera for application of particle image velocimetry in high-speed flows, *Proc. SPIE 2546, International Symposium on Optical Science, Engineering and Instrumentation*, pp. 124-134.

XIONG, W., KALKÜHLER, K. & MERZKIRCH, W. (2003) Velocity and turbulence measurements downstream of flow conditioners, *Flow measurement and instrumentation*, **14,** pp. 249-260.

XIONG, W. & MERZKIRCH, W. (1999) PIV experiments using an endoscope for studying pipe flow, *Journal of Flow Visualisation and Image Processing*, **6,** pp. 167-175.